Large-Eddy Simulations on Unstructured Grids using Explicit Differential Filters in Approximate Deconvolution Models

Mostafa Najafiyazdi

Doctor of Philosophy

Department of Mechanical Engineering

McGill University

Montreal,Quebec

March 24, 2020

A dissertation submitted to McGill University in partial fulfillment of the requirements for the degree of Doctor of Philosophy

DEDICATION

To Atefeh,

my closest friend,

and my beloved wife,

without whose never-failing support and encouragement

I would not have persevered.

To my father, Abbas

who passed away too soon,

who would have loved to see this page.

ACKNOWLEDGEMENTS

I am deeply indebted to Prof. Luc Mongeau and Prof. Siva Nadarajah, my supervisors, who guided me every step of the way in my PhD, and never wavered in their support. I learned a great deal from both of you, in research and in life. You provided me with encouragement and patience throughout the duration of this project. Thank you!

I would also like to extend my deepest gratitude to my committee, Prof. Evgeny Timofeev and Prof. Jeffery Bergthorson for their valuable feedback and advice. I very much appreciate Dr. Alireza Najafi-Yazdi, whose idea was the starting point of this research. I also had great pleasure of being acquainted with Prof. Massimo Germano, whose seminal work were inspiring for this research. His feedback on the filter design was invaluable.

I am also grateful to Prof. Laurent Mydlarski who introduced me to the beautiful field of Turbulence, and who planted the seeds of understanding this amazing phenomenon. My special thanks to Prof. Jean-Christophe Neve from Department of Mathematics and Statistics, whose teachings and feedback at the early stages of my PhD studies gave me great amount of knowledge into Navier-Stokes equations. I would also like to recognize the value of Prof. Bahar Firoozabadi, who taught me the fundamentals of fluid mechanics and made me fall in love with this subject. I very much appreciate Dr. Hossein Afshin's unrelenting support in giving me unparalleled opportunities to learn and grow as an engineer and a scientist.

I very much appreciate Dr. Kaveh Habibi whose help cannot be overestimated for their intellectual insights and discussions. Special thanks to Pooya Saberi, my friend, my colleague and my office-mate who always had time for me to bounce ideas and to help me resolve the never-ending bugs, who healed my mind with his humor and company when I was tired in the office, a true witch doctor.

My research benefited from the generous funding from multiple sources for which I am grateful. Thanks to: the Natural Sciences and Engineering Research Council of Canada (NSERC) grant No. RGPIN/342783-2012, McGill Engineering Doctoral Award (MEDA), Lorne Trottier Scholarship, and the National Institute of Health (NIH) award No. DC005788.

This research would have not been possible without the generous contributions of Calcul Québec and Compute Canada. The computations in this dissertation were made on various supercomputers managed by Calcul Québec and Compute Canada, including Graham, Beluga, Niagra, Cedar, Guillimin, and Mamuth Parallel. Many thanks to the support teams who extended their help at the time of need.

I would like to acknowledge the support of Anne-Marie Pierre whose consistent follow-ups made the completion of this dissertation possible. Many thanks to Shirley Baxendale, Gregory Doyle, and Bibi Emina who were always present when I needed their help. Special thanks to Mary Fiorilli for her timely support for financial bureaucracies.

I cannot leave McGill without mentioning the amazing staff of the department of Mechanical Engineering, the engineering cafeteria, and the undergraduates working at Frostbite, the ice cream shop, whose smiles brought joy to my days.

Last but not least is my family. Thanks Alireza and Mohsen for your brotherly

supports during all these years. Thanks Mom, Shahrzad, who endured a lonely life back in Iran to support our education abroad. But above all, is my best friend, my hero, my goddess, and my wife, Atefeh. I have not enough words to express my thanks to you for your unwavering love, relentless support and profound belief in me and my abilities. When Matthew McConaughey mentioned the three things needed each day, I could not think of anyone or anything other than you! I lookup to you, you are my inspiration, my proud, and my model. I look forward to you. You taught me to take care of myself, our love and our relationship. You taught me to never give up and fight. You are my hero, the one I chase. You have been the most wonderful person that I have ever met. I chase your relentless, your fighting spirit, your dreaming big, and your belief that we can do it! Thanks for teaching me that the thrill of life is in its moments. Thanks for filling those moments with your presence, with your sacred touch.

ABSTRACT

In Computational Aeroacoustic (CAA) applications of Large-Eddy Simulations (LES), accurate control over turbulent kinetic energy (TKE) dissipation is needed to minimize aliasing and obtain accurate broad-band noise estimations. Among different LES approaches, Approximate Deconvolution Models (ADM) allow direct control of the TKE dissipation rate for the resolvable wavenumber scales. This control is obtained by applying an explicitly defined spatial filter on the computed flow fields. In ADM schemes, filtered Navier-Stokes equations are used where the filtering operator is explicitly defined. Approximate deconvolution approaches are used to estimate the unfiltered quantities used in constructing the nonlinear flux terms. Given a filter operator, the energy dissipation associated with filtering can be quantified. ADM has been successfully applied on structured grids using discrete high-order filter operators. Its application on unstructured grid has been very limited due to lack of a proper filter.

The objective of the present work was to extend the application of Approximate Deconvolution Models (ADM) for LES on unstructured grids by using explicit differential filters. Germano's elliptic differential filter was successfully extended to include two free parameters. One ensured full attenuation at grid cut-off wavenumber, preventing aliasing due to LES and stabilizing the numerical scheme. The other controlled the filter cut-off wavenumber. The discretized formulation of this differential filter was developed for two- and three-dimensional elements. Dissipation and dispersion properties of the discrete differential filter were investigated in detail.

A second-order classical finite element method (FEM) was used for spatial discretization of the compressible Navier-Stokes equations. Time integration was performed through the use of the standard fourth-order explicit Runge-Kutta scheme. Interpolation on high resolution grids was used to obtain the fast Fourier transform (FFT) of the flow fields on perturbed and unstructured grids.

Decaying isotropic homogeneous turbulence at Reynolds number $3,400$ was modeled on both structured and unstructured grids. Results were compared to a reference direct numerical simulation (DNS) and other LES results reported in the literature. The effect of mesh anisotropy on the newly proposed differential filter performance was studied. It was observed that stable and sufficiently accurate LES results could be obtained on unstructured grids, even in the presence of highly skewed elements. Careful examination of the dissipation rate in the resolved wavenumbers suggested that grid anisotropy induces different cut-off wavenumbers in different directions resulting in higher dissipation rates than those obtained on an isotropic mesh.

Taylor-Green vortex (TGV) was also studied as an excellent canonical problem for laminar to turbulence transition of a flow. LES simulations using the ADM framework were conducted in which the filter extended to three-dimensional elements was used. Investigative studies on the ADM order, the ADM under-relaxation coefficient, the degree of anisotropy in the grid, and grid resolution were performed to benchmark the filter performance in conjunction with ADM. Finally, an LES of TGV on a fully unstructured grid was performed showing the range of application of the proposed filter.

ABRÉGÉ

Dans les applications en aéroacoustique, les simulations numérique par la method des grands courants de Foucault requient un contrôle précis de la dissipation de l'énergie cinétique turbulente afinde réduire l'aliasing et obtenir des estimations précises du bruit à large bande. Parmi les différentes approches LES, les modèles de déconvolution approximative (MDA) permettent de contrôler directement le taux de dissipation de l'énergie cinétique pour les échelles de turbulence à des nombres d'ondes résolubles. Ce contrôle est obtenu en appliquant un filtre spatial explicitement défini sur les champs d'écoulement calculés. Dans les schémas MDA, les équations de Navier-Stokes filtrées sont utilisées lorsque l'opérateur de filtrage est explicitement défini. Des approches approximatives de déconvolution sont utilisées pour estimer les quantités non filtrées utilisées dans la construction des termes de flux non linéaires. La dissipation d'énergie associée au filtrage peut étre quantifiée. La MDA a été appliqué avec succès sur des grilles structurées en utilisant des opérateurs de filtres discret d'ordre élevé. Elle n'a pas, a ce jour, ét'e appliqué des grilles non structurées a en raison de l'absence d'un filtre approprié.

L'objectif de cette étude était d'étendre l'application des MDA sur des grilles non structurées en utilisant des filtres différentiels explicites. Pour le faire, le filtre différentiel elliptique de Germano a d'abod été généralise. Un paramétre assure une atténuation complète au numbro d'onde de coupure de la grille, empéchant l'aliasing et stabilisant le schéma numérique. Un deuxiéme paramétre permit de contrôler le nombre d'ondes de coupure du filtre. La formulation discréte de ce filtre différentiel

a été développée pour des éléments bidimensionnels et tridimensionnels. La dissipation et les propriétés de dispersion du filtre différentiel discéret sont été étudiées en détail.

Pour la discrétisation spatiale des équations de Navier-Stokes compressibles, on a utilisé une méthode classique du deuxième ordre par éléments finis (FEM). L'intégration temporelle a été réalisée à l'aide du schéma Runge-Kutta explicite standard du quatrième ordre. L'interpolation sur des grilles à haute résolution a été utilisée pour obtenir la transformée de Fourier des champs d'écoulement sur des grilles perturbées et non structurées.

La turbulence isotrope homogène au nombre de Reynolds $3,400$ a été modélisée sur des grilles structurées et non structurées. Les résultats ont été comparés à une simulation numérique directe (DNS) de référence et à d'autres résultats de l'étude LES présentés dans la littérature. L'effet de l'anisotropie du maillage sur la performance du filtre différentiel proposé a été étudié. Il a été observé que des résultats de LES stables et suffisamment précis pouvaient étre obtenus sur des grilles non structurées, même en présence d'éléments très asymétriques. Un éxamen attentif du taux de dissipation des nombres d'ondes résolus a suggéré que l'anisotropie de la grille induit des nombres d'ondes de coupure différents dans différentes directions, entraînant des taux de dissipation plus élevés que ceux obtenus sur un maillage isotrope.

Le vortex de Taylor-Green (VTG) a également été étudié comme problème canonique pour la transition d'écoulement laminaire en écoulement turbulent. Des simulations LES utilisant le cadre MDA ont été réalisées dans lesquelles le filtre étendu aux éléments tridimensionnels a été utilisé. Des études d'investigation sur l'ordre ADM, le coefficient de sous-relaxation MDA, le degré d'anisotropie dans la grille et la résolution de la grille ont été réalisées pour comparer la performance du filtre avec MDA. Enfin, un LES de VTG sur une grille entièrement non structurée a été réalisé montrant le domaine d'application du filtre proposé.

TABLE OF CONTENTS

LIST OF TABLES

LIST OF FIGURES

Figure | page

Nomenclature

Constants

γ_{air} = 1.4, Air specific heat ratio

C_1 $= 1.458 \times 10^{-6}\ kg/m.s.\sqrt{K}$ for air, a constant in Sutherland's law

C_2 $= 110\ K$ for air, A constant in Sutherland's law

Greek Symbols

α, β Filter parameters

$\check{\sigma}_{i,j}$ Favre-filtered shear stress tensor

$\delta_{i,j}$ Kronecker delta function

η Kolmogorov length scale

γ Specific heat ratio

κ Wavenumber

λ_i The i-th eigenvalue for $\boldsymbol{\mathcal{L}}$

μ Molecular viscosity

μ_c Characteristic molecular viscosity

μ_i The i-th eigenvalue for $\boldsymbol{\mathcal{M}}$

ν_i The i-th eigenvalue for $\boldsymbol{\mathcal{N}}$

Ω Spatial domain of interest, also known as compact support

ω_i Vorticity component along i axis

$\overline{\phi}$ A spatially filtered arbitrary flow property

ϕ An arbitrary flow property

Π_{dil} SGS pressure-dilatation

$\Pi_{i,j}$ Turbulent kinetic energy diffusion by pressure gradient

ρ Density

ρ_c Characteristic density

τ_η Kolmogorov time scale

$\tau_{i,j}$ Shear stress tensor

ε Dissipation rate of turbulent kinetic energy

ε_v SGS viscous dissipation rate of turbulent kinetic energy

$S_{i,j}$ Strain rate tensor

Mathematical Operators

$\mathcal{D}\{\cdot\}$ Approximate deconvolution operator of arbitrary order

$\mathcal{F}\{\cdot\}$ Fourier transform operator

$\mathcal{O}\{\cdot\}$ Big O notation

$\mathcal{Z}\{\cdot\}$ Bilateral Z-transform operator

Roman Symbols

$\check{q}_{i,j}$ Computable Favre-filtered heat flux

$\mathbb{C}_{i,j}$ Cross term in subgrid scale stress tensor for LES

$\mathbb{D}_{i,j}$ Turbulent kinetic energy diffusion by viscosity tensor

$\mathbb{L}_{i,j}$ Leonard term in subgrid scale stress tensor for LES

$\mathbb{P}_{i,j}$ Turbulent kinetic energy production tensor

$\mathbb{R}_{i,j}$ Reynolds term in subgrid scale stress tensor for LES

$\mathbb{T}_{i,j}$ Turbulent kinetic energy diffusion by velocity fluctuations

$\boldsymbol{\mathcal{L}}$ The characteristics wave amplitudes vector for inviscid fluxes along n_1 in a local frame of reference normal to a boundary

$\boldsymbol{\mathcal{M}}$ The characteristics wave amplitudes vector for inviscid fluxes along n_2 in a local frame of reference normal to a boundary

$\boldsymbol{\mathcal{N}}$ The characteristics wave amplitudes vector for inviscid fluxes along n_3 in a local frame of reference normal to a boundary

$\mathbf{F}$ Net flux vector in Navier-Stokes equations

$\mathbf{F}_v$ Viscous flux vector in Navier-Stokes equations

$\mathbf{F}_{inv}$ Inviscid flux vector in Navier-Stokes equations

$\mathbf{M}$ Mass matrix of a FEM for Navier-Stokes equations

$\mathbf{M}_f$ Mass matrix for the left hand side of a FEM for filter

$\mathbf{N}_f$ Mass matrix for the right hand side of a FEM for filter

$\mathbf{RHS}$ Right hand side of a for Navier-Stokes equations

$\mathbf{RHS}_f$ Right hand side of a FEM for filter

$\mathbf{U}$ Vector of conserved variables

$\mathbf{U}_n$ Conservative variables expressed in a local frame of reference normal to a boundary

$\mathcal{F}_{inv,j}$ Inviscid flux vector along the n_j direction in a local frame of reference normal to a boundary

$\mathcal{F}_{visc,j}$ Viscous flux vector along the n_j direction in a local frame of reference normal to a boundary

$\mathcal{G}$ Filter transfer function in the spectral (Fourier) space

$\mathcal{L}_k$ The k-th characteristics wave amplitude for inviscid fluxes along n_1 in a local frame of reference normal to a boundary

$\mathcal{Q}$ Approximate deconvolution (inverse filter) transfer function in the spectral domain

$\mathcal{X}[z]$ Bilateral Z-transform of a uniformly sampled data

B_i SGS terms defined in Vreman's system I formulation for $i = 1, \cdots, 7$

c_c Characteristic speed of sound

c_p Heat capacity per unit mass at constant pressure

c_v Heat capacity per unit mass at constant volume

E Turbulent kinetic energy

e_i Internal energy per unit mass, a.k.a. specific internal energy

e_t Total energy per unit mass, a.k.a. specific total energy

f Frequency

f_s Sampling Frequency

G A filter kernel

h specific enthalpy

I Identity matrix

k Thermal conductivity

L_c Characteristic length

Ma Mach number

Ma_c Characteristic Mach number

p Static pressure

p_c Characteristic pressure

Pr	Prandtl number
q_i	Heat flux component along i axis
Q_j	SGS temperature flux
Q_M	An m-th order approximate deconvolution operator kernel
R	Gas constant
Re	Reynolds number
T	Mapping function from an arbitrary element in the physical domain to a reference element in the computational domain
T	Static temperature
t	Time
T_c	Characteristic temperature
U_c	Characteristic velocity
u_i	Velocity component along i axis
x	Spatial coordinate
$x[n]$	A discrete signal with n samples
z	A complex variable

Superscripts, Subscripts, and Accents

$(\cdot)''$	Sub-grid scale quantity
$(\cdot)_c$	Characteristic quantity
$(\cdot)_N$	A term projected onto a discretized computational domain
$(\cdot)_\infty$	Free stream condition
$(\cdot)_{disc}$	A term related to numerical discretization
$(\cdot)_G$	Related to Germano's filter

$(\cdot)_{LES}$	A term related to LES
$(\cdot)_{NY}$	Related to Najafi-Yazdi's filter
$(\cdot)_{visc}$	A term related to laminar viscosity
$< \cdot >$	Reynolds averaged quantity
$\overline{(\cdot)}$	Averaged or filtered quantity
$\widehat{(\cdot)}$	Non-dimensionalized variable
$\widetilde{(\cdot)}$	Favre-averaged or filtered quantity

KEY TO ABBREVIATIONS

CHAPTER 1
Introduction

1.1 Motivation

In the past two decades, large eddy simulations (LES) have become popular in computational aeroacoustics (CAA) responding to Sir James Lighthill's call for hybdrid CAA. In this approach the nonlinear process of sound generation is captured by simulating the near-field while the far-field is computed by the use of an acoustic theory [1]. Aviation applications typically have modest to high Reynolds numbers for which direct numerical simulations (DNS) are practically impossible due to excessive computational costs. In LES the energy-containing eddies are well-resolved only within a certain range of length scales while the effect of smaller scales, also known as subgrid scales (SGS), on the resolved scales are modeled. An ideal SGS model would capture all the physical effects of the missing scales, i.e. energy-cascade to smaller scales, back-scattering, and progressive decorrelation of large scales [2]. An SGS model should not negatively interact with the numerical scheme and result in nonphysical sound generation. Development of LES for aeroacoustic simulations is yet an active research field focusing on achieving better SGS models [2].

In LES, the accurate resolution of turbulent kinetic energy and length scales requires precise control over dissipation and dispersion properties of the numerical schemes used over the entire resolved wavenumber range [2, 3]. Sufficient dissipation at the grid cut-off wavenumber is required to prevent aliasing due to an accumulation of turbulent kinetic energy at the grid cut-off scale. For high Reynolds number flows, spurious node-to-node oscillations due to polynomial aliasing or under-integration of non-linear terms, especially in high order methods [4–6], add to the numerical stabilization challenges by directly injecting energy into the grid cut-off.

Despite the recognized merits of using LES for computational aeroacoustics (CAA) and the rich literature on LES methods, the impact of filtering small spatial and high-frequency fluctuations from the solution has not been well characterized [2]. The modeling of scales smaller than grid size, through subgrid-scale (SGS) modeling in LES approaches is likely to generate spurious acoustic radiation [2, 7, 8] if not properly designed. The effect of SGS modeling on the acoustics can be illustrated by the decomposition of the Lighthill stress tensor. The Lighthill [9] analogy for density fluctuations is given by

$$\left(\frac{\partial}{\partial t} - c_0^2 \frac{\partial^2}{\partial x_i \partial x_j}\right) \rho = \frac{\partial^2 T_{i,j}}{\partial x_i \partial x_j} \ , \tag{1.1}$$

where $T_{i,j} = \rho u_i u_j + p_{i,j} - \delta_{i,j} c_0^2 \rho$. The term $p_{i,j}$ includes both pressure and viscous stress contributions. In the absence of a solid surface, the viscous terms act as octupoles and have a negligible effect as a noise source [10]. The entropic term, $(p - c_0^2 \rho)\delta_{i,j}$, is usually neglected in the absence of strong temperature gradients. Adding and simultaneously subtracting $\rho_0 \overline{u}_i \overline{u}_j + \overline{u_i u_j}$ to the remaining source term, $\rho_0 u_i u_j$, and rearranging the terms yields

$$T_{i,j} \approx \rho_0 u_i u_j = \underbrace{\rho_0 \overline{u}_i \overline{u}_j}_{T_{i,j}^{LES}} + \underbrace{\rho_0 (\overline{u_i u_j} - \overline{u}_i \overline{u}_j)}_{T_{i,j}^{SGS}} + \underbrace{\rho_0 (u_i u_j - \overline{u_i u_j})}_{T_{i,j}^{MSG}} \ , \tag{1.2}$$

where the over-bar, $\overline{(\cdot)}$, denotes a spatial filtering operator [11]. Spatial filtering is mathematically defined as the convolution of a field with a filter kernel, $\overline{\phi} = \mathcal{G} \circledast \phi$, both defined on a D-dimensional space. The discrete form of a filtering operation for a flow field, Φ, takes the general form of

$$\overline{\Phi} = \mathbf{N}\Phi \ , \tag{1.3}$$

where $\mathbf{N}$ is obtained from the discretization of the filter kernel, $\mathcal{G}$, and the convolution operator. A decomposition using Favre filtering can be derived for compressible flows.

The term $T_{i,j}^{LES}$ is fully resolved from the velocity field. The second term, $T_{i,j}^{SGS}$, is the subgrid-scale contribution at the resolved scales which is generally inaccurate and not fully available for many popular SGS models including Smagorinsky (static and dynamic). $T_{i,j}^{SGS}$ represents the sound generation due to interaction of the SGS eddies with its fully resolved counterpart. The SGS modeling error may be of the same order of magnitude or even larger than the numerical dissipation. This generates a nonphysical acoustic radiation that deteriorates the far-field noise estimations at high wavenumbers. The last term, $T_{i,j}^{MSG}$, is the missing component that represents the broad-band acoustic sources at scales smaller than the grid size. Based on the Kolmogorov $-5/3$ hypothesis for the turbulent kinetic energy (TKE), the energy content of fluctuations at these scales is very small and negligible. The effect of $T_{i,j}^{MSG}$ can only be modeled since all the associated flow dynamics occurs at sub-grid resolution [2, 12].

The SGS contribution has been studied in some *a priori* studies using DNS of isotropic turbulence [13, 14], plane turbulent channel flow [15], and mixing layer [16].

Investigations of acoustic output from the SGS terms are mostly limited to simple flows [17–19]. Bogey and Bailly [20] noted that SGS models reduce the effective Reynolds number. They used *selective filtering* to overcome this issue. Bodony and Lele [16] used the approximate deconvolution method (ADM) of Stolz and Adams [21] as a post-processing step for the DNS data of turbulent mixing layer to estimate the source-term statistics. Their work showed the advantage of ADM not only in modeling the SGS contributions without any eddy viscosity terms but also in providing a systematic approach to measure statistics of sound generation from SGS terms.

Approximate deconvolution models (ADM) are based on reconstructing the unrepresented resolved scales, i.e. scales barely larger than grid size, after a spatial filtering is applied on the solution field [21–23]. First, the solution field, u, is filtered using a low-pass filter where high wavenumbers are attenuated and the filtered field, $\overline{u}$, is obtained. This is followed by the *approximate deconvolution* of the filtered variables resulting in a close approximation of the unfiltered values, i.e. $u \approx u^*$. The effectiveness of an ADM in anti-aliasing and its SGS contribution to the Lighthill stress tensor, $T_{i,j}^{SGS}$, highly depends on the dissipation and dispersion properties of the underlying spatial filter.

The extension of discrete filter operators to unstructured grids is not straightforward which has hampered the use of ADM and RF for LES on unstructured grids. Marsden *et al.* [24] and Haselbacher and Vasilyev [25] suggested explicit filtering procedures for unstructured grids based on a weighted sum of neighboring node values. Both of these methods have drawbacks which have hampered their application.

In particular, it is not possible to ensure the stability of the filter operator in a general mesh topology, i.e. $|G(\kappa)| \leq 1, \forall \kappa \in [0, \pi]$. Moreover, the spectral distribution of the filter kernel is strongly dependent on the distribution of surrounding nodes. The filter of Marsden *et al.* [24] also requires the careful selection of a subset of neighboring nodes which might not exist in the presence of skewed and stretched elements [26].

In the present work, a new discrete filter proposed by Najafi-Yazdi *et al.* [27] based on a differential equation was extended to two and three dimensions using the multidimensional Z-transform. The goal was to develop a new discrete filter for unstructured grids which adapts to the local topology of the grid for skewed and stretched elements. The aim was to design the filter to be adoptable by various numerical schemes suitable for unstructured grids, e.g. finite volume and finite element schemes.

1.2 Background and Literature Review on LES

One of the conventional methods in LES is to apply the filtering implicitly by solving the space filtered Navier-Stokes equations with an assumed subgrid-scale stress model incorporated into a desired numerical scheme [28]. This is analogous to spectral methods in which the intrinsic truncation of high frequencies is associated with the use of a finite number of nodes. In Implicit LES (ILES), the finite support of each node in the computational domain determines the wavenumber truncation errors based on the discretization of Navier-Stokes equations. It is assumed that the numerical truncation operates as the filter, and therefore no explicit filtering is needed. There are several compelling issues associated with implicit LES methods.

Lund [29, 30] argued that discrete derivative operators act as low-pass filters, but their effect is unidirectional, i.e. the filtering behavior is observable only in one single spatial direction. Any filtering operation acting on the Navier-Stokes equation should be three-dimensional to represent a spatial averaging over a small volume. Discretized differentiation operators represent averaging only in one direction, i.e. each term in the discretized Navier-Stokes equations is filtered by a different one-dimensional filter. The actual discretized equations that are filtered by finite difference operators for incompressible flow simulation are

$$\begin{aligned}\frac{\partial \overline{u}_i}{\partial t} + \overline{\left(\frac{\partial (u_i u_1)}{\partial x_1}\right)}^{x_1} + \overline{\left(\frac{\partial (u_i u_2)}{\partial x_2}\right)}^{x_2} + \overline{\left(\frac{\partial (u_i u_3)}{\partial x_3}\right)}^{x_3} &= \\ -\overline{\left(\frac{\partial p}{\partial x_i}\right)}^{x_i} - \overline{\left(\frac{\partial \tau_{i,1}}{\partial x_1}\right)}^{x_1} - \overline{\left(\frac{\partial \tau_{i,2}}{\partial x_2}\right)}^{x_2} - \overline{\left(\frac{\partial \tau_{i,3}}{\partial x_3}\right)}^{x_3}& \\ +\frac{1}{Re}\left[\overline{\overline{\left(\frac{\partial^2 u_i}{\partial x_1^2}\right)}}^{x_1} + \overline{\overline{\left(\frac{\partial^2 u_i}{\partial x_2^2}\right)}}^{x_2} + \overline{\overline{\left(\frac{\partial^2 u_i}{\partial x_3^2}\right)}}^{x_3}\right]&, \end{aligned} \tag{1.4}$$

where $\overline{(\cdot)}^{x_i}$ and $\overline{\overline{(\cdot)}}^{x_i}$ are the effective one-dimensional filtered values associated with the discretized first and second order derivatives respectively. This equation is not consistent with the actual Navier-Stokes equations since the effective filters are not distributed uniformly [29]. It means that implicit filtering by spatial discretization fails to reproduce a well-defined effective three-dimensional filter.

Implicit filtering also does not allow control of the frequency content for advective terms. This is due to the replacement of $\overline{u_i u_j}$ with $\overline{u}_i\overline{u}_j + \tau_{i,j}$. Although $\overline{u}_i$ and $\overline{u}_j$ would have correctly truncated wavenumbers, their product may give rise to higher wavenumbers. If these wavenumbers are larger than what the computational grid can resolve, aliasing occurs which in turn disturbs the turbulence dynamics.The numerical dissipation associated with discretization or the added artificial viscosity in low-order numerical schemes may create unrealistic energy build-up in the smallest resolved scales and destabilize numerical simulations of turbulent flows. High-order schemes are more prone to become unstable due to numerical artifacts such as Q-waves or aliasing. Numerical stability issues become critical for high-order methods without any artificial dissipation or hyper-viscosity terms. The filter spectral distribution and its energy dissipation cannot be quantified when implicit filtering is utilized [30–32]. This makes it difficult to make comparisons between ILES and experimental results in terms of the contribution of the spatial filtering on the dissipation terms. The use of ILES does not allow the calculation of the Leonard term, $L_{ij} = \overline{\overline{u}_i\overline{u}_j} - \overline{u}_i\overline{u}_j$, despite the importance of this term for removing a significant portion of energy from resolved scales. The Leonard term is a measure of the rate of turbulent kinetic energy dissipation and should be calculated accurately to quantify the effect of filtering on the flow kinematics [33, 34].

Due to the inherent dependencies of implicit filtering methodologies on the computational grid, as explained above, the solutions obtained from implicit LES (ILES) are very sensitive to the grid resolution [35, 36] since numerical dissipation is a direct function of grid resolution. The grid dependency is significant especially when dynamic models [37] are used since they rely on information contained in the smallest resolved scales. For example, Meyers and Sagaut [38] reported that the true shear stress in a turbulent channel flow, calculated using ILES, was correct only when the grid was coarsened in the streamwise and spanwise directions.

The most common approach for closure of the Navier-Stokes equations in LES is through subgrid-scale (SGS) modeling. The spatial discretization is effectively considered as a low-pass filtering operation, here denoted by $\overline{(\cdot)}^{\Delta x}$. The non-linear convective term $u_i u_j$ is expressed in terms of the resolved, $\overline{u}_i^{\Delta x}$, and the non-resolved scales, u', as

$$\frac{\partial}{\partial x_j}\left(u_i u_j\right) = \underbrace{\frac{\partial}{\partial x_j}\left(\overline{u}_i^{\Delta x}\overline{u}_j^{\Delta x}\right)}_{\text{Resolved term}} + \underbrace{\frac{\partial}{\partial x_j}\left(\overline{u}_i^{\Delta x}u_j' + u_i'\overline{u}_j^{\Delta x}\right)}_{\text{Resolved and SGS interaction terms}} + \underbrace{\frac{\partial}{\partial x_j}\left(u_i' u_j'\right)}_{\text{SGS term}} . \tag{1.5}$$

The last two terms are modeled as an *assumed* viscous term so that

$$\frac{\partial}{\partial x_j}\left(u_i u_j\right) \approx \frac{\partial}{\partial x_j}\left(\overline{u}_i^{\Delta x}\overline{u}_j^{\Delta x}\right) + \underbrace{\frac{\partial}{\partial x_j}\left(\nu_t \frac{\partial \overline{u}_i^{\Delta x}}{\partial x_j}\right)}_{\text{SGS model}} , \tag{1.6}$$

where ν_t is an equivalent *turbulent* viscosity. SGS models differ in the definition of ν_t. For example, it is given as

$$\nu_t = \left(C_s \Delta_g\right)^2 \sqrt{2\overline{S}_{ij}^{\Delta x}\overline{S}_{ij}^{\Delta x}} , \tag{1.7}$$

in the Smagorinsky SGS model where Δ_g is the grid size and C_s is a constant [39]. Such models usually have a constant, e.g. C_s, to be tuned for every particular flow problem. Therefore, they are frequently under- or over-diffused in most cases. Dynamic approaches for SGS models were first introduced by Germano *et al.* in 1991 [37] for the Smagorinsky SGS model. They defined the Smagorinsky coefficient as

$$C_s^2 = \frac{\mathcal{L}_{ij}\mathcal{M}_{ij}}{\mathcal{M}_{ij}\mathcal{M}_{ij}} , \tag{1.8}$$

where $\mathcal{L}_{ij}$ represents the contribution of eddies larger than the grid size, Δ_g and smaller than a *test* filter width Δ_f. The test filter, denoted by $\overline{(\cdot)}$, is user-defined, and lastly, $\mathcal{M}_{ij}$ is given by

$$\mathcal{M}_{ij} = 2\Delta_g^2 \left(\overline{|\overline{S}|\overline{S}_{ij}}^{\Delta x} - \alpha^2 |\overline{S}|\overline{S}_{ij} \right) \ , \tag{1.9}$$

where $\alpha = \Delta_f/\Delta_g$. This procedure was later improved by Lilly [40] using a least-squares technique to remove numerical singularities and enhance the method's applicability by defining the Smagorinsky coefficient, C_s, as

$$C_s^2 = \frac{\langle \mathcal{L}_{ij}\mathcal{M}_{ij} \rangle}{\langle \mathcal{M}_{ij}\mathcal{M}_{ij} \rangle} \ , \tag{1.10}$$

where $\langle \cdot \rangle$ denotes a spatial averaging over directions of statistical homogeneity. Without the averaging, the dynamic model has proved to have high variations and even yield non-physical negative eddy viscosity values [41]. Dynamic Smagorinsky models were later extended for compressible flows by Erlebacher *et al.* [42]. An important assumption inherent to the dynamic models, e.g. dynamic Smagorinsky [37], is the invariance of scale for the turbulence coefficients [43] which may not hold for modeling transition to turbulence. One recognized challenge with dynamic SGS models which involve spatial averaging over directions of statistical homogeneity is the lack of this condition [43]. These two considerations have been extensively studied in the literature and various remedies have been proposed, e.g. Piomelli *et al.* [15], Carati *et al.* [44], Meneveau *et al.* [45], Najjar and Tafti [46], Domaradzki [47], Piomelli *et al.* [48], Rouhi *et al.* [49], and Geurts *et al.* [50].

Similar procedures are used to develop subfilter-scale (SFS) models when explicit filtering is utilized for LES simulations and the unresolved scales are modeled analogous to SGS techniques [51–57]. Another stream of methodologies for LES are approximate deconvolution models (ADM) which are discussed in more details in the following subsection.

1.2.1 Approximate Deconvolution Models for LES

One alternative approach for the closure of the Navier-Stokes equations is the approximate deconvolution model (ADM) which alleviates the need for eddy-viscosity models for subfilter scales, e.g. modified or dynamic Smagorinsky model [26, 53, 58]. This idea was pioneered by Stolz and Adams [21], Stolz *et al.* [59], Stolz *et al.* [60], Adams and Stolz [32], and Adams [61] who used the notion of van Cittert deconvolution operators. In this method, the closure problem of Space Filtered Navier-Stokes (SFNS) equations is solved by computing the approximate deconvolution operator of the spatial filter. Consider the filtering operator to be G such that $\overline{u} = G \circledast u$ where $\circledast$ is the convolution operator, i.e.

$$\overline{u} = G \circledast u \ . \tag{1.11}$$

The approximate deconvolution operator, D, is an approximation to G^{-1} such that

$$D \circledast G \approx I \ . \tag{1.12}$$

This approximation can be obtained using van Cittert's approach [21, 62]. The N-th van Cittert approximate deconvolution operator, D_N, of order N is defined by the N-step Picard iteration for the fixed point problem of finding u from a given filtered value of $\overline{u}$. The algorithm starts from the initial guess $u_0 = \overline{u}$ and is updated in N steps such that

$$u^{(j+1)} = u^{(j)} + \left\{\overline{u} - Gu^{(j)}\right\} \ . \tag{1.13}$$

It can be verified that this procedure yields the deconvolution operator, D_N, to be explicitly expressed as

$$D_N\phi := \sum_{n=0}^{N} (I - G)^n \phi \ . \tag{1.14}$$

It is proven that

$$D_N\overline{u} = u + \mathcal{O}\left(\delta^{\beta}\right) \ . \tag{1.15}$$

where δ is the radius for the spatial filter kernel g_δ and $\beta \geq 2(N+1)$. Since $D_N\overline{u} \approx u$, the approximate deconvolution operator provides a systematic solution to the closure problem by

$$\overline{uu} \approx \overline{D_N\overline{u}\, D_N\overline{u}}\,. \tag{1.16}$$

The nonlinear non-closed term can be computed by applying the deconvolution operator on the filtered variable. The theory of ADM can be used with any filtering operator G. A thorough study of ADM with Germano's differential filter, i.e. $G = \left(-\delta^2\kappa h + 1\right)^{-1}$, where κ is the wavenumber and h is the grid spacing, is presented by Layton and Rebholz [62] in which consistency, commutation error and the conservation of energy cascade phenomena are studied. They showed that ADMs yield accurate statistics for homogeneous, isotropic turbulence by proving that for the turbulent kinetic energy spectrum

$$E(\kappa) \propto \varepsilon_{model}^{2/3}\kappa^{-5/3}, \text{ for } \kappa \leq 1/\delta \ , \tag{1.17}$$

and

$$E(\kappa) \propto \varepsilon_{model}^{2/3} \delta^{-2} \kappa^{-11/3}, \text{ for } \kappa > 1/\delta \ . \tag{1.18}$$

This signifies that ADM predicts the correct energy cascade above the cut-off length scale. Usually, ADMs are coupled with regularization techniques (RT), e.g. time regularization, in order to correct the modeled micro-scale, i.e. the scale at which the filter acts like viscosity at the Kolmogrov scale [62, 63].

Stolz *et al.* [21] performed an *a priori* study on implications of approximate deconvolution models for supersonic turbulent flow over a ramp, a flow that features shock/boundary-layer interactions. The performance of ADMs led them to perform an *a posteriori* test for decaying compressible isotropic turbulence. They compared their results with predictions from DNS [21]. Later, they applied ADMs in conjunction with relaxation regularization, to capture non-represented scales, to study wall-bounded incompressible flows [64]. They showed that the ADM formulation can be rewritten as a model for the subgrid scale term in SFNS equations. They compared their LES results for an incompressible turbulent channel flow with available DNS data and showed that an approximate deconvolution operator of order $N = 5$ is a good choice for the incompressible channel flow, the compressible isotropic turbulence as well as the supersonic compression ramp cases. They also introduced a technique for constructing discrete filters with high-order commutation error which are invariant to mesh anisotropy for polynomial distributions with minimal dispersion error. This work was followed by subgrid-scale deconvolution approaches for shock capturing [32, 60]. They proposed a sufficiently accurate representation of the filtered nonlinear terms which can be obtained by applying a regularized deconvolution to the filtered solution. This method is related to the spectral vanishing-viscosity method and the regularized Chapman-Enskog expansion method for conservation laws.

In their first work for shock capturing [32], Adams and Stolz applied the subgrid scale model to the inviscid and viscous Burgers' equations on periodic domains, and isothermal full one-dimensional Euler equations on finite domains to study the interactions between one shock and an entropy wave, as well as another shock. They showed that the use of a regularized deconvolution allows the filtered solution to remain well resolved during time advancement. Stolz *et al.* [60] first studied the applicability of ADMs with low-order methods showing very good results when the cut-off frequency of the filter was adjusted to the modified wavenumber of the finite difference scheme. They conducted an *a posteriori* study of supersonic flow over a compression ramp with ADMs. The results compared very well with filtered DNS data, demonstrating the ability of ADM for capturing both non-turbulent and turbulent subgrid-scales. It was found that in contrast to a DNS, no expensive shock-capturing techniques were required to ensure stability. Their work has recently been extended to stochastic formulations [61]. Recent finite element approaches have been devised to replace the original fourth order formulation of filtered viscous terms with a second order model [65].

ADMs have been successfully used for structured grids where a discrete high-order filter operator can be easily constructed. Bogey and Bailly [66], and Bogey and Marsden [67] applied ADMs for jet noise simulations using compact schemes on structured meshes. Berland *et al.* [68] studied the influence of filter shape on effective scale representation and numerical accuracy of ADM-based LES. Their results confirms the findings of Stolz *et al.* [59] for a discrete filter of at least fifth order to eliminate unwanted dissipation. They claim that increasing the filter order eventually results in solutions that are independent of the filter shape. Fauconnier *et al.* [69] studied the performance of LES based on relaxation factor (RF) techniques for the Taylor-Green Vortex flow. They investigated the effect of filter order and strength with both *a priori* and *a posteriori* studies. They reported that filter orders of $N \geq 8$ result in good accuracy. The results were nearly independent of the strength of the filter.

1.2.2 Explicit Filters for ADM

De Stefano *et al.* [70–72] studied the effects of a filter's shape on turbulence closure consistency and accuracy. They compared results from a top-hat filter, as an example of smooth filters, and sharp cut-off filter on a sufficiently refined grid such that the filter width to grid size ratio was 3.3 for both filters. The high resolution of the grid and the relatively large filter to grid size ratio ensured that the numerical and the filtering errors were kept apart by at least an order of magnitude. They demonstrated that the use of a smooth filter in an LES yields results that are more accurate than a sharp cut-off filter.

Berland *et al.* [73] studied the influence of filter shape on scale separation in LES using the eddy-damped quasi-normal Markovian (EDQNM) modeling approach combined with a spatial discretization. They differentiated between the EDQNM-DNS and the EDQNM-LES models by selecting the grid resolution corresponding to a DNS or LES simulation respectively. Despite the use of spectral eddy viscosity and a very high order discretizatoin scheme, i.e. a tenth-order finite difference, the EDQNM-LES model failed to yield theoretically correct trends in the temporal evolution of the kinetic energy spectra. This is caused by the limited wavenumber bandwidth due to spatial discretization and the resulting aliasing error. However, when a sharp cut-off filter was used, aliasing errors were significantly smaller. Berland *et al.* [68] related the significance of aliasing error contaminating the whole energy spectrum to numerical differentiation.

The extension of discrete filter operators to unstructured grids is not straightforward. Marsden and Vasilyev [24], and Haselbacher and Vasilyev [25] designed two discrete filters for unstructured grids, based on a weighted sum of nodal values in the neighborhood of a node within a radius equal to a given filter width. Marsden and Vasilyev [24] claimed that devising a mapping function to perform the filtering in the computational domain, is impossible for unstructured grids. They devised an approach based on polynomial interpolation such that they have $N-1$ zero moments to commute with an N-th order numerical scheme. They use neighbors of a particular node to construct hierarchical triangles which contain the node under study. The triangles (tetrahedra in 3D) are constructed by first taking neighbor nodes within a given radius, breaking the disk (or sphere) into three (or four) zones and taking points from each zone. The filter width, i.e. the radius of the selected domain is defined by the user *a priori*. Haselbacher and Vasilyev [25] continued this work by modifying the filter design approach to reduce computational costs. They recognized that the conditions for filtering a function to a given order of commutation error are identical to the requirements for constructing the gradient of a function to a given order of truncation error. In this method, neighbors (at least nearest ones) of a vertex are utilized in a modified least-square gradient-reconstruction procedure [74] for filtering purposes. One of the drawbacks of these two methods is that it is not possible to ensure the stability of the filter operator (i.e. $G(\kappa) \leq 1, \forall \kappa$) in a general mesh topology. The distribution of the surrounding nodes (i.e. the number of nodes and their relative position) strongly affects the spectral distribution of the filter kernel. These methods require the careful selection of neighboring nodes, which may be impossible in the case of skewed or stretched elements [26]. Even if such a filter is stable, its dissipative properties vary from location to location in a grid as its spectral distribution is highly dependent on local mesh topology.

The use of differential filters is a more promising approach for design of spatial filters for unstructured grids. Germano's elliptic differential filter [75, 76] has been successfully used for a limited number of LES on unstructured simulations [26, 77–81]. Najafi-Yazdi *et al.* [27] proposed an alternative differential filter with two free parameters. One ensured full attenuation at grid cut-off; while the other controlled the filter cut-off wavenumber. The filter stabilizes the numerical scheme by removing node-to-node oscillations known as spurious noise or q-waves. The authors presented a simple formulation of the discretized form of the filter using finite-element methods (FEM) and demonstrated the filter's performance on manufactured solutions in one and two dimensions as well as unfiltered results from a DNS simulation of the Taylor-Green Vortex.

1.3 Objectives

The literature review presented in section 1.2 sheds some light on the importance of the fitler operator and its application in ADMs. The differential filter by Najafi-Yazdi *et al.* [27] has shown promising results in removing high wavenumbers on both structured and unstructured grids. The present work, proposes a systematic procedure for the design of Najafi-Yazdi *et al.* 's filter [82] using a generalization of multi-dimensional nonuniform Z-transform. The goal was to achieve simple steps that start from discretization of the filter differential equation and end by determining appropriate values or bounds for the filter parameters. The designed filters were used for LES on structured and unstructured grids.

1.4 Organization of the Thesis

This thesis is organized in six chapters. In Chapter 2, the governing equations of fluid flow, i.e. Navier-Stokes equations and equations of state, and a suitable non-dimensionalization procedure are presented. A brief review of the Space Filtered Navier-Stokes (SFNS) equations for LES of both incompressible and compressible flows are provided and the theory behind ADMs is briefly visited.

Chapter 3 is dedicated to filter design, its transformation to the physical domain and its discretization using Finite Element Methods (FEM). A new definition for a generalized multi-dimensional Z-transform for unstructured sampling is proposed. Its application for discrete filter design is demonstrated in detail. Finally, Najafi-Yazdi *et al.* 's filter [82] is extended to two and three dimensions. Suitable values or bounds for filter parameters are proposed for various linear and bilinear element types.

Chapter 4 presents the details for the spatial discretization, i.e. classical weak-Galerkin FEM, and several time integration schemes. Navier-Stokes characteristic boundary conditions (NSCBC) formulations for an FEM solver are reviewed and conditions for common boundaries are presented. Finally, the numerical implementation of ADM is demonstrated.

The results of numerical studies are presented in Chapter 5. Validation cases for advection and viscous implementations are provided in two and three dimensions. The ADM-based LES solver (AD-LES), without any subgrid-scale (SGS) modeling, was used to conduct simulations for the decay of a homogeneous isotropic turbulence and time evolution of the Taylor-Green vortex.

Chapter 6 concludes this manuscript by providing detail discussions on the findings and several drawn conclusions. Limitations and shortcomings of this research are also summarized. Finally, some potential lines of research for future work are recommended.

1.5 Contributions

The following list summarizes the major contributions of the present work: (*i*) extension of Najafi-Yazdi *et al.* 's filter for two and three dimensions, (*ii*) proposition of a generalized multi-dimensional Z-transform for fields on unstructured grids, (*iii*) development of a systematic approach to determine the parameters in Najafi-Yazdi *et al.* 's filter to achieve full attenuation at grid cut-off at every node in an unstructured grid, (*iv*) extension of van Cittert ADM formulation for a generalized discrete filter definition, (*v*) full stabilization of the classical weak-Galerkin FEM using explicit spatial filtering with full attenuation at grid cut-off, and (*vi*) LES of a decaying homogeneous isotropic turbulence and the Taylor-Green Vortex using ADM-based LES without any SGS modeling.

CHAPTER 2
Governing Equations for Large-Eddy Simulation

2.1 Governing Equations for Compressible Turbulent Flow

In the present work, unsteady compressible Navier-Stokes equations are numerically solved for large-eddy simulations (LES). The governing equations for the conserved variables, $\mathbf{U}$, in the Einstein notation are given by

$$\frac{\partial \mathbf{U}}{\partial t} + \frac{\partial \mathbf{F}_i}{\partial x_i} = 0 \ , \tag{2.1}$$

where i is based on the dimension of the problem, and the net fluxes are defined as

$$\mathbf{F}_i \ = \ (\mathbf{F}_{inv} - \mathbf{F}_v)_i \ , \tag{2.2}$$

where inv and v denote the inviscid and viscous fluxes. The conserved variables for compressible flows are defined as

$$\mathbf{U} \ = \ [\ \rho \quad \rho u_1 \quad \rho u_2 \quad \rho u_3 \quad \rho e_t\ ]^T \ , \tag{2.3}$$

where ρ is density, u_i is a velocity component, and e_t is specific total energy. The inviscid flux vectors can be expressed as

$$(\mathbf{F}_{inv})_i = \begin{bmatrix} \rho u_i \\ \rho u_i u_1 + p\delta_{i,1} \\ \rho u_i u_2 + p\delta_{i,2} \\ \rho u_i u_3 + p\delta_{i,3} \\ (\rho e_t + p)u_i \end{bmatrix} , \tag{2.4}$$

while the viscous fluxes are defined in terms of shear stress tensor $\tau_{i,j}$ and heat flux vector q_i as follows:

$$(\mathbf{F}_v)_i = \begin{bmatrix} 0 \\ \tau_{i,1} \\ \tau_{i,2} \\ \tau_{i,3} \\ u_j \tau_{i,j} - q_i \end{bmatrix} . \tag{2.5}$$

The shear stress tensor, $\tau_{i,j}$, for Newtonian fluids is given by

$$\tau_{i,j} = 2\mu S_{i,j} - \frac{2}{3}\mu S_{kk}\delta_{i,j} , \tag{2.6}$$

where $S_{i,j}$ is the strain rate tensor defined as

$$S_{i,j} = \frac{1}{2}\left(\frac{\partial u_i}{\partial x_j} + \frac{\partial u_j}{\partial x_i}\right) , \tag{2.7}$$

and μ is the molecular viscosity. Heat flux, q_i is given by Fourier's law as

$$q_i = -k\frac{\partial T}{\partial x_i} , \tag{2.8}$$

where T is static temperature and k is the thermal conductivity. In this work, the medium is considered to be an ideal gas for which the equation of state is given by

$$p = \rho R T \ , \tag{2.9}$$

relating static pressure, p, density, ρ, static temperature T and gas constant R. It is also assumed that the working gas behaves as a calorically perfect gas which yields

$$\gamma = \frac{c_p}{c_v} \ , \tag{2.10}$$

$$c_v = \frac{R}{\gamma - 1} \ , \tag{2.11}$$

and

$$c_p = \frac{\gamma R}{\gamma - 1} \ , \tag{2.12}$$

for heat capacity ratio, γ, specific heat capacity at constant pressure, c_p, and specific heat capacity at constant volume, c_v. Using this equation of state, the specific enthalpy, h, the specific internal energy, e_i, and the specific total energy, e_t, can be written as

$$h = c_p T \ , \tag{2.13}$$

$$e_i = c_v T = \frac{p}{(\gamma - 1)\rho} \ , \tag{2.14}$$

and

$$e_t = \frac{p}{\rho(\gamma - 1)} + \frac{1}{2} u_i u_i \ . \tag{2.15}$$

For perfect gases, Sutherland's law is adopted to define molecular viscosity as a function of temperature by

$$\mu = \frac{C_1 T^{\frac{3}{2}}}{C_2 + T} \ , \tag{2.16}$$

where C_1 and C_2 are constants for a given fluid, e.g. $C_1 = 1.458 \times 10^{-6} \mathrm{kg/ms}\sqrt{\mathrm{K}}$ and $C_2 = 110.4\mathrm{K}$ for air.

2.2 Non-Dimensionalization

Physical phenomena, including fluid dynamics, are invariant to the system of units used to measure variables. It implies that the governing equations should also be invariant to scaling in variables. This is achieved when the governing equations are non-dimensionalized. In a scale-invariant problem, non-dimensionalization reduces the number of free parameters by expressing the governing equations in terms of non-dimensional numbers, e.g. Reynolds, Mach, or Prandtl numbers. These dimensionless numbers determine the importance of each term in a governing equation and consequently control the dynamics of the underlying physics. Non-dimensionalization improves the conditioning of the discretized equations by reducing the spread of various physical properties in terms of orders of magnitude.

For the purpose of this work, all variables are normalized using a set of characteristic variables including length, L_c, velocity, U_c, density ρ_c, molecular viscosity μ_c, temperature T_c, and pressure p_c. Non-dimensional variables, denoted by $\hat{(\cdot)}$, are defined as

$$\hat{x}_i = \frac{x_i}{L_c} , \tag{2.17}$$

$$\hat{u}_i = \frac{u_i}{U_c} , \tag{2.18}$$

$$\hat{\rho} = \frac{\rho}{\rho_c} , \tag{2.19}$$

$$\hat{T} = \frac{T}{T_c} , \tag{2.20}$$

$$\hat{p} = \frac{p}{p_c} , \tag{2.21}$$

$$\hat{t} = \frac{tU_c}{L_c} , \tag{2.22}$$

$$\hat{e}_t = \frac{e_t}{U_c^2} , \tag{2.23}$$

and

$$\hat{\mu} = \frac{\mu}{\mu_c} . \tag{2.24}$$

For most compressible flow simulations used in this work, the characteristic density, characteristic velocity and characteristic velocity are given. Therefore, the Density-Temperature-Velocity (DTV) scheme [83] was used. Nondimensionalizing the equation of state, i.e. Eq. 2.9, yields

$$\frac{p}{p_c} = \frac{\rho}{\rho_c} \times \frac{R}{R_c} \times \frac{T}{T_c} , \tag{2.25}$$

which implies that the dimensions of the characteristic variables must comply with

$$p_c = \rho_c R_c T_c . \tag{2.26}$$

Non-dimensionalizing the total energy yields

$$\frac{\hat{e}_t}{U_c^2} = \frac{R/R_c}{\gamma - 1}\frac{T}{T_c} + \frac{1}{2}\frac{u_i u_i}{U_c^2} \ . \tag{2.27}$$

The dimensions of the reference quantities, U_c, R_c, and T_c need to satisfy

$$R_c = U_c^2/T_c \ . \tag{2.28}$$

Substituting it into the non-dimensional gas constant, $\hat{R}$, definition yields

$$\hat{R} = \frac{R}{R_c} = \frac{1}{\gamma M_c^2} \ , \tag{2.29}$$

where $M_c = U_c/c_c$ is the characteristic Mach number, and $c_c = \sqrt{\gamma R T_c}$ is the characteristic speed of sound for an ideal gas. The characteristic Reynolds number is defined as

$$Re_c = \frac{\rho_c L_c U_c}{\mu_c} \ , \tag{2.30}$$

where μ_c and T_c satisfy Sutherland's law, Eq. (2.16). Non-dimensionalizing the momentum equations yields

$$\frac{L_c}{\rho_c U_c^2}\frac{\partial \rho u_i}{\partial t} = \frac{L_c}{\rho_c U_c^2}\frac{\partial(\rho u_i u_j + p\delta_{i,j})}{\partial x_j} - \frac{L_c^2}{\mu_c U_c}\frac{\partial \tau_{i,j}}{\partial x_j} \ . \tag{2.31}$$

The non-dimensional shear stress, $\hat{\tau}_{i,j}$, and heat flux, $\hat{q}_i$, are given by

$$\hat{\tau}_{i,j} = \frac{\hat{\mu}}{Re_c}\left[2\hat{S}_{i,j} - \frac{2}{3}\hat{S}_{kk}\delta_{i,j}\right] \ , \tag{2.32}$$

where $\hat{\mu} = \mu/\mu_c$, and

$$\hat{S}_{i,j} = \frac{1}{2}\left(\frac{\partial \hat{u}_i}{\partial \hat{x}_j} + \frac{\partial \hat{u}_j}{\partial \hat{x}_i}\right) \ . \tag{2.33}$$

The energy equation can be non-dimensionalized with a similar approach yielding the non-dimensionalized Navier-Stokes equations as

$$\frac{\partial \hat{\mathbf{U}}}{\partial \hat{t}} + \frac{\partial \hat{\mathbf{F}}_i}{\partial \hat{x}_i} = 0 \ , \tag{2.34}$$

using Eqs. (2.17)–(2.24) where $\hat{\mathbf{F}}_i = \left(\hat{\mathbf{F}}_{inv} - \hat{\mathbf{F}}_v\right)_i$,

$$\left(\hat{\mathbf{F}}_{inv}\right)_i = \begin{bmatrix} \hat{\rho}\hat{u}_i \\ \hat{\rho}\hat{u}_i\hat{u}_1 + \hat{p}\delta_{i,1} \\ \hat{\rho}\hat{u}_i\hat{u}_2 + \hat{p}\delta_{i,2} \\ \hat{\rho}\hat{u}_i\hat{u}_3 + \hat{p}\delta_{i,3} \\ (\hat{\rho}\hat{e}_t + \hat{p})\hat{u}_i \end{bmatrix} \ , \tag{2.35}$$

and

$$\left(\hat{\mathbf{F}}_{vis}\right)_i = \begin{bmatrix} 0 \\ \hat{\tau}_{i,1} \\ \hat{\tau}_{i,2} \\ \hat{\tau}_{i,3} \\ \hat{u}_j\hat{\tau}_{i,j} - \hat{q}_i \end{bmatrix} \ . \tag{2.36}$$

The non-dimensional heat flux, $\hat{q}_i$, is given by

$$\hat{q}_i = -\hat{k}\frac{\partial \hat{T}}{\partial \hat{x}_i} \ . \tag{2.37}$$

The Prandtl number, Pr, is defined as

$$Pr = \frac{c_p\mu}{k} = \frac{1}{Re_c}\frac{\hat{c}_p\hat{\mu}}{\hat{k}} \ , \tag{2.38}$$

where

$$\hat{c}_p = \frac{c_p}{U_c^2/T_c} = \frac{1}{(\gamma - 1)\, M_c^2} \ , \tag{2.39}$$

is the non-dimensional specific heat, and

$$\hat{k} = \frac{k}{\rho_c U_c^3 L_c/T_c} = \frac{\hat{\mu}}{(\gamma - 1)\, Re_c Pr M_c^2} \ , \tag{2.40}$$

is the non-dimensional thermal conductivity in terms of the characteristic Mach number. Appearance of the non-dimensional viscosity, $\hat{\mu}$, along with the $1/Re_c$ is because viscosity is considered as a function of temperature according to the Sutherland's law which can be expressed in non-dimensional form as

$$\hat{\mu} = \frac{\hat{C}_1 \hat{T}^{\frac{3}{2}}}{\hat{C}_2 + \hat{T}} \ , \tag{2.41}$$

where $\hat{C}_1 = C_1 T_c^{\frac{1}{2}}/\mu_c$ and $\hat{C}_2 = C_2/T_c$.

2.3 Turbulence Modeling and the Closure Problem

Flow properties randomly fluctuate as functions of position, x_i, and time, t in a turbulent flow. In the statistical approach to turbulence, the statistical mean, $< \phi(x_i, t) >$, of a variable, $\phi(x, t)$, is defined as

$$\langle \phi(x_i, t) \rangle = \lim_{N \to \infty} \frac{1}{N} \sum_{k=1}^{N} \phi^{(k)}(x_i, t) \ , \tag{2.42}$$

when a specific measurement is repeated N times. $\phi^{(k)}(x_i, t)$ is the k-th realization of the variable. If the statistical mean, $\langle \phi \rangle$, is independent of time, t, it is called a stationary turbulent field and a *temporal average* is defined as

$$\langle \phi \rangle_t = \lim_{T \to \infty} \frac{1}{T} \int_{t_0}^{t_0+T} \phi(x_i, t')dt' \ , \tag{2.43}$$

where T is observation time for a single experiment. A turbulent field is called *homogeneous* if the statistical average, $\langle\phi\rangle$, is independent of position, x_i, and a *spatial average* is defined as

$$\langle\phi\rangle_x = \lim_{V\to\infty} \frac{1}{V} \int_V \phi(x_i', t) dV \ . \tag{2.44}$$

The time scale T in temporal averaging and volume V in spatial averaging should be large relative to local turbulent time and spatial scales respectively. Kolmogorov microscales are the smallest scales in a turbulent flow [84]. Kolmogorov length scale is defined by

$$\eta = \left(\frac{\nu^3}{\varepsilon}\right)^{1/4} \ , \tag{2.45}$$

where ε is the average turbulent kinetic energy (TKE) dissipation rate per unit mass, and ν is the kinematic viscosity. Similarly, the Kolmogorov time scale is given by

$$\tau_\eta = \left(\frac{\nu}{\varepsilon}\right)^{1/2} \ . \tag{2.46}$$

As long as $T >> \tau_\eta$ and $V^{1/3} >> \eta$ the temporal and spatial averages given by Eqs. (2.43) and (2.44) are valid.

The oldest approaches to turbulence modeling are the Reynolds-averaged Navier-Stokes (RANS) for steady-state mean flows, and the Unsteady RANS (URANS) for statistically unsteady flows. In these approaches, any flow variable ϕ can be expressed in terms of a statistical mean, $\langle\phi\rangle$, and a fluctuation, ϕ', i.e. $\phi = \langle\phi\rangle + \phi'$. When this decomposition is based on time averaging, it is known as the *Reynolds decomposition.* Turbulent random fluctuations have a zero statistical mean, i.e. $\langle f'\rangle = 0$. Using this identity and applying the Reynolds decomposition on incompressible Navier-Stokes equations yields the unsteady Reynolds-averaged Navier-Stokes (URANS) equations given as follows:

$$\begin{aligned}
\frac{\partial}{\partial x_i}\left(\rho \langle u \rangle_i\right) &= 0 \ , & (2.47)\\
\frac{\partial\left(\rho \langle u \rangle_i\right)}{\partial t} + \frac{\partial\left(\rho \langle u \rangle_i \langle u \rangle_j\right)}{\partial x_j} &= -\frac{\partial \langle p \rangle}{\partial x_i} + \frac{\partial}{\partial x_j}\left[\langle \tau \rangle_{i,j} - \rho \left\langle u_i' u_j' \right\rangle\right] \ , & (2.48)
\end{aligned}$$

Appearance of a non-linear term, $-\rho \left\langle u_i' u_j' \right\rangle$, known as the *Reynolds stress tensor*, results in more unknowns than equations, a.k.a. the *closure problem*. Different methodologies have been proposed to surmount this difficulty. The Boussinesq approximation was the first strategy where Reynolds tensor is modeled using average values [84]. Another strategy is to derive additional transport equations as

$$\frac{\partial\left(\rho \left\langle u_i' u_j' \right\rangle\right)}{\partial t} + \frac{\partial\left(\rho \left\langle u_i' u_j' \right\rangle \langle u \rangle_k\right)}{\partial x_k} = \mathbb{P}_{i,j} + \mathbb{T}_{i,j} + \Pi_{i,j} + \mathbb{D}_{i,j} - \rho \varepsilon_{i,j} \ , \tag{2.49}$$

to solve for the Reynolds stress tensor [85]. $\mathbb{P}_{i,j}$ is turbulent kinetic energy transfer between mean and turbulent fields, $\mathbb{T}_{i,j}$ represents the diffusion of turbulent kinetic energy by velocity fluctuations. The terms $\mathbb{D}_{i,j}$ and $\Pi_{i,j}$ are diffusion by viscous stresses and pressure gradient. The term $\rho \varepsilon_{i,j}$ denotes turbulent kinetic energy dissipation rate. Turbulent kinetic energy (TKE) is the the mean kinetic energy per unit mass due to turbulent fluctuations and is given by

$$E = \frac{1}{2} \langle u' \rangle_i \langle u' \rangle_i \ . \tag{2.50}$$

2.4 Numerical Simulation of Turbulent Flows

Numerical simulation of fluid flows requires solving the complete fluid dynamics equations on a computational mesh using a time integration technique. Solving the governing equations as accurately as possible for a turbulent flow requires the computation of all the scales forming the turbulent kinetic energy spectrum [85, 86]. The spatial discretization should allow the accurate calculation of scales as small as the Kolmogorov length scale, η. Based on Kolmogorov's hypotheses, it can be shown that

$$\eta \simeq Re^{-3/4} L \ , \tag{2.51}$$

where L is the turbulent integral length scale. Spatial discretization should yield elements smaller than Kolomogrov scale to ensure an accurate computation of the entire turbulent energy spectrum. This implies that for example for modeling the homogeneous isotropic turbulence, the number of mesh points in space grows with the Reynolds number, Re, as $\mathcal{O}(Re^{9/4})$. This approach is known as *Direct Numerical Simulation* (DNS). It captures all flow-related physical phenomena in the full length and time scales of turbulent flows. It usually requires very large computational resources for practical computational aeroacoustics (CAA) applications.

One alternative approach is large-eddy simulation (LES) in which all flow scales are captured from large scales down to length and time scales associated with spatial discretization size, i.e. element size, and the effect of smaller scales are modeled. The differences between spatial discretization in LES and DNS are schematically demonstrated in Fig. 2–1 on a false-color image of the far-field of a submerged turbulent jet.

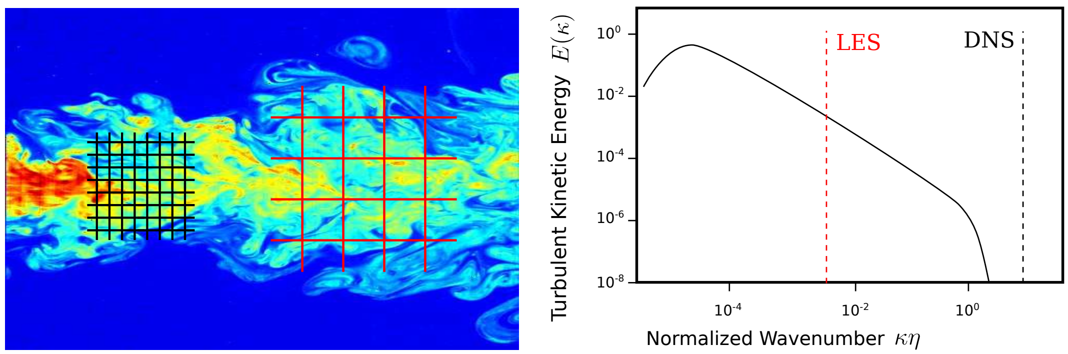

(a) (b)

Figure 2–1: Schematic representation of (a) a spatial discretization for DNS (black) and LES (red) and (b) their corresponding computational cut-offs in the spectral domain overlayed on a typical turbulent energy spectrum.
Figure (a) was adapted with permission from C. Fukushima and J. Westerweel, Technical University of Delft, The Netherlands.

Normalized cut-off wavenumbers (dashed lines in Fig. 2–1b) correspond with fluctuations at scales equal to the mesh size. The DNS cut-off is larger than the largest wavenumbers generated by the turbulence dynamics, i.e. those corresponding with the Kolmogorov length scale, η; while the LES cut-off falls in the inertial subrange of the turbulent kinetic energy spectrum.

2.5 Large-Eddy Simulation

In large-eddy simulations (LES), flow properties are decomposed into a *large-scale* or *resolved* component, $\overline{\phi}$, and a *small-scale* or *subgrid* component, ϕ_{sg}. Mathematically, this can be expressed as

$$\phi = \overline{\phi} + \phi_{sg} \ . \qquad (2.52)$$

This decomposition is achieved by applying a spatial-filter using a convolution operator and a filter kernel, G, [86],

$$\overline{\phi}(x_i,t) = G \circledast \phi = \int \phi(y_j,t) G(x_i,y_j;\Delta) dy_j \ , \tag{2.53}$$

where Δ denotes the filter characteristic scale related to its cut-off wavenumber, $\kappa_f = \pi/\Delta$. Filter cut-off wavenumber, κ_f, is usually defined as the wavenumber at which the magnitude of a filter's transfer function in the spectral domain is 1/2, i.e.

$$\mathcal{F}\{G\}(\kappa_f) = \mathcal{G}(\kappa_f) = \frac{1}{2}\,. \tag{2.54}$$

Filter kernel, G, satisfies the normalization condition

$$\int G(x_i,y_j;\Delta) dy_j = 1\,, \tag{2.55}$$

to ensure that a constant field is not affected by the filter [87].

The LES decomposition, Eq. (2.52), is analogous to Reynolds decomposition, except for two major differences. First, in LES decomposition, $\overline{\phi}$ is a *random* field in time and space and not some averaged value. Second, in LES $\overline{\phi_{sg}} \neq 0$ and $\overline{\overline{\phi}} \neq \overline{\phi}$ which is in contrast to the Reynolds decomposition.

Applying a spatial filter on compressible Navier-Stokes equations requires handling triple-variable terms, e.g. $\overline{\rho u_i u_j}$. To avoid additional subgrid scale (SGS) terms due to these terms, it is convenient to use Favre filtering, a.k.a. mass-weighted filtering. A Favre-filtered variable, $\widetilde{\phi}$, is defined as

$$\widetilde{\phi} = \frac{\overline{\rho\phi}}{\overline{\rho}}\,. \tag{2.56}$$

Favre-filtered Navier-Stokes equations are structurally similar to their corresponding non-filtered equations apart from the appearance of the subgrid scale terms, e.g. $\overline{\rho}\widetilde{u_i u_j}$. For example, The momentum equation is given by

$$\frac{\partial\overline{\rho}\widetilde{u}_i}{\partial t} + \frac{\partial\overline{\rho}\widetilde{u}_i\widetilde{u}_j}{\partial x_j} + \frac{\partial\overline{p}}{\partial x_j} - \frac{\partial\check{\sigma}_{i,j}}{\partial x_j} = -\frac{\partial\mathbb{T}_{i,j}}{\partial x_j} + \frac{\partial}{\partial x_j}\left(\overline{\sigma}_{i,j} - \check{\sigma}_{i,j}\right) \ , \tag{2.57}$$

where

$$\check{\sigma}_{i,j} = \mu(\widetilde{T})\left(2\widetilde{S}_{i,j} - \frac{2}{3}\delta_{i,j}\widetilde{S}_{k,k}\right) \ , \tag{2.58}$$

is the Favre-filtered shear stress tensor and $\mathbb{T}_{i,j}$ is the subgrid scale (SGS) tensor. For compressible flows, the SGS tensor, $\mathbb{T}_{i,j}$, is defined as the unresolved portion of the stress tensor given as

$$\mathbb{T}_{i,j} = \tau_{i,j} - \underbrace{\overline{\rho}\widetilde{u}_i\widetilde{u}_j}_{\text{unresolved}} = \overline{\rho}(\widetilde{u_i u_j} - \widetilde{u}_i\widetilde{u}_j) \ . \tag{2.59}$$

Accurate modeling of $\mathbb{T}_{i,j}$ is the main challenge in LES. This term can be expressed using the triple decomposition by Leonard [88] as

$$\mathbb{T}_{i,j} = \mathbb{L}_{i,j} + \mathbb{C}_{i,j} + \mathbb{R}_{i,j} \ , \tag{2.60}$$

where $\mathbb{L}_{i,j} = \overline{\rho}(\widetilde{\widetilde{u}_i\widetilde{u}_j} - \widetilde{u}_i\widetilde{u}_j)$ is the Leonard term relating filtered quantities. $\mathbb{C}_{i,j} = \overline{\rho}(\widetilde{\widetilde{u}_i(u_j)_{sg}} + \widetilde{(u_i)_{sg}\widetilde{u}_j})$ is a cross term representing the interactions between the resolved and the subgrid scales. $\mathbb{R}_{i,j} = \overline{\rho}(\widetilde{(u_i)_{sg}(u_j)_{sg}})$ is the Reynolds term accounting for the interactions among subgrid scales. For an LES, $\mathbb{C}_{i,j}$ and $\mathbb{R}_{i,j}$ need to be modeled.

2.6 Favre-filtered Energy Equation

Applying Favre filtering to the total energy definition results in

$$\overline{\rho}\widetilde{e}_t = \frac{\overline{p}}{\gamma - 1} + \frac{1}{2}\overline{\rho}\widetilde{u_i u_i} \ , \tag{2.61}$$

which cannot be computed directly due to appearance of the SGS term, $\overline{\rho}\widetilde{u_i u_j}$. Several different techniques have been proposed in the literature [89–95] (for more details refer to Chapter 2 of Ref. [87]). Among these methods, the Vreman's *system I* formulation [93] was adopted. Accordingly, the *computable* total energy denoted by $\check{E}$ is defined as

$$\overline{\rho}\check{E} := \frac{\overline{p}}{\gamma - 1} + \frac{1}{2}\overline{\rho}\widetilde{u}_i\widetilde{u}_j \ . \tag{2.62}$$

The governing equation for $\check{E}$ is given as

$$\frac{\partial \check{E}}{\partial t} + \frac{\partial(\check{E} + \overline{p})\widetilde{u}_j}{\partial x_j} - \frac{\partial \check{\sigma}_{i,j}\widetilde{u}_i}{\partial x_j} + \frac{\partial \check{q}_j}{\partial x_j} = -B_1 - B_2 - B_3 + B_4 + B_5 + B_6 - B_7 \ , \tag{2.63}$$

where

$$\check{q}_j = -k(\widetilde{T})\frac{\partial \widetilde{T}}{\partial x_j} \ , \tag{2.64}$$

is the computable Favre-filtered heat flux. The SGS terms, B_i, are defined as

$$B_1 = \frac{1}{\gamma-1}\frac{\partial}{\partial x_j}(\overline{pu_j} - \overline{p}\widetilde{u}_j) = \frac{\partial c_v Q_j}{\partial x_j} \ , \tag{2.65}$$

$$B_2 = \overline{p\frac{\partial u_j}{\partial x_j}} - \overline{p}\frac{\partial \widetilde{u}_j}{\partial x_j} = \Pi_{dil} \ , \tag{2.66}$$

$$B_3 = \frac{\partial}{\partial x_j}(\mathbb{T}_{k,j}\widetilde{u}_k) \ , \tag{2.67}$$

$$B_4 = \mathbb{T}_{k,j}\frac{\partial}{\partial x_j}\widetilde{u}_k \ , \tag{2.68}$$

$$B_5 = \overline{\sigma_{k,j}\frac{\partial}{\partial x_j}u_k} - \overline{\sigma}_{k,j}\frac{\partial}{\partial x_j}\widetilde{u}_k = \varepsilon_v \ , \tag{2.69}$$

$$B_6 = \frac{\partial}{\partial x_j}(\overline{\sigma}_{i,j}\widetilde{u}_i - \check{\sigma}_{i,j}\widetilde{u}_i) = \frac{\partial \mathbb{D}_j}{\partial x_j} \ , \tag{2.70}$$

and

$$B_7 = \frac{\partial}{\partial x_j}(\overline{q}_j - \check{q}_j) \ . \tag{2.71}$$

Q_j is the SGS temperature flux defined as

$$Q_j = \overline{\rho}(\widetilde{u_j T} - \widetilde{u}_j\widetilde{T}) \ , \tag{2.72}$$

where Π_{dil} is the SGS pressure-dilatation, and ε_v is the SGS viscous dissipation rate. In this formulation no modification is required for thermodynamic variables and the equation of state retains its form as

$$\overline{p} = \overline{\rho}R\widetilde{T} \ . \tag{2.73}$$

Vreman *et al.* [93, 96] showed that the L_2 norm of B_4 and B_5 are one order of magnitude, and those of B_6 and B_7 are two orders of magnitude smaller than B_1, B_2, B_3, and Navier-Stokes diffusive fluxes, i.e. $\partial\check{\sigma}_{i,j}\widetilde{u}_j/\partial x_j$. Most authors neglect these non-linear terms occurring in the viscous terms and the heat fluxes considering them as small and negligible [87] by assuming that $\overline{\sigma}_{i,j} = \check{\sigma}_{i,j}$ and $\overline{\sigma_{i,j}u_i} = \check{\sigma}_{i,j}\widetilde{u}_i$. The former assumption eliminates the last term in the momentum equation, i.e. Eq. (2.57). The remaining term $B_2 = \Pi_{dil}$ is either neglected [97] or merged with B_1 and modeled with a conservative approximation [93]. In some cases, e.g. Erlebacher *et al.* [42] and Moin *et al.* [11], $B_2 = \Pi_{dil}$ is neglected by assuming the incompressibility of the smallest scales. An alternative approach is using the approximate deconvolution model (ADM) introduced later in section 2.11.

2.7 Favre-Filtered Second Law of Thermodynamics

The generalized second law of thermodynamics is expressed as the Clasius-Duhem entropy inequality,

$$\rho\frac{ds}{dt} \geq -\nabla\cdot\left(\frac{\mathbf{q}}{T}\right) + \frac{\rho e_s}{T} \ , \tag{2.74}$$

where s is the specific entropy, $\mathbf{q}$ is the transferred heat vector and e_s is an energy source per unit mass. Multiplying Eq. (2.74) with T and filtering it yields

$$\check{\Phi} + \varepsilon_v + \frac{\partial\check{q}_j}{\partial x_j} + B_7 \geq 0 \ , \tag{2.75}$$

where

$$\check{\Phi} = \check{\sigma}_{i,j}\frac{\partial\widetilde{u}_i}{\partial x_j} \ , \tag{2.76}$$

is the Favre-filtered viscous dissipation,

$$\epsilon_v = \overline{\Phi} - \check{\Phi} \ , \tag{2.77}$$

is the SGS viscous dissipation, and

$$B_7 = \frac{\partial}{\partial x_j}\left(\overline{q}_j - \check{q}_j\right) \ , \tag{2.78}$$

is the SGS viscous heat flux. This inequality demonstrates the dependence of the subgrid viscous heat flux, B_7, and the SGS viscous dissipatoin, ε_v. SGS models which satisfy Eq. (2.75) are referred to as *thermodynamically consistent* by Garnier *et al.* [87]. In practice, this inequality cannot be numerically enforced but only evaluated when filtered fields, $\overline{(\cdot)}$, can be estimated from Favre-filtered ones, i.e. $\widetilde{(\cdot)}$ or $\check{(\cdot)}$.

2.8 Space Filtered Navier-Stokes Equations

Applying the filtering operation, as described above, on non-dimensional compressible Navier-Stokes Equations, i.e. Eq. (2.34), yields

$$\overline{\left(\frac{\partial \hat{\mathbf{U}}}{\partial \hat{t}}\right)} + \overline{\left(\frac{\partial \hat{\mathbf{F}}_i}{\partial \hat{x}_i}\right)} = 0 \ . \tag{2.79}$$

Filtering and derivation (temporal or spatial) do not generally commute, i.e. $\overline{(\partial\phi/\partial x_i)} \neq \partial\overline{\phi}/\partial x_i$, and $\overline{(\partial\phi/\partial t)} \neq \partial\overline{\phi}/\partial t$.

At each point (x_i, t) in a stationary domain of interest Ω, a filter G with influence radius (filter radius) of $\Delta(x_i, t)$ the commutation errors between spatial or temporal differentation and filtering operation are respectively given by

$$\left[\partial/\partial t, G\circledast\right]\phi = \left(\frac{\partial G}{\partial \Delta}\circledast\phi\right)\frac{\partial \Delta}{\partial t} \ , \tag{2.80}$$

and

$$[\partial/\partial x_i, G\circledast]\,\phi = \left(\frac{\partial G}{\partial \Delta} \circledast \phi\right)\frac{\partial \Delta}{\partial x_i} + \int_{\partial\Omega} G\left(x_i - \xi_i, \Delta(x_i.t)\right)\phi(\xi_i, t) n(\xi_i) d(\partial\Omega) \;, \tag{2.81}$$

where $\partial\Omega$ denotes the boundary of Ω and $d(\partial\Omega)$ represents an infinitesimal portion of the boundary. Equations (2.80) and (2.81) imply that for zero commutation error, first, the filter radius Δ should be constant in both time and space and second, filter kernel G should approach zero at domain boundary, i.e.

$$\lim_{x_i \to \partial\Omega} G(x_i) = 0 \;. \tag{2.82}$$

In mathematical terms, it means that the domain Ω is a compact support for the filter kernel function G. This property is rarely satisfied, e.g. in box filter $1/\Delta H(1/2\Delta - |x_i|)$. Most common filters defined in *physical space* such as Gaussian filter, $(6/\pi\Delta^2)^{1/2}\exp(-6|x_i|^2/\Delta^2)$, or sharp spectral filter, $\sin(\pi|x_i|/\Delta)/(\pi|x_i|)$, do not have compact support and would cause commutation error if used in LES.

The space commutation property of filter operator is satisfied only in unbounded domains and if the filter radius, Δ, is independent of position, i.e. homogeneous. In most practical problems, e.g. wall-bounded flows, the filter radius must vanish as one approaches a wall. The major challenge is that commutation error is not necessarily bounded for homogeneous filters applied on bounded domains [98].

2.9 Structural vs Functional LES

In large-eddy simulations, the resolution of the spatial discretization is not sufficient to capture all flow scales. Scales smaller than the element size corresponding to wavenumbers greater than the grid cut-off are not resolved because the spatial sampling frequency is lower than the Nyquist-Shannon criteria. It leads to aliasing errors, which means that energy that has been cascaded to subgrid scales (high wavenumbers) by nonlinear terms such as $\overline{u_i u_j}$ is fed back into larger scales (low wavenumbers). If untreated, this will lead to instability due to a build up of energy see Fig. 2–2.

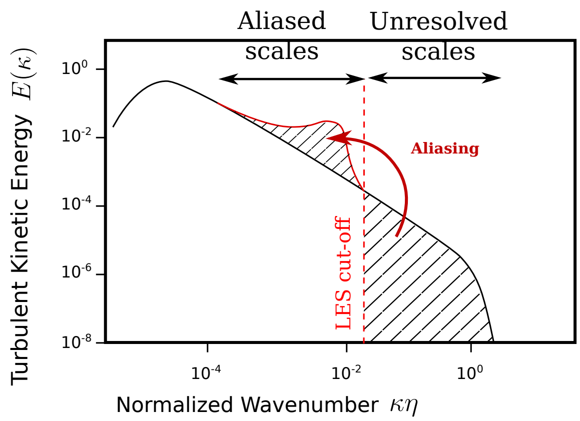

Figure 2–2: Schematic demonstration of aliasing and energy pile up near the grid cut-off for an untreated LES.

Turbulence modeling strategies are usually categorized in two groups [99]: *functional modeling*, and *structural modeling*. Functional methods model the effect of SGS terms on the resolved scales. Functional methods usually introduce a dissipative term to mimic the required turbulent kinetic energy dissipation rate, but may not demonstrate the same turbulence structure. On the contrary, structural methods are based on approximating SGS terms by constructing an evaluation of $\overline{\phi}$.

In SGS modeling it is assumed that the grid cut-off wavenumber, $k_g = \pi/\Delta x$, is within the inertial range, thereby ensuring local isotropy in turbulent structures.

Functional models require the additional assumption that subgrid scales merely balance the energy transfer between the resolved and subgrid scales. Energy is transferred from large scales to small ones representing TKE dissipation, and also from small to large scales, a mechanism known as *back scattering*. All the approaches consider the former and very few, and only for incompressible flows, take into account the back scattering phenomenon. Functional models are either *explicit* which model SGS terms as functions of computable filtered values, $\overline{\phi}$, or *implicit* by adjusting the numerical truncation error to induce similar effects. The former are generally referred to as *eddy-viscosity* models while the latter are known as *Implicit LES* (ILES). An extensive overview of functional models for LES of compressible flows can be found in Garnier *et al.* 's work [87].

Structural models try to approximate unfiltered fields [100] by partially reconstructing the interaction between subgrid scales and resolved scales. Despite this attempt, structural models still require an energy removal mechanism to avoid energy pile-up at grid cut-off and ensure stability through time. The advantage of structural models over purely functional models is their greater higher accuracy in predicting anisotropic energy distributions. In addition, in functional models the underlying filtering operator is either unknown [35, 36], the case of eddy-viscosity methods, or the discretized filtered equations are not consistent with the original Navier-Stokes equations, e.g. in ILES methods [28–30].

Structural models are mostly based on either scale-similarity hypothesis, approximate deconvolution, or multi-resolution reconstruction. Scale-similarity models approximate the SGS stress tensor up to the order $\mathcal{O}(\Delta_f^2)$ [42, 93, 96, 99, 101], for compressible flows by defining it as

$$\mathbb{T}_{i,j} \approx \check{\mathbb{T}}_{i,j} = \overline{\rho}(\widetilde{\widetilde{u}_i \widetilde{u}_j} - \widetilde{\widetilde{u}}_i \widetilde{\widetilde{u}}_j) \ , \tag{2.83}$$

where Δ_f is the filter radius. Similarly, any other SGS residual terms such as SGS heat flux or pressure-dilatation terms, can be approximated by replacing the non-compatible quantities by their computable counterparts using the filtered fields [87]. Most scale-similarity models require additional *regularization* to ensure stable time integration.

Multi-scale modeling of subgrid scales further decomposes non-resolved represented scales into different sub-scale ranges, some of which are solved for and the rest are modeled. Multi-level approaches [102–105], stretched-vortex models [91, 106], and Variational Multi-Scale (VMS) Models [107, 108] are well described in the literature. Multi-scale modelling approaches are usually difficult to develop. They depend on the underlying numerical scheme, require multi-resolution grids and are computationally expensive.

Approximate deconvolution models (ADM) filter discrete Navier-Stokes equations using a known filter kernel, in addition to the intrinsic filtering due to spatial discretization. *Approximate deconvolution* is applied on filtered values to approximately reconstruct the unfiltered fields. Deconvolved fields are used in non-linear terms to capture interaction of subgrid scales and resolved scales more accurately.

In the present work, ADM was adopted because it is based on an explicit filtering operation which separates LES related filtering from numerical discretization effects [30, 109]. Explicit filtering allows the control of numerical errors caused by

LES, since the filter spectral distribution and energy dissipation are quantifiable. Before introducing the ADM framework, some formal terminology is introduced to help distinguish notions of resolved scales vs represented scales.

2.10 Resolved vs Represented Scales

Every filter kernel is usually characterized by a cut-off wavenumber κ_f which is a matter of definition. On a discretized domain, i.e. mesh, the smallest *represented* scale is the mesh size and corresponds with the largest *represented* wavenumber.

Definition 1. *Represented* scales on a computation grid of size Δx with $\kappa_g = \pi/\Delta x$ are defined as those represented with wavenumbers $|\kappa| \leq \kappa_g$.

Definition 2. *Resolved* scales by a filter kernel with cut-off wavenumber κ_f are defined as those corresponding to $|\kappa| \leq \kappa_f$.

Figure 2–3 schematically demonstrates different contributions of the resolved, non-resolved represented, and non-represented scales to an evolving turbulent flow energy spectrum. The main goal of structural models is to reconstruct non-resolved scales from resolved scales. For filter kernels with positive transfer functions, i.e. no amplification $|G| \leq 1$, it is achieved by using *defiltering* via *approximate deconvolution* for non-resolved *represented* scales and via *regularization* for non-resolved *non-represented* scales.

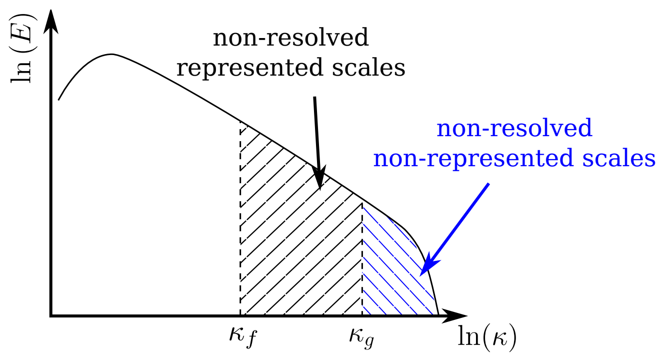

Figure 2–3: Schematic demonstration of non-resolved represented, and non-resolved non-represented scales due to discretizing and filtering Navier-Stokes equations.

2.11 Approximate Deconvolution Models

Approximate deconvolution models use *defiltering* via *approximate deconvolution* for reconstruction of *non-resolved represented scales*. To demonstrate this approach, we start from the Navier-Stokes equations, Eq. (2.1), projected onto a discrete computational domain yielding

$$\frac{\partial(\mathbf{U}_i)_N}{\partial t} + \frac{\partial(\mathbf{F}_j)_N}{\partial x_j} \approx 0 \;, \tag{2.84}$$

where $(\cdot)_N$ denotes projected fields onto a mesh. Equation (2.84) is the projection of the continuous solution onto a discrete domain *without* discretizing the derivative operators. It means that the only approximation originates from truncation due to spatial sampling.

The contribution of non-represented scales $(\mathbf{U}_i)_{sg} = \mathbf{U}_i - (\mathbf{U}_i)_N$ corresponding to wavenumbers $|\kappa| \geq \kappa_g$ is lost and cannot be recovered by any approximation methods. The effect of non-resolved scales can only be modeled using either functional or regularization approaches. It cannot be fully ignored as the turbulent dissipation mechanisms physically occur at Kolmogorov scales but control the entire dynamics of the energy cascade.

In the ADM framework, Navier-Stokes equations projected onto a discrete domain are explicitly filtered to create an artificial energy dissipation mechanism at near grid cut-off wavenumbers, κ_g [62]. Filtering Eq. (2.84) yields

$$\frac{\partial(\overline{\mathbf{U}}_i)_N}{\partial t} + G \circledast \frac{\partial(\mathbf{F}_j)_N}{\partial x_j} = \frac{\partial(\overline{\mathbf{U}}_i)_N}{\partial t} + \overline{\frac{\partial(\mathbf{F}_j)_N}{\partial x_j}} \approx 0 \ , \tag{2.85}$$

where G is the filter kernel and $\circledast$ denotes the convolution operator. The approximate deconvolution approach estimates u_N as

$$\mathcal{D}\{\overline{u}_N\} \coloneqq u_N^* = Q \circledast \overline{u}_N = Q \circledast G \circledast \overline{u}_N \approx u_N, \tag{2.86}$$

where Q is the kernel for the *approximate inverse* of the filter G [21]. In the Fourier domain it can be expressed as $\mathcal{QG} \approx I$. It can be used to re-write Eq. (2.85) in two forms [87], either in the approximate deconvolution form as

$$\frac{\partial(\overline{\mathbf{U}}_i)_N}{\partial t} + \overline{\frac{\partial(\mathbf{F}_N(u_N^*)_j)}{\partial x_j}} \approx 0 \ , \tag{2.87}$$

or in the residual form as

$$\frac{\partial(\overline{\mathbf{U}}_i)_N}{\partial t} + \frac{\partial(\mathbf{F}_N(\overline{u}_N)_j)}{\partial x_j} = \frac{\partial(\mathbf{F}_N(\overline{u}_N)_j)}{\partial x_j} - \overline{\frac{\partial(\mathbf{F}_N(u_N)_j)}{\partial x_j}} = \mathbb{T}_{sgs} = 0 \ . \tag{2.88}$$

The deconvolution form, Eq. 2.87, violates Galilean invariance by an error with an order of magnitude equal to that of the deconvolution error [110], e.g. the L_2-norm $\|u_N - Q \circledast \overline{u}_N\|_2$. This error is usually negligible in practical computations [21–23, 32, 60, 62, 66, 111–113]. The residual form satisfies Galilean invariance but requires further SGS modeling.

A bounded approximate deconvolution operator, Q, re-amplifies the represented non-resolved scales filtered by G and ensures that $|Q \circledast G| \leq 1$ such that aliasing due to deconvolution does not occur [87].

2.12 Approximate Deconvolution Schemes

Various approximate deconvolution operators can be defined for a given filter operator G. The van Cittert approximate deconvolution operator was used in the original ADM framework by Stolz and Adams [21]. An M-th order van Cittert approximate deconvolution operator in the Fourier domain, $\mathcal{Q}_M$, is given by a fixed-point iteration

$$\mathcal{Q}_M = \sum_{m=0}^{M} (\mathcal{I} - \mathcal{G})^m \ , \tag{2.89}$$

where $\mathcal{I}$ is the identity operator. This scheme can be formulated as M steps of a first order Richardson iteration for solving the operator $G \circledast \overline{\phi} = \phi$. This procedure is presented in the Algorithm 1. Convergence for a fixed M as $\Delta \to 0$ is guaranteed. Uniform convergence for $M \to \infty$ is obtained if $||I - G|| < 1$. For practical applications $M = 5$ is most commonly used [32, 60].

Algorithm 1: van Cittert approximate deconvolution iterative scheme

Data: Given filtered field $\overline{\phi}$

Result: Approximate defiltered field ϕ^*

Assume $\phi^{(0)} = \overline{\phi}$;

for $m = 1$ *to* M **do**

$\phi^{(m)} = \phi^{(m-1)} + \left(\overline{\phi} - G \circledast \phi^{(m-1)}\right)$;

end

For a bounded self-adjoint and positive filter operator G, the van Cittert deconvolution is a self-adjoint positive semi-definite operator [62]. The deconvolution operator is bounded, $||\mathcal{Q}_M|| \leq M+1$, approximating the inverse filter to high asymptotic accuracy, i.e.

$$\overline{u_i u_j} = \overline{u_i^* u_j^*} + \mathcal{O}(\Delta^{2M+2}) \ , \tag{2.90}$$

where ADM ensures energy stability of the approximation [114] and preserves consistency with the theoretical scaling laws of turbulence for kinetic energy and helicity [62, 63].

Stolz *et al.* [59] formulated ADM for the conservative form of the compressible Navier-Stokes equations. The continuity equation is given as

$$\frac{\partial \overline{\rho}}{\partial t} + \overline{\frac{\partial (\rho u)_j^*}{\partial x_j}} \approx 0 \ . \tag{2.91}$$

The momentum equations is expressed as

$$\overline{\frac{\partial (\rho u)_j}{\partial t}} + \overline{\frac{\partial}{\partial x_j}\left(\frac{(\rho u)_i^*(\rho u)_j^*}{\rho^*} + \check{p}^*\delta_{i,j} - \check{\tau}_{i,j}^*\right)} \approx 0 \ , \tag{2.92}$$

where

$$\check{p}^* = (\gamma - 1)\left(e_t^* - \frac{(\rho u)_k^*(\rho u)_k^*}{\rho^*}\right) \ , \tag{2.93}$$

is the deconvolved pressure, and $e_t^* = (\rho e_t)^*/\rho^*$ is the deconvolved specific total energy. The deconvolved viscous stress tensor $\check{\tau}_{i,j}^*$ and heat flux $\check{q}_i^*$ are computed by computing the viscosity μ^* from the deconvolved temperature $\check{T}^* = \check{p}^*/(\rho^* R)$ (for an ideal gas) and the deconvolved strain rate $S_{i,j}^*$ obtained from $(\rho u)_i^*/\rho^*$. Using deconvolved fields $\check{\tau}_{i,j}^*$ and $\check{q}_j^*$, one obtains the energy equation as

$$\frac{\partial\overline{(\rho e_t)}}{\partial t} + \overline{\frac{\partial}{\partial x_j}\left(\frac{(\rho u)_j^*}{\rho^*}\left((\rho e_t)^* + \check{p}^*\right) - \check{\tau}_{i,j}^*\frac{(\rho u)_i^*}{\rho^*} + \check{q}_j^*\right)} \approx 0 \ , \tag{2.94}$$

2.13 Regularization

Stolz *et al.* [59, 60, 64] argued that since the effect of non-represented scales, $|\kappa| > \kappa_g$, on the resolved scales, $|\kappa| \le \kappa_f$, cannot be captured by using the deconvolved properties, i.e. using ϕ^* instead of ϕ, a *relaxation term* in the form of $-\chi(I - Q_M \circledast G) \circledast \overline{\phi}$ with $\chi > 0$ should be added to the right hand side of the filtered and deconvolved equations, i.e. Eqs. (2.91) to (2.94). This modification yields the regularized ADM equation, Eq. (7) in Stolz *et al.* [115], as

$$\frac{\partial\overline{\mathbf{U}}}{\partial t} + \frac{\overline{\partial F(\mathbf{U}^*}}{\partial x} = -\chi_{\mathbf{U}}\left(\overline{\mathbf{U}} - \overline{\mathbf{U}}^*\right) = -\chi_{\mathbf{U}}\left(I - Q_N \circledast G\right) \circledast \mathbf{U} \ . \tag{2.95}$$

The continuity, momentum and energy equations are re-expressed as

$$\begin{aligned}
\frac{\partial\overline{\rho}}{\partial t} + \overline{\frac{\partial(\rho u)_j^*}{\partial x_j}} \quad &\approx \quad -\chi_\rho(\overline{\rho} - \overline{\rho}^*) \ , & (2.96)\\
\frac{\partial\overline{(\rho u)_j}}{\partial t} + \overline{\frac{\partial}{\partial x_j}\left(\frac{(\rho u)_i^*(\rho u)_j^*}{\rho^*} + \check{p}^*\delta_{i,j} - \check{\tau}_{i,j}^*\right)} \quad &\approx \quad -\chi_{\rho u}(\overline{\rho u}_i - \overline{\rho u}_i^*) \ , & (2.97)
\end{aligned}$$

and

$$\frac{\partial\overline{(\rho e_t)}}{\partial t} + \overline{\frac{\partial}{\partial x_j}\left(\frac{(\rho u)^*_j}{\rho^*}\left((\rho e_t)^* + \check{p}^*\right) - \check{\tau}^*_{i,j}\frac{(\rho u)^*_i}{\rho^*} + \check{q}^*_j\right)} \approx -\chi_e(\overline{\rho e_t} - \overline{\rho e_t}^*) \ . \tag{2.98}$$

The relaxation terms drain energy from non-resolved represented scales, i.e. $\kappa_f < |\kappa| \leq \kappa_g$ and consequently act as if filtered fields $\overline{\phi}$ are filtered once more every $1/(\chi\Delta t)$ time steps where Δt is the numerical integration time-step size. The operator $(I - Q_M \circledast G)$ mainly affects the non-resolved represented scales, i.e. $\kappa_f < |\kappa| < \kappa_g$. The regularization is not very sensitive to the relaxation coefficient χ which can be either chosen or determined dynamically [59] for instantaneous filtered solution. Without a proper energy drain at non-resolved represented scales, e.g. by regularization, numerical simulations will become unstable except maybe for comparably low Reynolds number isotropic turbulence.

An alternative ADM formulation was proposed by Mathew *et al.* [116, 117] where all equations are kept in the deconvolved form as

$$\frac{\partial u^*_N}{\partial t} + \frac{\partial F_N(u^{**}_N)}{\partial x_j} \approx 0 \ . \tag{2.99}$$

They estimated the ADM modeling error to be

$$e_2 \approx -G \circledast \frac{\partial}{\partial x_j}\left[\frac{\partial F_N}{\partial u}|_{u=u^*_N}(Q \circledast G - I)^2 u_N\right] \ , \tag{2.100}$$

by keeping the leading terms in a Taylor series expansion about u^*_N. The fields' fluxes are calculated based on doubly deconvolved variables, i.e. $u^{**}_N = Q \circledast G \circledast u^*_N = Q \circledast G \circledast (Q \circledast G \circledast u_N)$. In the present work, Mathew *et al.* 's version of ADM framework [116], i.e. Eq. (2.13), is adopted.

CHAPTER 3
Filter Design for Approximate Deconvolution Models

A low-pass spatial filter is the main building block of an ADM and determines its overall performance. Considerable efforts have been made to design low-pass filters with minimal commutation error, first for dynamic subgrid-scale modeling, e.g. [46, 68, 75, 76, 118–122], and later for approximate deconvolution methods, e.g. [24, 25, 27, 123]. An ideal spatial filter for LES should have a uniform response,with no amplification at any resolved wavenumber to prevent energy injection. The filter cut-off wavenumber should be as close as possible to the grid cut-off wavenumber to minimize the increase of the effective cut-off wavenumber in the simulation. The filter transfer function should be as close as possible to the sharp cut-off filter to minimize the commutation error.

Note that the complete removal of disturbances above the grid cut-off wavenumber may not always be desirable for all LES simulation. It should prevent spurious noise caused either by the numerical scheme or the turbulence dynamics. But it could also interfere with the backscatter of turbulent kinetic energy. Backscatter of the turbulent kinetic energy is a process which energy is transferred from the small to the large scales [124]. This phenamenon has been observed as a non-negligible mechanism of turbulence dynamics in turbulent channel flow [125–127], reactive turbulent flows [128], and stratified turbulent flows [129]. Backscattering originates from the triadic interactions between the large and the small scales in a flow, i.e. $\tau_{ij}\overline{S}_{ij}$. In the spectral space it appears as a negative rate of energy change of an individual wavenumber mode [130]. In the physical space, this local phenomenon is observed as negative values of the SGS dissipation when the velocity fields from DNS [125] or experiment [126] are filtered. When such phenomena can be neglected, e.g. in the case of unbounded non-reactive flows, complete attenuation at and beyond the grid cut-off is desirable for accurate LES simulations.

A short review of Z-transform is presented and its key features are explained for a single-dimension discrete data, e.g. a time series or a one-dimensional data set. It was found that the Z-transform can be used to design a filter in one-dimension and obtain Najafi-Yazdi *et al.* 's original formulation [27]. Extension to multi-dimensional data is presented and used to demonstrate filter design on both structured and unstructured grid topologies in 2D.

3.1 Discrete Filters for Structured Grids

Discrete filters with uniform sampling (structured grids) have long been used for signal processing, image processing, and video processing using temporal convolution networks. In the field of Computational Fluid Dynamics (CFD), many scholars have contributed to the design of discrete high-order filter operators among which are Lele's compact filters [131].

In their seminal work on commutative filters for LES, Vasilyev, Lund and Moin [31] demonstrated that for a filter with $n-1$ zero moments, see Eq. (3.2), at the grid cut-off, the commutation error is $\mathcal{O}(\Delta^n)$ where Δ is the filter radius. They showed that a filtered field, $\overline{\phi}$, on a one-dimensional computational grid $\xi \in [\alpha, \beta]$

can be expressed as

$$\overline{\phi} \equiv \int_{\frac{\xi-\beta}{\Delta}}^{\frac{\xi-\alpha}{\Delta}} G(\zeta,\xi)\phi(\xi-\Delta\zeta)d\zeta = \sum_{k=0}^{+\infty} \frac{(-1)^k}{k!} \Delta^k M^k(\xi) D_\xi^k \phi(\xi) \ , \tag{3.1}$$

where $D_\xi^k \equiv d^k/d\xi^k$ is the k-th derivative operator, and $G(\zeta,\xi)$ is a spatial filter kernel. The k-th filter moment, $M^k(\xi)$, is defined as

$$M^k(\xi) \equiv \int_{\frac{\xi-\beta}{\Delta}}^{\frac{\xi-\alpha}{\Delta}} \zeta^k G(\zeta,\xi) d\zeta \ , \tag{3.2}$$

where ζ is a non-dimensional variable.

Consider a physical domain $x \in [a,b]$ which is mapped into a computational domain $\xi \in [\alpha,\beta]$ by a monotonic differentiable function $f(x)$, i.e. $\xi = f(x)$. The commutation error is defined as the difference between the filtered derivative, $\overline{d\phi/d\xi}$, and the derivative of the filtered variable, $d\overline{\phi}/d\xi$ [31]. Mathematically, it is expressed as

$$\left[\frac{d\phi}{d\xi}\right] \equiv \overline{\frac{d\phi}{d\xi}} - \frac{d\overline{\phi}}{d\xi} = \sum_{k=1}^{\infty} A_k M^k(\xi)\Delta^k + \sum_{k=1}^{\infty} B_k \frac{dM^k}{d\xi}(\xi)\Delta^k \ , \tag{3.3}$$

where A_k and B_k are in general non-zero coefficients determined based on the mapping from the physical to the computational domain. This error is zero when a filter operator and the derivative operator are commutative. The order of applying these two operators has no effect on the outcome.

Vasileyv *et al.* [31] proposed a general class of filters such that

$$M^0(\xi) = 1 \ , \qquad \text{for } \xi \in [\alpha,\beta]; \tag{3.4a}$$

$$M^k(\xi) = 0 \ , \qquad \text{for } k = 1,\cdots,n-1 \text{ and } \xi \in [\alpha,\beta]; \tag{3.4b}$$

$$M^k(\xi) \ , \qquad \text{exists for } k \geq n. \tag{3.4c}$$

Equations (3.4a) and (3.4b) result in

$$\frac{dM^k}{d\xi}(\xi) \;=\; 0\,, \tag{3.5}$$

for $k = 1, \cdots, n-1$ and $\xi \in [\alpha, \beta]$ [31]. This implies that the commutation error, $[d\phi/d\xi] = \mathcal{O}(\Delta^n)$, is an n-th order term with respect to the filter cut-off, Δ.

Most of the time, a discrete filter is defined as

$$\overline{\phi}_j = \sum_{l=-L_j}^{R_j} w_l^j \phi_{j+l}\ , \tag{3.6}$$

with the filter kernel defined in the spectral space as

$$\mathcal{G} = \sum_{l=-L_j}^{R_j} w_l^j \exp\left(i\kappa\Delta_{j+l}\right)\ , \tag{3.7}$$

where Δ_{j+l} is a location vector with respect to the node j. The k-th moment, M^k, is given by

$$M^k = \sum_{l=-L_j}^{R_j} l^k w_l^j\ , \tag{3.8}$$

where L_j and R_j represent the left and right extremes of the discrete filter stencil [31]. If $w_l^j = w_{-l}^j$ and $L_j = R_j$, then the filter is symmetric and for interior nodes has zero dispersive error. In this case, moment equations (3.4a)- (3.4c) are reduced to

$$\sum_{l=-L_j}^{R_j} w_l^j \;=\; 1\ , \tag{3.9}$$

and

$$\sum_{l=-L_j}^{R_j} l^k w_l^j \;=\; 0 \quad \text{for } k = 1, \cdots, n-1\ . \tag{3.10}$$

A more general formulation for discrete filters can be expressed as

$$\sum_{l=-L_j}^{R_j} v_l^j \overline{\phi}_{j+l} = \sum_{l=-L_j}^{R_j} w_l^j \phi_{j+l} \ , \tag{3.11}$$

or in a matrix form as

$$\mathbf{V}\overline{\Phi} = \mathbf{W}\Phi \ , \tag{3.12}$$

where Φ and $\overline{\Phi}$ denote the vector of ϕ_j and $\overline{\phi}_j$ fields over the *entire computational domain.* Generally, $\mathbf{V} \neq \mathbf{I}$ which means that the filter operation is a global operation given by

$$\overline{\Phi} \ = \ \boldsymbol{\mathcal{W}}\Phi = \mathbf{V}^{-1}\mathbf{W}\Phi \ , \tag{3.13}$$

when $\mathbf{V}$ is invertable. This is in contrast to Eq. (3.6) which is a local operation. The filter kernel for the j-th node can be expressed as

$$\begin{aligned} \overline{\Phi}_j &= \boldsymbol{\mathcal{W}}^j\Phi \\ &= \int_{\frac{\xi-\beta}{\Delta}}^{\frac{\xi-\alpha}{\Delta}} \mathbf{G}_j(\zeta,\xi)\Phi(\xi-\Delta\zeta)d\zeta \ . \end{aligned} \tag{3.14}$$

where $\boldsymbol{\mathcal{W}}^j$ is the j-th row of the matrix $\boldsymbol{\mathcal{W}}$. The filter's transfer function in the spectral domain is given by

$$\mathcal{G} = \frac{\sum_{l=-L_j}^{R_j} w_l^j \exp\left(i\kappa\Delta_{j+l}\right)}{\sum_{l=-L_j}^{R_j} v_l^j \exp\left(i\kappa\Delta_{j+l}\right)} \ . \tag{3.15}$$

The k-th moment for j-th node, M_i^k, is given by

$$M_j^k = \sum_l l^k \boldsymbol{\mathcal{W}}_l^j \ . \tag{3.16}$$

The conditions proposed by Vasilyev *et al.* [31] can still be applied on the moments, but with more difficulty as $\boldsymbol{\mathcal{W}} = \mathbf{V}^{-1}\mathbf{W}$ requires a matrix inversion which is computationally very expensive.

It is worthwhile to mention that Vasilyev *et al.* 's [31] first condition, Eq. (3.4a), is equivalent to assume zero attenuation for a uniform solution, i.e. $\mathcal{G}(\kappa = 0) = 1$. This can be easily shown by setting $\kappa = 0$ in eqs. (3.7) and (3.15), and $k = 0$ in eqs. (3.8) and (3.16).

3.2 Differential Filters for Unstructured Grids

Marsden *et al.* [24] proposed an approach to design discrete filters on unstructured meshes by extending Vasilyev *et al.* 's commutative filter [31]. Their methodology is based on choosing a set of neighboring points based on which discrete filter coefficients are calculated. Neighboring nodes are chosen as vertices of two layers of surrounding elements. Three overlapping simplex elements, i.e. triangles in 2D or tetrahedrons in 3D, are formed form the neighboring nodes and their vertices are used for calculating the filter coefficients.

Building upon Marsden et al's. work [24], Haselbacher and Vasilyev [31] proposed an alternative commutative discrete filter based on using least-squares gradient-reconstruction procedure as a filtering operator. Although this method results into a filter operator in the form of a weighted sum, it is highly dependent on the choice of neighboring nodes. The number of vanishing moments depends on the choice of neighboring nodes, i.e. stencil construction. Subsequently it affects the order of accuracy of the filter, its cut-off wavenumber and its sharpness. A second drawback is the non-vanishing filter magnitude at the grid cut-off, failing to prevent aliasing for LES.

One alternate approach was proposed in 1986 by Germano to use elliptic and parabolic differential equations as filtering operators [75, 76]. The next section provides a more detailed review of this methodology. The advantage of using a differential equation as a filter operator is its broad applicability to both structured and unstructured grids for any sufficiently stable numerical scheme. The challenge, however, remains the control over the filter transfer function.

The application of differential filters in LES started with the celebrated works of Germano in 1986 [75, 76]. He proposed a linear elliptic differential filter as the solution to the differential equation

$$\overline{\phi} - \delta^2 \frac{\partial^2 \overline{\phi}}{\partial x_i^2} = \phi \ , \tag{3.17}$$

where δ is a free parameter determining the filter strength. It can be further extended to anisotropic filters expressed as

$$\overline{\phi} - \delta_{i,j}^2 \frac{\partial^2 \overline{\phi}}{\partial x_i \partial x_j} = \phi \ . \tag{3.18}$$

Equation (3.18) can always be reduced to the canonical form given in Eq. (3.17). The filter function always results in attenuation since the differential operator is elliptic. Later he extended this concept to propose a parabolic differential filter as the particular solution of the canonical differential equation

$$\overline{\phi} + \delta' \frac{\partial \overline{\phi}}{\partial t} - \delta^2 \frac{\partial^2 \overline{\phi}}{\partial x_i \partial x_i} = \phi \ , \tag{3.19}$$

Note that this filter depends both on space and time. Germano's elliptic differential filter [75, 76] has been successfully used for a limited number of LES on unstructured grids [26, 77–81].

Germano's elliptic, Eq. (3.17), and parabolic, Eq. (3.19), filters intrinsically attenuate, but do not completely remove oscillations at any wavenumber. The transfer functions of Germano's filters approach zero only asymptotically. The filters' drop-off rates towards zero, the attenuation magnitudes at the grid cut-off and the filter cut-off wavenumbers are all controlled by one single parameter, δ. This suggests that any decrease in the effective resolved wavenumber can only be achieved at the cost of increasing the commutation error and reducing the filter's anti-aliasing characteristic.

Najafi-Yazdi *et al.* [27] proposed a modification to Germano's elliptic differential filter by adding a second-order derivative term for the unfiltered solution. Their filter is given as

$$\overline{\phi} + \alpha \frac{\partial^2 \overline{\phi}}{\partial \xi_i \partial \xi_i} = \phi + \beta \frac{\partial^2 \phi}{\partial \xi_i \partial \xi_i} \ , \tag{3.20}$$

where α and β are two free parameters, and ξ_i denotes the local coordinate system in a reference computational domain. This filter is an elliptic differential equation, like Germano's, and intrinsically guarantees no wavenumber amplification. The parameter β is determined after discretiation of the differential equation to ensure complete attenuation at the grid cut-off wavenumber, thereby unconditional numerical stability as well as strong anti-aliasing.

The parameter, α, controls the filter shape, i.e. its roll off, and the filter cut-off wavenumber. The independent control of the filter sharpness and its wavenumber requires higher order differential terms with corresponding free parameters. The addition of odd-order derivatives is not recommended as the global attenuating property cannot be guaranteed anymore. The addition of higher even-order spatial derivatives provides better control over the shape of the filter transfer function.

A more general form of the same differential filter, again in a reference computational domain, is

$$\overline{\phi} + \frac{\partial}{\partial \xi_i}\left(\alpha \frac{\partial \overline{\phi}}{\partial \xi_i}\right) = \phi + \frac{\partial}{\partial \xi_i}\left(\beta \frac{\partial \phi}{\partial \xi_i}\right) \ , \tag{3.21}$$

where α and β are functions of the spatial coordinate system, i.e. generally $\partial\alpha/\partial\xi_i \neq 0$ and $\partial\beta/\partial\xi_i \neq 0$. This general form was used here to implement the filter for two- and three-dimensional linear elements, e.g. triangles, quadrilaterals, tetrahedrals, and hexahedrals as described in section 3.4.

3.3 Discrete vs Continuous Differential Filter Design

The design of a given family of filters requires the appropriate selection of filter parameters for a given set of objectives. Again, the fundamental objectives are complete attenuation at the grid cut-off wavenumber, no amplification at any wavenumbers, high filter cut-off wavenumber, and sharp roll off. The filter parameters, e.g. δ for Germano's and α and β for Najafi-Yazdi's filter, are chosen based on its transfer function in the continuous domain. The transfer function for Germano's differential filter, $\mathcal{G}_G$, in a continuous one-dimensional domain is

$$\mathcal{G}_G = \frac{1}{1+\delta^2\kappa^2} \ . \tag{3.22}$$

This filter is intrinsically attenuating, i.e. $|\mathcal{G}_G| \leq 1$, and asymptotically tends towards zero, i.e. $\lim_{\kappa\to\infty} \mathcal{G}_G = 0$. The filter cut-off wavenumber is given as $\kappa_f = 1/\delta$. Najafi-Yazdi's filter transfer function is given by

$$\mathcal{G}_{NY} = \frac{1-\beta\kappa^2}{1-\alpha\kappa^2} \ , \tag{3.23}$$

in a continuous computational domain. The prescription $\beta = 1/\kappa_g^2$ ensures complete attenuation at a chosen wavenumber, κ_g. If $\alpha < \beta$, the filter is attenuating, $|\mathcal{G}_{NY}| \leq 1$, for $0 \leq \beta\kappa^2 < 1$.

Importantly, the discrete form of these filters have different behavior than their continuous form. For example, a central finite difference discretization of Najafi-Yazdi's filter on a one-dimensional domain would have a transfer function given by

$$\mathcal{G}_{NY,CFD} = \frac{\beta e^{-i\kappa} + (1-2\beta) + \beta e^{i\kappa}}{\alpha e^{-i\kappa} + (1-2\alpha) + \alpha e^{i\kappa}} = \frac{1-2\beta(1-\cos(\kappa))}{1-2\alpha(1-\cos(\kappa))} \ , \tag{3.24}$$

where $0 \leq \kappa \leq \pi$ is the normalized wavenumber with respect to grid size. It can be shown that $\mathcal{G}_{NY,CFD}(\kappa = 0) = 1$. Complete attenuation at the grid cut-off wavenumber, $\mathcal{G}_{NY,CFD}(\kappa = \pi) = 0$, is obtained if and only if $\beta = 1/4$. This is different than the condition for the continuous filter, $\beta = 1/\pi^2$, or the condition for an FEM formulation, $\beta = 1/12$ [27].

From this simple derivation, it can be concluded that the filter parameters should be selected after discretization. In other words, the discrete differential filter should only prevail, not its continuous form. A detailed guideline for designing Najafi-Yazdi's discrete differential filter using classical weak-Galerkin Finite Element Methods (FEM) is presented in this chapter and later used for numerical simulations.

3.4 One-dimensional Discrete Filter for weak-Galerkin FEM

Najafi-Yazdi *et al.* [27] presented the derivation and design of the discrete filter for 1D and 2D elements using classical weak-Galerkin FEM.

Considering constant piece-wise values for filter coefficients α and β in Eq. (3.21) on uniform elements, and utilizing a finite element Galerkin projection with one-dimensional linear elements, the discretized filter equation around a given node i is

$$\alpha_f\overline{\phi}_{i-1} + \overline{\phi}_i + \alpha_f\overline{\phi}_{i+1} = a\phi_i + \frac{b}{2}(\phi_{i+1} + \phi_{i-1}) \ , \tag{3.25}$$

where $\alpha_f = (1/6+\alpha)/(2/3-2\alpha)$, $a = (1/3-\beta)/(1/3-\alpha)$, and $b = (1/6+\beta)/(1/3-\alpha)$. Najafi-Yazdi *et al.* [27] showed that this filter is the differential counterpart of a compact filter, i.e. the second order compact filter by Lele [131]. The one-dimensional discrete filter, Eq. (3.25), is stable when $-1/2 < \alpha_f < 1/2$. The transfer function of this one-dimensional filter is

$$\mathcal{G}(\kappa) = \frac{a + b\cos(\kappa)}{1 + 2\alpha_f\cos(\kappa)} \ . \tag{3.26}$$

The selection $\beta = 1/12$ ensure complete attenuation at the grid cut-off, i.e $\mathcal{G}(\kappa = \pi) = 0$, for the discrete filter. The filter cut-off wavenumner, i.e. κ_f where the magnitude of the transfer function is $|\mathcal{G}(\kappa_f)| = 1/2$, is set by properly selecting the coefficient α_f (or α). Figure 3–1 compares the magnitude of the filter transfer function, Eq. (3.26) with the continuous form of the filter, as well as continuous and discretized forms of Germano's filter. The filter cut-off for all these filters is $\kappa_f = 0.9\pi$.

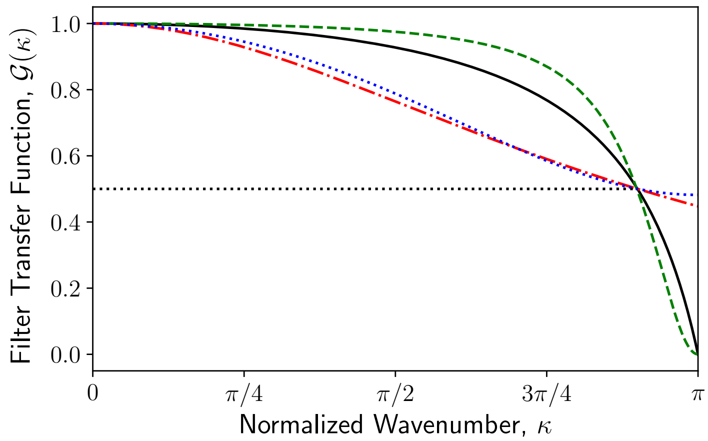

Figure 3–1: Filter transfer function magnitude in the wavenumber domain; in continuous form (solid); in discrete form Eq. (3.26) (dashed); Germano's filter in continuous form (dotted line); Germano's filter in discrete form (dashed-dotted line) with the same filter cut-off, κ_f where $|\mathcal{G} = 1/2|$ (dotted).

3.4.1 Spectral Accuracy of the One-dimensional Filter: *a priori* Analysis

The performance of the filter for LES was first investigated via a one-dimensional *a priori* analysis proposed by Bogey *et al.* [132]. The transfer functions of the viscous contribution in the Navier-Stokes equations were compared in the spectral space with that of a filtering operator. This analysis determines scales at which the filter dominates the molecular viscosity [69].

The one-dimensional equivalent of the molecular viscosity dissipation, i.e. $\nu\partial^2 u/\partial x^2$, is given by

$$\mathcal{D}_\nu = \nu\kappa^2 = \frac{\nu}{\Delta^2}\left(\kappa\Delta\right)^2 \quad , \tag{3.27}$$

where Δ is the grid spacing [132]. The one-dimensional dissipation transfer function of the spectral eddy-viscosity model by Chollet and Lesieur [133] is expressed as

$$\mathcal{D}_{\nu,t} = \nu_t \kappa^2 = \left(C_k^{-3/2} \left[0.441 + 15.2 e^{-3.03 \frac{\kappa_c}{\kappa}} \right] \sqrt{\frac{E(\kappa_c, t)}{\kappa_c}} \right) \frac{1}{\Delta^2} \left(\kappa \Delta \right)^2 \ , \tag{3.28}$$

where $C_k = 1.5$, κ_c is the spectral cut-off for an LES simulation, and $E(\kappa_c, t)$ is the energy content of the spectral cut-off Fourier mode at a given time, t.

Data from a DNS Taylor-Green vortex simulation at non-dimensional time $t^* = 9$ and $Re = 3000$ on a computational grid of 384^3 by Fauconnier *et al.* [69] was used to estimate the dissipation magnitudes from molecular viscosity and the spectral eddy viscosity. The LES simulation on a computational grid of 64^3 yields $\Delta = \pi/32$ and $\kappa_c = 32$. The energy content of the spectral cut-off Fourier mode, $E(\kappa_c, t) \approx 0.0652$ was obtained from the DNS data. The one-dimensional dissipation transfer function of a filter with kernel $\mathcal{G}$ is simply defined as $\mathcal{D} = 1 - \mathcal{G}$. Figure 3–2 compares the filter dissipation against that of molecular viscosity, the spectral eddy-viscosity model by Chollet and Lesieur [133], and the relaxation filter (RF) proposed by Visbal and Rizzetta [134], Rizzetta *et al.* [135], Mathew *et al.* [116], Bogey *et al.* [112, 113, 132]. These filters were tuned so that they all have a cut-off frequency of $\kappa_f = 0.9\pi$.

The dissipation from Najafi-Yazdi *et al.* 's filter is about one-order of magnitude smaller than molecular viscosity for low to medium wavenumbers. At high wavenumbers (close to grid cut-off) the filter becomes more dissipative, preventing aliasing in LES simulations. In contrast with relaxation filtering, Najafi-Yazdi *et al.* 's filter, as for spectral eddy-viscosity models, has a similar order of magnitude as molecular

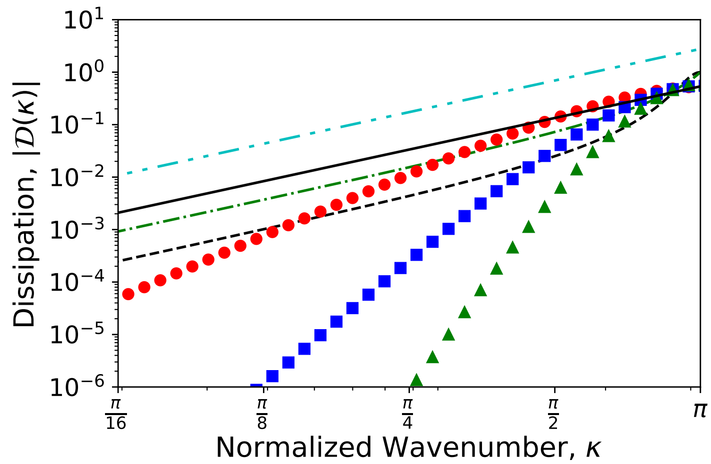

Figure 3–2: Dissipation transfer function of molecular viscosity (solid), Najafi-Yazdi *et al.* 's [27] discrete (dashed) and continuous forms (dash-dotted), the spectral eddy-viscosity model by Chollet and Lesieur [133] (dash-double dotted), and Relaxation Filtering (RF) of 4th order (circle), 8th order (square), and 14th (triangle).

viscosity. This charactersitic yields more realistic turbulence dynamics [69] than relaxation filtering. The later requires addition of relaxation terms to Navier-Stokes equations to compensate for their lack of dissipation at large scales [62].

3.5 Multi-dimensional Discrete Filter for weak-Galerkin FEM

Najafi-Yazdi *et al.* 's filter [27] can be extended to multiple dimensions using the same fundamental differential equation, i.e. Eq. (3.20), and an appropriate mapping from the computational domain to the physical domain. In unstructured grids, a unique mapping from the physical domain to a well-defined computational domain is not feasible. Instead, each single element is mapped separately into a reference element. Each element can be transformed into a reference element using a non-affine mapping, T, as shown for example in figure 3–3.

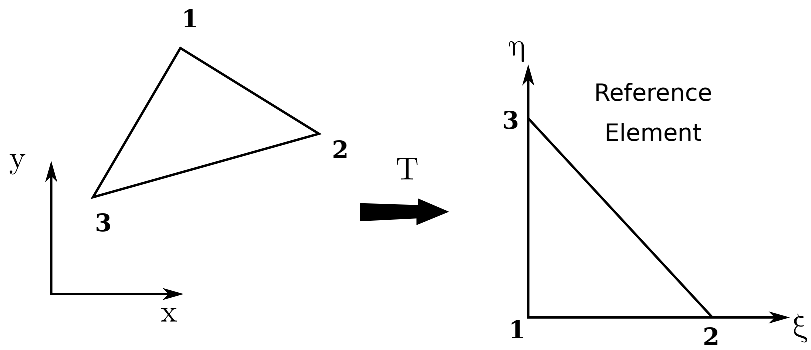

Figure 3–3: Mapping an arbitrary triangular element into a reference triangle using a non-affine mapping function T.

The differential equation (3.20) is defined in the computational domain of one single element, i.e. a reference element. Consider a transfer function $T = (T_{x_1}, T_{x_2}, \cdots, T_{x_n})$ mapping an n-dimensional element in $(x_1, x_2, \cdots, x_n)$ into its reference element in $(\xi_1, \xi_2, \cdots, \xi_n)$, a general relation between the two domains can be written in Einstein notation as

$$\xi_i = T_{x_i}(x_1, x_2, \cdots, x_n) \ , \tag{3.29}$$

and

$$\frac{\partial}{\partial \xi_i} = \frac{\partial T_{x_j}}{\partial \xi_i} \frac{\partial}{\partial x_j} \ , \tag{3.30}$$

where the repeated subscript j denotes a summation. Substituting Eq. (3.30) into the filter differential equation, i.e. Eq. (3.20), yields

$$\overline{\phi} + \frac{\partial T_{x_j}}{\partial \xi_i} \frac{\partial}{\partial x_j} \left(\alpha \frac{\partial T_{x_j}}{\partial \xi_i} \frac{\partial \overline{\phi}}{\partial x_j} \right) = \phi + \frac{\partial T_{x_j}}{\partial \xi_i} \frac{\partial}{\partial x_j} \left(\beta \frac{\partial T_{x_j}}{\partial \xi_i} \frac{\partial \phi}{\partial x_j} \right) \ . \tag{3.31}$$

Applying the weak formulation in the physical domain, Ω, with a test function w yields

$$\begin{aligned}\int_\Omega w\overline{\phi} d\Omega + \int_\Omega w \frac{\partial T_{x_j}}{\partial \xi_i}\frac{\partial}{\partial x_j}\left(\alpha \frac{\partial T_{x_j}}{\partial \xi_i}\frac{\partial \overline{\phi}}{\partial x_j}\right) d\Omega = \\ \int_\Omega w\phi d\Omega + \int_\Omega w \frac{\partial T_{x_j}}{\partial \xi_i}\frac{\partial}{\partial x_j}\left(\beta \frac{\partial T_{x_j}}{\partial \xi_i}\frac{\partial \phi}{\partial x_j}\right) d\Omega \ .\end{aligned} \tag{3.32}$$

When space is discretized into elements, integrals can be written as summations of piecewise integrals over each element giving

$$\begin{aligned}\sum_e \int w\overline{\phi} d\Omega_e + \sum_e \int w \frac{\partial T_{x_j}}{\partial \xi_i}\frac{\partial}{\partial x_j}\left(\alpha \frac{\partial T_{x_j}}{\partial \xi_i}\frac{\partial \overline{\phi}}{\partial x_j}\right) d\Omega_e = \\ \sum_e \int w\phi d\Omega_e + \sum_e \int w \frac{\partial T_{x_j}}{\partial \xi_i}\frac{\partial}{\partial x_j}\left(\beta \frac{\partial T_{x_j}}{\partial \xi_i}\frac{\partial \phi}{\partial x_j}\right) d\Omega_e \ ,\end{aligned} \tag{3.33}$$

where Ω_e represents one single element. The Galerkin projection approximates a variable $\phi(x_i)$ inside the single element with an interpolation relation given by

$$\phi = \sum_k N_k(x_i)\phi_k \ , \tag{3.34}$$

where k represents vertices of the element, and $N_k(x_i)$ is called a shape function with the following properties: $N_k(x_k) = 1$ and $N_k(x_j) = 0$ for $j \neq k$. Substituting Eq. (3.34) in Eq. (3.33) yields

$$\begin{aligned}\sum_e \sum_k \left\{ \int \left[wN_k^{(e)} + w \frac{\partial T_{x_j}}{\partial \xi_i}\frac{\partial}{\partial x_j}\left(\alpha \frac{\partial T_{x_j}}{\partial \xi_i}\frac{\partial N_k^{(e)}}{\partial x_j}\right)\right] d\Omega^{(e)} \right\} \overline{\phi}_k = \\ \sum_e \sum_k \left\{ \int \left[wN_k^{(e)} + w \frac{\partial T_{x_j}}{\partial \xi_i}\frac{\partial}{\partial x_j}\left(\beta \frac{\partial T_{x_j}}{\partial \xi_i}\frac{\partial N_k^{(e)}}{\partial x_j}\right)\right] d\Omega^{(e)} \right\} \phi_k \ ,\end{aligned} \tag{3.35}$$

The use of the classical assumption in the weak-Galerkin formulation, the governing equation for an arbitrary node p is obtained by assuming that $w = N_p$. It can be written in a matrix form as

$$\mathbf{M}\overline{\Phi} = \mathbf{N}\Phi \ , \tag{3.36}$$

where $\Phi = [\phi_p]$ is the array of nodal values, $\overline{\Phi} = [\overline{\Phi}_p]$ is the array of filtered nodal values, $\mathbf{M} = [m_{pq}]$, and $\mathbf{N} = [n_{pq}]$ where

$$m_{pq} = \sum_e \left[\int \left(N_p^{(e)} N_q^{(e)} \right) d\Omega^{(e)} + \int N_p^{(e)} \frac{\partial T_{x_j}}{\partial \xi_i} \frac{\partial}{\partial x_j} \left(\alpha \frac{\partial T_{x_j}}{\partial \xi_i} \frac{\partial N_q^{(e)}}{\partial x_j} \right) d\Omega^{(e)} \right] \ , \tag{3.37}$$

and

$$n_{pq} = \sum_e \left[\int \left(N_p^{(e)} N_q^{(e)} \right) d\Omega^{(e)} + \int N_p^{(e)} \frac{\partial T_{x_j}}{\partial \xi_i} \frac{\partial}{\partial x_j} \left(\beta \frac{\partial T_{x_j}}{\partial \xi_i} \frac{\partial N_q^{(e)}}{\partial x_j} \right) d\Omega^{(e)} \right] \ . \tag{3.38}$$

Generally, the parameters α and β are not constant. A Galerkin projection can be used to express them as $\alpha = \sum_k N_k \alpha_k$ and $\beta = \sum_k N_k \beta_k$. The main challenge is to select nodal values for the filter parameters, i.e. α_k and β_k. The goal is to satisfy filter design requirements for an ideal filter mentioned at the beginning of this chapter, while ensuring complete attenuation at the grid cut-off wavenumber. Two problems arise: (i) in an unstructured grid, the surrounding nodes of any given node form a non-uniform sampling in space; and (ii) the spectral response of the filter is in a multi-dimensional wavenumber domain, and much harder to control.

Borrowing from the signal processing literature, the Z-transform was adopted to systematically meet the target specifications along any direction in space. Uniform and non-uniform Z-transforms are briefly reviewed to help better understand the filter design methodology.

3.6 Z-Transform: Uniform and Non-Uniform

The Z-transform is the discrete equivalent of the Laplace transform. As the later is a generalization of the Fourier transform, the Z-transform extends the Discrete Fourier Transform (DFT). A one-dimensional bilateral Z-transform of a uniformly sampled data, $x[n]$, is defined as

$$\mathcal{X}(z) = \mathcal{Z}\{x[n]\} = \sum_{n=-\infty}^{\infty} x[n] z^{-n} \ , \tag{3.39}$$

where n is an integer and z is a complex variable. Every Z-transform possesses a region of convergence (ROC) defined as the set of points in the complex plane (for z) for which the Z-transform converges, i.e.

$$\text{ROC} = \{z : \|\mathcal{Z}\left(x[n]\right)\| < \infty\} \ , \tag{3.40}$$

where $||\cdot||$ is the absolute value, and z is complex. A Z-transform with multiple poles is very common to have an ROC that excludes both $z = 0$ and $z \to \infty$, i.e. a circular band in the complex domain, see figure 3–4.

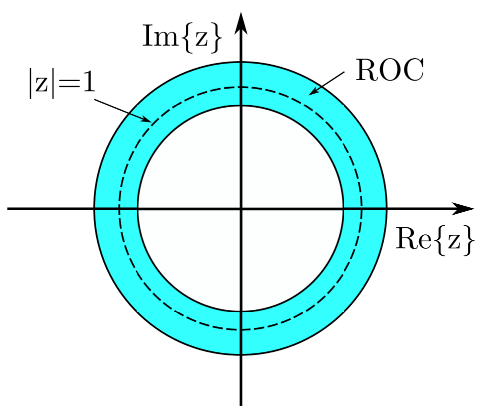

Figure 3–4: Typical region of convergence for a bilateral one-dimensional Z-transform with multiple poles.

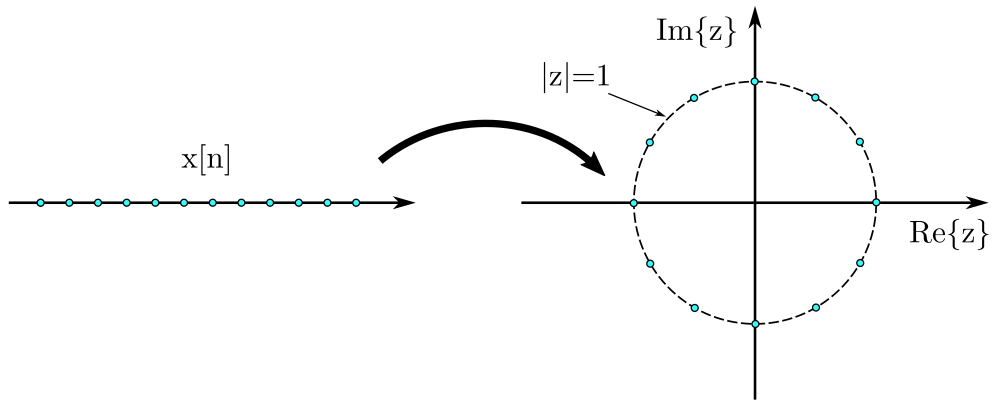

Figure 3–5: Sample locations obtained by a 12-point DFT in the z plane.

The discrete Fourier transform (DFT) is a special case of Z-transform with $z = e^{j\omega}$, where ω defines the frequency for time-dependent signals or wavenumber for spatially sampled fields. The DFT of a uniformly sampled field $x[n]$ is therefore equivalent to finding the value of Z-transform function $\mathcal{X}[k] = \mathcal{X}\{z_n\}$ at equally spaced points around the unit circle in the complex plane, i.e. $z_k = e^{j2\pi k/n}$, see figure 3–5. Some important properties of a bilateral Z-transform for a uniform sample $x[n]$ are:

Linearity : If $x[n] = a_1 x_1[n] + a_2 x_2[n]$ then

$$\mathcal{Z}\{x[n]\} = a_1 \mathcal{Z}\{x_1[n]\} + a_2 \mathcal{Z}\{x_2[n]\} \ . \tag{3.41}$$

Time (Spatial) Shift : For an integer number k

$$\mathcal{Z}\{x[n-k]\} = z^{-k} \mathcal{Z}\{x[n]\} \ . \tag{3.42}$$

Convolution : If $x[n] = x_1[n] \circledast x_2[n]$ then

$$\mathcal{Z}\{x[n]\} = \mathcal{Z}\{x_1[n]\} \mathcal{Z}\{x_2[n]\} \ . \tag{3.43}$$

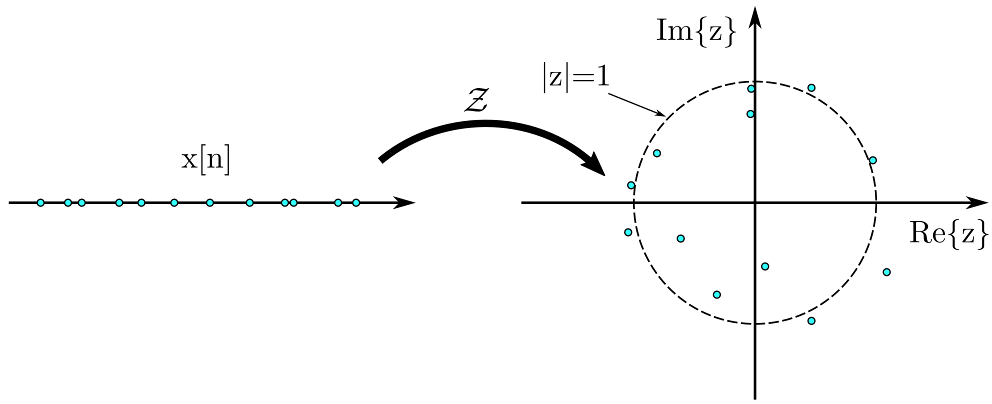

Figure 3–6: Sample locations obtained by a 12-point Z-transform in the complex plane.

A *non-uniform Z-Transform* can be defined as the Z-transform of a non-uniformly sampled sequence $x[n]$ of length N [136]. Mathematically it is written as

$$\mathcal{X}\{z_k\} = \sum_{n=0}^{N} x[n] z_k^{-n} \ , \qquad \text{for} k = 0, 1, \cdots, N-1 \ , \tag{3.44}$$

where $z_0, z_1, \cdots, z_{N-1}$ are N *arbitrary distinct* points located *arbitrarily* in the complex plane, see figure 3–6. When z_k's are selected as arbitrary distinct points on the unit circle, i.e. $z_k = e^{-2\kappa_k}$ where $\kappa_k \in [0, \pi]$, the result is the NUDFT. There are three types of NUDFT

1. **NUDFT-I** which uses *uniform* sampling in time (or space) but *non-uniform* sampling in frequency (or wavenumber).
2. **NUDFT-II** which uses *non-uniform* sampling in time (or space) but *uniform* sampling in frequency (or wavenumber).
3. **NUDFT-III** which uses *non-uniform* sampling in both time (or space) and frequency (or wavenumber).

Linearity, time (spatial) shift, and convolution properties also hold for the non-uniform bilateral Z-transform, i.e.

$$x[n] = a_1 x_1[n] + a_2 x_2[n] \quad \rightarrow \quad \mathcal{X}\{z_k\} = a_1 \mathcal{X}_1\{z_k\} + a_2 \mathcal{X}_2\{z_k\} \ , \tag{3.45}$$

$$y[m] = x[m-n] \quad \rightarrow \quad \mathcal{Y}\{z_k\} = z_k^{-m} \mathcal{X}\{z_k\} \ , \tag{3.46}$$

assuming $m, n \in \mathbb{Z}$, and

$$x[n] = x_1[n] \circledast x_2[n] \rightarrow \mathcal{X}\{z_k\} = \mathcal{X}_1\{z_k\}\mathcal{X}_2\{z_k\} \ . \tag{3.47}$$

When $x[n]$ is real, Z-transform is symmetric in the complex plane with respect to the real axis, i.e.

$$\mathcal{X}\{z_k\} = \mathcal{X}^*\{z_k^*\} \ , \tag{3.48}$$

where $(\cdot)^*$ denotes the complex conjugate.

3.7 Filter Design with One-Dimensional Non-Uniform Z-transform

Filter design procedure is first demonstrated on a one-dimensional space. Equation (3.36) for an arbitrary node i in a one-dimensional domain can be written as

$$m_{p,p-1}\overline{\phi}_{p-1} + m_{p,p}\overline{\phi}_p + m_{p,p+1}\overline{\phi}_{p+1} = n_{p,p-1}\phi_{p-1} + n_{p,p}\phi_p + n_{p,p+1}\phi_{p+1} \ . \tag{3.49}$$

To avoid infinite series associated with complete bilateral Z-transform, it is assumed that $\phi_j = 0$ for $j < p-1$ and $j > p+1$. For generality, we assume that the nodes $p-1$, i, and $p+1$ are not equally spaced and form a non-uniform sampling. Applying a non-uniform Z-transform to both sides of Eq. (3.49) and using the linearity and time-shift (space-shift) properties, i.e. eqs. (3.45) and (3.46), yields

$$\begin{aligned} m_{p,p-1}z_k\overline{\Phi}\{z_k\} + m_{p,p}\overline{\Phi}\{z_k\} + m_{p,p+1}z_k^{-1}\overline{\Phi}\{z_k\} &= \\ n_{p,p-1}z_k\Phi\{z_k\} + n_{p,p}\Phi\{z_k\} + n_{p,p+1}z_k^{-1}\Phi\{z_k\} \ , & \qquad (3.50) \end{aligned}$$

where $\overline{\Phi} = \mathcal{Z}\{\overline{\phi}_p\}$ and $\Phi = \mathcal{Z}\{\phi_p\}$. A Discrete filtering can be considered as the linear convolution of two N-point sequences, $x[n]$ and $h[n]$ expressed in vector notation as

$$\mathbf{y}_L = \mathbf{h} \circledast \mathbf{x} \ , \qquad (3.51)$$

where

$$\mathbf{x} = [x[0], x[1], \cdots, x[N-1]]^T \ , \qquad (3.52)$$

$$\mathbf{h} = [h[0], h[1], \cdots, h[N-1]]^T \ , \qquad (3.53)$$

and

$$\mathbf{y}_L = [y[0], y[1], \cdots, y[2N-2]]^T \ . \qquad (3.54)$$

This is equivalent to zero-padding $x[n]$ and $h[n]$ up to a length $2N-1$, taking their NUDFTs using a Z-transform, multiply the NUDFTs, and taking the inverse NUDFT of the result. The filter transfer function in the complex domain, i.e. z-plane, is defined as

$$\mathcal{H}\{z_k\} = \frac{\mathcal{Y}\{z_k\}}{\mathcal{X}\{z_k\}} \ , \qquad (3.55)$$

where $z_k \in \mathbb{C}$ for $k = 0, \cdots, N-1$. The one-dimensional discrete filter transfer function can consequently be derived from Eq. (3.50) as

$$\mathcal{H}_{NY}\{z_k\} = \frac{\overline{\Phi}\{z_k\}}{\Phi\{z_k\}} = \frac{n_{p,p-1}z_k + n_{p,p} + n_{p,p+1}z_k^{-1}}{m_{p,p-1}z_k + m_{p,p} + m_{p,p+1}z_k^{-1}} \; . \tag{3.56}$$

It should be recalled that $n_{j,p}$ and $m_{j,p}$ are functions of the yet-to-be-determined β_k and α_k parameters respectively. Complete attenuation of waves with grid cut-off wavenumber is required to prevent aliasing and energy pile up at small scales.

The grid cut-off wavenumber, $\kappa_g = \pi/\Delta x$, on a uniform one-dimensional grid corresponds to a wavelength $\lambda_{min} = 2\Delta x$ where Δx is the grid size. This implies that $\mathcal{H}_{NY}\{z\} = 0$ when $z = e^{\kappa_g \Delta x} = -1$. Substitution into Eq. (3.56) yields

$$n_{p-1,j} - n_{p,p} + n_{p,p+1} = 0 \; . \tag{3.57}$$

Substituting eqs. (3.57) into Eq. (3.50), and assuming $\beta_{p,p} = \beta_{p,p-1} = \beta_{p,p+1} = \beta$, yields the same condition, $\beta = 1/12$, as was reported by Najafi-Yazdi *et al.* [27]. It results in $n_{p,p} = 2n_{p,p-1} = 2n_{p,p+1}$. One alternative choice is to assume $\beta_{p,p} = 1$, reflecting the influence of a nodal value on itself, leading to $\beta_{p,p-1} = \beta_{p,p+1} = -5/6$. This yields the same relation $n_{p,p} = 2n_{p,p-1} = 2n_{p,p+1}$.

For a non-uniform grid, the grid cut-off wavenumber varies with location within the computational domain as the grid spacing is not fixed and can only be defined locally. The grid spacing is also generally not the same on either side of any node, implying that the grid cut-off is also direction dependent. To clarify this point, consider a non-uniform one-dimensional grid as shown in figure 3–7. The grid cut-off wavenumbers corresponding to the left and right sides are different, and obtained

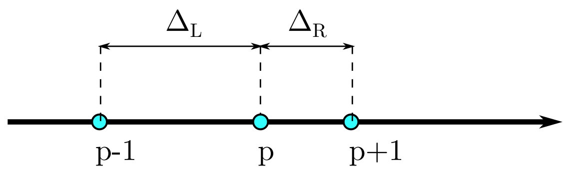

Figure 3–7: Schematics of a one-dimensional non-uniform grid spacing.

from $\kappa_{f,L} = \pi/\Delta_L$ and $\kappa_{f,R} = \pi/\Delta_R$ respectively. The filter transfer function should be able to remove both such waves. Taking a closer look at the definitions for $n_{p,p-1}$, $n_{p,p}$, and $n_{p,p+1}$, one can see that Eq. (3.57) yields

$$\left(n_{p-1,j} - n^L_{p,p}\right) + \left(n_{p,p+1} - n^R_{p,p}\right) = 0 \ , \tag{3.58}$$

where $n^L_{p,p}$ and $n^R_{p,p}$ are the contributions from the left and right elements respectively given by

$$n^L_{p,p} = \int \left(N^L_p N^L_q\right) d\Omega^L + \int N^L_p \frac{\partial T_{x_j}}{\partial \xi_i} \frac{\partial}{\partial x_j} \left(\beta \frac{\partial T_{x_j}}{\partial \xi_i} \frac{\partial N^L_q}{\partial x_j} \right) d\Omega^L \ , \tag{3.59}$$

and

$$n^R_{p,q} = \int \left(N^R_p N^R_q\right) d\Omega^R + \int N^R_p \frac{\partial T_{x_j}}{\partial \xi_i} \frac{\partial}{\partial x_j} \left(\beta \frac{\partial T_{x_j}}{\partial \xi_i} \frac{\partial N^R_q}{\partial x_j} \right) d\Omega^R \ . \tag{3.60}$$

To satisfy the full-attenuation condition on a non-uniform grid, it is sufficient to satisfy it in each element, i.e. $n^L_{p,p} = n_{p-1,j}$ and $n^R_{p,p} = n_{p+1,j}$. The reason is $n^L_{p,p}$ and $n_{p-1,j}$ are only defined in the left element, and the right element has no effect on their values. This implies that the filter could be defined in an element-wise manner. Simply put, there is *no need* to transform the filter original differential equation, Eq. (3.21), from the reference computational domain into the physical domain, Eq. (3.31). This simplifies the procedure for determining β_k's to obtain

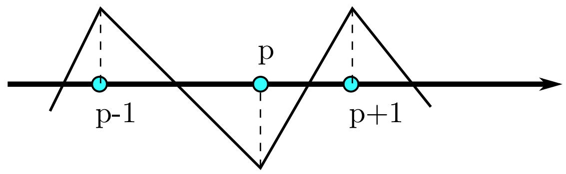

Figure 3–8: Schematics of a saw-tooth wave on a non-uniform grid.

complete attenuation at the grid cut-off. In a reference element, the $n^e_{p,q}$ coefficients are defined as

$$n^e_{p,q} = \int_{\Omega^e} N_p N_q d\Omega^e + \int N_p \frac{\partial}{\partial \xi_j} \left[\left(\sum_k \beta_k N_k \right) \frac{\partial N_q}{\partial \xi_j} \right] d\Omega^e \ , \tag{3.61}$$

which can be calculated either analytically or numerically.

Another implication of considering different grid cut-off wavenumbers for different directions is that a saw-tooth wave on a non-uniform grid is not defined as a monochromatic wave, but is a wave with alternative values across adjacent nodes irrespective of their distance, see figure 3–8. It also means that the filter's property of complete attenuation at the grid cut-off becomes independent of any stretching or anisotropy of elements. When applied to linear one-dimensional elements and assuming $\beta = \beta_k$ and $\alpha = \alpha_k$, this methodology yields exactly the same procedure and results as demonstrated by Najafi-Yazdi *et al.* [27] for both uniform and non-uniform one-dimensional grids, i.e.

$$\alpha_f \overline{\phi}_{p-1} + \overline{\phi}_p + \alpha_f \overline{\phi}_{p+1} = a\phi_p + \frac{b}{2}(\phi_{p+1} + \phi_{p-1}) \ , \tag{3.62}$$

where

$$
\begin{aligned}
\alpha_f &= \frac{\frac{1}{6}+\alpha}{\frac{2}{3}-2\alpha}\ , &(3.63)\\
a &= \frac{\frac{1}{3}-\beta}{\frac{1}{3}-\alpha}\ , &(3.64)
\end{aligned}
$$

and

$$
b = \frac{\frac{1}{6}+\beta}{\frac{1}{3}-\alpha}\ . \tag{3.65}
$$

The filter parameters α_k's control the filter strength. A quantifiable indicator of filter strength is the filter cut-off wavenumber, κ_f, defined as the wavenumber at which the magnitude of filter transfer function is $\mathcal{G}(\kappa_f) = 1/2$.

Figure 3–9 shows the effectiveness of Najafi-Yazdi *et al.* 's filter with $\alpha_f = 0.45$ in one dimension for a uniform grid and an exponentially stretched grid. A manufactured field of the form

$$
\phi(x) = e^{-5x}\left[2\sin(2\pi x) + 3\sin(4\pi x) + 0.5\sin(2\pi/x)\right]\ , \tag{3.66}
$$

was considered in one dimension which was further augmented with a saw-tooth wave of amplitude 0.5. The saw-tooth wave represents a q-wave generated due to aliasing or numerical errors generated at boundaries.

3.8 Filter Design with Multi-Dimensional Non-Uniform Z-transform

The one-dimensional filter design using non-uniform Z-transform can be extended to multiple dimensions. The most general approach is to use multi-dimensional Z-transform. The Z-transform of a D-dimensional non-uniformly sampled signal

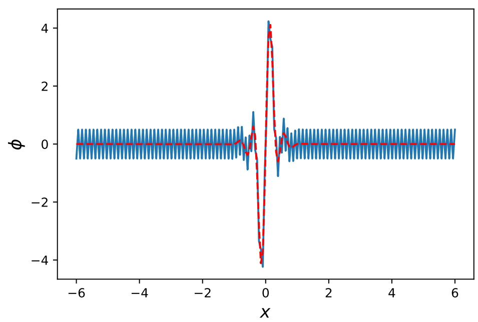

(a)

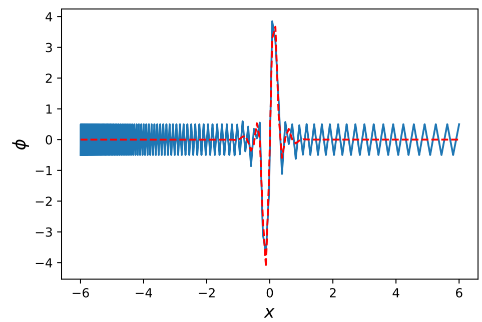

(b)

Figure 3–9: Explicit filtering of a one-dimensional noisy signal (solid) and the filtered signal (dashed) on (a) a uniform grid, and (b) exponentially stretched grid.

$x[n_1, n_2, \cdots, n_D]$ of size $N_1 \times N_2 \times \cdots \times N_D$ is defined as

$$\mathcal{X}\{z_{1,k}, z_{2,k}, \cdots, z_{D,k}\} = \sum_{n_1} \sum_{n_2} \cdots \sum_{n_D} x\left[n_1, n_2, \cdots, n_D\right] z_{1,k}^{-n_1} z_{2,k}^{-n_2} \cdots z_{D,k}^{-n_D} \ , \tag{3.67}$$

where $z_{k,j}$ for $j = 1, 2, \cdots, d$ are d sets of n_j arbitrarily distinct points in d complex planes. The D-dimensional DFT is a *special case* obtained when the z points are chosen to correspond to a uniform grid in the $(\kappa_1, \kappa_2, \cdots, \kappa_D)$ space, i.e.

$$z_{1,\kappa_1} = e^{j\frac{2\pi}{N_1}\kappa_1}, \qquad \kappa_1 = 0, 1, \cdots, N_1 - 1 \ , \tag{3.68}$$

$$z_{2,\kappa_2} = e^{j\frac{2\pi}{N_2}\kappa_2}, \qquad \kappa_2 = 0, 1, \cdots, N_2 - 1 \ , \tag{3.69}$$

$$\vdots \tag{3.70}$$

$$z_{D,\kappa_D} = e^{j\frac{2\pi}{N_D}\kappa_D}, \qquad \kappa_D = 0, 1, \cdots, N_D - 1 \ . \tag{3.71}$$

Linearity, time (space) shift and convolution properties hold for a multi-dimensional Z-transform. Following the same steps as for one-dimensional filter design, the Z-transform can be applied on the multi-dimensional discrete filter Eq. (3.36) and linearity and convolution properties used to obtain the filter transfer function. This general approach works well for structured grids, but suffers several nested complexities for unstructured grids which renders it almost impractical.

I Structured Cartesian Grid

On a structured Cartesian grid, see figure 3–10a, nodes are identified by IJK indexing and the shift property for Z-transform becomes an extension of the one-dimensional formulation. For example, a shift in both x and y directions for a structured Cartesian grid in 2D can be expressed as

$$\mathcal{Z}\{\phi_{i+1,j+1}\} = \Phi_{i+1,j+1}\{z_1, z_2\} = z_1^{-1} z_2^{-1} \Phi_{i,j}\{z_1, z_2\} \ . \tag{3.72}$$

The z_1 and z_2 planes correspond to waves traveling along x and y directions respectively. In the multi-dimensional signal processing literature, such fields are called *separable* as they are the tensor product of two one-dimensional signals (e.g. along x and y directions). The 2D filter transfer function in the z-plane for an arbitrary node (i, j) is expressed as

$$\mathcal{H}\{z_1, z_2\} = \frac{\sum\limits_{p=-1}^{1} n_{i+p,j+q} z_1^{-p} z_2^{-q}}{\sum\limits_{p=-1}^{1} m_{i+p,j+q} z_1^{-p} z_2^{-q}} \ . \tag{3.73}$$

As for the one-dimensional approach, a two-dimensional DFT is obtained if a uniformly distributed sampling from the (z_1, z_2) space is used. Complete attenuation

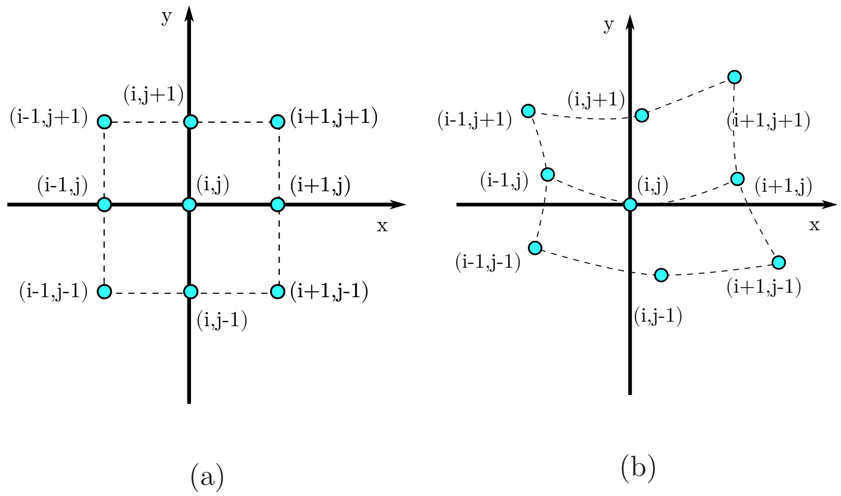

Figure 3–10: Schematics of (a) a Cartesian, and (b) a curvilinear 2D structured grids.

at the grid cut-off wavenumbers in all directions is obtained if $\mathcal{H}\{z_1 = -1, z_2\} = 0$, $\mathcal{H}\{z_1, z_2 = -1\} = 0$, and $\mathcal{H}\{z_1 = -1, z_2 = -1\} = 0$ are satisfied simultaneously. The use of the FEM-based discrete filter, Eq. (3.36), assuming $\beta = \sum_{k=1}^{k=4} \beta_k N_k$ in *each element* such that β_1 corresponds to node (i, j), and letting $\beta_1 = 1$ yields

$$\beta_2 = -2/3, \text{ and } \quad \beta_3 = 2 \ , \tag{3.74}$$

ensuring complete attenuation in all directions. The parameters α_k should be chosen carefully to i) avoid any wavenumber amplification, i.e.

$$|\mathcal{H}| \leq 1 \quad \{\forall (z_1, z_2) : |z_1| = 1 \text{ and } |z_2| = 1\} \tag{3.75}$$

and ii) control filter cut-off wavenumbers in all directions such that the filter is not too dissipative at low to moderate wavenumbers. A parameter sweep for $0.5 \leq \alpha_2/\beta_2 \leq 2$ and $0.5 \leq \alpha_3/\beta_3 \leq 2$ was conducted and $|\mathcal{H}_{max}\{z_1 = e^{i\kappa_1}, z_2 = e^{i\kappa_2}\}|_{max}$ was determined over $\kappa_1 \in [0, \pi]$ and $\kappa_2 \in [0, \pi]$ for each pair of (α_2, α_3), as shown in

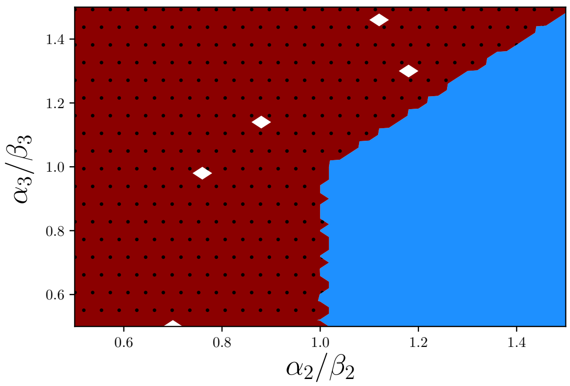

Figure 3–11: Maximum value of the filter transfer function magnitude in a 2D structured Cartesian grid (quadrilateral elements) for various combinations of α_2/β_2 and α_3/β_3; (dotted red) invalid, and (blank blue) valid regions.

Fig. 3–11. The dotted red region shows values for $(\alpha_2/\beta_2, \alpha_3/\beta_3)$ which violate the first condition, i.e.

$$\exists(\kappa_1, \kappa_2) : |\mathcal{H}\{\kappa_1, \kappa_2\}| > 1 \ . \tag{3.76}$$

Figures (3–12) shows the values of the filter cut-off wavenumber, $\kappa_f \in [0, \pi]$, if a wave was moving along x or y (Δ_1), and $x - y$ (Δ_3) directions respectively for the same value ranges. Figure 3–13 shows the magnitude of the filter transfer function and its phase angle for $\alpha_2/\beta_2 = 1.2$ and $\alpha_3/\beta_3 = 1.05$. The filter is stable, i.e. $|\mathcal{H}| \leq 1$, with a very high resolution and almost no attenuation for $0 \leq \kappa < 3\pi/4$. Since the FEM-based discrete filter is designed on a symmetric stencil, it shows no dispersion as expected from symmetric central operators.

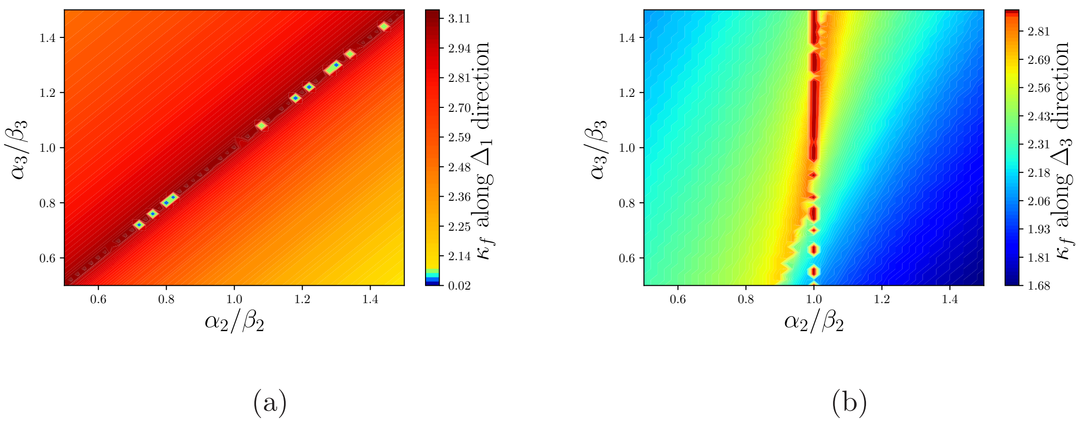

Figure 3–12: Filter cut-off wavenumber, $\kappa_f \in [0, \pi]$, as a function of α_2/β_2 and α_3/β_3 for a 2D structured Cartesian grid (quadrilateral elements) for a wave moving along (a) x- or y-axis denoted by Δ_1, and (b) along $x-y$-axis denoted by Δ_3.

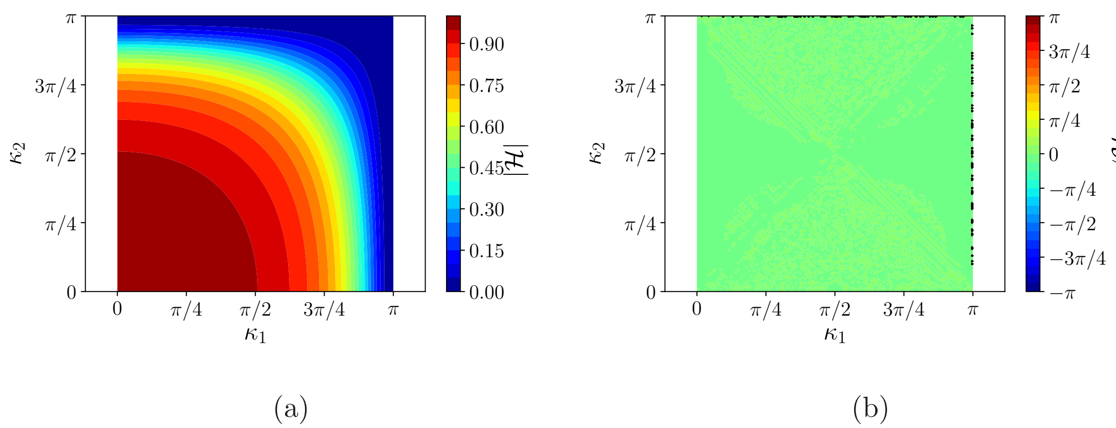

Figure 3–13: Filter transfer function (a) magnitude and (b) phase angle for $\alpha_2/\beta_2 = 1.2$ and $\alpha_3/\beta_3 = 1.05$ for a 2D structured Cartesian grid (quadrilateral elements).

II Structured Curvilinear Grid

A curvilinear grid, figure 3–10b, is structured and can be mapped into a Cartesian grid. It implies that a non-uniform sampling in the (z_1, z_2) space can be transformed into a uniform sampling from a $(\hat{z}_1, \hat{z}_2)$ space corresponding to the mapped Cartesian grid, see figure 3–14.

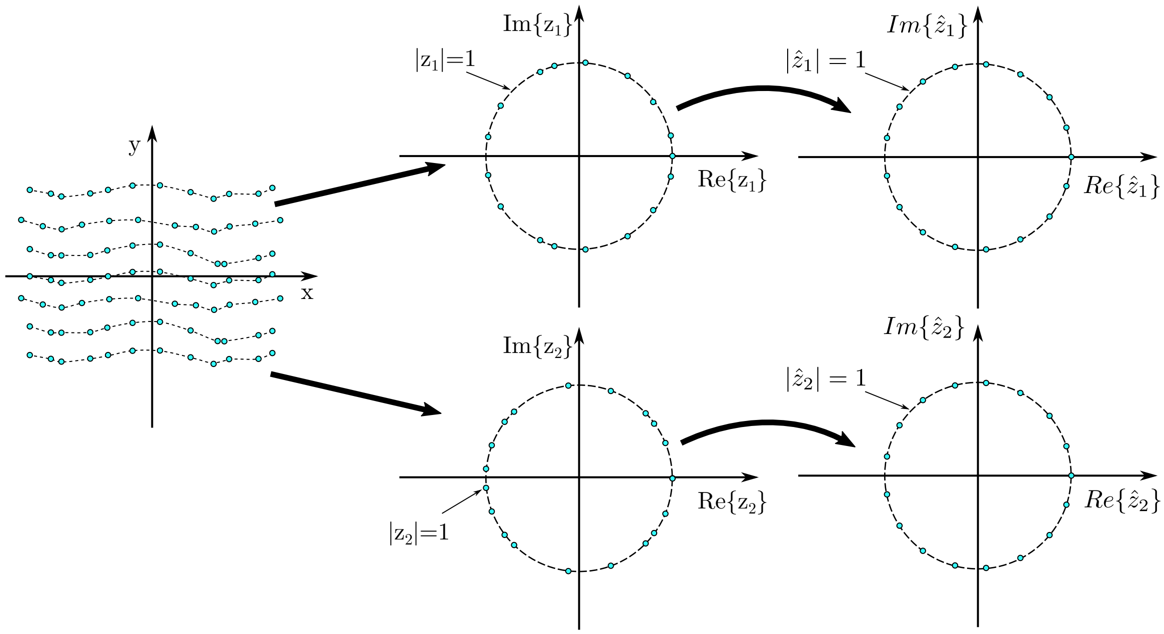

Figure 3–14: Schematics of non-uniform sampling in space and its corresponding non-uniform sampling in (z_1, z_2) space (NUDFT-III) for a 2D curvilinear structured grid, followed by transformation into a corresponding uniform sampling in $(\hat{z}_1, \hat{z}_2)$ space (NUFT-II).

By analogy with the one-dimensional case, one can conclude that the multi-dimensional filter design for a curvilinear structured grid is identical to that of a structured Cartesian grid. The parameters β_k are determined in the same manner, as justified for the one-dimensional case, by defining a saw-tooth wave along a direction (e.g. x-axis) as a wave with alternating amplitudes (1 and -1) from one node to its adjacent node (along the same I or J or K line). More details can be found in chapter 2 of Ref. [136].

III Unstructured Grid

A solution field on a fully unstructured grid is *no longer* a well-defined D-dimensional signal of the form $x[n_1, n_2, \cdots, n_D]$ of size $N_1 \times N_2 \times \cdots \times N_D$. Therefore, the definition of the multi-dimensional Z-transform as given in Eq. (3.67) is not applicable anymore. A more general definition for the Z-transform of a finite signal of the form $u[N] = [u_1, u_2, \cdots, u_N]$ defined on N points in a D-dimensional space

$$\boldsymbol{\mathcal{U}}\{z_{1,k}, z_{2,k}, \cdots, z_{D,k}\} = \sum_{m=1}^{N} u[m] \prod_{d=1}^{D} z_{d,k}^{-\hat{r}_{d,m}} \ , \tag{3.77}$$

for the data in a *local* vicinity of an arbitrary point 1, and where $\hat{r}_{d,m} = (r_{d,m}/r_{d,\min})$ is a normalized distance, and $r_{d,m} = x_{d,m} - x_{d,1}$ is the d-th component of the relative coordinate from point 1 to point m. $r_{d,\min}$ is the minimum distance of surrounding points to point 1 in the d-th direction, i.e.

$$r_{d,\min} = \min(r_{d,j} \text{ for } j = 1, 2, \cdots, m) \ . \tag{3.78}$$

More details about this definition, its relation to the classical definitions on uniform and non-uniform grids and its properties are provided in Appendix C.

The non-uniform DFT (NUDFT) of data on an unstructured grid corresponds to the generalized Z-transform with points $\mathbf{z}_k = (z_{1,k}, z_{2,k}, \cdots, z_{D,k})$ for $k = 1, 2, \cdots, N$ selected on the unit circles in D different z-planes. Applying the generalized Z-transform on the discrete filter, Eq. (3.36), for node i yields

$$m_{i,i}\overline{\Phi}_i\{\mathbf{z}_k\} + \sum_{j\neq i} m_{i,j}\overline{\Phi}_j\{\mathbf{z}_k\} = n_{i,i}\Phi_i\{\mathbf{z}_k\} + \sum_{j\neq i} n_{i,j}\Phi_j\{\mathbf{z}_k\} \ . \tag{3.79}$$

If $\mathbf{z}_k$ are uniformly selected points on the unit circles in z_1, z_2, $\cdots$, and z_D spaces, the result is a D-dimensional NUDFT-II, figure 3–15. Otherwise, $\mathbf{z}_k$ are non-uniform samples and result in a D-dimensional NUDFT-III, as shown in Fig. 3–16. The use of the *shift* property of the generalized Z-transform, see Appendix C, the transfer function of Eq. (3.79) can be expressed as

$$\boldsymbol{\mathcal{H}}\{\mathbf{z}_k\} = \frac{\overline{\Phi}_i}{\Phi_i} = \frac{n_{i,i} + \sum_{j\neq i} n_{i,j} \prod_{d=1}^{D} z_{d,k}^{-\hat{r}_{d,j}}}{m_{i,i} + \sum_{j\neq i} m_{i,j} \prod_{d=1}^{D} z_{d,k}^{-\hat{r}_{d,j}}} \ . \tag{3.80}$$

3.8.1 Complete attenuation at the grid cut-off

A correct choice of β_k's in elements around node i such that $\boldsymbol{\mathcal{H}}\{z_{d,k} = -1\} = 0$ for any $d = 1, 2, \cdots, D$, results in complete attenuation at the grid cut-off in all major directions, i.e. along the x_1-, x_2-, ..., and x_D-axes.

One alternate approach is to convert the D-dimensional generalized Z-transform into a set of D one-dimensional Z-transforms along edges connected to the point i where the filter transfer function is defined. Only nodes belonging to the elements sharing both points can directly affect the filter. Effectively, all the nodes belonging to the elements surrounding the edge $i - j$ are projected on the edge and a one-dimensional *projection* Z-transform along that direction is defined as

$$\boldsymbol{\mathcal{H}}_j\{z_j\} = \sum_{n=1}^{N} u[n] z_j^{-r_n} \ , \tag{3.81}$$

where z_j is a complex variable corresponding to the direction along $i - j$ edge. The use of the projected Z-transform instead of the multi-dimensional one is equivalent

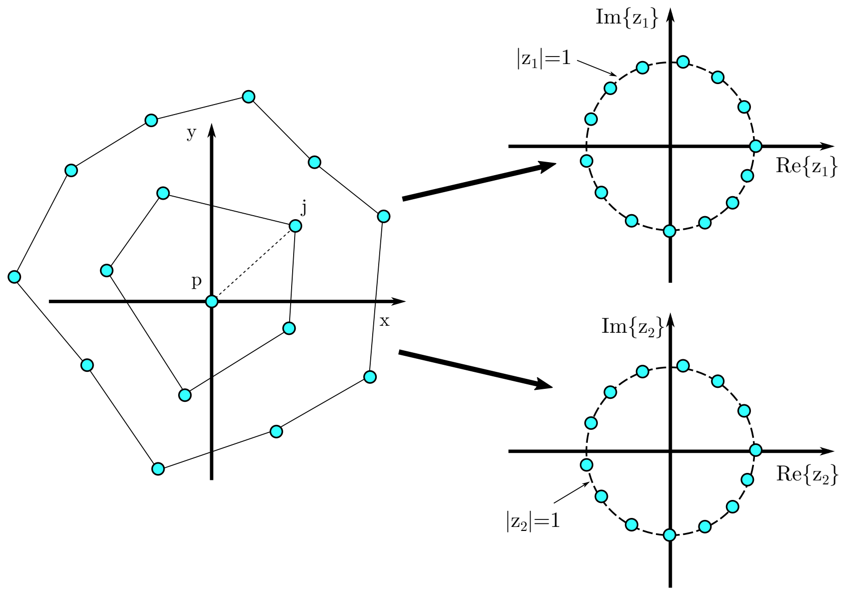

Figure 3–15: Schematics of an unstructured 2D grid and the corresponding 2D NUDFT-II.

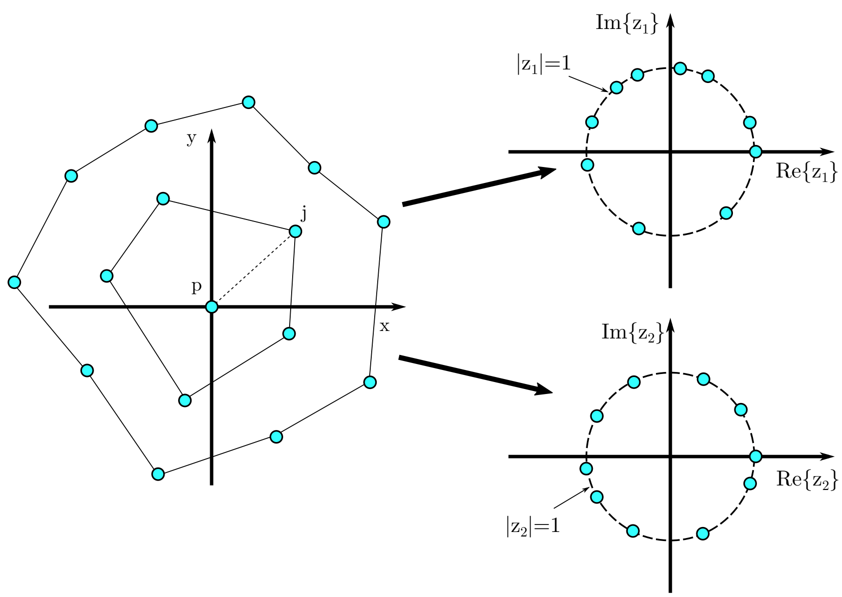

Figure 3–16: Schematics of an unstructured 2D grid and the corresponding 2D NUDFT-III.

to studying plane waves moving along the $i - j$ edge. Now complete attenuation is achieved by $\boldsymbol{\mathcal{H}}_j = 0$ when $z_j = -1$. This is equivalent to assuming a plane wave moving along $i - j$ edge such that the values at projected nodes alternate between $+1$ and -1, see figure 3–17. A closer look shows that within any element, these

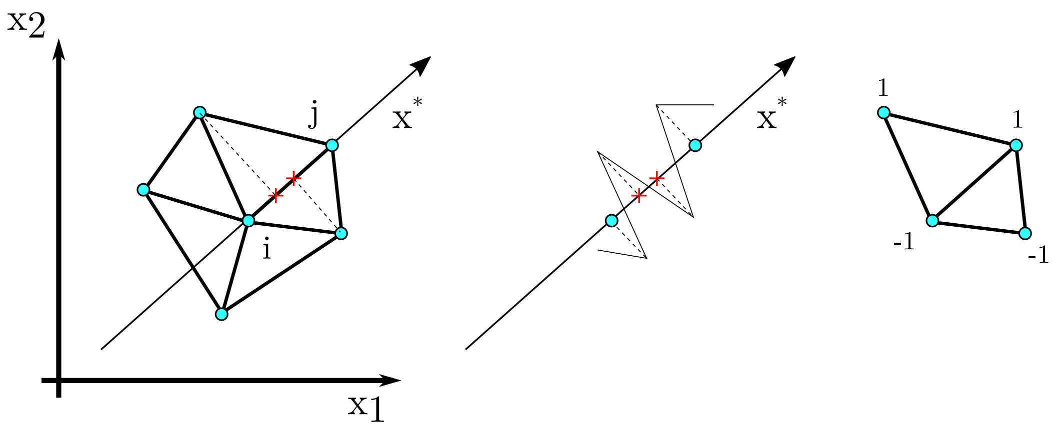

Figure 3–17: Projection of a computational stencil in 2D onto the direction between point 1 and an arbitrary point m.

alternating values corresponds to a plane wave moving along one of that element's major directions at a wavenumber corresponding to $\kappa = 2\pi/\Delta_j$ where Δ_j is a characteristic length along that direction. More details about various element types are provided later in this chapter. Similar to the one-dimensional problem, it is sufficient to satisfy the complete attenuation property element by element to achieve it over the entire stencil. Consequently, one needs to study only reference elements without need for calculating $n_{i,j}$ and $m_{i,j}$ coefficients in the physical domain. In what follows, element-wise derivations for β_k coefficients are presented for various element types.

I Bilinear Quadrilateral Element

A bilinear quadrilateral element, figure 3–18, has the following shape functions in its reference coordinate system, $(\xi, \eta) \in [-1, 1] \times [-1, 1]$:

$$N_1 = \frac{1}{4}(1-\xi)(1-\eta) \ , \tag{3.82}$$

$$N_2 = \frac{1}{4}(1+\xi)(1-\eta) \ , \tag{3.83}$$

$$N_3 = \frac{1}{4}(1+\xi)(1+\eta) \ , \tag{3.84}$$

$$N_4 = \frac{1}{4}(1-\xi)(1+\eta) \ . \tag{3.85}$$

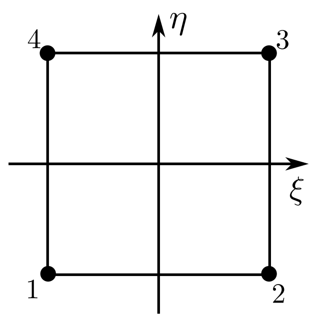

Figure 3–18: A reference bilinear (4-node) quadrilateral element.

In this reference element, (ξ, η), the discrete filter coefficients are given by

$$m_{p,q}^{(e)} = \int_{\Omega^e} (N_p N_q)\, d\Omega^{(e)} - \int_{\Omega^e} \left[\frac{\partial N_p}{\partial x_i} \frac{\partial N_q}{\partial x_i} \left(\sum_k \alpha_k N_k \right) \right] d\Omega^{(e)} \ , \tag{3.86}$$

and

$$n_{p,q}^{(e)} = \int_{\Omega^e} (N_p N_q)\, d\Omega^{(e)} - \int_{\Omega^e} \left[\frac{\partial N_p}{\partial x_i} \frac{\partial N_q}{\partial x_i} \left(\sum_k \beta_k N_k \right) \right] d\Omega^{(e)} \ . \tag{3.87}$$

Note that separation by parts was used on the second integrals in both eqs. (3.86) and (3.87). Without loss of generality, we conduct the analysis only for node 1. The right hand side of the discrete filter for node 1 is given by

$$\mathbf{N}^{(e)}\boldsymbol{\phi} = n_{1,1}^{(e)}\phi_1 + n_{1,2}^{(e)}\phi_2 + n_{1,3}^{(e)}\phi_3 + n_{1,4}^{(e)}\phi_4 \ . \tag{3.88}$$

The use of analytical tools, one can show that

$$\begin{aligned} n_{1,1}^{(e)} &= \frac{1}{36}\left(16 - 9\beta_1 - 6\beta_2 - 3\beta_3 - 6\beta_4\right) \ , & (3.89)\\ n_{1,2}^{(e)} &= \frac{1}{36}\left(8 + 3\beta_1 + 3\beta_2\right) \ , & (3.90)\\ n_{1,3}^{(e)} &= \frac{1}{9} + \frac{1}{12}\left(\beta_1 + \beta_2 + \beta_3 + \beta_4\right) \ , & (3.91) \end{aligned}$$

and

$$n_{1,4}^{(e)} = \frac{1}{36}\left(8 + 3\beta_1 + 3\beta_4\right) \ . \tag{3.92}$$

Applying the Z-transform on the element-wise right hand side, Eq. (3.88) yields

$$\boldsymbol{\mathcal{H}}_{rhs} = \mathbf{N}^{(e)}\boldsymbol{\Phi} = n_{1,1}^{(e)}\Phi_1 + n_{1,2}^{(e)}z_1^{-1}\Phi_1 + n_{1,3}^{(e)}z_1^{-1}z_2^{-1}\Phi_1 + n_{1,4}^{(e)}z_2^{-1}\Phi_1 \ . \tag{3.93}$$

To achieve complete attenuation, $\boldsymbol{\mathcal{H}}_{rhs} = 0$ for $z_1 = -1$ or $z_2 = -1$. These two conditions result in

$$z_1 = -1 \ \ \rightarrow \ \ n_{1,1}^{(e)} - n_{1,2}^{(e)} - n_{1,3}^{(e)}\frac{1}{z_2} + n_{1,4}^{(e)}\frac{1}{z_2} = 0 \ , \tag{3.94}$$

and

$$z_2 = -1 \ \ \rightarrow \ \ n_{1,1}^{(e)} + n_{1,2}^{(e)}\frac{1}{z_1} - n_{1,3}^{(e)}\frac{1}{z_1} - n_{1,4}^{(e)} = 0 \ . \tag{3.95}$$

Multiplying one by z_1 and the other by z_2 and setting all coefficients for these two variables to zero, one yields

$$3(\beta_2 + \beta_3) = 4 \; , \tag{3.96}$$

$$12\beta_1 + 9\beta_2 + 3\beta_3 + 6\beta_4 = 8 \; , \tag{3.97}$$

and

$$12\beta_1 + 6\beta_2 + 3\beta_3 + 6\beta_4 = 8 \; . \tag{3.98}$$

One trivial conclusion is that $\beta_4 = \beta_2$ as is expected from the symmetrical effect of the nodes 2 and 4 on node 1. Setting $\beta_1 = 1$ into these equations and solving them yields $\beta_2 = -2/3$ and $\beta_3 = 2$. These are exactly the same values as were obtained for structured grids in section I. Substituting these results back into eqs. (3.89) to (3.92) yields

$$n^{(e)}_{1,1} = n^{(e)}_{1,2} = n^{(e)}_{1,3} = n^{(e)}_{1,4} = \frac{1}{4}. \tag{3.99}$$

II Linear Triangular Element

A linear triangular element, figure 3–19, has the following shape functions in its reference coordinate system, $(\xi, \eta) \in [0, 1] \times [0, 1]$:

$$N_1 = (1 - \xi)(1 - \eta) \; , \tag{3.100}$$

$$N_2 = \xi \; , \tag{3.101}$$

$$N_3 = \eta \; . \tag{3.102}$$

The right hand side of the discrete filter for node 1 is given by

$$\mathbf{N}^{(e)}\boldsymbol{\phi} = n_{1,1}^{(e)}\phi_1 + n_{1,2}^{(e)}\phi_2 + n_{1,3}^{(e)}\phi_3 \ , \tag{3.103}$$

where

$$n_{1,1}^{(e)} = \frac{1}{12}\left(1 - 4\beta_1 - 4\beta_2 - 4\beta_3\right) \ , \tag{3.104}$$

$$n_{1,2}^{(e)} = \frac{1}{24}\left(1 + 4\beta_1 + 4\beta_2 + 4\beta_3\right) \ , \tag{3.105}$$

and

$$n_{1,3}^{(e)} = \frac{1}{24}\left(1 + 4\beta_1 + 4\beta_2 + 4\beta_3\right) \ . \tag{3.106}$$

One can readily deduce that $\beta_2 = \beta_3$ due to element's symmetry. Applying the Z-transform and setting $z_1 = -1$ and $z_2 = 1$, or $z_2 = -1$ and $z_1 = 1$ with $\beta_1 = 1$ yields

$$\beta_3 = \beta_2 = -\frac{3}{8} \ . \tag{3.107}$$

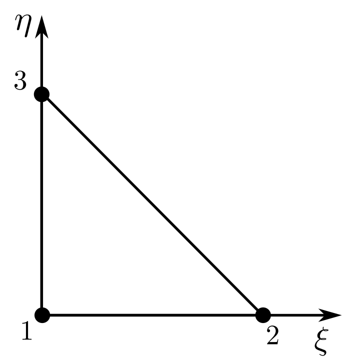

Figure 3–19: A reference linear (3-node) triangular element.

Alternatively, one can choose $\beta_1 = 1/12$ which results in $\beta_2 = \beta_3 = 1/12$ as well. Both choices result in

$$n_{1,1}^{(e)} = 0 \ , \quad \text{and} \quad n_{1,2}^{(e)} = n_{1,3}^{(e)} = \frac{1}{12} \ . \tag{3.108}$$

Note that for linear elements (triangular, tetrahedral, etc.) one should design the filter for complete attenuation along ξ and η or only along $\xi = \eta$ direction. Both cannot be achieved simultaneously. It is not the case for bilinear elements (quadrilateral, hexahedral, etc.) or higher order elements where complete attenuation at all directions can be achieved.

III Bilinear Hexahedral Element

The shape functions of a bilinear hexahedral element, figure 3–20, in its reference coordinate system $(\xi, \eta, \zeta) \in [-1, 1] \times [-1, 1] \times [-1, 1]$ are defined as follows:

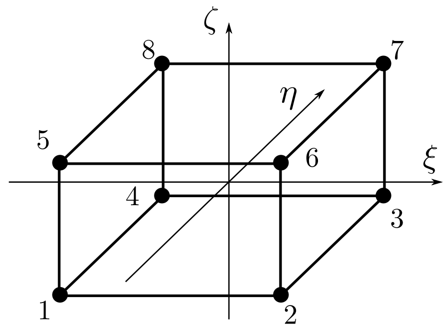

Figure 3–20: A reference bilinear (8-node) hexahedral element.

$$
\begin{aligned}
N_1 &= \frac{1}{8}(1-\xi)(1-\eta)(1-\zeta) \ , && (3.109)\\
N_2 &= \frac{1}{8}(1+\xi)(1-\eta)(1-\zeta) \ , && (3.110)\\
N_3 &= \frac{1}{8}(1+\xi)(1+\eta)(1-\zeta) \ , && (3.111)\\
N_4 &= \frac{1}{8}(1-\xi)(1+\eta)(1-\zeta) \ , && (3.112)\\
N_5 &= \frac{1}{8}(1-\xi)(1-\eta)(1+\zeta) \ , && (3.113)\\
N_6 &= \frac{1}{8}(1+\xi)(1-\eta)(1+\zeta) \ , && (3.114)\\
N_7 &= \frac{1}{8}(1+\xi)(1+\eta)(1+\zeta) \ , && (3.115)\\
N_8 &= \frac{1}{8}(1-\xi)(1+\eta)(1+\zeta) \ . && (3.116)
\end{aligned}
$$

The right hand side of the discrete filter for node 1 is given by

$$
\mathbf{N}^{(e)}\boldsymbol{\phi} = \sum_{j=1}^{8} n_{1,j}^{(e)}\phi_j \ , \qquad (3.117)
$$

where the coefficients are expressed as follows:

$$
\begin{aligned}
n_{1,1}^{(e)} &= \frac{1}{432}(128 - 81\beta_1 - 45\beta_2 - 21\beta_3 - 45\beta_4 - 45\beta_5 - 21\beta_6 \\
&\quad -9\beta_7 - 21\beta_8)\ , && (3.118)\\
n_{1,2}^{(e)} &= \frac{1}{432}(64 + 9\beta_1 + 9\beta_2 - 3\beta_3 - 3\beta_4 - 3\beta_5 - 3\beta_6 - 3\beta_7 - 3\beta_8)\ , && (3.119)\\
n_{1,3}^{(e)} &= \frac{1}{432}(32 + 15\beta_1 + 15\beta_2 + 15\beta_3 + 15\beta_4 + 3\beta_5 + 3\beta_6 + 3\beta_7 + 3\beta_8)\ , && (3.120)\\
n_{1,4}^{(e)} &= \frac{1}{432}(64 + 9\beta_1 - 3\beta_2 - 3\beta_3 + 9\beta_4 - 3\beta_5 - 3\beta_6 - 3\beta_7 - 3\beta_8)\ , && (3.121)\\
n_{1,5}^{(e)} &= \frac{1}{432}(64 + 9\beta_1 - 3\beta_2 - 3\beta_3 - 3\beta_4 + 9\beta_5 - 3\beta_6 - 3\beta_7 - 3\beta_8)\ , && (3.122)\\
n_{1,6}^{(e)} &= (32 + 15\beta_1 + 15\beta_2 + 3\beta_3 + 3\beta_4 + 15\beta_5 + 15\beta_6 + 3\beta_7 + 3\beta_8)\ , && (3.123)\\
n_{1,7}^{(e)} &= \frac{1}{27} + \frac{1}{48}(\beta_1 + \beta_2 + \beta_3 + \beta_4 + \beta_5 + \beta_6 + \beta_7 + \beta_8)\ , && (3.124)\\
n_{1,8}^{(e)} &= \frac{1}{432}(32 + 15\beta_1 + 3\beta_2 + 3\beta_3 + 15\beta_4 + 15\beta_5 + 3\beta_6 + 3\beta_7 + 15\beta_8) && (3.125)
\end{aligned}
$$

The element's symmetry imposes $\beta_5 = \beta_4 = \beta_2$ and $\beta_8 = \beta_6 = \beta_3$. Applying the Z-transform and setting $z_1 = -1$ or $z_2 = -1$ or $z_3 = -1$ with $\beta_1 = 1$ yields

$$\beta_5 = \beta_4 = \beta_2 = -\frac{7}{9}, \quad \beta_8 = \beta_6 = \beta_3 = \frac{4}{3}, \quad \text{and} \quad \beta_7 = \frac{14}{9}\ . \tag{3.126}$$

This yields

$$n_{1,1}^{(e)} = n_{1,2}^{(e)} = n_{1,3}^{(e)} = n_{1,4}^{(e)} = n_{1,5}^{(e)} = n_{1,6}^{(e)} = n_{1,7}^{(e)} = n_{1,8}^{(e)} = \frac{1}{8}\ . \tag{3.127}$$

IV Linear Tetrahedral Element

A linear tetrahedral element, see figure 3–21, has the following shape functions defined in the reference coordinate system $(\xi, \eta, \zeta) \in [0,1] \times [0,1] \times [0,1]$:

$$N_1 = (1-\xi)(1-\eta)(1-\zeta) \ , \tag{3.128}$$

$$N_2 = \xi \ , \tag{3.129}$$

$$N_3 = \eta \ , \tag{3.130}$$

$$N_4 = \zeta \ . \tag{3.131}$$

The coefficients for the right hand side of the discrete filter are given as follows:

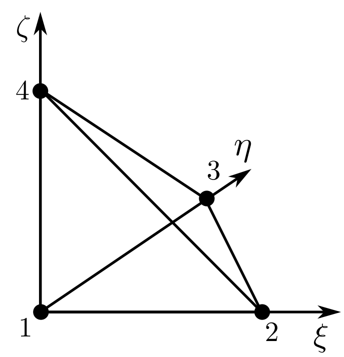

Figure 3–21: A reference linear (4-node) tetrahedral element.

$$n_{1,1}^{(e)} = \frac{1}{60} - \frac{1}{8}\left(\beta_1 + \beta_2 + \beta_3 + \beta_4\right) \ , \tag{3.132}$$

$$n_{1,2}^{(e)} = \frac{1}{120} + \frac{1}{24}\left(\beta_1 + \beta_2 + \beta_3 + \beta_4\right) \ , \tag{3.133}$$

$$n_{1,3}^{(e)} = \frac{1}{120} + \frac{1}{24}\left(\beta_1 + \beta_2 + \beta_3 + \beta_4\right) \ , \tag{3.134}$$

$$n_{1,4}^{(e)} = \frac{1}{120} + \frac{1}{24}\left(\beta_1 + \beta_2 + \beta_3 + \beta_4\right) \ , \tag{3.135}$$

The element's symmetry yields $\beta_2 = \beta_3 = \beta_4$. Substituting $z_1 = -1$, $z_2 = z_3 = 1$ and $\beta_1 = 1$ yields

$$\beta_2 = \beta_3 = \beta_4 = -\frac{7}{30} \ , \tag{3.136}$$

and

$$n_{1,1}^{(e)} = -\frac{1}{48} \ , \quad \text{and} \quad n_{1,2}^{(e)} = n_{1,3}^{(e)} = n_{1,4}^{(e)} = \frac{1}{48} \ . \tag{3.137}$$

An alternative choice is $\beta_1 = 3/40$ resulting in $\beta_2 = \beta_3 = \beta_4 = 3/40$. The use of these values still yields the same filter parameters $n_{i,j}^{(e)}$ as Eq. (3.137).

3.8.2 Zero Attenuation for Uniform Field

A low pass filter should have zero attenuation at $\kappa = 0$, i.e.

$$\boldsymbol{\mathcal{H}}\{\mathbf{z}_k = 1\} = 1 \ . \tag{3.138}$$

This guarantees that the uniform component of a field is not affected by the low-pass filtering operation. Substituting $\mathbf{z}_k = 1$ in the Z-transform function, Eq. (3.77) yields

$$n_{i,i} + \sum_{j \neq i} n_{i,j} = m_{i,i} + \sum_{j \neq i} m_{i,j} \ . \tag{3.139}$$

Every $n_{i,k}$ coefficient is obtained from a summation of integrals over elements around a node i and represents the total effect of node k on node i from all elements where both of these nodes belong to. Thus, Eq. (3.139) can be re-written as

$$\sum_{e=1}^{E} \left(n_{i,i}^{(e)} + \sum_{j \neq i} n_{i,j}^{(e)} \right) = \sum_{e=1}^{E} \left(m_{i,i}^{(e)} + \sum_{j \neq i} m_{i,j}^{(e)} \right) \ , \tag{3.140}$$

where E is the number of elements around node i, and (e) denotes one single element. The summation should be zero for *each* element.

The discrete filter is obtained by using FEM, a conservative discretization scheme, on an elliptic differential equation, i.e. Eq. (3.20). Automatically the condition

$$n_{i,i}^{(e)} + \sum_{j \neq i} n_{i,j}^{(e)} = m_{i,i}^{(e)} + \sum_{j \neq i} m_{i,j}^{(e)} \ , \tag{3.141}$$

is intrinsically satisfied. This is equivalent to the first condition proposed by Vasilyev *et al.* [31] for developing commutative filters, Eq. (3.9).

3.8.3 Filter Stability

For CFD applications, a filter is stable if the magnitude of its transfer function is always equal or less than unity, i.e. $|\boldsymbol{\mathcal{H}}| \leq 1$ for $\kappa \in [0, \pi]$. This definition guarantees that no matter how many times the filter is used, even every time step, no artificial energy is added to the field. Mathematically this requirement can be expressed as

$$|\boldsymbol{\mathcal{H}}\{\mathbf{z}_k = e^{-i\boldsymbol{\kappa}}\}| = \left| \frac{n_{i,i} + \sum_{j \neq i} n_{i,j} \prod_{d=1}^{D} z_{d,k}^{-\hat{r}_{d,j}}}{m_{i,i} + \sum_{j \neq i} m_{i,j} \prod_{d=1}^{D} z_{d,k}^{-\hat{r}_{d,j}}} \right| \leq 1 \ . \tag{3.142}$$

This condition should be satisfied at every node. In an unstructured grid, nodes generally have different computational stencil, i.e. number of surrounding elements and their geometry. The Z-transform consequently varies from one node to another. Equation (3.142) can be expressed as

$$\left| n_{i,i} + \sum_{j \neq i} n_{i,j} \prod_{d=1}^{D} z_{d,k}^{-\hat{r}_{d,j}} \right| \ \leq \ \left| m_{i,i} + \sum_{j \neq i} m_{i,j} \prod_{d=1}^{D} z_{d,k}^{-\hat{r}_{d,j}} \right| \ . \tag{3.143}$$

A sufficient condition to ensure $|\boldsymbol{\mathcal{H}}| \leq 1$ is to ensure

$$\left| n_{i,i}^{(e)} + \sum_{j \neq i} n_{i,j}^{(e)} \prod_{d=1}^{D} z_{d,k}^{-\hat{r}_{d,j}} \right| \leq \left| m_{i,i}^{(e)} + \sum_{j \neq i} m_{i,j}^{(e)} \prod_{d=1}^{D} z_{d,k}^{-\hat{r}_{d,j}} \right| \ , \tag{3.144}$$

for every element e and $\forall z_{k,d} \in |z_{k,d}| = 1$. It should be noted that this may result in a filter more dissipative than needed as it is merely *a sufficient* condition. Working with Eq. (3.144) is much easier than with Eq. (3.142) as the condition can be examined element by element. Once more, an element-wise analysis can be performed in the element's reference coordinate system. This reduces the problem to satisfying Eq. (3.144) only for each element type. Defining a filter stability index

$$\mathcal{I}_f = \left| m_{i,i}^{(e)} + \sum_{j \neq i} m_{i,j}^{(e)} \prod_{d=1}^{D} z_{d,k}^{-\hat{r}_{d,j}} \right| - \left| n_{i,i}^{(e)} + \sum_{j \neq i} n_{i,j}^{(e)} \prod_{d=1}^{D} z_{d,k}^{-\hat{r}_{d,j}} \right| \,, \tag{3.145}$$

Eq. (3.144) can be expressed simply as $\mathcal{I}_f \geq 0$. It is sufficient to ensure that $\mathcal{I}_f \geq 0$ is satisfied when a monotonic wave is moving in the $i-j$ direction, i.e. $\hat{e}_j = \vec{r}_j / |\vec{r}_j|$. This gives rise to a system of inequalities for α_k. For example, in a bilinear quadrilateral element, the filter stability conditions for node 1 are given by

$$z_1 = -1 \Rightarrow \qquad m_{1,1}^{(e)} - m_{1,2}^{(e)} - m_{1,3}^{(e)} + m_{1,4}^{(e)} \geq$$

$$n_{1,1}^{(e)} - n_{1,2}^{(e)} - n_{1,3}^{(e)} + n_{1,4}^{(e)} \,, \tag{3.146}$$

$$z_2 = -1 \Rightarrow \qquad m_{1,1}^{(e)} + m_{1,2}^{(e)} - m_{1,3}^{(e)} - m_{1,4}^{(e)} \geq$$

$$n_{1,1}^{(e)} + n_{1,2}^{(e)} - n_{1,3}^{(e)} - n_{1,4}^{(e)} \,, \tag{3.147}$$

and

$$z_1 = z_2 = -1 \Rightarrow \qquad m_{1,1}^{(e)} - m_{1,2}^{(e)} + m_{1,3}^{(e)} - m_{1,4}^{(e)} \geq$$

$$n_{1,1}^{(e)} - n_{1,2}^{(e)} + n_{1,3}^{(e)} - n_{1,4}^{(e)} \,. \tag{3.148}$$

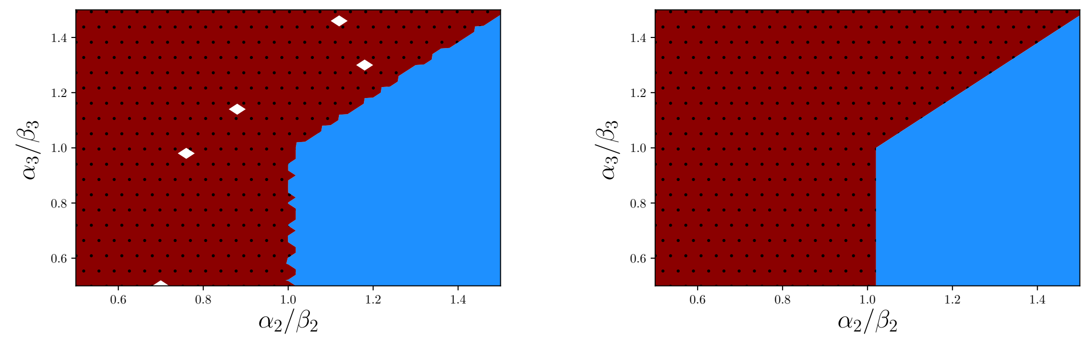

(a) (b)

Figure 3–22: Filter stability region (a) from brute force numerical search (see section I), and (b) from analytical derivation, Eq. (3.149).

Substituting values of parameters $n_{1,j}^{(e)}$ from Eq. (3.99) into these inequalities yields

$$\alpha_2 < -\frac{2}{3} \quad \Rightarrow \quad \frac{\alpha_2}{\beta_2} > 1 \ , \quad \text{and} \quad \alpha_3 < -3\alpha_2 \quad \Rightarrow \quad \frac{\alpha_3}{\beta_3} < \frac{\alpha_2}{\beta_2}. \tag{3.149}$$

Figure 3–22 compares the stability region of α_2/β_2 and α_3/β_3 found for 2D structured grids using brute force search with the analytical conditions stated in Eq. (3.149). Table 3–1 summarizes the stability conditions for different 2D and 3D elements in terms of α_k's. Note that the element symmetry appears for stability constraints as well.

3.8.4 Filter Cut-Off Wavenumber

A filter cut-off wavenumber is a wavenumber, κ_f at which the magnitude of the filter transfer function is 1/2, i.e. $|\boldsymbol{\mathcal{H}}\{\mathbf{z}_k = e^{-i\boldsymbol{\kappa}_f}\}| = 1/2$ or $|\boldsymbol{\mathcal{G}}_{NY}(\kappa_f)| = 1/2$. In two- and three-dimensional filters, the filter cut-off is a set of wavenumbers, $\boldsymbol{\kappa}_f$. The filter cut-off wavenumbers are determined by α_k parameters. Identifying appropriate values for α_k such that a desired set of $\boldsymbol{\kappa}_f$ are achieved requires finding a family of

Table 3–1: Stability conditions for Najafi-Yazdi *et al.* 's filter for different 2D and 3D element types.

	β_k	α_k
Linear Triangle	$\beta_1 = 1/12$	$\alpha_1/\beta_1 = 1$
	$\beta_2 = 1/12$	$\alpha_2/\beta_2 < 1$
	$\beta_3 = 1/12$	$\alpha_3/\beta_3 < 1$
Bilinear Quad	$\beta_1 = 1$	$\alpha_1/\beta_1 = 1$
	$\beta_2 = -2/3$	$\alpha_2/\beta_2 > 1$
	$\beta_3 = 2$	$\alpha_3/\beta_3 < \alpha_2/\beta_2$
	$\beta_4 = -2/3$	$\alpha_4/\beta_4 > 1$
Linear Tetrahedron	$\beta_1 = 3/40$	$\alpha_1/\beta_1 = 1$
	$\beta_2 = 3/40$	$\alpha_2/\beta_2 < 1$
	$\beta_3 = 3/40$	$\alpha_3/\beta_3 < 1$
	$\beta_4 = 3/40$	$\alpha_4/\beta_4 < 1$
Bilinear Hexahedron	$\beta_1 = 1$	$\alpha_1/\beta_1 = 1$
	$\beta_2 = -7/9$	$\alpha_2/\beta_2 > 1$
	$\beta_3 = 4/3$	$\alpha_3/\beta_3 < -\frac{3}{4} + \frac{7}{4}\frac{\alpha_2}{\beta_2}$
	$\beta_4 = -7/9$	$\alpha_4/\beta_4 > 1$
	$\beta_5 = -7/9$	$\alpha_5/\beta_5 > 1$
	$\beta_6 = 4/3$	$\alpha_6/\beta_6 < -\frac{3}{4} + \frac{7}{4}\frac{\alpha_2}{\beta_2}$
	$\beta_7 = 14/9$	$\frac{\alpha_7}{\beta_7} < \frac{9}{7} + 4\frac{\alpha_2}{\beta_2} - \frac{30}{7}\frac{\alpha_3}{\beta_3}$
	$\beta_8 = 4/3$	$\alpha_8/\beta_8 < -\frac{3}{4} + \frac{7}{4}\frac{\alpha_4}{\beta_4}$

solutions for the following nonlinear equation (3.150),

$$|\boldsymbol{\mathcal{H}}\{\mathbf{z}_k = e^{-i\boldsymbol{\kappa}_f}\}| = \left| \frac{n_{i,i} + \sum\limits_{j\neq i} n_{i,j} \prod\limits_{d=1}^{D} z_{d,k}^{-\hat{r}_{d,j}}}{m_{i,i} + \sum\limits_{j\neq i} m_{i,j} \prod\limits_{d=1}^{D} z_{d,k}^{-\hat{r}_{d,j}}} \right| = \frac{1}{2} \; . \tag{3.150}$$

The first point of caution is that the filter cut-off depends on the local topology of the grid and the full form of the Z-transform should be used, i.e. after assembling the effect of all surrounding elements. It is not the same as using the element-wise transfer function, i.e.

$$|\boldsymbol{\mathcal{H}}\{\mathbf{z}_k = e^{-i\boldsymbol{\kappa}_f}\}| \neq |\boldsymbol{\mathcal{H}}^{(e)}\{\mathbf{z}_k = e^{-i\boldsymbol{\kappa}_f}\}| = \left| \frac{\mathbf{N}^{(e)} \prod_{d=1}^{D} z_{d,k}^{-\hat{\mathbf{r}}_d}}{\mathbf{M}^{(e)} \prod_{d=1}^{D} z_{d,k}^{-\hat{\mathbf{r}}_d}} \right| . \tag{3.151}$$

The second point is that Eq. (3.150) should be solved separately for each node i in the grid. Generally, the number and geometry of elements around each node in an unstructured grid is different. The Z-transform of a field also varies from one node to another. These two observations imply that fixing $\boldsymbol{\kappa}_f$ and determining α_k is very tedious and may not be practically feasible.

An alternate approach is to determine α_k's by assuming appropriate ratios α_k/β_k such that $\boldsymbol{\kappa}_f$ are in an acceptable range. For aeroacoustic applications, it is customary to use filters with $\kappa_f \geq \pi/2$. It is ideal to achieve $\kappa_f \geq 3\pi/4$ to minimize the effect of filtering dissipation and dispersion on the acoustic fields. A brute-force approach was used for a 2D structured Cartesian grid, see figures (3–12), to study the effect of α_2/β_2 and α_3/β_3 coefficients on the filter cut-off wavenumbers. It was shown that for $\alpha_2/\beta_2 = 1.2$ and $\alpha_3/\beta_3 = 1.05$, the filter cut-off wavenumbers $|\boldsymbol{\kappa}_f| \geq 3\pi/4$ and $|\boldsymbol{\mathcal{H}} \geq 0.9|$ for $|\boldsymbol{\kappa}_f| \leq \pi/2$.

CHAPTER 4
Numerical Methodology

The classical continuous weak Galerkin finite element discretization scheme was adopted for spatial discretization. Finite element methods and discontinuous Galerkin methods (DG) are the two widely used methods using unstructured grids for Computational aeroacoustics (CAA) applications. Finite difference (FD) schemes are limited to structured grids, and Finite volume (FV) methods are limited by the order of accuracy, generally second order, and they are too dissipative. FEMs use less memory than DGs and are easier to implement in most programming languages.

The time integration schemes used included the standard fourth-order explicit Runge-Kutta scheme (RK4), the second-order six-stage Runge-Kutta scheme of Bogey and Bailly (RK26-Bogey) [137], the low-stage fourth-order six-stage Runge-Kutta scheme of Berland *et al.* (RK46-NL) [138], and the low-dissipation low-dispersion Multistage Taylor-Galerkin schemes of Najafiyazdi *et al.* (MSTG) [139]. These schemes, apart from RK4, were developed for CAA applications, where low dissipation and low dispersion properties are very important.

4.1 Spatial Discretization: Finite Element Method

Low order finite element computations of second derivatives in the Navier-Stokes equations, Eq. (2.1), give rise to numerical inaccuracies for the weak forms, i.e. multiplying the governing equations by a test function $w(x)$ and integrating them over the entire computational domain Ω

$$\iiint_{\Omega} w(x) \left[\frac{\partial \mathbf{U}}{\partial t} + \frac{\partial \mathbf{F}_k}{x_k} \right] d\Omega = 0 \ , \tag{4.1}$$

improves accuracy [140]. Discretizing the computational domain, Ω, into finite elements and splitting the integrals into summation of element-wise integrals yields

$$\sum_{e=1}^{n_e} \iiint_{\Omega_e} w(x) \left[\frac{\partial \mathbf{U}}{\partial t} + \frac{\partial \mathbf{F}_k}{x_k} \right] d\Omega_e = 0 \ , \tag{4.2}$$

where n_e is the total number of finite elements, and Ω_e is one single finite element.

The most common method of mapping a continuous solution field into a discretized computational domain is the Galerkin method of weighted residuals. In this method, an independent variable, ϕ, inside a finite element is *approximated* as a sum of basis functions, $N_j(x_i)$, and its values at the computational nodes, ϕ_j. This is mathematically expressed as

$$\phi(x,t) \approx \sum_{j=1}^{n} N_j(x)\phi_j(t) \ , \tag{4.3}$$

where x denotes the one, two, or three-dimensional coordinates of an arbitrary point inside the finite element, and n is the number of computational nodes in the element. The shape functions should satisfy $N_j(x = x_j) = 1$ and $N_j(x = x_k) = 0$ for $k \neq j$ where x_j and x_k are the coordinates of two computation nodes j and k in the finite element. Note that the shape functions are generally not functions of time (except in space-time FEMs [141]).

Using the Galerkin method for Eq. (4.2) results in a semi-discrete weak form of the Navier-Stokes equations, given as

$$\sum_{e=1}^{n_e} \iiint_{\Omega_e} w(x) \left[\sum_{j=1}^{n} N_j(x) \frac{\partial \mathbf{U}_j(t)}{\partial t} + \frac{\partial}{x_k} \mathbf{F}_k(\mathbf{U}) \right] d\Omega_e = 0 \ . \tag{4.4}$$

Note that there are three different approaches to discretize the derivative terms for flux functions, i.e. $\partial \mathbf{F}_k(\mathbf{U})/\partial x_k$. In the first method, the derivative is cast into a Jacobian form, i.e.

$$\frac{\partial}{x_k} \mathbf{F}_k(\mathbf{U}) = \frac{\partial \mathbf{F}_k}{\partial \mathbf{U}} \frac{\partial \mathbf{U}_k}{\partial x_k} \ , \tag{4.5}$$

which is non-conservative and not recommended for computational methods. In the second approach, the flux terms are expanded and the derivative of each term is integrated separately. For example, for the x-momentum equation one could write

$$\frac{\partial}{x_1} \mathbf{F}_1(\mathbf{U}) = \frac{\partial}{x_1} \left(\rho u_1 u_1 + p - \tau_{1,1} \right) + \frac{\partial}{x_2} \left(\rho u_2 u_1 - \tau_{2,1} \right) + \frac{\partial}{x_3} \left(\rho u_3 u_1 - \tau_{2,1} \right) \ , \tag{4.6}$$

and each flow variable, i.e. u_1, u_2, u_3, p, etc., are approximated by the weighted residual approach. It is a tedious and rather unnecessary approach for discretization. The third approach, is to consider the flux functions, $\mathbf{F}$, as field variables and use weighted residual approximation on them. The flux functions in one single finite element is written as

$$\mathbf{F}_k = \sum_{j=1}^{n} N_j(x) \mathbf{F}_{j,k} \ , \tag{4.7}$$

where $\mathbf{F}_{j,k}$ are flux functions calculated at the computational nodes of the element. This approach is known as *group finite element* in the literature [142–145]. Substitution into Eq. (4.4) yields

$$\sum_{e=1}^{n_e} \iiint_{\Omega_e} w(x) \left[\sum_{j=1}^{n} N_j(x) \frac{\partial \mathbf{U}_j(t)}{\partial t} + \left(\frac{\partial}{x_k} N_j(x) \right) \mathbf{F}_{j,k}(t) \right] d\Omega_e = 0 \ . \tag{4.8}$$

This equation holds for all computational nodes in the underlying grid. Consider an arbitrary node i, and a test function $w_i(x)$ defined around this node. The governing equation, Eq. (4.8), for this node is given as

$$\sum_{e=1}^{n_e} \iiint_{\Omega_e} w_i(x) \left[\sum_{j=1}^{n} N_j(x) \frac{\partial \mathbf{U}_j(t)}{\partial t} + \left(\frac{\partial}{x_k} N_j(x) \right) \mathbf{F}_{j,k}(t) \right] d\Omega_e = 0 \ . \tag{4.9}$$

In most variations of the Galerkin method, the test function is usually defined only in the vicinity of a computational node, i.e. finite elements around each node. In other words, for an arbitrary node i, the test function $w_i(x)$ is defined such that

$$w_i(x = x_i) \ = \ 1 \ , \tag{4.10}$$

$$w_i(x = x_j) \ = \ 0 \quad \text{for } j \neq i \ , \tag{4.11}$$

and

$$w_i(x \in \Omega^{(i)}) \neq 1 \ , \tag{4.12}$$

where $\Omega^{(i)}$ is the union of all the finite elements around the node i. This eliminates all terms except the integrals over elements surrounding this node, i.e.

$$\sum_{e=1}^{n_e^{(i)}} \iiint_{\Omega_e} w_i(x) \left[\sum_{j=1}^{n} N_j(x) \frac{\partial \mathbf{U}_j(t)}{\partial t} + \left(\frac{\partial}{x_k} N_j(x) \right) \mathbf{F}_{j,k}(t) \right] d\Omega_e = 0 \ , \tag{4.13}$$

where $n_e^{(i)}$ is the number of elements around the node i. This can be written in a matrix form as

$$\mathbf{M}\frac{\partial \mathbf{U}}{\partial t} = \mathbf{RHS} \ , \tag{4.14}$$

where $\mathbf{M} = [m_{ij}]$, $\mathbf{RHS} = [RHS_{ij}]$,

$$m_{ij} = \sum_{e=1}^{n_e^{(i)}} \iiint_{\Omega_e} w_i(x) N_j(x)\, d\Omega_e \ , \tag{4.15}$$

and

$$RHS_{ij} = -\sum_{e=1}^{n_e^{(i)}} \iiint_{\Omega_e} w_i(x) \left(\frac{\partial}{x_k} N_j(x) \right) \mathbf{F}_{j,k}(t)\, d\Omega_e \ . \tag{4.16}$$

Different forms of the Galerkin scheme can be expressed as different definitions for $w_i(x)$ over $\Omega^{(i)}$. In the classical Galerkin scheme, it is assumed that $w_i(x) = N_i(x)$. In this work, the classical Galerkin was used in most cases. An alternative formulation, i.e. streamline upwind/Petrov-Galerkin (SUPG) [145], was used as a stablizied FEM scheme to evaluate the performance of explicit filtering on stabilizing the classical weak-Galerkin FEM for highly convective flow simulations. More details on the SUPG method are provided in Appendix A.

4.2 Temporal Integration

Several time integration schemes were used to conduct large eddy simulations, including the standard fourth-order Runge-Kutta (RK4), the second-order six-stage Runge-Kutta scheme of Bogey and Bailly (RK26-Bogey) [137], the low-stage fourth-order six-stage Runge-Kutta scheme of Berland *et al.* (RK46-NL) [138], and the low-dissipation low-dispersion Multistage Taylor-Galerkin schemes of Najafiyazdi *et* *al.* (MSTG) [139]. Consider the governing equation in the form

$$\frac{\partial \mathbf{U}}{\partial t} = \mathbf{R}\left(\mathbf{U}; t\right) \ . \tag{4.17}$$

An explicit p-stage Runge-Kutta scheme can be written in a general form as

$$\mathbf{U}^{n+1} = \mathbf{U}^{n} + \Delta t \sum_{j=1}^{p} b_j \, K_j \ , \tag{4.18}$$

where $K_1 = \mathbf{U}^n$, $K_j = \mathbf{R}\left(\mathbf{U}^{(j)}; t_n + c_j \Delta t\right)$ and $\mathbf{U}^{(j)} = \mathbf{U}^n + \Delta t \sum_{l=1}^{j-1} a_{l,j} K_l$. The Butcher tableau is given as

$$\begin{array}{c|ccccc}
0 & & & & & \\
c_2 & a_{2,1} & & & & \\
c_3 & a_{3,1} & a_{3,2} & & & \\
\vdots & \cdots & & \ddots & & \\
c_p & a_{p,1} & a_{p,2} & \cdots & a_{p,p-1} & \\
\hline
 & b_1 & b_2 & \cdots & b_{p-1} & b_p
\end{array} \ . \tag{4.19}$$

The coefficients b_k are set such that a desirable m-th order accuracy is achieved. For a linear operator $\mathbf{R}(\mathbf{U}; t)$, equation (4.18) can be collapsed into a single equation as

$$\mathbf{U}^{n+1} = \mathbf{U}^{n} + \sum_{j=1}^{p} \ q_j \, \Delta t^j \, \frac{\partial^j \mathbf{U}^n}{\partial t^j} \ . \tag{4.20}$$

For an m-th order accurate scheme $q_j = 1/j!$ for $j = 1, \cdots, m$. The standard RK4 scheme is obtained by setting $a_{2,1} = a_{3,2} = 1/2$, $a_{4,3} = 1$, $c_2 = c_3 = 1/2$, $c_4 = 1$, and $b_1 = 1/6$, $b_2 = b_3 = 1/3$, and finally $b_4 = 1/8$. RK4 is fourth order for linear equations, but only second order for nonlinear problems.

Bogey and Bailly [137] proposed a six-stage second-order Runge-Kutta algorithm (RK26-Bogey) by optimizing the dissipation and the dispersion errors. RK26-Bogey is defined as

$$\mathbf{U}^{(l)} = \mathbf{U}^{(l)} + \alpha_l \, \Delta t \, \mathbf{R}\left(\mathbf{U}^{(l-1)}\right) \ , \tag{4.21}$$

where $\mathbf{U}^{n+1} = \mathbf{U}^{(p)}$ and $\mathbf{U}^{(0)} = \mathbf{U}^n$. The Butcher tableau for this scheme is

$$\begin{array}{c|ccccc}
0 & & & & & \\
c_2 & \alpha_1 & & & & \\
c_3 & 0 & \alpha_2 & & & \\
\vdots & \cdots & & \ddots & & \\
c_5 & 0 & 0 & \cdots & \alpha_5 & \\
\hline
 & 0 & 0 & \cdots & 0 & \alpha_6
\end{array} \ , \tag{4.22}$$

where $\alpha_1 = 0.117979902$, $\alpha_2 = 0.184646966$, $\alpha_3 = 0.246623604$, $\alpha_4 = 0.331839543$, $\alpha_5 = 1/2$, and $\alpha_6 = 1$.

Berland *et al.* [138] proposed a low-dissipation and low-dispersion six-stage fourth-order Runge-Kutta scheme (RK46-NL) with the same Butcher tableau as Eq. (4.22) with $\alpha_1 = 0.122187406$, $\alpha_2 = 0.0188562529$, $\alpha_3 = 1/4$, $\alpha_4 = 1/3$, $\alpha_5 = 1/2$, and $\alpha_6 = 1$. A multi-stage approach was proposed by Najafiyazdi *et al.* [139] for the development of high-order Taylor-Galerkin (TG) schemes. The three-stage third-order Taylor-Galerkin (TTGNC3-1), and three-stage fourth-order Taylor-Galerkin

(TTGN4A-1) schemes were used in this work. The TTGNC3-1 scheme is defined as

$$\mathbf{U}^{(1)} = \mathbf{U}^n + \frac{1}{6\alpha}\,\Delta t\,\partial_t \mathbf{U}^n \ , \tag{4.23}$$

$$\mathbf{U}^{(2)} = \mathbf{U}^n + \alpha\,\Delta t\,\partial_t \mathbf{U}^{(1)} \ , \tag{4.24}$$

$$\mathbf{U}^{n+1} = \mathbf{U}^n + \Delta t\,\partial_t \mathbf{U}^{(2)} + \gamma\,\Delta t^2\,\partial_{tt} \mathbf{U}^n \ , \tag{4.25}$$

where $\alpha = 1/2 - \gamma$, and γ is a free parameter which controls scheme dissipation at high frequencies. The TTGN4A-1 scheme is given by

$$\mathbf{U}^{(1)} = \mathbf{U}^n + \frac{1}{4}\,\Delta t\,\partial_t \mathbf{U}^n \ , \tag{4.26}$$

$$\mathbf{U}^{(2)} = \mathbf{U}^n + \frac{1}{3}\,\Delta t\,\partial_t \mathbf{U}^{(1)} \ , \tag{4.27}$$

$$\mathbf{U}^{n+1} = \mathbf{U}^n + \Delta t\,\partial_t \mathbf{U}^n + \frac{1}{2}\,\Delta t^2\,\partial_{tt} \mathbf{U}^{(2)} \ . \tag{4.28}$$

Figure 4–1 shows the amount of dissipation, $1 - |\mathcal{G}(\omega\Delta t)|$, and the phase error, $|\omega\Delta t - \omega^*\Delta t|/\pi$, for these semi-discrete methods. The TTGN4A in the semi-discrete form (with only temporal discretization) has the same dissipation and dispersion properties as RK44, while they are different after spatial discretization. More details about TTGNC3-1 and TTGN4A-1 are provided in Appendix B.

4.3 Navier-Stokes Characteristic Boundary Conditions

The non-reflective Navier-Stokes Characteristic Boundary Conditions (NSCBC) of Poinsot and Lele [146] were used to minimize acoustic reflections from boundaries. It is an extension to the Local One-Dimensional Inviscid (LODI) relations where values for the wave amplitude variations in the viscous multi-dimensional case are inferred. To generalize the NSCBCs for an arbitrary oriented boundary face (see Fig. 4–2). The Navier-Stokes equations can be expressed in the orthonormal local

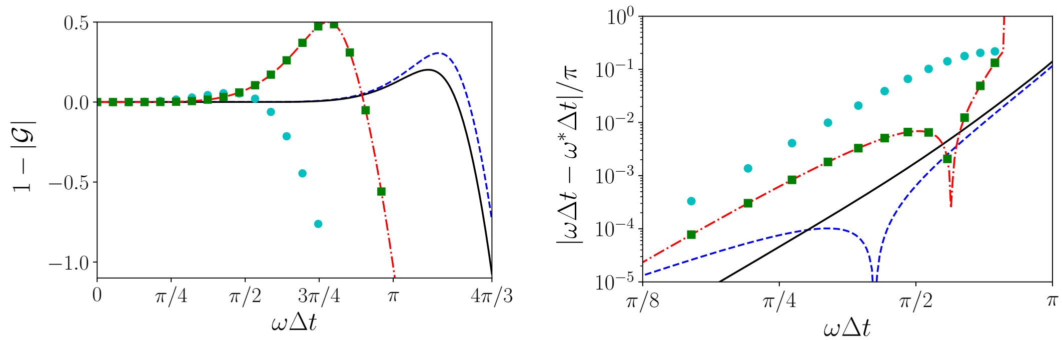

(a) (b)

Figure 4–1: The (a) dissipation and (b) dispersion errors of RK4 (dash-dotted red), RK26-Bogey (dashed blue), RK46-NL (solid black), TTGNC3-1 (cyan circle), and TTGN4A-1 (green square) schemes as a function of angular frequency $\omega\Delta t$.

frame of reference , $(\hat{n_1}, \hat{n}_2, \hat{n}_3)$, as

$$\frac{\partial \mathbf{U}_n}{\partial t} + \frac{\partial \mathcal{F}_{inv,j}}{\partial n_j} = \frac{\partial \mathcal{F}_{vis,j}}{\partial n_j} \ , \tag{4.29}$$

where $\mathbf{U}_n = (\rho, \rho u_{n_1}, \rho u_{n_2}, \rho u_{n_3}, \rho e_t)$ is the vector of conservative variables in the local frame of reference. The inviscid, $\mathcal{F}_{inv,j}$, and viscous , $\mathcal{F}_{vis,j}$, flux vectors along the n_j-direction are defined similar to Eq. (2.1) by substituting u_j and $\tau_{i,j}$ with u_{n_j} and τ_{n_i,n_j}.

Applying the characteristic lines analysis on the normal direction derivative term, $\partial \mathcal{F}_{inv,1}/\partial n_1$, yields [147]

$$\frac{\partial \mathbf{U}_n}{\partial t} + \mathbf{Pd} + \frac{\partial \mathcal{F}_{inv,2}}{\partial n_2} + \frac{\partial \mathcal{F}_{inv,3}}{\partial n_3} = \frac{\partial \mathcal{F}_{vis,j}}{\partial n_j} \ , \tag{4.30}$$

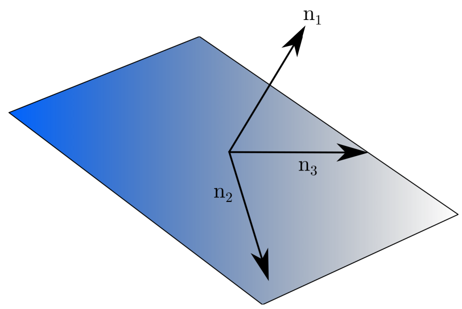

Figure 4–2: A local frame of reference on an arbitrary oriented boundary face with the normal vector $\hat{n}$ pointing into the computational domain.

where

$$\mathbf{d} = \mathbf{P}^{-1}\frac{\partial \mathcal{F}_{inv,1}}{\partial n_1} = \mathbf{S}_1\boldsymbol{\mathcal{L}} = \begin{bmatrix} \frac{1}{c^2}\left[\mathcal{L}_2 + \frac{1}{2}(\mathcal{L}_5 + \mathcal{L}_1)\right] \\ \frac{1}{2\rho c}(\mathcal{L}_5 - \mathcal{L}_1) \\ \mathcal{L}_3 \\ \mathcal{L}_4 \\ \frac{1}{2}(\mathcal{L}_5 + \mathcal{L}_1) \end{bmatrix}, \tag{4.31}$$

$$\mathbf{P} = \begin{bmatrix} 1 & 0 & 0 & 0 & 0 \\ u_{n_1} & \rho & 0 & 0 & 0 \\ u_{n_2} & 0 & \rho & 0 & 0 \\ u_{n_3} & 0 & 0 & \rho & 0 \\ \frac{1}{2}u_{n_j}u_{n_j} & \rho u_{n_1} & \rho u_{n_2} & \rho u_{n_3} & 1/k \end{bmatrix}, \tag{4.32}$$

with $k = (\gamma - 1)$,

$$\mathbf{P}^{-1} = \begin{bmatrix} 1 & 0 & 0 & 0 & 0 \\ -u_{n_1}/\rho & 1/\rho & 0 & 0 & 0 \\ -u_{n_2}/\rho & 0 & 1/\rho & 0 & 0 \\ -u_{n_3}/\rho & 0 & 0 & 1/\rho & 0 \\ k/2u_{n_j}u_{n_j} & -ku_{n_1} & -ku_{n_2} & -ku_{n_3} & k \end{bmatrix}, \tag{4.33}$$

$$\mathbf{S}_1 = \begin{bmatrix} 1/2c^2 & \delta_{1,1}/c^2 & \delta_{2,1}/c^2 & \delta_{3,1}/c^2 & 1/2c^2 \\ -\delta_{1,1}/2\rho c & 1-\delta_{1,1} & 0 & 0 & \delta_{1,k}/2\rho c \\ -\delta_{2,1}/2\rho c & 0 & 1-\delta_{2,1} & 0 & \delta_{2,k}/2\rho c \\ -\delta_{3,1}/2\rho c & 0 & 0 & 1-\delta_{3,1} & \delta_{3,k}/2\rho c \\ 1/2 & 0 & 0 & 0 & 1/2 \end{bmatrix}, \tag{4.34}$$

and

$$\boldsymbol{\mathcal{L}} = \mathbf{\Lambda}^1 \mathbf{S}_1^{-1} \frac{\mathbf{U}_n}{\partial n_1} = \begin{bmatrix} \lambda_1(\frac{\partial p}{\partial n_1} - \rho c \frac{\partial u_{n_1}}{\partial n_1}) \\ \lambda_2(c^2 \frac{\partial \rho}{\partial n_1} - \frac{\partial p}{\partial n_1}) \\ \lambda_3 \frac{\partial u_{n_2}}{\partial n_1} \\ \lambda_4 \frac{\partial u_{n_3}}{\partial n_1} \\ \lambda_5(\frac{\partial p}{\partial n_1} + \rho c \frac{\partial u_{n_1}}{\partial n_1}) \end{bmatrix}. \tag{4.35}$$

The eigenvalues $\lambda_1 = u_{n_1} - c$, $\lambda_{2,3,4} = u_{n_1}$, and $\lambda_5 = u_{n_1} + c$ are the diagonal terms of the eigenvalue matrix $\mathbf{\Lambda}^1$. The inverse matrix $\mathbf{S}_1^{-1}$ can be directly calculated by

$$\mathbf{S}_1^{-1} = \begin{bmatrix} 0 & -\delta_{1,1}\rho c & -\delta_{1,2}\rho c & -\delta_{1,3}\rho c & 1 \\ \delta_{1,1}c^2 & 1-\delta_{1,1} & 0 & 0 & -\delta_{1,1} \\ \delta_{2,1}c^2 & 0 & 1-\delta_{2,1} & 0 & -\delta_{2,1} \\ \delta_{3,1}c^2 & 0 & 0 & 1-\delta_{3,1} & -\delta_{3,1} \\ 0 & \delta_{1,1}\rho c & \delta_{2,1}\rho c & \delta_{3,k}\rho c & 1 \end{bmatrix} . \tag{4.36}$$

The aforementioned formulation is for boundary *faces*. Following the analysis proposed by Hirsch [148] and Thompson [149, 150], Lodato *et al.* [147] extended this approach to boundary *edges* and *corners*. In their formulation, Lodato *et al.* [147] assumed that a boundary *edge* and a boundary *corner* are shared between two and three *orthogonal* boundary *faces* respectively.

Consider a boundary *edge* orthogonal to n_1 and n_2. The characteristic waves considered on this edge will be traveling along these directions, and consequently $\mathcal{F}_{inv,1}$ and $\mathcal{F}_{inv,2}$ are both decomposed, i.e.

$$\frac{\partial \mathbf{U}_n}{\partial t} + \mathbf{Pd} + \mathbf{Pe} + \frac{\partial \mathcal{F}_{inv,3}}{\partial n_3} = \frac{\partial \mathcal{F}_{vis,j}}{\partial n_j} , \tag{4.37}$$

where

$$\mathbf{e} = \mathbf{S}_2 \boldsymbol{\mathcal{M}} = \begin{bmatrix} \frac{1}{c^2}\left[\mathcal{M}_3 + \frac{1}{2}(\mathcal{M}_5 + \mathcal{M}_1)\right] \\ \mathcal{M}_2 \\ \frac{1}{2\rho c}(\mathcal{M}_5 - \mathcal{M}_1) \\ \mathcal{M}_4 \\ \frac{1}{2}(\mathcal{M}_5 + \mathcal{M}_1) \end{bmatrix} . \tag{4.38}$$

The vector $\boldsymbol{\mathcal{M}}$ is the counterpart of $\boldsymbol{\mathcal{L}}$ along the n_2 direction given by

$$\boldsymbol{\mathcal{M}} = \begin{bmatrix} \mu_1(\frac{\partial p}{\partial n_2} - \rho c \frac{\partial u_{n_2}}{\partial n_2}) \\ \mu_2 \frac{\partial u_{n_1}}{\partial n_2} \\ \mu_3(c^2 \frac{\partial \rho}{\partial n_2} - \frac{\partial p}{\partial n_2}) \\ \mu_4 \frac{\partial u_{n_3}}{\partial n_2} \\ \mu_5(\frac{\partial p}{\partial n_2} + \rho c \frac{\partial u_{n_2}}{\partial n_2}) \end{bmatrix} . \tag{4.39}$$

Similarly, for a *corner* boundary orthogonal to n_1, n_2, and n_3, the term $\mathcal{F}_{inv,3}$ is also decomposed so that

$$\frac{\partial \mathcal{F}_{inv,3}}{\partial n_3} = \mathbf{Pf}, \tag{4.40}$$

where

$$\mathbf{f} = \mathbf{S}_3 \boldsymbol{\mathcal{N}} = \begin{bmatrix} \frac{1}{c^2}\left[\mathcal{N}_4 + \frac{1}{2}(\mathcal{N}_5 + \mathcal{N}_1)\right] \\ \mathcal{N}_2 \\ \mathcal{N}_3 \\ \frac{1}{2\rho c}(\mathcal{N}_5 - \mathcal{N}_1) \\ \frac{1}{2}(\mathcal{N}_5 + \mathcal{N}_1) \end{bmatrix} , \tag{4.41}$$

and

$$\boldsymbol{\mathcal{N}} = \begin{bmatrix} \nu_1(\frac{\partial p}{\partial n_3} - \rho c \frac{\partial u_{n_3}}{\partial n_3}) \\ \nu_2 \frac{\partial u_{n_1}}{\partial n_3} \\ \nu_3 \frac{\partial u_{n_2}}{\partial n_3} \\ \nu_4(c^2 \frac{\partial \rho}{\partial n_3} - \frac{\partial p}{\partial n_3}) \\ \nu_5(\frac{\partial p}{\partial n_3} + \rho c \frac{\partial u_{n_3}}{\partial n_3}) \end{bmatrix} . \tag{4.42}$$

The required conditions for each of the adjacent boundary faces are applied on their relevant direction. If two or more boundary faces that form a boundary edge or a boundary corner are not orthogonal, then the LODI relations should be re-derived in a non-orthonormal system, (t_1, t_2, t_3) by mapping it into an orthonormal coordinate system so Eq. (4.29) can be used.

The signs of eigenvalues $(u_1, u_1 + c, u_1 - c)$ at a specific boundary condition and LODI relations (see e.g. Eqs. (4.43)-(4.46)). The outgoing waves are computed from inside of the domain while the incoming waves are calculated using the boundary condition information. The LODI method assumes that the flow crossing a boundary (incoming or outgoing) is inviscid, normal to it and, consequently, one-dimensional along the normal direction. The term $\mathcal{D}$ can then be computed using characteristic wave amplitudes $\mathcal{L}$. The transverse convective fluxes and viscous fluxes of the Navier-Stokes equations are computed as usual.

Many different forms of the LODI equations have been proposed. Gradient normal to the boundary of primitive variables is very useful when boundary conditions are imposed in terms of gradients. The LODI equations can be expressed as

$$\frac{\partial \rho}{\partial x} = \frac{\mathcal{L}_0}{u_1} + \frac{\rho}{2c}\left(\frac{\mathcal{L}_3}{u_1 + c} - \frac{\mathcal{L}_4}{u_1 - c}\right) , \tag{4.43}$$

$$\frac{\partial p}{\partial x} = \frac{\rho c}{2}\left(\frac{\mathcal{L}_3}{u_1 + c} - \frac{\mathcal{L}_4}{u_1 - c}\right) , \tag{4.44}$$

$$\frac{\partial u_1}{\partial x} = \frac{1}{2}\left(\frac{\mathcal{L}_3}{u_1 + c} + \frac{\mathcal{L}_4}{u_1 - c}\right) , \tag{4.45}$$

and

$$\frac{\partial T}{\partial x} = \frac{T}{c}\left[-\frac{c\mathcal{L}_0}{\rho u_1} + \frac{1}{2}(\gamma - 1)\left(\frac{\mathcal{L}_3}{u_1 + c} - \frac{\mathcal{L}_4}{u_1 - c}\right)\right] . \tag{4.46}$$

To apply any boundary condition, see sections 4.3.1-4.3.3, three steps are generally taken:

Step 1 : For each inviscid boundary condition, derive the related LODI relations, for example Eqs. (4.43)-(4.46) for gradient-based boundary conditions.

Step 2 : Use the corresponding LODI relations to compute the unknown characteristic waves amplitudes, $\mathcal{L}$.

Step 3 : Use the remaining LODI relations and definitions of $\mathcal{L}$'s to compute all primitive and/or conservative variables required at the boundary.

The additional viscous conditions at each boundary for the Navier-Stokes equations are applied only during step 3. Thus, viscous conditions are generally not strictly enforced, and are used to modify the calculated variables from $\mathcal{L}$'s. The conditions for various types of boundaries are provided in sections 4.3.1-4.3.3.

4.3.1 Inflow Boundary

Three possibilities for inflow boundary are considered as studied by Poinsot and Lele [146]. Table 4–1 summarizes the different physical conditions used in the NSCBC method for a three-dimensional *inflow* boundary. The theoretical number of conditions required for well posedness are according to Strikwerda [151].

4.3.2 Wall Boundary

Three possibilities for wall boundary are considered, namely isothermal no-slip wall, adiabatic slip wall, and adiabatic no-slip wall. Table 4–2 summarizes the different physical conditions used in the NSCBC method for a three-dimensional *wall* boundary. The theoretical number of conditions required for well-posedness are according to Oliger and Sundström [152].

Table 4–1: Physical boundary conditions for three-dimensional *inflows* for Navier-Stokes equations.

		Inviscid conditions	Viscous conditions
BCI-1	No well-posedness proof for Euler or NS	u_1 imposed u_2 imposed u_3 imposed T imposed	
BCI-2	Well-posed for Euler, no proof for NS	u_1 imposed u_2 imposed u_3 imposed ρ imposed	$\frac{\partial \tau_{1,1}}{\partial x_1} = 0$
BCI-3	Non-reflecting, No proof for Euler or NS	$\mathcal{L}_0 = 0$ $\mathcal{L}_1 = 0$ $\mathcal{L}_2 = 0$ $\mathcal{L}_3 = 0$	$\frac{\partial \tau_{1,1}}{\partial x_1} = 0$

Note: For *subsonic inflows* and assuming that the boundary normal is pointing into the computational domain along x_1-direction.

Table 4–2: Physical boundary conditions for three-dimensional *walls* for Navier-Stokes equations.

		Inviscid conditions	Viscous conditions
BCW-1	Isothermal no-slip wall	$u_1 = 0$ $u_2 = 0$ $u_3 = 0$ $T = T_{targ}$	
BCW-2	Adiabatic no-slip wall	$u_1 = 0$ imposed $u_2 = 0$ imposed $u_3 = 0$ imposed $\mathcal{L}_0 = \mathcal{L}_\triangle$	
BCW-3	Adiabatic slip wall	$u_1 = 0$ imposed $u_2 = 0$ imposed $u_3 = 0$ imposed $T = T_{targ}$ imposed	

Note: For *subsonic inflows* and assuming that the boundary normal is pointing into the computational domain along x_1-direction.

4.3.3 Outflow

The theoretical number of conditions required for well-posedness are according to Oliger and Sundström [152].

For a subsonic outflow condition, $u_1 > 0$ and $u_1 + c > 0$, and only $u_1 - c$. All characteristic wave amplitudes except from $\mathcal{L}_4$ can be computed by evaluating spatial derivatives from inside the domain. To have a non-reflective outflow, the incoming wave should vanish, i.e.

$$\mathcal{L}_4 = 0 \ . \tag{4.47}$$

Setting the incoming characteristic wave amplitude to absolute zero can lead to drifting the mean pressure in the domain as no constraints are applied. Poinsot and Lele [146] recommended

$$\mathcal{L}_4 = K(p - p_{tar}) \ , \tag{4.48}$$

where p_{tar} is the target pressure for the boundary, and K is a relaxation coefficient and suggested by Rudy and Strickwerda [153] to be set as

$$K = \sigma c \frac{1 - Ma_{max}^2}{L} \ , \tag{4.49}$$

where L is a characteristic length, Ma_{max} is the maximum Mach number on the boundary, c is the speed of sound, and σ is a free parameter generally set to 0.25 [154]. For a constant pressure condition, $\partial p/\partial x = 0$, Eq. (4.44) yields

$$\mathcal{L}_4 = \mathcal{L}_3 \ . \tag{4.50}$$

4.4 LES Parallelization

The parallelization of the code was achieved through using Message Passing Interface (MPI) and domain decomposition. The parallel linear solver package PETSc [155–157] was used to march through time. By default GMRES iterative solvers were used for both flow solution and filtering operation.

Domain decomposition was obtained by using METIS and ParMETIS packages developed by Karypis Lab [158]. These packages are based on multilevel recursive-bisection, multilevel k-way, and multi-constraint partitioning schemes and produce fill reducing orderings for sparse matrices. The mesh was decomposed such that the resulting sparse matrix for FEM had a minimal order. This made iterative linear solvers, e.g. GMRES, to converge in fewer iterations. In periodic grids, element pairs were identified and considered as one super-element. The dual-graph is constructed based on a connectivity graph with these super-elements. This ensured that periodic element pairs were assigned to the same domain, consequently reducing amount of message passing for periodic nodes.

4.5 van Cittert Deconvolution for Najafi-Yazdi *et al.* 's Filter

The well-known van Cittert approach for approximating the deconvolution of a filter kernel G was given in the Algorithm 1, p. 46, as an M-step procedure. This formulation requires prior knowledge of the filter kernel G in the discrete physical space. The newly proposed filter yields a linear system of equations given as

$$\mathbf{M}_f \overline{\phi} = \mathbf{N}_f \phi \ , \tag{4.51}$$

when discretized. The numerical implementation of the iterative van Cittert method for approximate deconvolution can be written as

$$\mathbf{M}_f \phi^{(m)} = \mathbf{M}_f \phi^{(m-1)} + \left(\mathbf{M}_f \overline{\phi} - \mathbf{N} \phi^{(m-1)} \right) , \tag{4.52}$$

where $\overline{\phi}$ is obtained from solving Eq. (4.51). Usually iterative solutions are obtianed rather than direct calculations of the inverse matrix $\mathbf{M}_f^{-1}$, to reduce computational costs. Equation (4.52) is re-expressed in a residual form as

$$\mathbf{M}_f \Delta\phi^{(m)} = \mathbf{M}_f \left(\phi^{(m)} - \phi^{(m-1)} \right) = \left(\mathbf{M} \overline{\phi} - \mathbf{N} \phi^{(m-1)} \right) , \tag{4.53}$$

where $\Delta\phi^{(m)} = (\phi^{(m)} - \phi^{(m-1)})$. As $m \to \infty$, the residual $\Delta\phi \to 0$. Noting that the solution of Eq. (4.53) requires a matrix inversion or an iterative solver, a preferable approach is to solve the lumped mass form given by

$$\mathbf{M}_{L,f} \Delta\phi^{(m)} = \mathbf{M}_{L,f} \left(\phi^{(m)} - \phi^{(m-1)} \right) = \left(\mathbf{M} \overline{\phi} - \mathbf{N} \phi^{(m-1)} \right) . \tag{4.54}$$

to reduce computational costs. $\mathbf{M}_{L,f} = [m_{i,i}^{(L)}]$ is the lumped mass matrix defined as

$$m_{i,i}^{(L)} = \sum_{j=0}^{N} m_{i,j} . \tag{4.55}$$

An improved formulation is achieved from the *accelerated van Cittert* approach [159] where a relaxation $\omega_{(m-1)}$ is used to update the deconvolved field, $\phi^{(m)} = \phi^{(m-1)} + \omega_{(m-1)} \Delta\phi^{(m)}$. As long as $\omega_{(m-1)} > 0$, the accelerated van Cittert operator is symmetric and positive definite [160].

CHAPTER 5
Numerical Results

Numerical results are presented in two sections: (i) validation cases, and (ii) large-eddy simulations. The code order of convergence for different solvers was investigated using two cases. The first validation case is the case of sound propagation from a monopole in a mean flow, modeled by solving Euler's equations. The second case is the supersonic advection of a strong vortex, again from Euler's equations. A lid-driven cavity flow was then modeled to demonstrate the ability of the extended filter to stabilize the classical FEM scheme for the unsteady compressible Navier-Stokes equations. The fourth test case is the two-dimensional doubly periodic shear flow for a viscous compressible flow.

Three large-eddy simulations were performed. The case of decaying homogeneous isotropic turbulence was modeled on structured, perturbed structured, and fully unstructured grids. The Taylor-Green Vortex (TGV) was simulated on structured, perturbed structured and unstructured grids to investigate the effects of filter strength, and ADM order on LES results.

5.1 Validation Studies

To validate the developed weak-Galerkin FEM code for compressible viscous fluid flows, several test cases were investigated to verify the code's stability, its order of convergence, and its accuracy for solving: (i) the Euler's equations (advection terms), (*ii*) the Navier-Stokes equations (viscous terms), and (*iii*) non-reflecting boundary conditions including inlet, outlet, and slip and no-slip wall.

5.1.1 Sound Propagation in a Mean Flow

To validate the implementation of Euler equations, and investigate the order of accuracy of the FEM code with various time integration schemes, the case of sound propagation from a monopole in a mean flow was modeled. The initial condition was defined as

$$\rho = \rho_\infty \left(1 + \epsilon e^{-\alpha r^2}\right) , \tag{5.1}$$

$$p = p_\infty \left(1 + \epsilon e^{-r^2/\alpha^2}\right) , \tag{5.2}$$

and

$$(u, v) = (u_\infty, 0) , \tag{5.3}$$

where $r = \sqrt{(x - x_c)^2 + (y - y_c)^2}$ is the distance from the initial location of the monopole center, $\epsilon = 0.01$ is the disturbance strength and $\alpha = 0.03$ represents the half-width of the Gaussian distribution. The free stream properties were $\rho_\infty = 1$, $p_\infty = 1$, $u_\infty = 0.5$.

Computations were performed with $CFL = 0.8$ on a computational domain defined as $(x, y) \in [-1, 1] \times [-1, 1]$. Several structured grids, i.e. 32×32, 64×64, 128×128, 256×256 and 512×512, and triangular unstructured grids, very coarse with $1,980$ triangles, coarse with 8018 triangles, medium with $32,294$ triangles, fine with $129,848$ triangles, and very fine with $520,248$ triangles were used to study orders of convergence. Density profiles at $t = 0.07$ were compared with a reference solution.

The reference solution was obtained on a high-resolution structured grid, i.e. 1024×1024, with $CFL = 0.8$ using a 5-th order WENO scheme [161] and a 5-stage 4th-order Strong Stability Preserving Runge-Kutta (SSPRK) temporal integration [162] with the SharpClaw library [163]. Figure (5–1) illustrates the obtained density field at $t = 0.07$ and compares the reference solution with the ones obtained on the structured 32×32 and 64×64 grids using the classical continuous FEM. Results for higher resolutions or other more accurate schemes are not shown to avoid confusion.

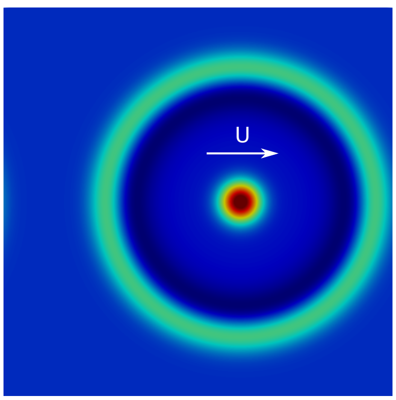

(a)

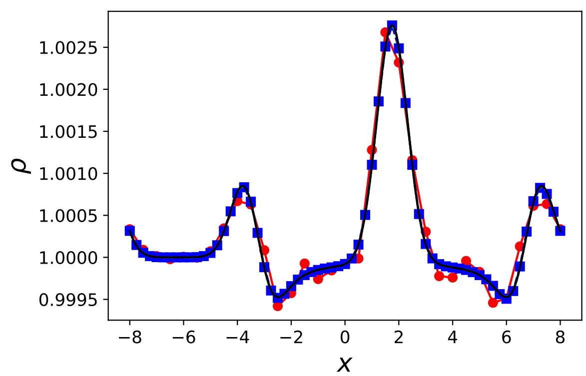

(b)

Figure 5–1: Density field at $t = 0.07$ for sound propagation from a monopole in a uniform mean flow: (a) Reference solution on a 2D 1024×1024 grid using a 5-th order WENO scheme and a SSPRK(5, 4); (b) Profiles along the horizontal midsection for the reference solution (solid), FEM on the 32×32 (circle), and the 64×64 structured grids (square); results for higher resolutions are not shown.

The error was estimated from the difference between the discrete solution, f_h, and the reference solution, f_r, as obtained from

$$E = ||f_r - f_h||_k = C\Delta x^p + \text{higher order terms} \ , \tag{5.4}$$

where $|\cdot|_k$ denotes an L_k-norm operator, and p is the order of convergence with respect to the norm. Results for the L_1-, L_2-, and L_∞-norms of the density error are shown in Tables 5–1 to 5–4 for the continuous FEM, the SUPG FEM, the continuous FEM with Najafi-Yazdi *et al.* 's extended filter, and the continuous FEM with Najafi-Yazdi *et al.* 's extended filter and a 5-th order ADM on structured and unstructured grids respectively. The same results are shown graphically in Fig. 5–2.

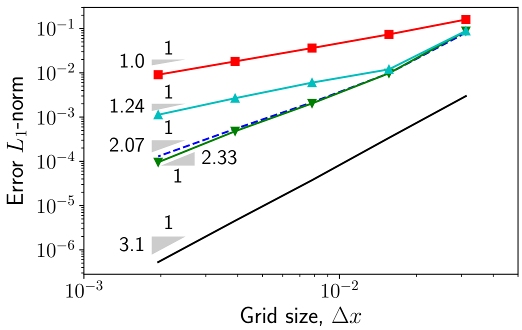

(a)

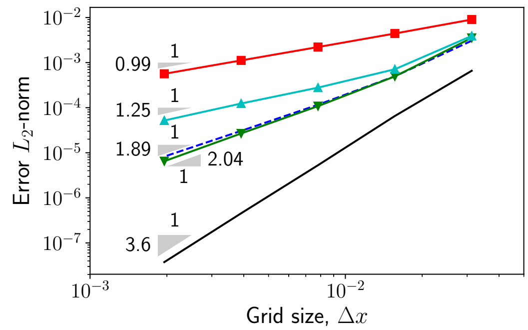

(b)

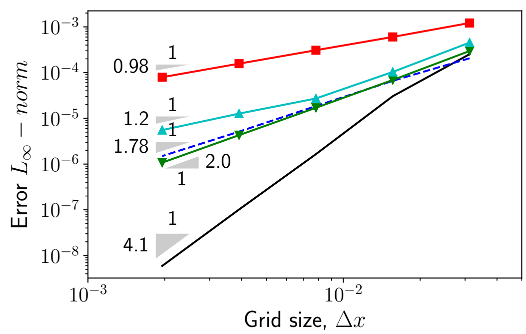

(c)

Figure 5–2: Grid convergence study for the classical continuous FEM (solid), the continuous SUPG FEM (dashed), the continuous FEM with Najafi-Yazdi *et al.* 's extended filter (square), and the continuous FEM with Najafi-Yazdi *et al.* 's extended filter and a a 5-th order ADM (ADM5) on structured (downward triangle) and triangular unstructured grids (upward triangle); (a) L_1-norm, (b) L_2-norm, and (c) L_∞-norm.

Table 5–1: L_1-, L_2-, and L_∞-norms of error for the density field at $t = 0.07$ for the simulation of Euler equations using classical continuous FEM with an initial Gaussian distribution in density and pressure on structured grids.

Grid	# Elements	L_1	L_2	L_∞
	32×32	2.98×10^{-3}	6.59×10^{-4}	2.53×10^{-4}
	64×64	3.39×10^{-4}	6.54×10^{-5}	3.05×10^{-5}
Structured	128×128	3.75×10^{-5}	5.30×10^{-6}	1.65×10^{-6}
	256×256	4.54×10^{-6}	4.54×10^{-7}	1.05×10^{-7}
	512×512	5.28×10^{-7}	3.75×10^{-8}	5.93×10^{-9}

Table 5–2: L_1-, L_2-, and L_∞-norms of error for the density field at $t = 0.07$ for the simulation of Euler equations using SUPG FEM on structured grids.

Grid	# Elements	L_1	L_2	L_∞
	32×32	8.0×10^{-2}	3.1×10^{-3}	2.06×10^{-4}
	64×64	9.76×10^{-3}	4.98×10^{-4}	6.63×10^{-5}
Structured	128×128	2.15×10^{-3}	1.16×10^{-4}	1.85×10^{-5}
	256×256	5.41×10^{-4}	3.06×10^{-5}	5.12×10^{-6}
	512×512	1.29×10^{-4}	8.24×10^{-6}	1.49×10^{-6}

Table 5–3: L_1-, L_2-, and L_∞-norms of error for the density field at $t = 0.07$ for the simulation of Euler equations using continuous FEM and Najafi-Yazdi *et al.* 's extended filter ($\alpha_2/\beta_2 = 0.95$) on structured grids.

Grid	# Elements	L_1	L_2	L_∞
	32×32	1.60×10^{-1}	9.03×10^{-3}	1.22×10^{-3}
	64×64	7.39×10^{-2}	4.42×10^{-3}	6.02×10^{-4}
Structured	128×128	3.63×10^{-2}	2.21×10^{-3}	3.09×10^{-4}
	256×256	1.81×10^{-2}	1.11×10^{-3}	3.09×10^{-4}
	512×512	9.07×10^{-3}	5.64×10^{-4}	7.94×10^{-5}

Table 5–4: L_1-, L_2-, and L_∞-norms of error for the density field at $t = 0.07$ for the simulation of Euler equations using continuous FEM, Najafi-Yazdi *et al.* 's extended filter ($\alpha_2/\beta_2 = 0.95$) and a 5-th order ADM with an initial Gaussian distribution in density and pressure on structured and unstructured.

Grid	# Elements	L_1	L_2	L_∞
	32×32	8.77×10^{-2}	3.53×10^{-3}	2.97×10^{-4}
	64×64	9.77×10^{-3}	4.94×10^{-4}	6.89×10^{-5}
Structured	128×128	2.04×10^{-3}	1.08×10^{-4}	1.70×10^{-5}
	256×256	4.79×10^{-4}	2.68×10^{-5}	4.28×10^{-6}
	512×512	9.54×10^{-5}	6.50×10^{-6}	1.08×10^{-6}
	1980	8.86×10^{-2}	3.91×10^{-3}	4.53×10^{-4}
	8018	1.20×10^{-2}	7.13×10^{-4}	1.03×10^{-4}
Unstructured	32294	6.01×10^{-3}	2.79×10^{-4}	2.72×10^{-5}
	129848	2.67×10^{-3}	1.24×10^{-4}	1.27×10^{-5}
	520248	1.13×10^{-3}	5.20×10^{-5}	5.54×10^{-6}

Approximately, 4-th orders of convergence (superconvergence) for the L_2-norm and the L_∞-norm was observed for the continuous FEM on uniform structured grids using the standard 4-th order Runge-Kutta (RK4) time integration. This superconvergence has been reported and studied exhaustively in the literature, e.g. [164, 165] for linear and [166, 167] for nonlinear hyperbolic equations.

An order of convergence of approximately 2 was obtained for the SUPG FEM scheme which is better than the expected $p + 1/2 = 1.5$ for convection-dominated flows [168]. This quasi-superconvergence can be related to potential error cancellation in uniform structured grids.

FEM with filtering and ADM shows orders of convergence between $p = 1$ and $p + 1$ for structured grids and $p + 1/2$ for unstructured grids. The orders of convergence for FEM with filtering and various ADM orders on very fine structured and unstructured grids, i.e. 512×512 and 520248 triangles, are shown in Fig. 5–3. The 0-th order ADM is equivalent to filtering without any deconvolution. The order of convergence approaches 2 for the structured grid with ADM orders of 6 and above. For the unstructured triangular grid, an exponential asymptotic trend was observed. A regression of the exponential asymptote yielded $-0.569 \exp(-0.1124 * N) + 1.493$, where N is the order. The coefficients were estimated within a 95% confidence interval with an R-square value of $R^2 = 0.9983$. The asymptotic regression suggests that the order of convergence approaches 1.493 when $N \to \infty$. This approaches the $p + 1/2$ order of convergence for finite elements combined with RK schemes, demonstrated by Burman *et al.* [169]. They showed that under usual CFL conditions, i.e. $\Delta t \leq C\Delta x/a$, the L_2-norm of error for the standard explicit RK2 scheme and

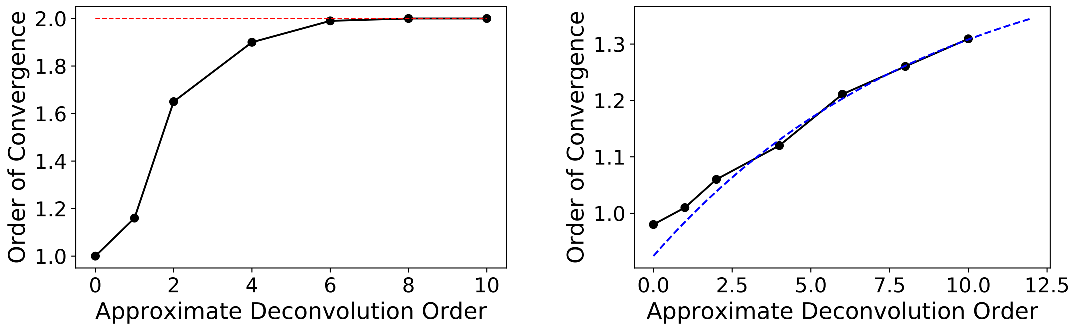

(a) (b)

Figure 5–3: Orders of convergence obtained on very fine (a) structured, 512×512, and (b) unstructured grids, 520248 elements, using FEM with filtering and various orders of ADM.

piecewise affine finite elements is $\mathcal{O}(\Delta t^2 + \Delta x^{3/2})$, where Δt is the time step, Δx is the minimal mesh size, a is a reference velocity and C is a dimensionless constant. The L_2-norm of error for the standard RK3 scheme for finite elements with polynomials of total degree $\leq p$ is $\mathcal{O}(\Delta t^3 + \Delta x^{p+1/2})$. As $\tau \leq \Delta x$, it seems that a higher order time integration scheme would increase the order of convergence only in time, and not in space. One can conclude that, under a fixed CFL number and for *linear* elements, the L_2-norm of error is $\mathcal{O}(\Delta x^{3/2})$.

5.1.2 Isentropic Vortex Advection

Advection of a strong isotropic vortex moving along a path at 45° from the x-axis was studied to demonstrate the effects of multidimensional propagation. A two-dimensional computational domain given by $(x, y) \in [-5, 5] \times [-5, 5]$ was selected with periodic boundaries in both directions. The flow variables were initialized as

$$
\begin{aligned}
\rho &= \left[\rho_\infty\left(1 - \frac{(\gamma-1)\epsilon^2}{8\gamma\pi^2}e^{1-r^2}\right)\right]^{1/(\gamma-1)} , && (5.5)\\
T &= T_\infty\left(1 - \frac{(\gamma-1)\epsilon^2}{8\gamma\pi^2}e^{1-r^2}\right) , && (5.6)\\
p &= p_\infty , && (5.7)\\
u &= u_\infty\left(1 - \frac{\epsilon}{2\pi}e^{\frac{1}{2}(1-r^2)}(y-y_c)\right) , && (5.8)
\end{aligned}
$$

and

$$
v = u_\infty\left(1 + \frac{\epsilon}{2\pi}e^{\frac{1}{2}(1-r^2)}(x-y_c)\right) , \tag{5.9}
$$

where $\epsilon = 5$ is the vortex strength and $r = \sqrt{(x-x_c)^2 + (y-y_c)^2}$ is the distance from the vortex initial center position $(x_c, y_c) = (0, 0)$. This is equivalent to the imposition of a mean flow $(\rho_\infty, p_\infty, T_\infty, u_\infty, v_\infty)$ perturbed such that the equation of state $p = \rho RT$ still holds, and the entropy $S = p/\rho^\gamma$ is not perturbed.

The exact solution of Euler's equations for these initial and boundary conditions should yield the passive convection of the vortex with the imposed mean velocity. A structured grid of 64×64 elements was used and the simulations were performed for one flow-through time, i.e. $t* = u_\infty t/L = 10$ where $L = 10$ is the domain edge length. The standard 4-th order Runge-Kutta time integration was used for: FEM; SUPG+FEM; FEM+filtering; and FEM+filtering+ADM5.

Figure 5–4 compares contour plots of x-velocity, y-velocity components and density. The SUPG method resulted in a slight warpage of the solution which can be related to the stream-wise dissipation of the SUPG scheme. The FEM with filtering remained symmetric but significantly dissipated the solution. The5-th order ADM yielded the least dissipation and kept the solution symmetric.

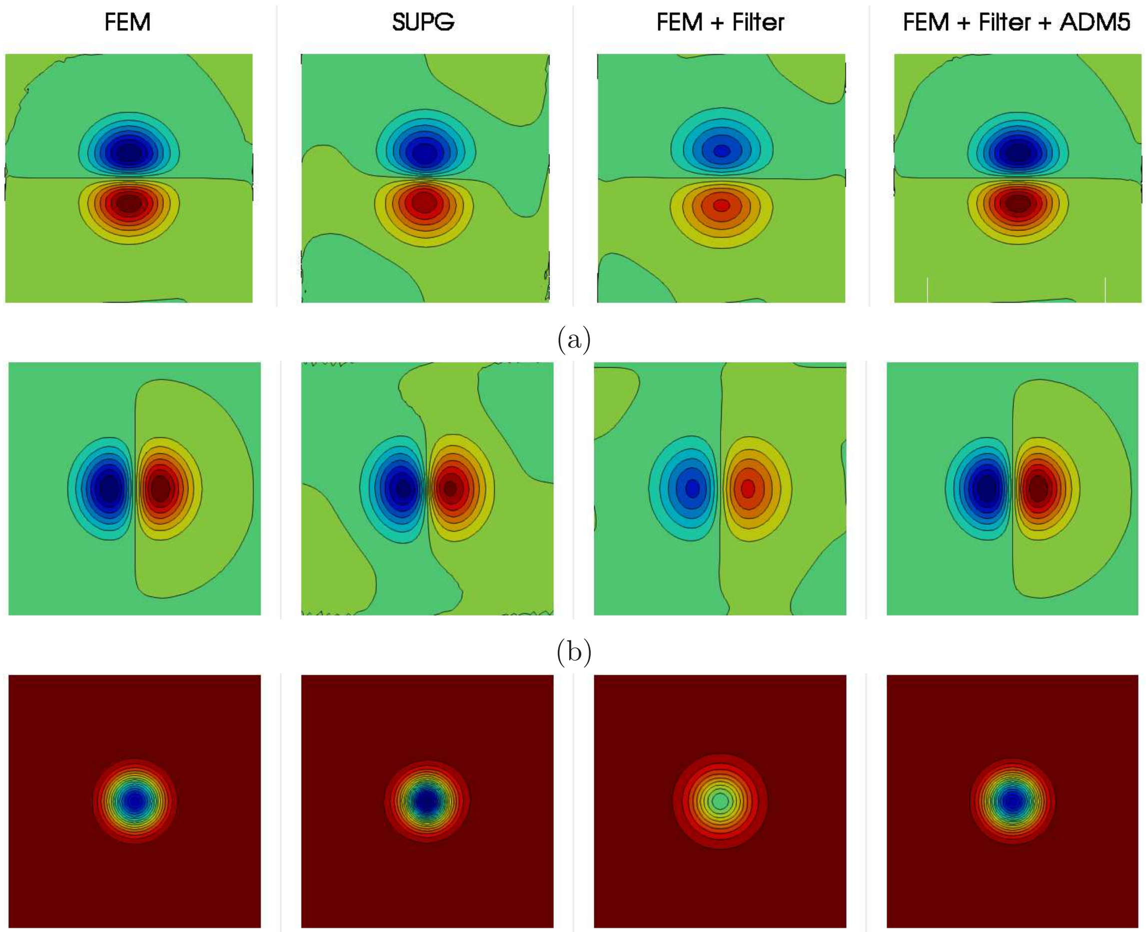

(a)

(b)

(c)

Figure 5–4: Contour plots of (a) the normalized x-velocity, u/u_{∞}, (b) the normalized y-velocity, v/u_{∞}, and (c) the normalized density, ρ/ρ_{∞}. From left to right: FEM, SUPG+FEM, FEM+filtering, FEM+filtering+ADM5.

5.1.3 Two-Dimensional Lid-Driven Cavity

To demonstrate the stability of the extended filter numerical scheme, with no turbulence, the unsteady compressible Navier-Stokes equations were solved for a lid-driven cavity flow at Reynolds number $Re = \rho u L/\mu = 1000$, where $u = 1$ is the lid horizontal velocity and $L = 1$ is the cavity streamwise length. The flow was simulated at Mach number $Ma = 0.1$, i.e. in the incompressible regime. The classical Weak-Galerkin FEM scheme and the standard RK4 time integration were used for this problem. Due to the persistence of node-to-node oscillations in the classical weak-Galerkin FEM formulation, an ADM of order 8 with Najafi-Yazdi *et al.* 's [27] filter for triangular elements was used to stabilize the simulation. The filter had a non-dimensional cut-off wavenumber of about $\kappa_f \approx 3\pi/4$.

Two structured grids, 64×64 and 128×128, and one triangular unstructured grid with 128 segments on each side (32294 elements in total) were used for this simulation. The velocity magnitude distribution and velocity streamlines are shown in Fig. 5–5. The velocity profiles normal to the horizontal and vertical midsections are compared with the results of Ghia *et al.* [170] in Fig. 5–6. Reasonable agreement between the stabilized scheme and the reference results was observed. The velocity profiles follow the same trend as the reference solution and have the location of peak values correctly captured. The peak velocity values were underestimated by %12 and %7 for the structured and unstructured grids respectively which can be related to the additional dissipation from the filtering operation.

To demonstrate effectiveness of the extended filter to remove node-to-node oscillations, referred to as q-waves, the simulation was repeated on a 64×64 structured grid without any filtering. Figure 5–7 illustrates the pressure field inside the cavity at three consecutive instants, $t^* = tU/L = 0.25, 0.75, 1.125$, for the filtered and the unfiltered solutions. The singularities at the top corners, i.e. between the top moving

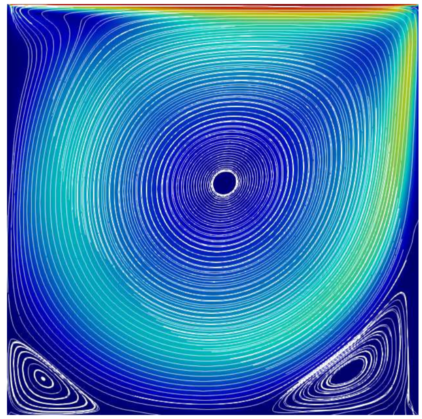

(a)

Figure 5–5: The velocity magnitude and streamlines for the solution of a lid-driven cavity at $Re = 1000$ and $Ma = 0.1$.

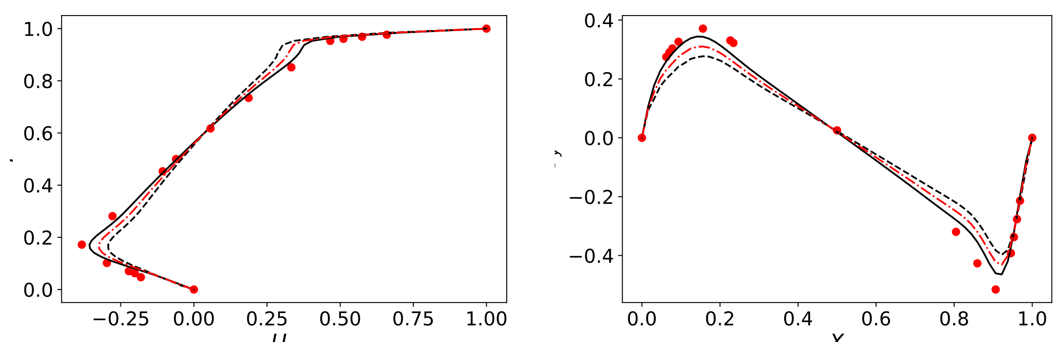

(a) (b)

Figure 5–6: Velocity profiles, (red circles) Ghia *et al.* [170], and FEM with ADM and explicit filtering: (solid) 128×128, (dashed) 64×64 structured meshes and (dash-dotted) unstructured mesh: (a) U_x along the vertical midsection, and (b) U_y along the horizontal midsection of a lid-driven cavity flow at $Re = 1000$ and $Ma = 0.1$.

wall and the side walls, create physical pressure waves, called p-waves by Vichnevetsky [171], as well as some spurious noise, called q-waves by Poinsot and Lele [146]. The q-waves move ahead of the physical waves and faster than the speed of sound. They usually have very short wavelengths on the order of twice the mesh size [172], reaching a maximum for node-to-node (saw-tooth) oscillations. The q-waves reach boundaries long before the arrival of the physical pressure waves, and are reflected in the form of unrealistic p-waves [173]. This phenomenon was clearly observed in the unfiltered solution, where the reflected q-waves from top right and left corners were reflected as p-waves. This problem is exacerbated over time as each p-wave reaching a boundary generates in turn but a p-wave and a q-wave. When left untreated, the cascade of q-wave reflections destabilizes numerical simulations, as was the case for the unfiltered simulation. This problem was not observed when explicit filtering was used. The oscillatory pressure variations near the walls had a wavelength four times larger than the grid size, corresponding to a wavenumber smaller than the filter cut-off wavenumber, i.e. $\kappa_p = \pi/2 < \kappa_f = 3\pi/4$. These oscillations are stationary and do not correspond to q-waves. They are caused by one-sided derivative approximations in the classical FEM scheme.

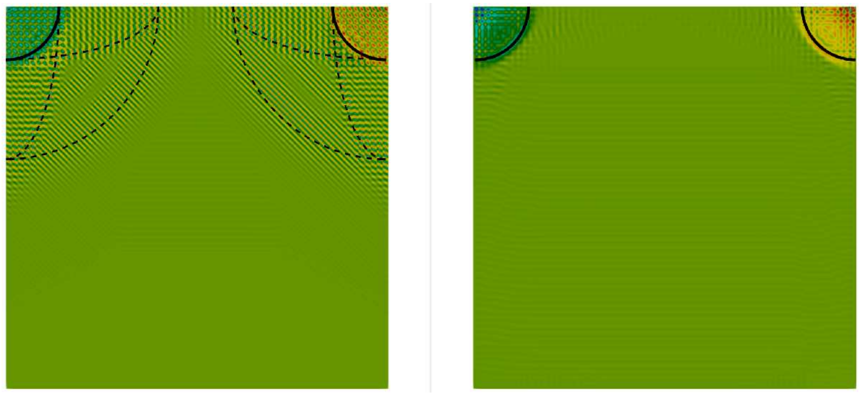

(a)

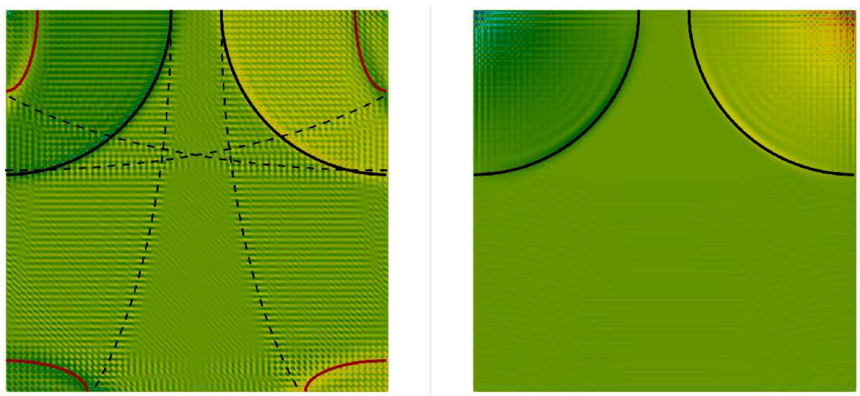

(b)

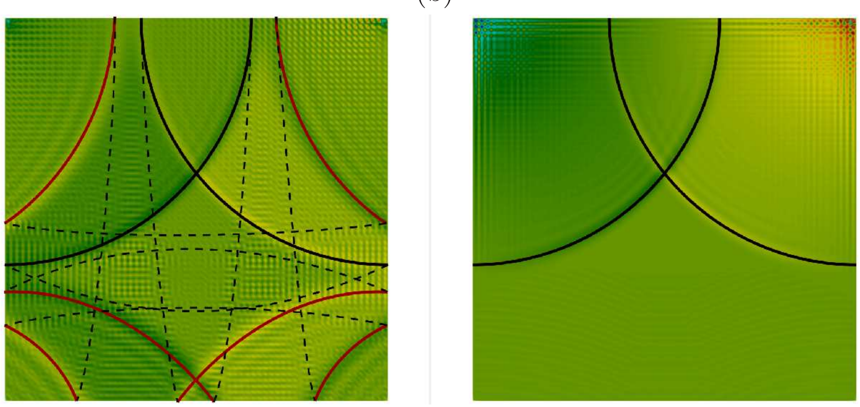

(c)

Figure 5–7: Pressure contours for (left) unfiltered and (right) filtered FEM at (a) $t^* = 0.25$, (b) $t^* = 0.45$, and (c) $t^* = 1.125$. Physical p-waves are shown by solid black lines while q-waves and their p-wave reflections are shown by dashed black lines and solid red lines respectively.

5.1.4 Two-Dimensional Double Periodic Shear Flow

The evolution of Kelvin-Helmholtz instabilities in shear flows is one fundamental sound generation mechanism involved in jet noise. A two-dimensional doubly periodic shear flow was simulated at $Re = 1000$ and $Ma = 0.2$ with the initial conditions defined as

$$u_x = \begin{cases} \tanh\left(30(y-0.25)\right) & y \geq 0 \\ \tanh\left(30(y+0.25)\right) & y < 0 \end{cases} , \qquad u_y = 0.1\sin(4\pi(x+0.5)) \ , \tag{5.10}$$

$\rho = 1$, and $p = 1$, see Fig. 5–8. A 64×64 quadrilateral grid was used as the computational domain, with periodic boundary conditions on all sides. The transition layer thickness was approximatly $h \approx 8\Delta y$. Figure 5–9 shows the vorticity contours obtained from FEM without filtering, SUPG, and FEM+filtering at $t^* = tU/L = 25$. The SUPG and the FEM+filtering cases remain fully stable. Vorticity and density contours at $t^* = 75$ are shown in Fig. 5–10.

The Kelvin-Helmholtz Instability (KHI) results in vortex formation, roll-up and growth. It also stretches the transition layer, making it thinner in the region between every two vortices. This phenomenon locally increases the velocity gradient, potentially causing insufficient spatial discretization resolution. The under-resolved sharp gradient of the velocity field across the shear layer generates node-to-node spurious oscillations. If left untreated, they may result in numerical instabilities, as for the case of the continuous FEM without SUPG nor filtering.

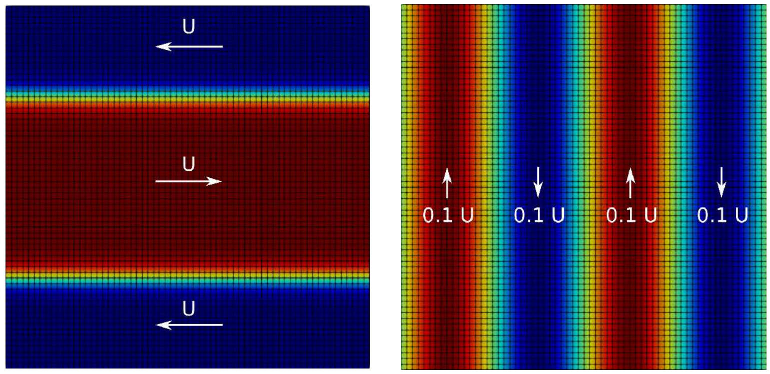

(a) (b)

Figure 5–8: Initial condition for (a) the horizontal and (b) the vertical velocity components in a doubly periodic shear flow.

.

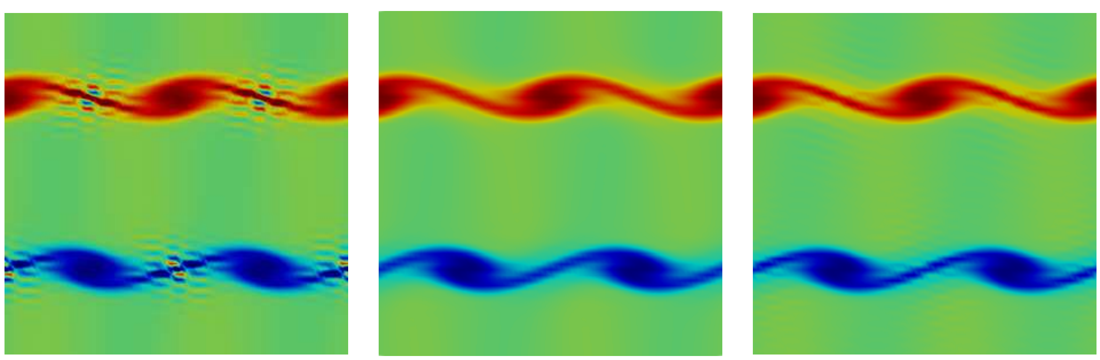

(a) (b) (c)

Figure 5–9: Vorticity contours for a 2D doubly periodic shear flow at $t^* = tU/L = 25$ using (a) FEM without filtering, (b) SUPG, and (c) FEM with filtering.

The SUPG stabilized the FEM but was unable to remove node-to-node spurious oscillations in the density field while the FEM with filtering and ADM significantly removed them, see Fig. 5–10.

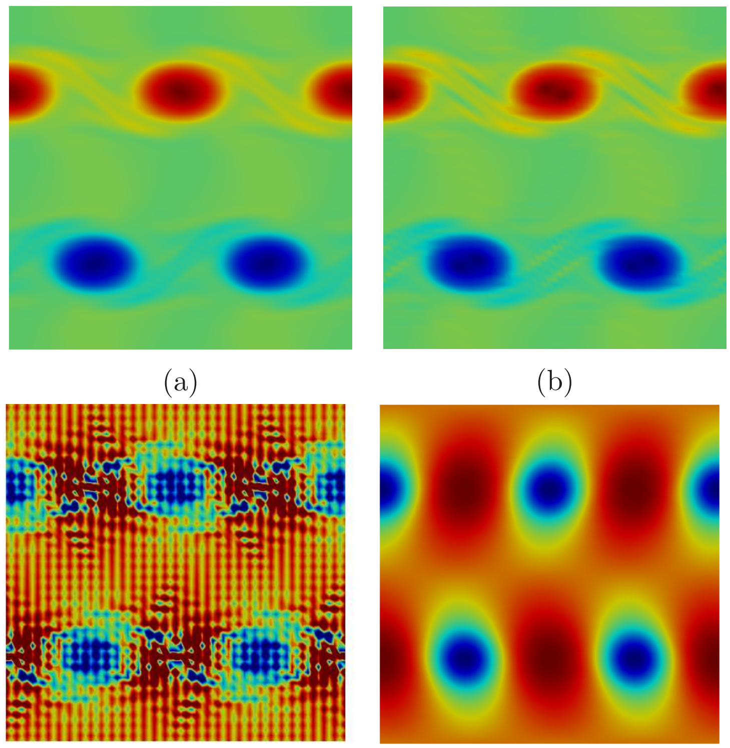
(a) (b) (c) (d)

Figure 5–10: Solution field contours for a 2D doubly periodic shear flow at $t^* = tU/L = 75$: (a) vorticity using SUPG; (b) vorticity using FEM with filtering; (c) density using SUPG; and (d) density using FEM with filtering.

5.2 Large-Eddy Simulations

The main purpose of extending the approach of Najafi-Yazdi *et al.* [27] was to use it within an ADM framework to act as the SGS modelling methodology with a direct control over the SGS dissipation in the spectral domain. Two numerical benchmarks which demonstrate the performance of the proposed ADM-based LES were investigated: (*i*) the Comte-Bellot-Corrsin Decay of Homogeneous Isotropic Turbulence [174] (CBC-DHIT); and (*ii*) the Taylor-Green Vortex (TGV).

5.2.1 Comte-Bellot-Corrsin Decay of Homogeneous Isotropic Turbulence

Comte-Bellot and Corrsin (CBC) studied the decay of isotropic grid generated turbulence [174]. In this experiment, a uniform mean flow of $U_0 = 10\ cm/s$ was driven over a wire grid with a mesh spacing of $M = 2\ in$ ($5.08\ cm$), these values forming a Reynolds number of $Re_M = 34,000$. Flow motion at the mean velocity is replaced by a decay of stationary homogeneous isotropic turbulence (DHIT) downstream of the grid. The turbulent kinetic energy spectra were extracted at three different times, $t^* = tU_0/M = 42$, 98, and 171. The Taylor micro-scale Reynolds number was estimated to decay from $Re_\lambda = 71.6$ to $Re_\lambda = 60.6$ over this period. Results from this experiment are widely used as a benchmark test case for subgrid scale models for LES.

The initial pressure, density and temperature fields were assumed to be uniform such that the reference Mach number was $Ma_{ref} = u_{ref}/c_{ref} = 0.1$ where $u_{ref} = \sqrt{3\overline{\overline{u}_1^2}/2}$. The root-mean square of the velocity fluctuations, $\bar{u}$, was obtained from the reported measured data at $t^* = 42$. The initial condition for the velocity field was obtained from the method introduced by Kwak *et al.* [175] on a high-resolution uniform structured grid, i.e. 512^3. The generated velocity field was divergence-free and isotropic. This initial condition was interpolated from the high resolution grid 512^3 onto other meshes.

In the presented LES results, the standard non-dimensionalization proposed by Misra and Lund [176] and Ghosal *et al.* [177] were used. The characteristic velocity, length and time were chosen as $U_{ref} = \sqrt{3U_0^2/2}$, $L_{ref} = L/2\pi = 11M/2\pi$ and

$t_{ref} = L_{ref}/U_{ref}$ respectively. The simulations were performed with a classical weak-Galerkin Finite Element Method (FEM) for compressible flows and the standard 4-th order Runge-Kutta time integration. Stabilization as well as LES anti-aliasing were achieved by using the explicit filter operator of Najafi-Yazdi *et al.* [27] within the approximate deconvolution operator of van Cittert [87]. A deconvolution order of $N = 8$ was used as suggested in the literature for the simulation of isotropic turbulence and shock-boundary-layer interaction [115], turbulent channel flow [178], and turbulent shear layer using a Lattice-Boltzmann Method (LBM) [179].

The extended formulation of Najafi-Yazdi *et al.* 's filter [27] for hexahedral elements was used with $\alpha_1/\beta_1 = 1$, $\alpha_2/\beta_2 = 1.2$, $\alpha_3/\beta_3 = 1.1$, and $\alpha_7/\beta_7 = 1.05$. The initial condition was $\rho = 1$ and $p = 1$ for the non-dimensional density and pressure fields, respectively. The velocity components were estimated assuming a divergence-free isotropic velocity field. A Cartesian hexahedral mesh of 64^3 was initially used. It was later perturbed by randomly displacing the nodes over a distance equal to 20% of the element size. A third fully unstructured mesh with 64 segments on each edge was also used, as shown in Fig. 5–11. A Non-uniform Fast Fourier Transform (NFFT) library developed at the Mathematical Institute of the University of Lbeck, at the Mathematical Institute of the University Osnabrck and at the Faculty of Mathematics of the Chemnitz University of Technology by Keiner, Kunis and Potts [180] was adopted to calculate the turbulent kinetic energy spectrum, $E(\kappa)$, on the perturbed and the unstructured meshes.

Figure 5–12 illustrates the TKE, $E(\kappa)$, and eddy turn-over frequency, $f_e = (\kappa^3 E)^{1/2}$, spectra at the non-dimensional time $t^* = 48.3$ for the 20%-perturbed grid and the unstructured grid against that of the unperturbed 64^3 structured grid. The TKE spectrum was well-preserved for wavenumbers below $\kappa = 8/\Delta x$. The $-5/3$ slope of the spectrum in the inertial subrange was preserved and full attenuation at grid cut-off $\kappa \to 32\Delta x$ was achieved for all three cases. Slightly larger dissipation was observed for the unstructured mesh in comparison to the 20%-perturbed mesh which can be related to the non-uniformity of the grid size, and consequently the cut-off wavenumber. Using tetrahedrons instead of hexahedrons leads to smaller local grid sizes than the average $\overline{\Delta x} = 1/64$. Turbulence dynamics at slightly smaller scales were captured on the unstructured mesh as the explicit filter gets automatically adjusted to the local grid size. The filter cut-off filter was set as $\kappa_f \approx \kappa/\Delta x = 3\pi/4$ relative to the local grid size. Consequently, the filter retains the resolved dynamics at higher wavenumbers when the grid resolution is higher. This can be seen in the TKE spectrum of the solution on the unstructured mesh with some energy content beyond what was obtained for the 20%-perturbed or the unperturbed meshes.

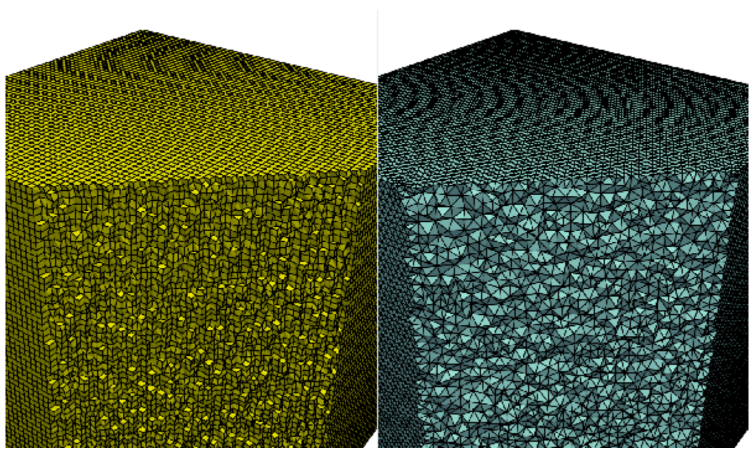

Figure 5–11: Comparing a perturbed hexahedral mesh using 20% of the uniform element size for non-periodic nodes (left), and a fully unstructured mesh made of tetrahedrons with 64 equal segments on each edge (right).

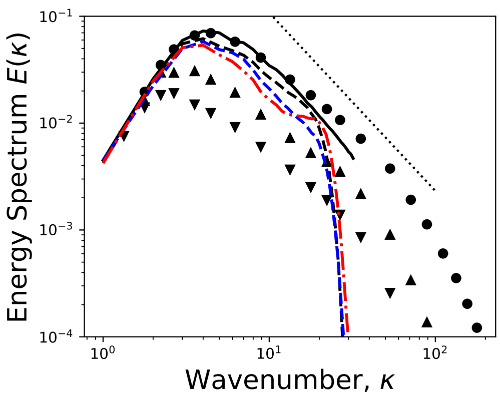

(a)

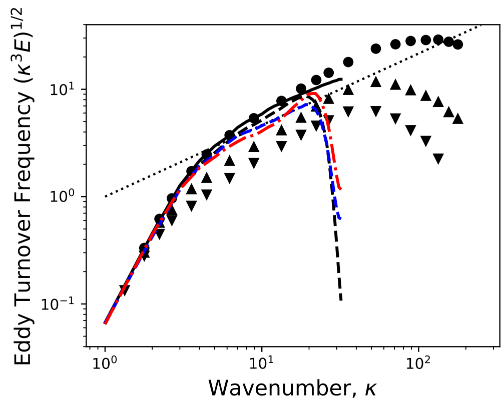

(b)

Figure 5–12: (a) Turbulent kinetic energy spectrum, $E(\kappa)$, and (b) eddy turn-over frequency, f_e, for the decay of homogeneous isotropic turbulence at $Re_M = 34000$ at (solid) initial condition, $\tau = 0$, and at $\tau \approx 48.3$ on (dashed) an unperturbed 64^3 Cartesian grid, (dash-dotted) a 20% perturbed mesh, and (dash-double-dotted) an unstructured mesh; compared with the experimental data of Comte-Bellot & Corrsin [174] at (circles) $t^* = tU_0/M = 42$, (upward triangles) $t^* = 98$, and (downward triangles) $t^* = 171$.

5.2.2 Taylor-Green's Vortex

The second fundamental test case was the three-dimensional Taylor-Green Vortex (TGV) [181] as it demonstrates a laminar-turbulent transition. This is one of the most demanding tests for SGS models [182] as they should not affect the instability modes of the laminar flow. This property is not satisfied by many eddy-viscosity models, e.g. Smagorinsky [39] or the structure-function model [124, 183]. The flow initialization was adopted from Bull and Jameson [184] where

$$
\begin{aligned}
u_1 &= U_0 \sin(\frac{x}{L}) \cos(\frac{y}{L}) \cos(\frac{z}{L}) \ , && (5.11)\\
u_2 &= -U_0 \cos(\frac{x}{L}) \sin(\frac{y}{L}) \cos(\frac{z}{L}) \ , && (5.12)\\
u_3 &= 0 \ , && (5.13)\\
\rho &= \rho_0 \ , && (5.14)
\end{aligned}
$$

and

$$
p = p_0 + \rho_0 \frac{U_0^2}{16} \left(2 + \cos(\frac{2z}{L})\right) \left(\cos(\frac{2x}{L}) + \cos(\frac{2y}{L})\right) \ . \tag{5.15}
$$

$\rho_0 = 1$, and $p_0 = 1$, and U_0 is determined such that the flow Mach number is $Ma = 0.1$. The temperature field is initialized by $T_0 = 1$ everywhere. The domain is a triple periodic cube, i.e. $(x, y, z) \in [-\pi L, \pi L] \times [-\pi L, \pi L] \times [-\pi L, \pi L]$.

Initially the TGV evolution is laminar and strongly anisotropic, $t^* < 4$. Vortex stretching transfers energy to larger wavenumbers. Eventually, for $t^* > 9$, the flow becomes turbulent exhibiting a nearly isotropic structure for small scales with a fully developed $\kappa^{-5/3}$ inertial range for the kinetic-energy spectrum. Early Direct Numerical Simulations (DNS) results were provided by Brachet *et al.* [185] which were obtained on a 256^3 [185]. These results were obtained using a pseudo-spectral method for spatial discretization, a second-order leapfrog for nonlinear terms and a second-order Crank-Nicolson implicit time-stepping for the viscous terms. Dealiasing was achieved by spectral truncation. Brachet *et al.* revisited this problem in more detail using a 864^3 grid [186]. In the present work, the reference DNS solution was adopted from Jammy *et al.* [187] since the full dataset was readily available to the research community from the University of Southampton Institutional Repository[1] . This dataset was obtained on a 512^3 structured grid using a fourth-order central finite-difference scheme and a low storage Runge-Kutta (RK) scheme with three stages of temporal discretisation [188]. Their results were validated against the DNS results by Wang *et al.* [7] provided in the 1st International Workshop on High–Order CFD Methods. Wang *et al.* 's data was obtained on a 512^3 grid using a dealiased pseudo-spectral code developed at Université Catholique de Louvain [189]. The time integration was performed using a low-storage three-step Runge-Kutta scheme [188] with a time step of $\Delta t^* = 1 \times 10^{-3}$.

The most important quantity is the dissipation rate of turbulent kinetic energy which can be measured in two different ways for incompressible flows: the *energy-based* dissipation rate,

$$\epsilon_E = -dE/dt \ , \tag{5.16}$$

and the *vorticity-based* dissipation rate,

$$\epsilon_\omega = 2\mu/\rho_0 \zeta \ . \tag{5.17}$$

This terminology was first proposed by Bull and Jameson [184]. E is the volume-averaged kinetic energy, i.e.

$$E = \frac{1}{2\Omega} \int_\Omega \frac{1}{2} \rho \mathbf{u} \cdot \mathbf{u} d\Omega \ , \tag{5.18}$$

[1] Enstrophy and kinetic energy data from 3D Taylor-Green vortex simulations: `https://eprints.soton.ac.uk/401892/`
Solution field data from a three-dimensional Taylor-Green vortex simulation: `https://eprints.soton.ac.uk/402073/`

and ζ is the volume-averaged enstrophy, i.e.

$$\zeta = \frac{1}{2\Omega} \int_{\Omega} \frac{1}{2} \rho \boldsymbol{\omega} \cdot \boldsymbol{\omega} d\Omega \ , \tag{5.19}$$

where $\boldsymbol{\omega}$ is the vorticity vector. Shu *et al.* [190] showed that $\epsilon_\omega = \epsilon_E$ for incompressible flows, which is the case for the TGV case. The vorticity-based dissipation rate, ϵ_ω, is a kinematic-based metric and measures the *accuracy* of a numerical scheme in resolving vorticity-carrying small scales in the inertial range of turbulence [184], i.e the measured physical dissipation. The energy-based dissipation rate, ϵ_E, is a dynamic metric for the numerical *stability* of an LES simulation as it measures the sum of physical and numerical dissipation dynamics. The difference between these two quantities is a useful error measure for LES simulations independent of the physical problem, and could be used for complex flows [189] to study the development of turbulence dynamics.

The evolution of turbulent kinetic energy, $E(\kappa)$, enstrophy $\zeta(\kappa)$, and vorticity, $\Phi_\omega(\kappa)$, spectra can shed some light on the quality of laminar-turbulent transition. The energy spectrum, $E(\kappa)$, is defined as

$$E(\kappa) = \frac{1}{2} \iint_{S(\kappa)} E_{ii}(\vec{\kappa}) ds \ , \tag{5.20}$$

where $S(\kappa)$ is a a sphere of radius $\kappa = \|\vec{\kappa}\|$,

$$E_{ij}(\vec{\kappa}) = \frac{1}{(2\pi)^3} \iiint_{-\infty}^{\infty} e^{-i\vec{\kappa}\cdot\vec{x}} R_{ij}(\vec{x}) d\vec{x} \ , \tag{5.21}$$

is the energy spectrum tensor, and

$$R_{ij}(\vec{x}) = \langle u_i(\vec{x}_0, t) u_j(\vec{x}_0 + \vec{x}, t) \rangle = \iiint_{-\infty}^{\infty} u_i(\vec{x}_0, t) u_j(\vec{x}_0 + \vec{x}, t) d\vec{x} \ , \tag{5.22}$$

is the spatial cross correlation of velocity components u_i and u_j. Substitution of Eq. (5.22) into Eq. (5.21) and use of the correlation theorem yields

$$E_{ij}(\vec{\kappa}) = \frac{1}{(2\pi)^3} U_i(\kappa) U_j^*(\kappa) \ , \tag{5.23}$$

where $U_i = \mathcal{F}\{u_i\}$ is the Fourier transform of u_i and U_j^* is the complex conjugate of the Fourier transform of u_j. Since u_i and u_j are both real, $U_j^*(\kappa) = U_j(-\kappa)$, resulting in $E_{ij}(\vec{\kappa}) = U_i(\kappa)U_j(-\kappa)$. For a well-developed homogeneous turbulent flow $E(\kappa) \propto \kappa^{-5/3}$ in the inertial subrange [86].

The enstrophy spectrum is defined in a similar way as

$$\zeta(\kappa) = \frac{1}{2} \iint_{S(\kappa)} \zeta_{ii}(\vec{\kappa}) ds \ , \tag{5.24}$$

where

$$\zeta_{ij}(\vec{\kappa}) = \Omega_i(\kappa) \Omega_j(-\kappa) \ , \tag{5.25}$$

is the enstrophy spectrum tensor and $\Omega_i = \omega$ is the Fourier transform of the vorticity vector, ω_i. For isotropic flows, $\zeta(\kappa) = \kappa^2 E(\kappa)$ [191].

The one-dimensional spectra of the cross stream vorticity, $\Phi_{22}(\kappa_i)$, is defined as

$$\Phi_{22}(\kappa_i) = 2 \iint_{-\infty}^{\infty} \zeta_{22}(\kappa_i) d\kappa_2 d\kappa_3 \ . \tag{5.26}$$

This is the integral of one single component of ζ_{ij} over a plane perpendicular to one given wavenumber direction [191]. For simplicity, the term *vorticity spectrum* has been used for Φ_{22}. Morris and Foss [191] suggested that $\Phi_{22}(\kappa_i)$ demonstrates turbulence anisotropy more accurately than the energy and enstrophy spectra. The vorticity spectrum, $\Phi_{22}(\kappa_i)$, can be written in terms of the enstrophy spectrum function as

$$\Phi_{22}(\kappa_i) = \frac{1}{2}\kappa_i \int_{\kappa_i}^{\infty} \frac{\zeta(\kappa)}{\kappa^3} d\kappa + \frac{1}{4}\int_{\kappa_i}^{\infty} \frac{\zeta(\kappa)}{\kappa^3}\left(\kappa^2 - \kappa_i^2\right) d\kappa \ . \tag{5.27}$$

Morris and Foss estimated the vorticity spectrum, Φ_{22}, from the measured turbulence data from a turbulent shear layer and an atmospheric surface layer, two highly anisotropic turbulent flows. They showed that $\Phi_{22} \propto \kappa^{-2}$ in the inertial subrange. Using Pope's model for the energy-spectrum function [86], they demonstrated that $\Phi_{22}(\kappa)$ in the inertial subrange of a homogeneous isotropic turbulence cannot be represented with any power-law functions. Based on this contradiction, they concluded that the vorticity spectrum is a better measure of turbulence anisotropy.

In the present work, these three spectra were used for analysis along with the energy-based and vorticity-based dissipation rate estimates. The empirically modified von Kármán-Kraichnan energy spectrum [2] for the three-dimensional energy spectrum,

$$E(\kappa) = \frac{3}{2I_1}\frac{u_0^2}{\kappa_0}\frac{\left(\kappa/\kappa_0\right)^4}{\left[1+\frac{12}{5}\left(\kappa/\kappa_0\right)^2\right]^{17/6}} e^{-\beta Re^{-3/4}(\kappa/\kappa_0)} \ , \tag{5.28}$$

was used as a reference spectrum model for homogeneous isotropic turbulence. This spectrum is proportional to κ^4 at low wavenumbers, to $\kappa^{-5/3}$ within the Kolmogorov inertial subrange. The viscous roll-off at high wavenumbers is consistent with Kraichnan's theory [192]. The velocity scale u_0 is assumed to satisfy

$$\frac{3}{2}u_0^2 = \int_0^{\infty} E(\kappa) d\kappa \ . \tag{5.29}$$

This yields $I_1 = 0.1149$ for high Reynolds numbers. The normalizing wavenumber, κ_0 is chosen such that $\kappa_0 L = 1.608$ where L is the longitudinal integral scale. This is obtained by assuming $A \approx 1$ to match the turbulent kinetic energy dissipation rate $\epsilon = Au_0^3/L$ with the experimental data from a grid turbulence by Sreenivasan [193]. Matching the viscous roll-off to the experimental data by Saddoughi and Veerravalli [194] and Saddoughi [195] results in $\beta = 8.36$.

DNS and LES Simulations

To validate the capability of the numerical method in capturing the laminar-turbulent transition, DNS simulations at $Re = 200$ were performed on a 256^3 uniform structured grid and a fully unstructured mesh with 256 segments on each side, i.e. about 5 million nodes and 29.6 million tetrahedra. The FEM code with Najafi-Yazdi *et al.* 's extended filter for dealiasing was used. The approximate total velocity, $u \approx D_N \overline{u}$, was used for all the reported results (DNS and LES) obtained with this scheme. The results are compared to the dissipation rate of the DNS results by Brachet *et al.* [185] in Fig. 5–13. The error in the dissipation rate are presented in Fig. 5–14 in terms of two indicators, the ratio of energy-based dissipation rate to the vorticity-based one, $\epsilon_E/\epsilon_\omega$, and the difference between the two, $\epsilon_E - \epsilon_\omega$. The DNS results obtained from the FEM code with Approximate Deconvolution-based FEM (AD-FEM) are nearly identical to the reference DNS data with negligible error confirming the accuracy and consistency of the developed numerical scheme.

The TGV test case was also simulated at a much higher Reynolds number, $Re = 1600$. The extended filter of Najafi-Yazdi *et al.* was used within an ADM, i.e. AD-LES, for these simulations. Two uniform structured grids, $S48$ and $S128$, two

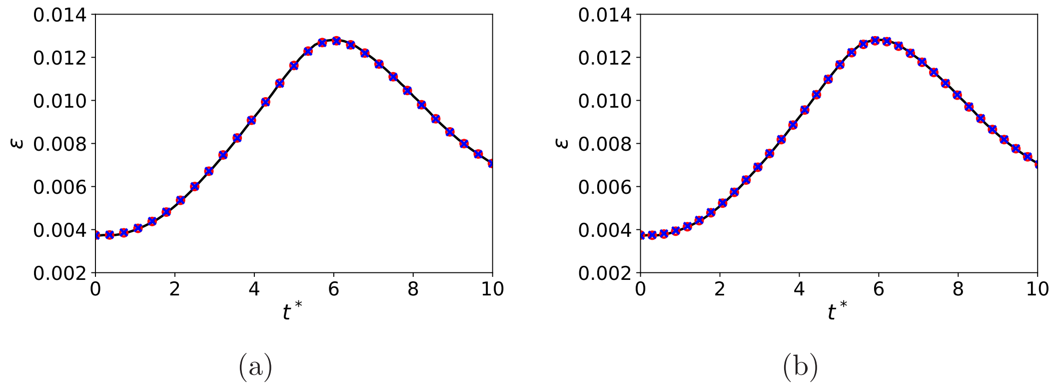

Figure 5–13: The turbulent kinetic energy dissipation rates for TGV at $Re = 200$ obtained (a) on a 256^2 structured grid, and (b) on a 256-unstructured grid: Reference DNS data by Brachet *et al.* [185] (solid line), energy-based dissipation rate, ϵ_E, (red circles), and vorticity-based dissipation rate, ϵ_ω, (blue cross).

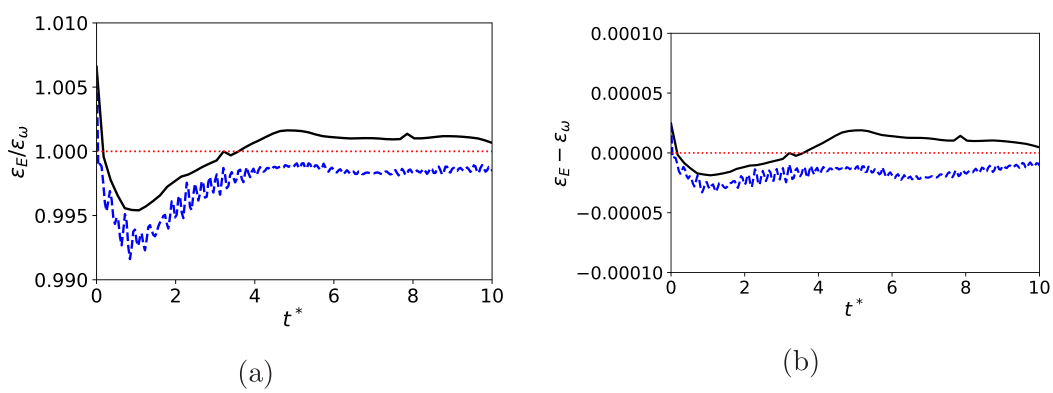

Figure 5–14: The dissipation rate error indicators for DNS results of TGV at $Re = 200$ obtained on a 256^2 structured grid (solid black), and on a 256-unstructured grid (dashed blue): (a) dissipation rate ratio, $\epsilon_E/\epsilon_\omega$, (b) dissipation rate difference, $\epsilon_E - \epsilon_\omega$.

perturbed structured grids, $S64-10\%$ (10% perturbation) and $S64-20\%$ (20% perturbation), and one unstructured mesh, $U64$, were used for these simulations whose details are summarized in Table 5–5. The filter strength for hexahedral elements was specified by setting $(\alpha_2/\beta_2, \alpha_3/\beta_3, \alpha_7/\beta_7) = (1.1, 1.05, 1.025)$. For tetrahedral elements $\alpha_2/\beta_2 = 0.95$ was assumed. The filter cut-off frequency for both element types was $\kappa_f \approx \pi/2$. Five case studies were conducted to study the performance of the extended Najafi-Yazdi *et al.* 's filter: (i) effect of ADM order, (ii) effect of ADM under-relaxation, (iii) effect of grid resolution, (iv) effect of grid anisotropy, and (v) effect of unstructured meshes.

Table 5–5: Specifications of structured and unstructured grids used for large-eddy simulation of TGV at $Re = 1600$.

Grid Type	Grid Name	# edge segments	# Elements	# Nodes
Uniform Structured	$S64$	$64 \times 64 \times 64$	$262,144$	$274,625$
	$S128$	$128 \times 128 \times 128$	$2,097,152$	$2,146,689$
Perturbed Structured	$S64 - 10\%$	$64 \times 64 \times 64$	$262,144$	$274,625$
	$S64 - 20\%$	$64 \times 64 \times 64$	$262,144$	$274,625$
Unstructured	$U64$	$64 \times 64 \times 64$	$109,914$	$617,392$
	$U128$	$128 \times 128 \times 128$	$2,146,689$	$10,485,760$

I Effect of ADM Order

Large-eddy simulations with ADMs (AD-LES) of order 5, 7, 8, and 10 were performed on $S64$ to study the accuracy and the stability of the numerical simulations. The Q-criterion iso-surface $Q = 0.001$ colored with vorticity magnitude is shown in Fig. 5–15 for times $t^* \approx 3.2$, 8.85, 12 and 20. The Q-criterion is defined as

$$Q = \frac{1}{2}\left(\|\boldsymbol{\Omega}\|^2 - \|\mathbf{S}\|^2\right) \ , \tag{5.30}$$

where

$$S_{ij} = \frac{1}{2}\left(\frac{\partial u_i}{\partial x_j} + \frac{\partial u_j}{\partial x_i}\right) \ , \tag{5.31}$$

and

$$\Omega_{ij} = \frac{1}{2}\left(\frac{\partial u_i}{\partial x_j} - \frac{\partial u_j}{\partial x_i}\right) \ , \tag{5.32}$$

are the symmetric and skew-symmetric parts of the velocity gradient tensor,$D_{ij} = S_{ij} + \Omega_{ij}$, respectively. S_{ij} is also known as the rate-of-strain tensor, and Ω_{ij} is the vorticity tensor.

The small ripples seen in Fig. 5–15b suggest that some vortices at scales close to the grid size exist in the flow at $t^* \approx 3.2$. At $t^* \approx 8.85$, the kinetic energy dissipation rate is almost at its maximum as vortex structures break down from anisotropic to homogeneous isotropic coherent structures. At $t^* \approx 12$ the coherent structures within the flow are in their final stages of transition to fully turbulent flow. At $t^* \approx 20$, the flow has become fully turbulent with well-developed energy and enstrophy cascades.

The evolutions of estimated energy-based, ϵ_E, and vorticity-based, ϵ_ω, dissipation rates over time are presented in Fig. 5–16. Results are compared to the DNS data by Jammy [187] and the LES results from a flux reconstruction (FR) framework corresponding to nodal discontinuous Galerkin (FR-NDG), optimized flux reconstruction discontinuous Galerkin (FR-OFR), and spectral difference (FR-SD) [184] with 128 degrees of freedom, i.e. p_1 Legendre polynomials on a 64^3 grid.

The AD-LES results are more accurate than those from the FR-NDG, FR-OFR, and FR-SD schemes for both energy-based, ϵ_E, and vorticity-based, ϵ_ω, dissipation

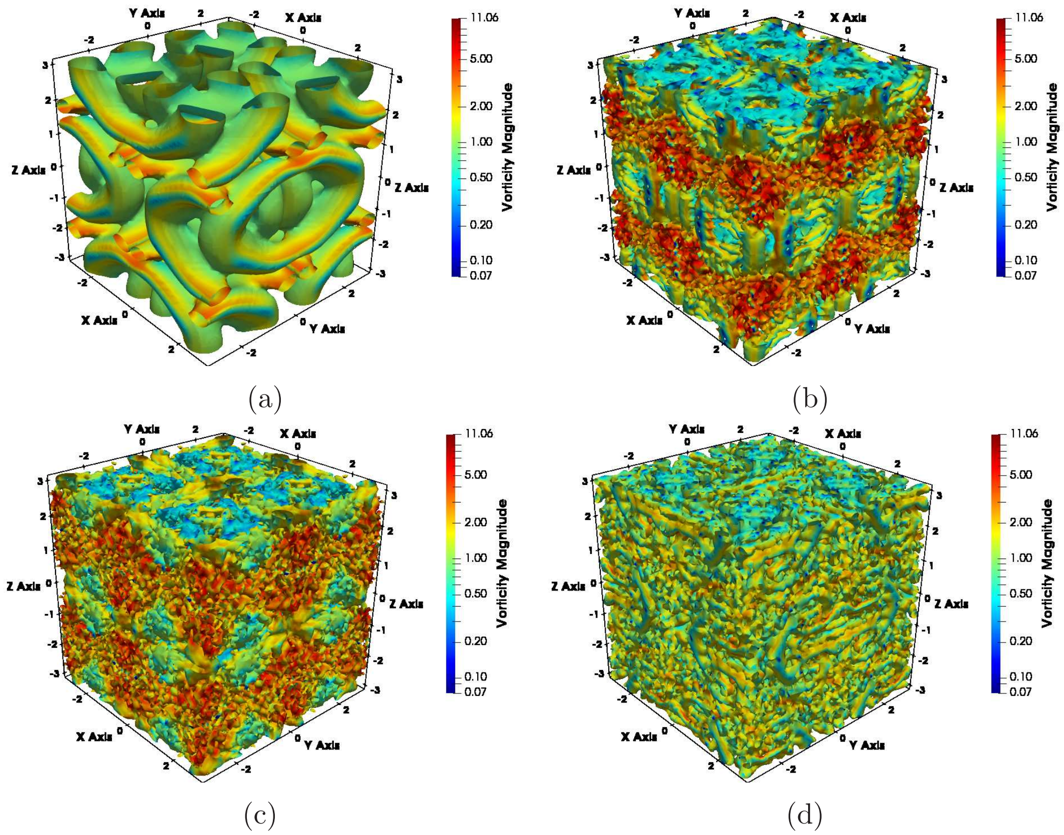

Figure 5–15: Iso-contours of Q-criterion at $Q = 0.001$ for TGV at $Re = 1600$ on $S64$ for ADM8 colored with vorticity magnitude at (a) $t^* \approx 3.2$, (b) $t^* \approx 8.85$, (c) $t^* \approx 12$, (d) $t^* \approx 20$.

rates. Note that the OFR and SD lines almost overlap each other. The energy-based dissipation rates of AD-LES are almost the same up to $t^* \approx 4$, suggesting that filtering and deconvolution of the flow fields does not affect laminar flow structures. As the laminar-turbulent transition occurs, $4 < t^* < 7$, higher ADM orders show less dissipation. This is expected as *approximate deconvolution* of a filtered variable is effectively similar to filtering the original field with a less dissipative (sharper) filter. The ADM10 evolution shows some oscillations in the energy-based dissipation rate.

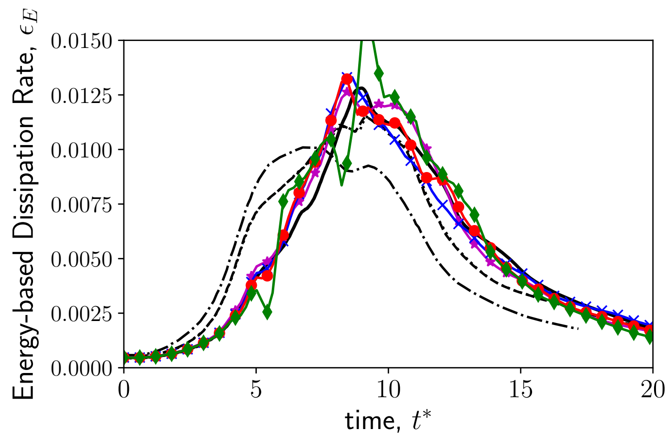

(a)

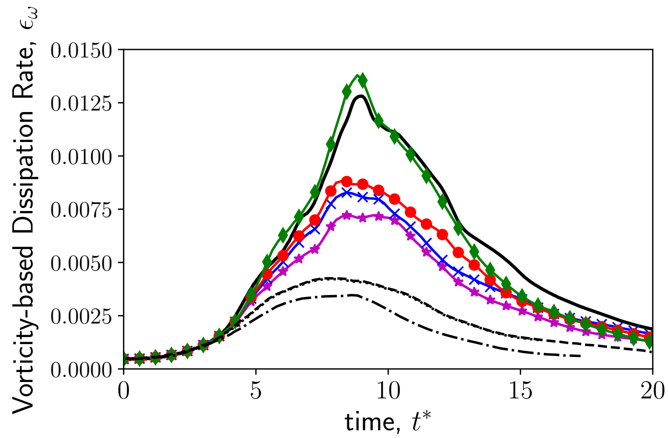

(b)

Figure 5–16: Turbulent kinetic energy dissipation rates: (a) energy-based, ϵ_E, (b) vorticity-based, ϵ_ω, for TGV at $Re = 1600$: reference DNS results by Jammy *et al.* [187] (solid), LES results on $S64$ for ADM orders of 5 (magenta asterisk), 7 (blue cross), 8 (red circle), and 10 (green diamond) compared to LES results by Bull and Jameson [184] for FR-NDG (dashed), FR-OFR (dash-dotted), and FR-SD (dotted).

This phenomenon may be the result of temporary energy pile-up near the grid cut-off, $\kappa \approx \kappa_g$, before being completely dissipated by the filter. One alternate explanation is numerical aliasing of turbulent kinetic energy at wavenumbers smaller than the filter cut-off, $\kappa < \kappa_f$. A lower ADM order implies a stronger (more dissipative), filter resulting in fewer oscillations with smaller amplitudes.

The vorticity-based dissipation rates become more accurate as the order of ADM is increased. This is because higher ADM orders allows more vorticity transfer from large scales to small scales, resulting in higher enstrophy and estimated dissipation rates. This behavior is related to lower dissipation at the wavenumbers close to the grid cut-off, $\kappa \lesssim \kappa_g$. A noteworthy point is the stability and accuracy of the LES at very high ADM orders, e.g. 10th, where there is practically no dissipation due to filtering except at $\kappa \approx \kappa_g$. Although the energy-based dissipation rate oscillates and slightly over-predicts the peak dissipation rate, the vorticity-based dissipation rate closely follows the DNS profile up to $t^* \approx 12$. This extreme case not only demonstrates the strong stabilizing effect of the proposed extension to Najafi-Yazdi *et al.* 's differential filter for AD-LES, but also suggests that increasing ADM order enhances the resolved vortex dynamics by preserving scales near the grid cut-off.

Figure 5–17 shows the energy and enstrophy spectra, i.e. $E(\kappa)$ and $\zeta(\kappa)$, at $t^* \approx 20$. The enstrophy spectrum for isotropic turbulence can be modelled as

$$\zeta(\kappa) = \kappa^2 E_{vKK}(\kappa) \ , \tag{5.33}$$

where E_{vKK} is the empirically modified von Kármán-Kraichnan for the three-dimensional energy spectrum, i.e Eq. (5.28). A dimensional analysis applied to the enstrophy spectrum suggests that $\zeta(\kappa) \propto \kappa^{1/3}$ for the intertial subrange [191]. This relationship was validated against experiments by Poulain *et al.* [196] through direct measurements of spatial enstrophy spectra using a novel ultrasonic scattering approach.

The energy spectra for all ADM orders demonstrate a $-5/3$ theoretical slope in the log-log scale for the inertial subrange, $7 \leq \kappa \leq 20$. No energy pile-up is observed near the grid cut-off, $\kappa_g = 32$, showing the ability of the filter in providing the necessary energy dissipation while preserving the flow dynamics. The noticeable drop in the wavenumber range $30 \leq \kappa \leq 50$ is merely caused by the lack of sample points in the spectral domain when estimating the turbulent kinetic energy, $E(\kappa)$, for a thin spherical region of $\kappa' \in (\kappa - \delta\kappa/2, \kappa + \delta\kappa/2)$. The ADM5 results demonstrate the highest dissipation at wavenumbers close to the grid cut-off, i.e. $\kappa \gtrsim 20$ due to a stronger effective filter.

The enstrophy spectra, $\zeta(\kappa)$, match the theoretical $-1/3$ slope in the log-log scale for the inertial subrange. Higher ADM orders show more vorticity content at near-grid cut-off wavenumbers, $\kappa \gtrsim 20$, demonstrating better reconstruction of small-scale vortex structures.

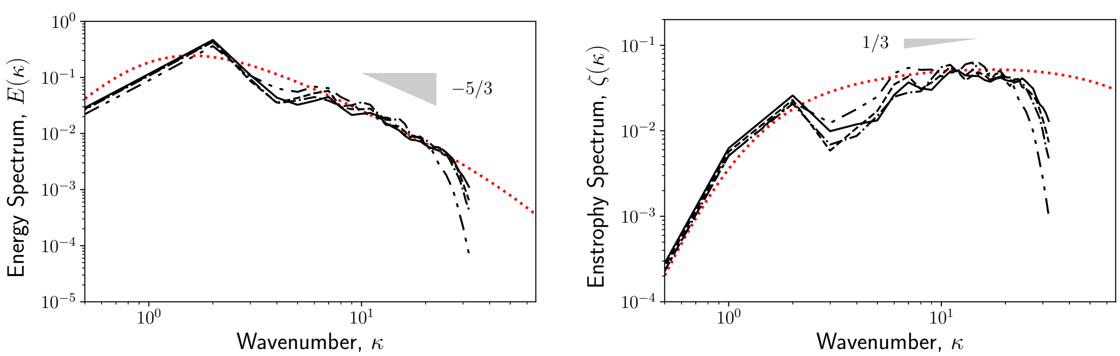

(a) (b)

Figure 5–17: The (a) energy and (b) enstrophy spectra of LES at $t^* \approx 20$ using ADM5 (dash double-dotted), ADM7 (dash-dotted), ADM8 (dashed), and ADM10 (solid) compared to the empirically modified von Kármán-Kraichnan model [2](red dotted).

The vorticity spectra at $t^* \approx 3.2$, 8.85, 12, and 20 are shown in Fig. 5–18. The profiles are compared with the theoretical spectrum obtained from the empirically modified von Kármán-Kraichnan model [2] for homogeneous isotropic turbulence. The LES results show a rapid decay near grid cut-off, $\kappa_g = 32$, due to lack of grid resolution to resolve the entire scale range of vortex structures. At the early stages, i.e. $t^* < 5$, the flow is laminar and highly anisotropic. The vorticity content of small scales is near zero and, therefore, the vorticity spectrum is not affected by the filter nor the ADM order. As the flow undergoes a transition to turbulence, $5 < t^* < 18$, the interaction between small and large scale vorticies becomes significant. Higher ADM orders have less dissipative effect on the flow and preserve small-scale vortex structures better. The vorticity spectrum becomes almost independent of the ADM order once again when the turbulence becomes homogeneous and isotropic, i.e. $t^* \approx 20$.

II Effects of ADM Under-Relaxation

The *accelerated* formulation of van Cittert approximate deconvolution operator, i.e. $\phi^{(m)} = \phi^{(m-1)} + \omega_{(m-1)}\Delta\phi^{(m)}$, is effectively an under-relaxation formulation. Three values for the under-relaxation coefficient, i.e. $\omega_{(m-1)} = 0.5$, 0.85 and 0.9, were used for ADM8 on the $S64$ grid to simulate the TGV flow. The temporal evolution of the energy-based and vorticity-based dissipation rates are presented in Fig. 5–19. Varying the under-relaxation coefficient, $\omega_{(m-1)}$, has a more significant impact on the flow dynamics than varying the ADM order. Strong under-relaxation, $\omega_{(m-1)} = 0.5$, yield a stronger effective filtering resulting in lower estimated vorticity-based dissipation rates. A weak under-relaxation, e.g. $\omega_{(m-1)} = 0.9$, preserves the

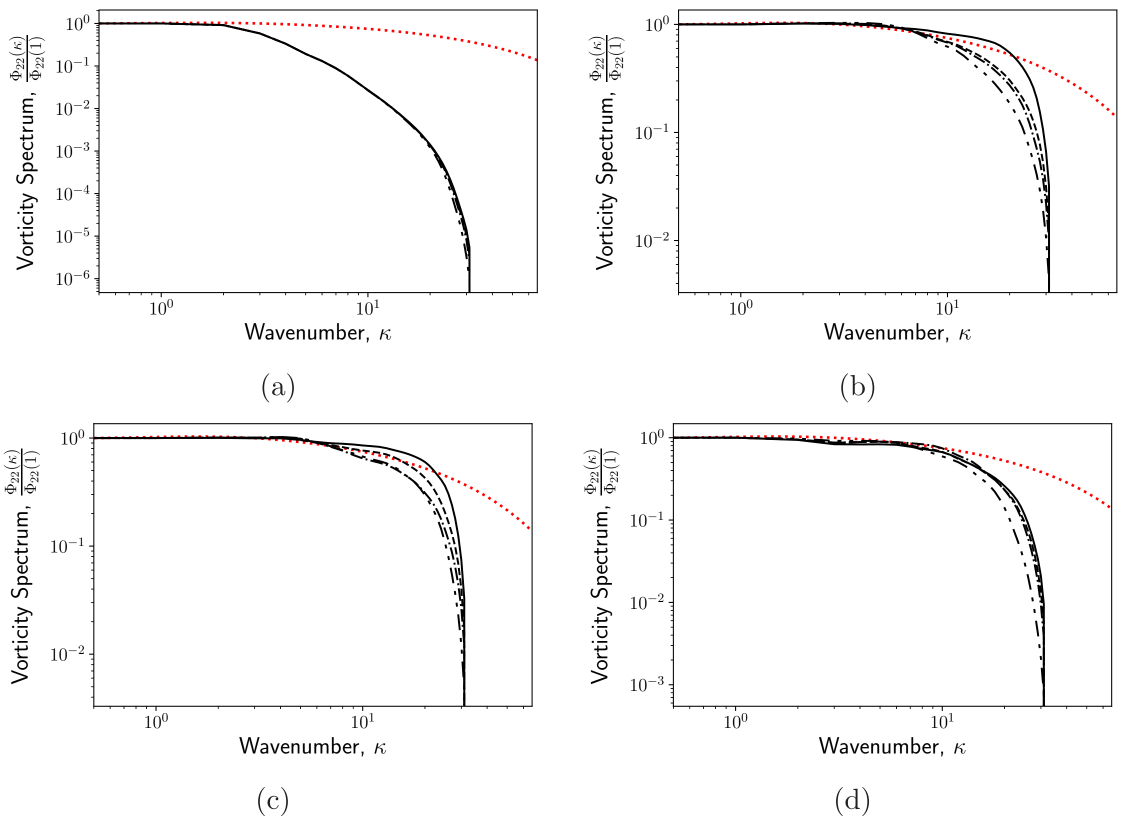

Figure 5–18: The vorticity spectra, $\Phi_{22}(\kappa)$, of LES at (a) $t^* \approx 3.2$, (b) $t^* \approx 8.85$, (c) $t^* \approx 12$, and (d) $t^* \approx 20$ using ADM8 (dash double-dotted), ADM7 (dash-dotted), ADM8 (dashed), and ADM10 (solid) compared to the theoretical profile obtained from he empirically modified von Kármán-Kraichnan model [2] (red dotted).

vortex dynamics more accurately. The vorticity-based dissipation rate is almost identical to the DNS results up to $t^* \approx 8$ and later deviates from it only by a small amount. However, the energy-based dissipation rate demonstrates oscillations suggesting numerical aliasing due to a sharp filter roll off.

The energy and enstrophy spectra of strong under-relaxation, e.g. $\omega_{(m-1)} = 0.5$, yields strong dissipation at high wavenumbersm hindering the interaction between small and large scale dynamics. This is observed in Fig. 5–20 as an over-estimation

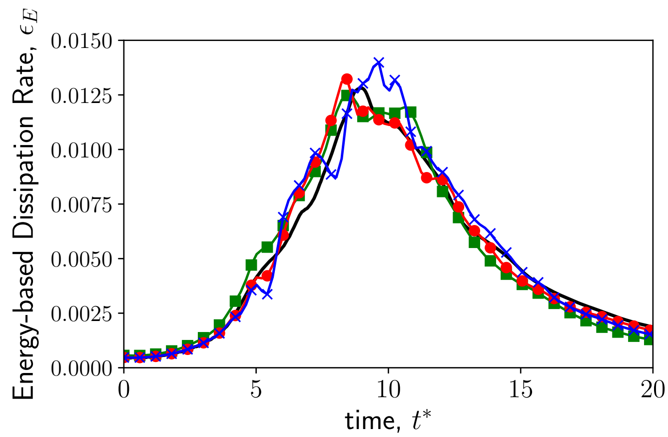

(a)

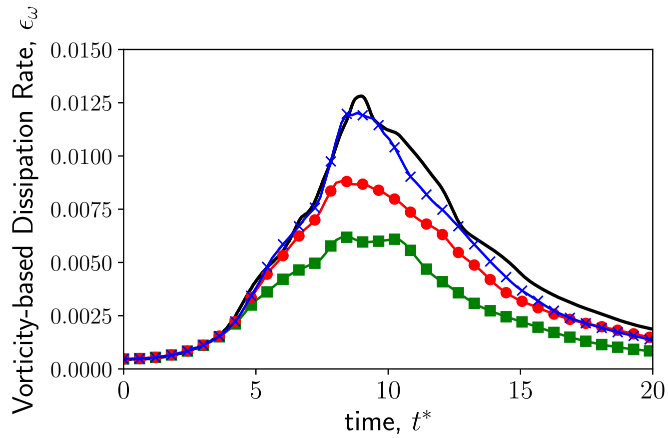

(b)

Figure 5–19: Turbulent kinetic energy dissipation rates: (a) energy-based, ϵ_E, and (b) vorticity-based, ϵ_ω, for TGV at $Re = 1600$: reference DNS results by Jammy *et al.* [187] (solid), LES results on $S64$ for ADM8 with under relaxation coefficient $\omega_{(m-1)} = 0.5$ (green square), $\omega_{(m-1)} = 0.8$ (red circle), and $\omega_{(m-1)} = 0.9$ (blue cross).

of the vorticity spectrum in the intermediate wavenumber range, $2 \leq \kappa \leq 10$, and an underestimation of both spectra, energy- and vorticity-based, at high wavenumbers, $\kappa \geq 10$.

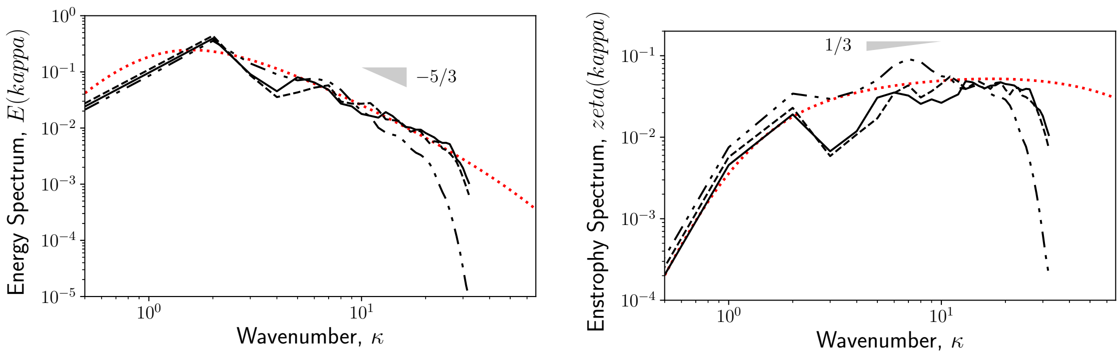

(a)

(b)

Figure 5–20: The (a) energy and (b) enstrophy spectra of LES at $t^* \approx 20$ using ADM8 with under-relaxation coefficient $\omega_{(m-1)} = 0.5$ (dash double-dotted), $\omega_{(m-1)} = 0.8$ (dashed), and $\omega_{(m-1)} = 0.9$ (solid) compared to the theoretical profile obtained from the empirically modified von Kármán-Kraichnan model [2] (red dotted).

The temporal evolution of the vorticity spectrum, Fig. 5–21, shows the underdevelopment of vortex dynamics more clearly. The vorticity spectrum for $\omega_{(m-1)} = 0.5$ does not vary between $t^* \approx 8.85$ and $t^* \approx 20$, suggesting that the strong filter removes the high-wavenumber vorticies and prevents the vorticity spectrum to evolve into a homogeneous isotropic flow. The vorticity spectra for higher $\omega_{(m-1)}$ values converge to the same distribution at $t^* \approx 20$, unlike $\omega_{(m-1)} = 0.5$.

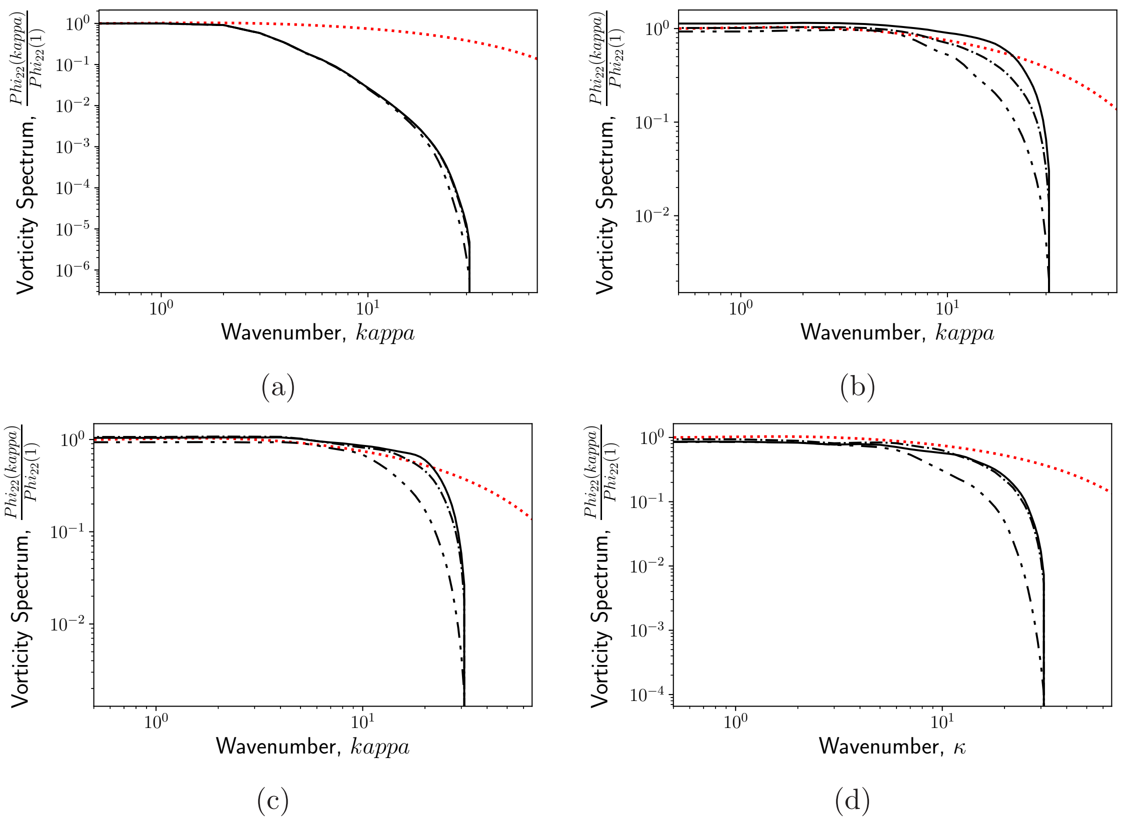

Figure 5–21: The vorticity spectra, $\Phi_{22}(\kappa)$, of LES at (a) $t^* \approx 3.2$, (b) $t^* \approx 8.85$, (c) $t^* \approx 12$, and (d) $t^* \approx 20$ using ADM8 with under-relaxation coefficient $\omega_{(m-1)} = 0.5$ (dash double-dotted), $\omega_{(m-1)} = 0.8$ (dashed), and $\omega_{(m-1)} = 0.9$ (solid) compared to the theoretical profile obtained from he empirically modified von Kármán-Kraichnan model [2] (red dotted).

III Effect of Grid Resolution

A 5-th order ADM was used on $S64$ and $S128$ grids with under-relaxation coefficient $\omega_{(m-1)} = 0.8$ to investigate the effect of grid resolution. A higher resolution, $S128$, improves the accuracy of the vortex structures, resulting in more accurate estimation of both energy-based and vorticity based dissipation rates, see Fig. 5–22b. The trends are comparable to those obtained with a flux reconstruction-based discontinuous Galerkin (DG) scheme on a 32^3 grid using p_3 polynomials, i.e. 128^3 degrees of freedom, by Bull and Jameson [184]. Figure 5–23 shows the energy-based dissipation rates near their peaks. The AD-LES scheme has a better accuracy in predicting the peak value at $t^* \approx 9$, and has less over-dissipation later at $t^* \approx 11$. This can be related to the reconstruction of vortex structures near grid cut-off yielding better estimation of turbulent kinetic energy dissipation rate.

The energy and enstrophy spectra resolve more wavenumbers, $\kappa < 64$, on the $S128$ compared to the $S64$, see Fig. 5–24. However, the result on $S128$ show a smoother decline in the viscous wavenumber range than the one on $S64$. It may be due to the low order of ADM, i.e. 5-th order.

The evolution of vorticity spectrum on $S128$ ans $S64$ are very similar, with more scales resolved on the former.

IV Effect of Grid Anisotropy

An 8-th order ADM was used for LES on $S64$, $S64-10\%$ and $S64-20\%$ grids to investigate the effect of grid anisotropy. Adding 10% anisotropy to the grid had no significant effect on the estimated energy- or vorticity-based dissipation rates until near the peak dissipation time, $t^* \approx 9$. The dissipation was overestimated afterwards which can be related to under-resolving vortex dynamics at certain locations. Perturbing the $S64$ grid by 20% resulted in under-estimation of the grid dissipation rate until the peak value, and over-estimation afterwards. The dissipation peak also shifted from $t^* \approx 9$ to $t^* \approx 10$. These deviations may be related to the local grid anisotropy. An anisotropic mesh does not resolve vortex structures in an isotropic

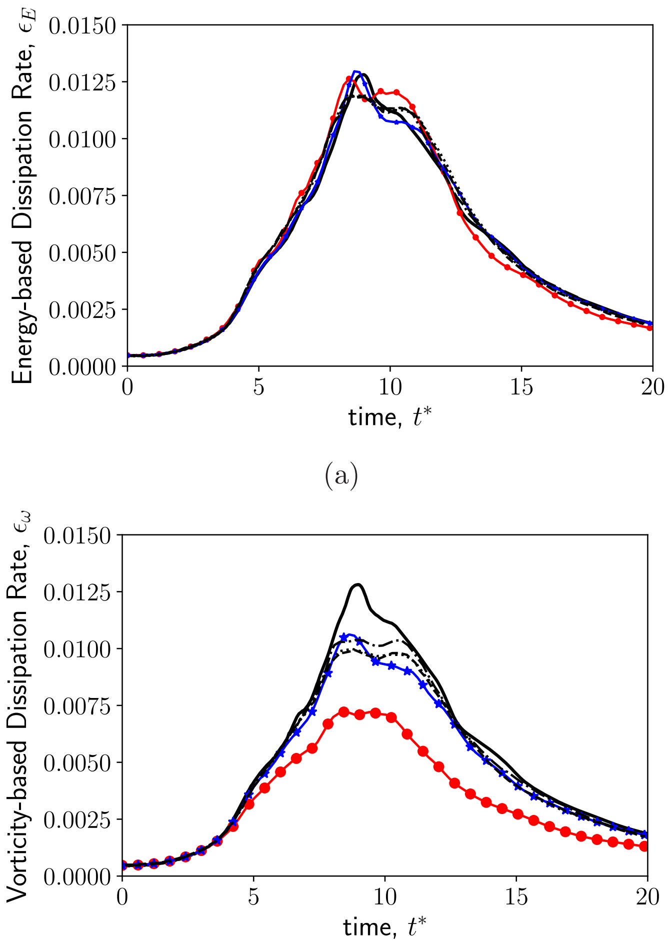

(a)

(b)

Figure 5–22: Turbulent kinetic energy dissipation rates: (a) energy-based, ϵ_E, (b) vorticity-based, ϵ_ω, for TGV at $Re = 1600$: reference DNS results by Jammy *et al.* [187] (solid), LES results using ADM5 with under relaxation coefficient $\omega_{(m-1)} = 0.8$ on $S64$ (red circle), and $S128$ grid (blue asterisk) compared to LES results by Bull and Jameson [184] for FR-NDG (dashed), FR-OFR (dash-dotted), FR-SD (dotted) on a 32^3 grid using p_3 polynomials.

way. This disturbs the interaction of small and large scale eddies. As the initial condition for TGV is anisotropic, the underlying anisotropic space discretization delays

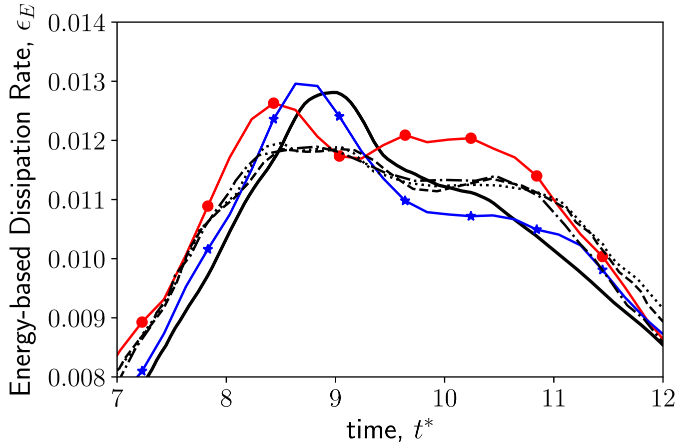

Figure 5–23: Comparing AD-LES and FR schemes in resolving the energy-based dissipation rate of TGV at $Re = 1600$ using 128^3 degrees of freedoms: reference DNS results by Jammy *et al.* [187] (solid), LES results using ADM5 with under relaxation coefficient $\omega_{(m-1)} = 0.8$ on $S64$ (red circle), and $S128$ (blue asterisk) compared to LES results by Bull and Jameson [184] for FR-NDG (dashed), FR-OFR (dash-dotted), and FR-SD (dotted) on a 32^3 grid using p_3 polynomials.

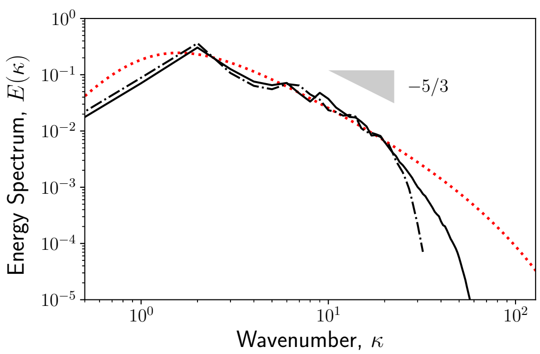

(a)

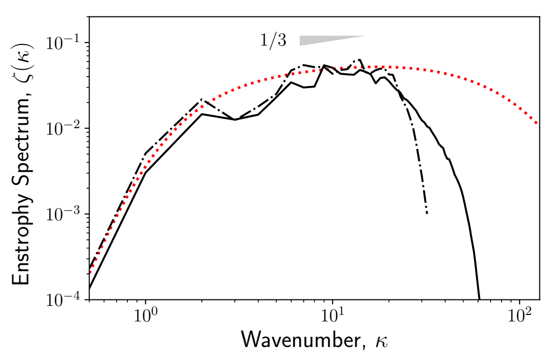

(b)

Figure 5–24: The (a) energy and (b) enstrophy spectra of LES at $t^* \approx 20$ using ADM5 with with under relaxation coefficient $\omega_{(m-1)} = 0.8$ on $S128$ grid (solid) and $S64$ grid (dash dotted); compared to the theoretical profile obtained from he empirically modified von Kármán-Kraichnan model [2] (red dotted).

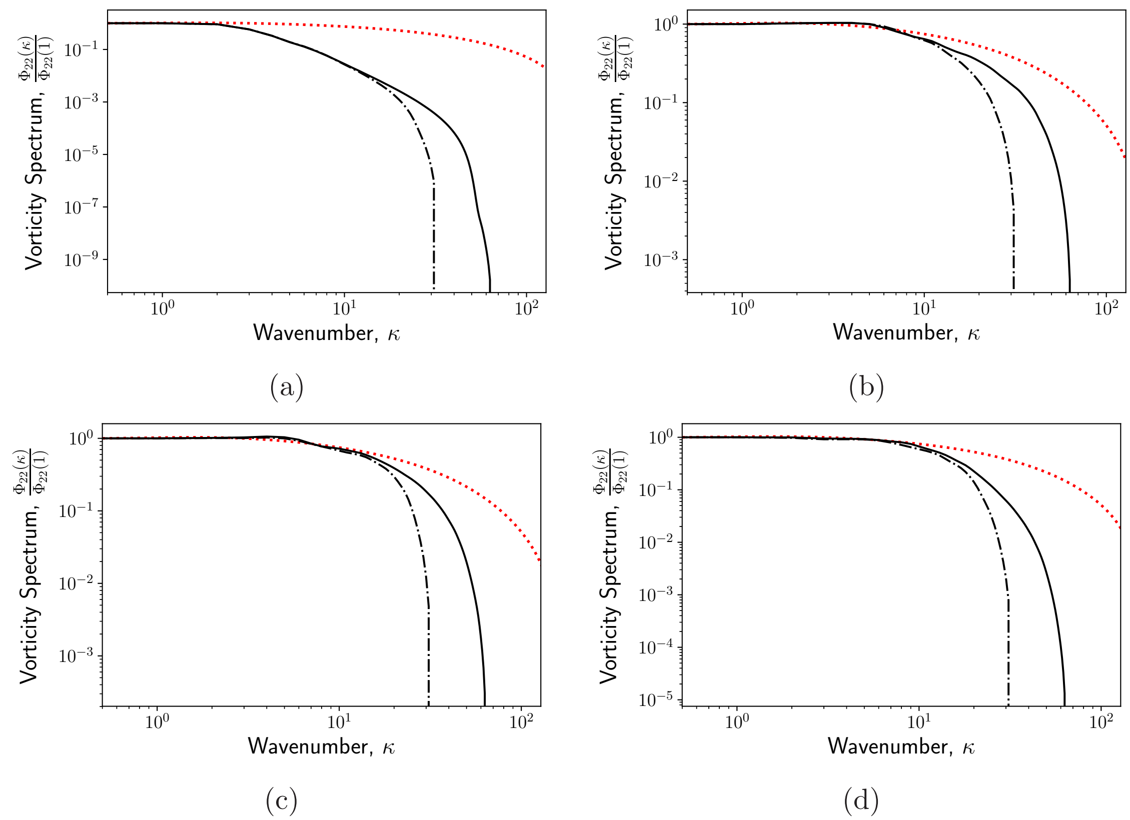

Figure 5–25: The vorticity spectra, $\Phi_{22}(\kappa)$, of LES at (a) $t^* \approx 3.2$, (b) $t^* \approx 8.85$, (c) $t^* \approx 12$, and (d) $t^* \approx 20$ using ADM5 with with under relaxation coefficient $\omega_{(m-1)} = 0.8$ on $S128$ grid (solid) and $S64$ grid (dash dotted); compared to the theoretical profile obtained from he empirically modified von Kármán-Kraichnan model [2] (red dotted).

vortex breakdown towards isotropic structures. This means that vortices tend to remain longer along certain directions than they should. As most of the estimated dissipation is due to coherent isotropic vortex structures, the non-physical extended life of anisotropic structures results in under-estimation of the dissipation rate as well as the lag in the peak time of the dissipation rate. This is based on the Kolomogorov hypotheses and the fact that the TKE dissipation rate is proportional to $\kappa^2 E(\kappa)$.

It should be noted that these are merely conjectures and a further investigation in turbulence anisotropy is needed to support this claim. One could further investigate the two-point correlation of velocity fields.

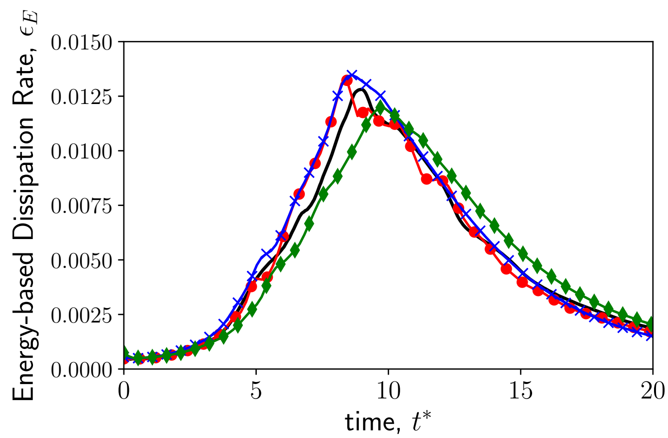

(a)
//

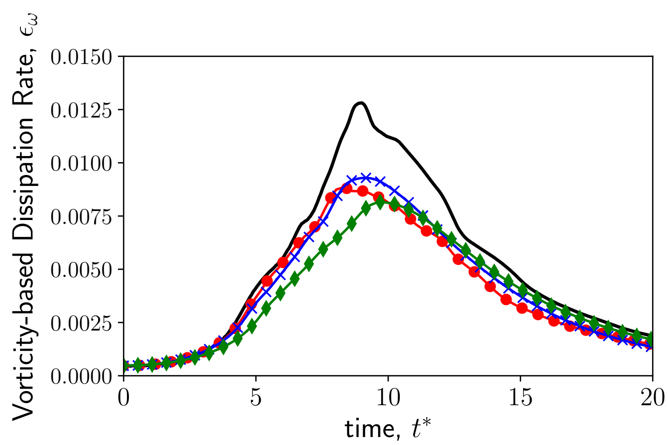

(b)

Figure 5–26: Turbulent kinetic energy dissipation rates: (a) energy-based, ϵ_E, (b) vorticity-based, ϵ_ω, for TGV at $Re = 1600$: reference DNS results by Jammy *et al.* [187] (solid), LES results on $S64$ grid (red circle), on $S64 - 10\%$ grid (blue cross), and on $S64 - 20\%$ grid (green diamond), using ADM8 with $\omega_{(m-1)} = 0.8$.

As $S64{-}10\%$ and $S64{-}20\%$ grids are not uniform, energy and enstrophy spectra were calculated by interpolating the solutions on a very fine uniform structured grid with 256^3 degrees of freedom, $S256$. The reported spectra were calculated using fast Fourier transform (FFT) on the $S256$ and truncating the results at $\kappa = 32$. Both the energy and enstrophy spectra show higher dissipation at high wavenumbers for more anisotropic grids. The grid anisotropy also skews the energy and enstrophy distributions near the grid cut-off as it depends on the local mesh topology at each computational node. This is the reason for an observed smaller grid cut-off for $S64 - 10\%$ and $S64 - 20\%$ grids.

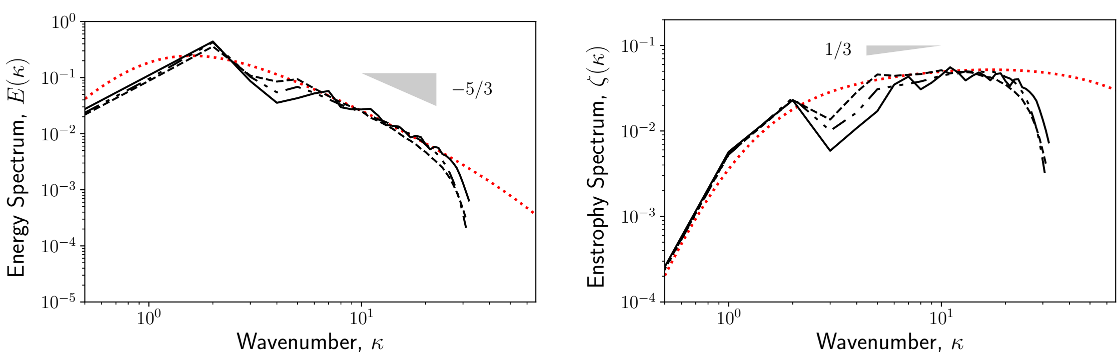

(a) (b)

Figure 5–27: The (a) energy and (b) enstrophy spectra of LES at $t^* \approx 20$ using ADM8 with with under relaxation coefficient $\omega_{(m-1)} = 0.8$ on $S64$ grid (solid), $S64{-}10\%$ grid (dash dotted), and $S64-20\%$ (dashed); compared to the theoretical profile obtained from he empirically modified von Kármán-Kraichnan model [2] (red dotted).

As suggested by Morris and Foss [191], the vorticity spectrum is a better measure for the flow anisotropy. The spectra at $t^* \approx 3.2$ show that grid anisotropy results in lower estimated vorticity content in the inertial subrange, see Fig. 5–28. The over-estimation of vorticity near the grid cut-off, $\kappa_g \approx 32$, on $S64 - 10\%$ and $S64 - 20\%$

are related to the aliasing error due to interpolation. The estimated vorticity content in the inertial subrange is consistently lower for higher values of grid perturbation. This observation supports the hypothesis that the grid anisotropy contributes to maintaining anisotropic vortex structures in the flow.

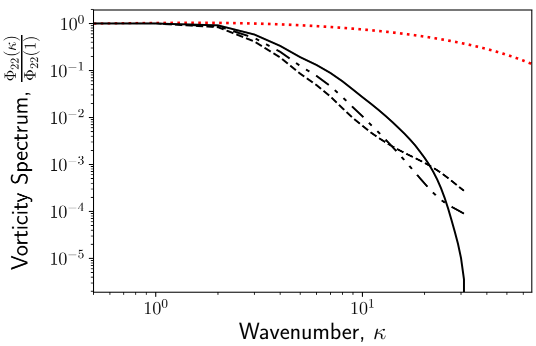

(a)

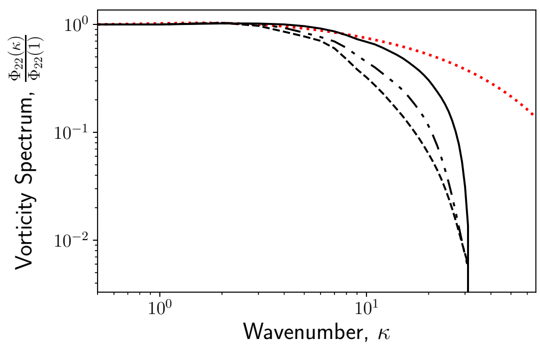

(b)

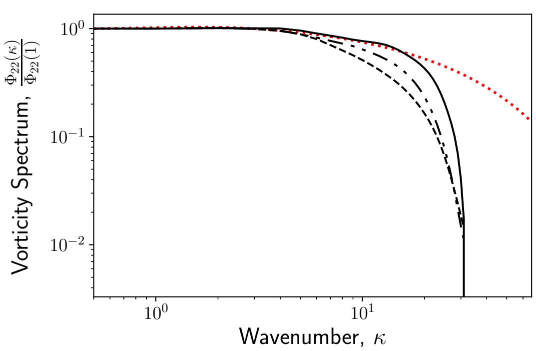

(c)

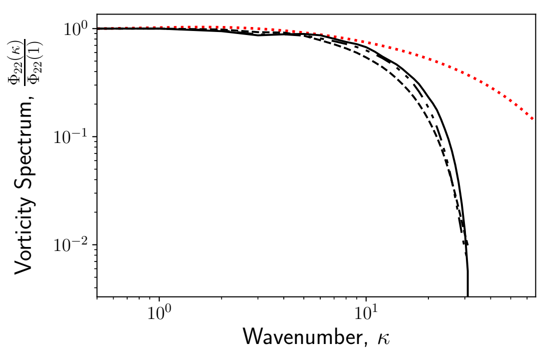

(d)

Figure 5–28: The vorticity spectra, $\Phi_{22}(\kappa)$, of LES at (a) $t^* \approx 3.2$, (b) $t^* \approx 8.85$, (c) $t^* \approx 12$, and (d) $t^* \approx 20$ using ADM8 with with under relaxation coefficient $\omega_{(m-1)} = 0.8$ on $S64$ grid (solid), $S64 - 10\%$ grid (dash dotted), and $S64 - 20\%$ (dashed); compared to the theoretical profile obtained from he empirically modified von Kármán-Kraichnan model [2] (red dotted).

V Unstructured Mesh

Finally, the AD-LES scheme with the extended filter was used on a fully unstructured mesh consisting of tetrahedrons, $U64$, using ADM5 with $\omega_{(m-1)} = 0.8$. The filter on linear tetrahedral elements has a single tuning parameter, α_2, to control its strength. For these simulations $\alpha_2/\beta_2 = 0.95$ is assumed yielding an effective filter cut-off wavenumber of $\kappa_f \approx 3/5\pi$.

The evolution of estimated dissipation rates based on energy and vorticity are compared to the DNS data and the AD-LES results obtained on $S64$ in Fig. 5–29. The peak energy-based dissipation rate occurred at an earlier time, $t^* \approx 7.5$, which can be related to the higher numerical dissipation rate of linear tetrahedron elements compared to hexahedron elements. The early excessive dissipation removed some energy from the flow structures at the grid size scale resulting in underestimation of the peak dissipation rate value. The vorticity-based dissipation shows slightly higher values for $4 < t^* < 7$ than the trend estimated on $S64$. This can be related to the increased degrees of freedom in a tetrahedron-based unstructured mesh than that of an hexahedron-based structured grid when element edge sizes are almost equal. After the peak, the vorticity-based dissipation rate on $U64$ is lower than that obtained on $S64$. This can be related to the additional dissipation due to the element type as well as a more dissipative filter on tetrahedrons compared to hexahedrons.

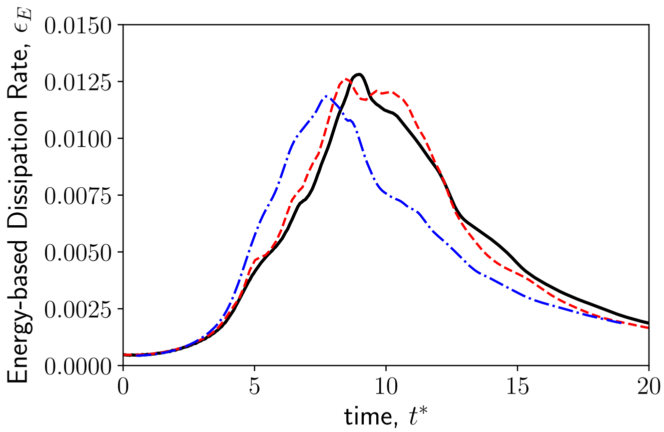

(a)

Figure 5–29: Turbulent kinetic energy dissipation rates: (a) energy-based, ϵ_E, and (b) vorticity-based, ϵ_ω, for TGV at $Re = 1600$: reference DNS results by Jammy *et al.* [187] (solid), LES results on $S64$ grid (red dashed), and on $U64$ grid (blue dash-dotted) using ADM5 with $\omega_{(m-1)} = 0.8$.

CHAPTER 6
Discussions and Conclusions

6.1 FEM Stabilization with Explicit Filtering

The numerical results for the lid-driven cavity flow at $Re = 1000$ and the doubly-periodic shear flow showed strong stabilization of FEM when the extended Najafi-Yazdi*et al.* filter was used. The node-to-node oscillations known as q-waves were almost entirely removed by this filter, a property very appealing for aeroacoustics simulations. The SUPG FEM could stabilize the shear-flow simulation but could not remove spurious oscillations in the density field. These observations are related to the stability of the underlying numerical schemes. This was discussed in lecture notes by Clason [197] which provide in-depth understanding of stability conditions for conforming and non-confirming Galerkin approaches.

6.1.1 Continuous SUPG Stability

The stability of the continuous SUPG method combined with a finite difference discretization in time was studied by Burman [198] for the advection problem. Consider the problem of finding a solution field u satisfying

$$\begin{cases} \partial_t u + \mathbf{v} \cdot \nabla u = f & x \in \Omega, t > 0 \ , \\ u(x,0) = u_0 & x \in \Omega \ , \end{cases} \tag{6.1}$$

where $\mathbf{v}$ is a given Libschitz[1] continuous velocity field, f is a source function, u_0 is an initial distribution of u on a domain Ω defined in $\mathbb{R}^d$ (d = 1,2, or 3), and $\partial\Omega$ is the domain boundary. Consider N_h to denote the standard finite element space of continuous, pieces-wise polynomial shape functions, and $W_h = N_h + (\tau \mathbf{v} \cdot \nabla N_h)$ to be the space of SUPG test functions where τ is a stabilization parameter.

Burman [198] derived the coercivity condition for the SUPG scheme and *multi-level* time-stepping schemes with time-step size of Δt and spatial discretization size of h as

$$\|u_h^n\|_{\mathbf{v}}^2 + \Delta t \sum_{m=1}^{n} |||u_h^m|||^2 \lesssim \Delta t \sum_{m=1}^{n} t^n \left(1 + \frac{\tau}{\Delta t}\right) \left\|f(\breve{t}^m)\right\|^2 + \left\|u_h^0\right\|_{\mathbf{v}}^2 \ . \tag{6.2}$$

where $\lesssim$ indicates an inequality up to a multiplicative constant, u_h^n and $\breve{u}^n$ denote the approximate discrete solutions at time $t^n = n\Delta t$ and intermediate time-step $\breve{t} = \sum \omega_k t^{n-k}$ respectively, $\partial_{\breve{t}}$ is the discrete temporal derivative operator, $\|\cdot\|$ is the L_2 norm, $\|\cdot\|_{\partial\Omega}$ is the L_2 norm on the boundary, $\|\cdot\|_{\mathbf{v}}$ is the SUPG-like norm defined as

$$\|u\|_{\mathbf{v}} \coloneqq \left(\|u\|^2 + \tau^2 \|\mathbf{v} \cdot \nabla u\|^2\right)^{1/2} \ , \tag{6.3}$$

and $|||\cdot|||$ is a semi-norm of discretized quantities defined as

$$|||u_h^n|||^2 \coloneqq \tau \|\partial_{\breve{t}} u_h^n + \mathbf{v} \cdot \nabla \breve{u}_h^n\|^2 + \frac{1}{2}\tau^2 \|\sqrt{v_n}\partial_{\breve{t}}\breve{u}_h^n\| \, \partial\Omega^2 + \frac{1}{2} \|\sqrt{v_n}\breve{u}_h^n\|_{\partial\Omega}^2 \ , \tag{6.4}$$

with $v_n = \mathbf{v} \cdot n$ as the velocity field component normal to the boundary $\partial\Omega$. He found $\tau^2 \leq \Delta t$ for the backward Euler, and $\tau \leq \Delta t$ for the Crank-Nicolson as the stability conditions even for a non-solenoidal velocity field $\mathbf{v}$, i.e. $\nabla \cdot \mathbf{v} \neq 0$.

[1] Libschitz continuity a stronger form of uniform continuity by putting a constraint on the rate of change of a function. A real-valued function $f : \mathbb{R} \to \mathbb{R}$ is Libschitz continuous if there exists a positive real constant K such that $|f(x_1) - f(x_2)| \leq K|x_1 - x_2|$ for any $x_1, x_2 \in \mathbb{R}$.

The stability condition for the θ-scheme (a semi-implicit method) and the second-order backward Euler schemes (an explicit method) was given as

$$
\begin{aligned}
&\|u_h^n - u(t^n)\|_{\mathbf{v}}^2 + \Delta t \sum_{m=1}^{n} |||u_h^m - u(t^m)|||^2 \lesssim \\
&h^{2p+1}\left(t^n U_2^{1,p+1} + t^n \tau^2 U_2^{2,p+1} + t^n U_\infty^{0,p+1} + \tau^2 U_\infty^{2,p+1} + \tau^2 \Delta t^2 U_\infty^{3,p+1}\right) \\
&\times \Delta t^4 \left(t^n U_2^{3,0} + t^n \tau^2 U_2^{4,0} + U_\infty^{3,0}\right) \\
&+ \left\|u(t^1) - u_h^1\right\|_{\mathbf{v}}^2 + \left\|u(0) - u_h^0\right\|_{\mathbf{v}}^2 \ ,
\end{aligned}
\tag{6.5}
$$

where

$$
U_2^{i,j} := \int_0^{t^n} \left|\partial_t^i \partial_x^j u\right|^2 dt \ , \tag{6.6}
$$

$$
U_\infty^{i,j} := \sup_{t\in(0,t^n]} \left|\partial_t^i \partial_x^j u\right|^2 \ , \tag{6.7}
$$

and p is the degree of shape function polynomials.

Burman observed a degradation evidently in the growth of spurious oscillations upstream of a Gaussian distribution for u. He argued that "these oscillations may persist close to strong transients due to cancellation between the time derivative and the space derivative" [198]. These observations correlate with the spurious oscillations observed in the density field of the shear flow obtained by the SUPG method in Chapter 5. It suggests that a four-level time-stepping scheme, e.g. the standard 4-th order Runge-Kutta (RK), may also cause spurious oscillations when used in conjunction with the SUPG scheme.

To test this hypothesis, the acoustic propagation of an initial Gaussian distribution in pressure and density was simulated using the SUPG and the standard 4-th order RK on a very fine grid, 2048×2048. Due to a very small grid size $h \approx 4.8\times10^{-4}$, a much larger number of time-steps are required to reach the same simulation time, $t = 0.07$. The density field is shown in Fig. 6–1 for $t = 0.0175$, 0.035, 0.0525, and 0.07. Note that SUPG is more dissipative in front of the acoustic wave due to higher absolute velocity of the flow. Similar behavior was observed in the results for advection of an isotropic vortex in an inviscid mean flow. The rapid growth of spurious oscillations is clearly visible in the last two snapshots. These results support the hypothesis. Further analytical investigation is required, following the work of Burman [198].

6.1.2 Approximate Deconvolution Finite Element Method Stability

For the sake of simplicity, the term *approximate deconvoltuion finite element method (AD-FEM)* is used when the FEM solution u_h^n is filtered and then an approximate deconvolution is applied on it, i.e. $u_h^{n*} \approx Q \circledast G \circledast u_h^n$. For a non-amplifying filter kernel, i.e. $|\mathcal{G}(\boldsymbol{\kappa})| \leq 1$ for all wavenumbers $\boldsymbol{\kappa}$, the combined operator $Q \circledast G$ is also a non-amplifying filter, i.e. $|\mathcal{H}| \leq 1$, when the accelerated van Cittert iterative method is used (for proof see Layton *et al.* [62]). This results in

$$\|u_h^{n*}\|^2 \leq \|u_h^n\|^2 \ , \tag{6.8}$$

which is only an upper bound for the L^2 norm of the AD-FEM solution and does not guarantee its coercivity nor its stability. One approach to study coercivity and convergence of AD-FEM is to assume that the effective filtering due to $H = Q \circledast G$ enriches the *test* function w in a weak formulation. For example, the advection problem, Eq. (6.1) can be formulated in a discrete consistent weak form as

$$(\partial_t u_h^n, w_h) + a(u_h^{n*}, w_h) = F^{n*}(w_h) \ , \tag{6.9}$$

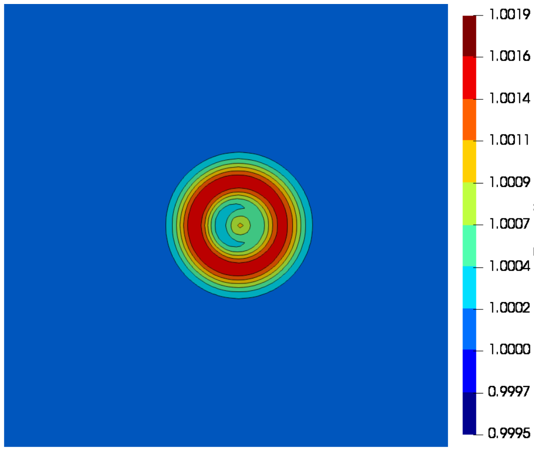

(a)

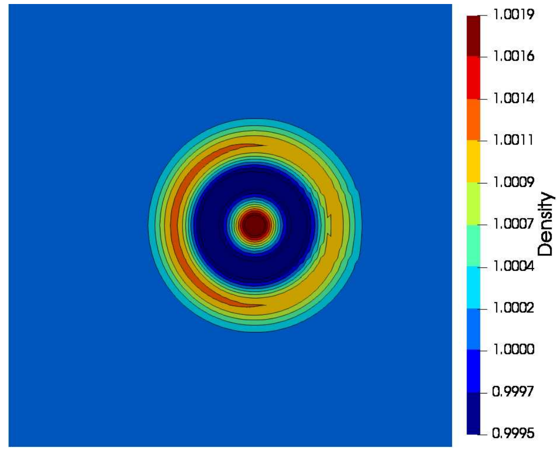

(b)

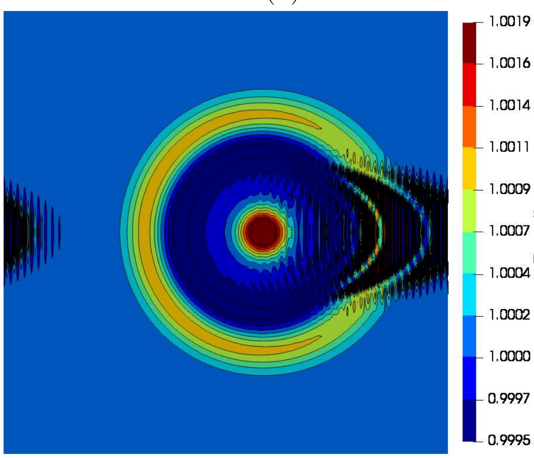

(c)

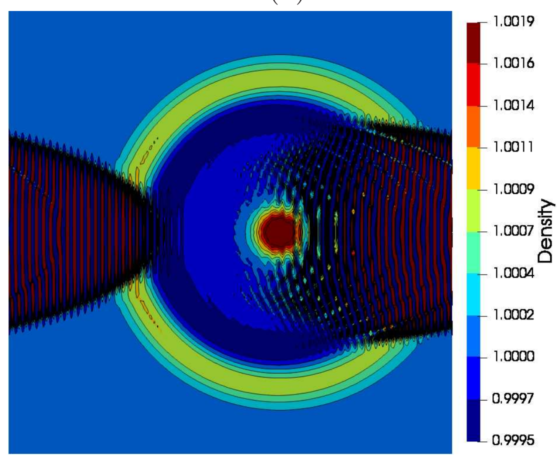

(d)

Figure 6–1: Density field at (a) $t = 0.0175$, (b) $t = 0.035$, (c) $t = 0.0525$, and (d) $t = 0.07$ for acoustic propagation of a monopole in a free stream on a 2048×2048 grid using a SUPG FEM.

where $(\cdot,\cdot)$ is the inner product, and $a(\cdot,\cdot)$ represents the weak form of the convective term, i.e.

$$(u, w) = \int_{\Omega} w\,(\mathbf{v} \cdot \nabla u)\, d\Omega \ . \tag{6.10}$$

The test function w can be defined such that

$$(u_h^n, w_h) \coloneqq (u_h^{n*}, N_h) \ , \tag{6.11}$$

where N_h denotes the standard finite element space of continuous shape functions. The test function w_h can be defined as $w_h = N_h + \mathfrak{W}_h$ where $\mathfrak{W}_h(\boldsymbol{\kappa})$ is a wavenumber-dependent enriching function resulting in a low-pass filtering. This approach allows one to follow the rich theoretical works studying the coercivity and convergence of nonconforming FEMs, see Part III of Ref. [197]. The challenge is to either find an explicit definition for $\mathfrak{W}_h(\boldsymbol{\kappa})$ from $H = Q \circledast G$, or to find upper bounds for (u_h^n, w_h) in terms of u_h^{n*}. In-depth analytical work is required to develop the stability theory of the AD-FEM which is out of the scope of this work.

6.2 Over- and Under-Dissipation with ADM

The parametric studies conducted on ADM order and its under-relaxation coefficient, $\omega_{(m-1)}$ suggested that varying the former has a more significant impact on the reconstruction of flow dynamics at scales close to the grid size. When $\omega_{(m-1)}$ is too close to unity or the ADM order is too high, the net effect of deconvolution after filtering, i.e. $\mathcal{F}(Q \circledast G) = \mathcal{Q}\mathcal{G}$, is similar to a filter with a very rapid roll off and yet complete attenuation at the grid cut-off. It still stabilizes the simulation, but it cannot completely prevent aliasing at wavenumbers smaller than the filter cut-off. The result is temporary energy pile-up over a range of wavenumbers slightly lower than the filter cut-off, $\kappa < \kappa_f$. Further evolution of the flow transfers this excess energy towards the grid cut-off where it is removed eventually. This hypothesis is based on the observed oscillations in the energy-based dissipation rate, ϵ_E, obtained for high ADM orders, see Fig. 5–16a for ADM10, or under-relaxation coefficients close to unity, see Fig. 5–19a for $\omega_{(m-1)} = 0.9$.

The rapid roll-off of the energy and enstrophy spectra, Figs. 5–17 and 5–20, near the grid cut-off suggests that the effect of filtering and deconvolution is similar to a wavenumber-dependent hyper viscosity. It denotes that it has the necessary energy drain to allow development of the inertial subrange but does not necessarily mimic the effect of molecular viscosity. To investigate this hypothesis, the empirically modified von Kármán-Kraichnan spectrum model [2] can be tailored such that its roll-off wavenumber range overlaps that of the LES results obtained on $S64$ using $ADM10$ with $\omega_{(m-1)} = 0.8$ and using ADM8 with $\omega_{(m-1)} = 0.9$. To do that, the von Kármán-Kraichnan model is modified as

$$E_m(\kappa) = \frac{3}{2I_1'}\frac{u_0^2}{\kappa_0}\frac{(\kappa/\kappa_0)^4}{\left[1+\frac{12}{5}(\kappa/\kappa_0)^2\right]^{17/6}}e^{-\beta Re^{-3/4}(\kappa/\kappa')^n} \ , \qquad (6.12)$$

where the exponential term is expressed in terms of $(\kappa/\kappa')^n$ rather than κ/κ_0. Larger values of n result in sharper roll-off while larger values of κ' shift the roll-off to higher wavenumbers. Figure 6–2 shows the effect of these two parameters on the LES-like von Kármán-Kraichnan model where $I_1' = I_1$. These modified LES-like spectra are very similar to the kinetic energy spectra obtained from an eddy-damped quasi-normal Markovian analysis for LES (EDQNM-LES) by Berland *et al.* , e.g. Fig. (3) of Ref. [199].

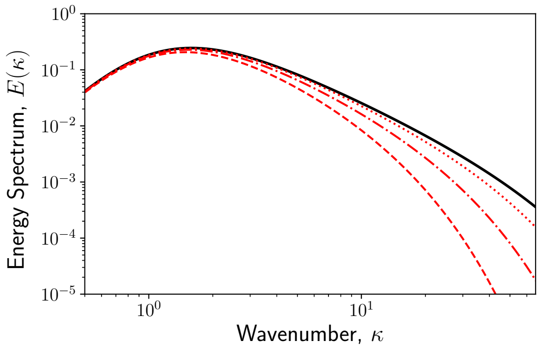

(a)

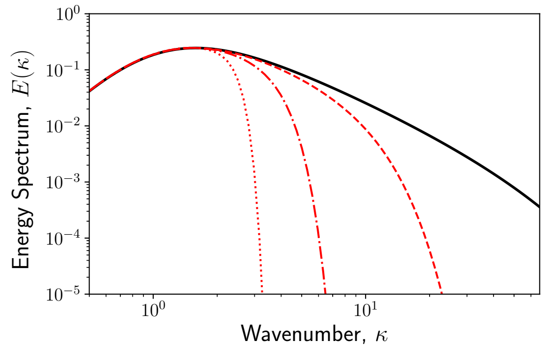

(b)

Figure 6–2: The effect of (a) κ', and (b) n on the LES-like von Kármán-Kraichnan model, Eq. (6.12), where $I_1' = I_1$.

Figure 6–3 illustrates the LES-like von Kármán-Kraichnan model, Eq. (6.12), matched with the LES spectrum from ADM10 and ADM8 and $\omega_{(m-1)} = 0.9$. The spectrum roll-off wavenumber was chosen to match the filter cut-off, i.e. $\kappa' = \kappa_f \approx 22$. The power exponent, $n = 9.8$, was obtained by matching the last resolved roll-off slope, i.e. the slope between $\kappa = 30$ and $\kappa = 31$. Finally, the scaling factor $I_1' = 0.2$ was found by approximately matching the energy content at low wavenumbers $\kappa < 1.0$ with the spectra from LES results.

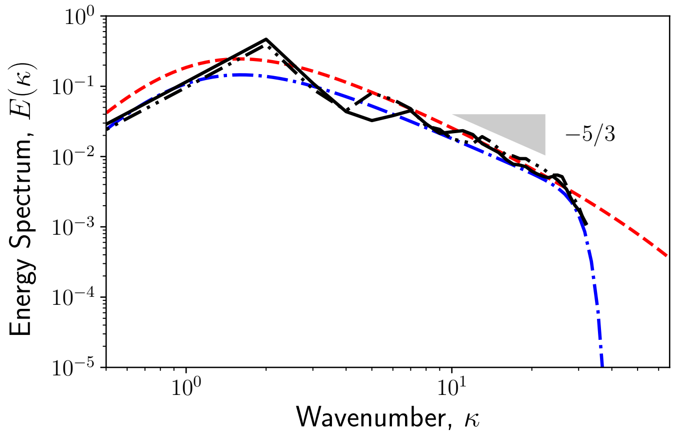

Figure 6–3: The modified LES-like von Kármán-Kraichnan model, Eq. (6.12), matched spectra from ADM10 with $\omega_{(m-1)} = 0.8$ and ADM8 with $\omega_{(m-1)} = 0.9$; $\kappa' = \kappa_f \approx 22$, $I_1' = 0.2$, and $n = 9.8$.

The extremely rapid energy spectrum roll off results in a narrow disspation subrange which may not be able to remove all the energy cascade that surpasses the grid cut-off. Using the EDQNM analysis [200], the time evolution of the kinetic energy spectrum, $E(\kappa)$, for an incompressible freely decaying homogeneous isotropic turbulent flow at a wavenumber κ can be written as

$$\left[\frac{\partial}{\partial t} + 2\nu\kappa^2\right] E(\vec{\kappa}, t) = T(\vec{\kappa}, t) \ , \tag{6.13}$$

where $T(\kappa, t)$ represents the energy transfers due to triadic interactions, i.e. the energy transfer for a given wavenumber $\vec{\kappa}$ with all the wavenumber pairs $(\vec{p}, \vec{q})$ such that they form a triangle, i.e. $\vec{q} = \vec{\kappa} - \vec{p}$. The detailed definition of triadic interaction term, $T(\vec{\kappa}, t)$, can be found in Ref. [122]. The triadic interactions between resolved scales transfer energy to scales which are non-represented, i.e. scales smaller than the grid size, or $\kappa > \kappa_g$. When $|\vec{p}| < \kappa_g$ and $|\vec{q}| < \kappa_g$, representing resolved scales, some of the energy is transferred into the wavenumber $\vec{\kappa}$ knowing that $\vec{\kappa} = \vec{p} + \vec{q}$. As long as the angle between the two wavenumber vectors $\vec{p}$ and $\vec{q}$ is more than 60°, the energy receiving wavenumber vector $\vec{\kappa}$ is beyond the grid cut-off, i.e. $|\vec{\kappa}| = \kappa > \kappa_g$. This is schematically illustrated in Fig. 6–4.

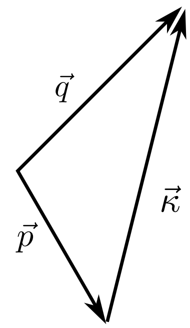

Figure 6–4: Schematics of energy transfer from two small wavenumbers p and q, i.e. large scales, to a large wavenumber κ, i.e. small scales.

This causes aliasing of energy from the wavenumber $\kappa > \kappa_g$, i.e. energy content *appearing* at a wavenumber smaller than the grid cut-off.

Aliasing is the effect that under-sampling a signal causes it to become indistinguishable from another signal. For example, Fig. 6–5 shows how a high frequency sinusoidal (red) signal, when under-sampled, may be conceived as a different sinusoidal signal with lower frequency (blue). If a signal of frequency f is sampled at

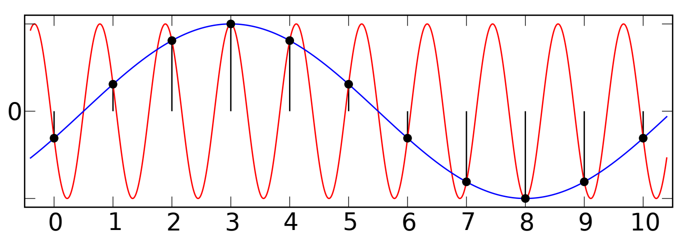

Figure 6–5: Identical sampling results from two different sinusoidal signals.

a frequency f_s, the number of cycles per sample, a.k.a. normalized frequency, is defined as $\widehat{f} = f/f_s$. Family of normalized aliasing frequencies caused by a sampling frequency, f_s, for a given signal with frequency, f, is defined as

$$\widehat{f}_{alias}(N) := \left|\widehat{f} - N\right| \ . \tag{6.14}$$

For example, the sampling frequency in Fig. 6–5 is 1 times per second, i.e. $f_s = 1\ Hz$. The normalized frequencies for red and blue signals are $\widehat{f}_{red} = 0.9\ Hz$, and $\widehat{f}_{blue} = 0.1\ Hz$ respectively, making them $N = 1$ aliases of each other.

According to the Nyquist-Shannon theorem, aliasing will occur when sampling frequency is lower than twice a signal's frequency. In this case, reconstruction of a signal from its samples produces the smallest of aliasing frequencies, e.g. the blue signal in Fig 6–5. When a real-valued signal is sampled by a frequency f_s, its Fourier transform exhibits a symmetry around $f_s/2$ known as *folding* and $f_s/2$ is referred to as *folding frequency*.

Aliasing in wavenumbers is similar to aliasing in frequency. It means that aliasing in LES causes distortion in the energy spectrum by *folding* energy content from subgrid scales to resolved. Any LES needs a mechanism to dissipate the piled-up energy due to folding and to eliminate aliasing errors.

For a computational grid with Δx as its element size, unresolved scales correspond to wavenumbers larger than grid cut-off wavenumber, i.e. $k > k_g = 2\pi/2\Delta x$. This range can be split into the unresolved inertial subrange, i.e.

$$i) \quad k_g < \hat{k} < k_\eta \ , \tag{6.15}$$

and the unresolved dissipation subrange, i.e.

$$ii) \quad \hat{k} > k_\eta \ , \tag{6.16}$$

where $k_\eta = \pi/\eta$, and$\eta \approx l_0 Re^{-3/4}$ are the Kolmogorov dissipation wave number and length scale respectively [86]. Grid cut-off wavenumber, k_g, can be considered as the sampling wavenumber, analogous to sampling frequency f_s, and consequently the *folding wavenumber*. It means that the energy content at wavenumbers above k_g will be folded to lower wavenumbers about k_g. Figure 6–6 demonstrates folding of energy content in the energy spectrum presented in linear and log scales. The wavenumber $k_{\eta'} = k_g - (k_\eta - k_g) = 2k_g - k_\eta$ denotes the aliasing pair of Kolmogorov wavenumber k_η. Aliased energy spectrum,E_a, can be expressed as

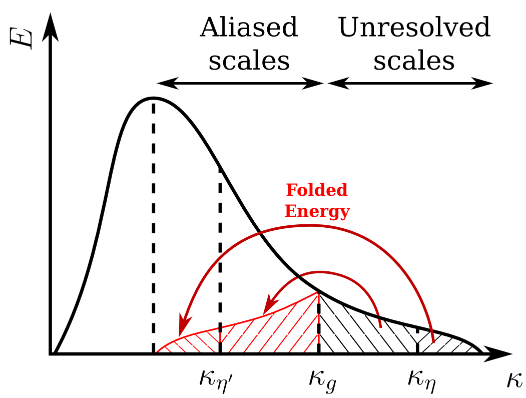

(a)

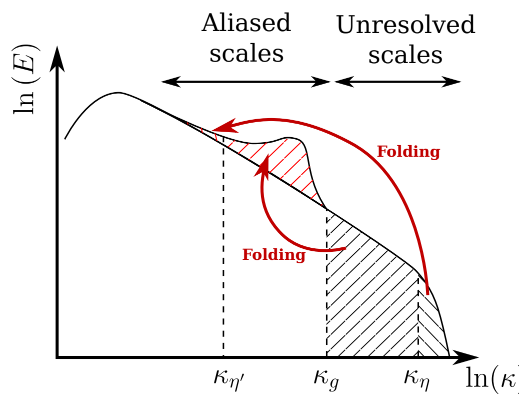

(b)

Figure 6–6: Aliasing error schematically demonstrated as folding of turbulent kinetic energy spectrum in (a) linear scale, and (b) log scale.

$$E_a(\kappa) = E(\kappa) + E'(\kappa) \ , \tag{6.17}$$

where E' is the folded part of the spectrum corresponding to unresolved scales. The net effect of dissipation mechanisms in an LES simulation including dissipation through molecular viscosity, numerical dissipation, and any turbulence modeling (including explicit filtering if any) should be able to eliminate the folded spectrum, i.e. E'.

It should be noted that the net dissipation rate should only remove the aliased energy due to the temporal evolution of the energy spectrum. A not-fully developed energy spectrum does not necessarily have any energy content above the grid cut-off, κ_g, as is the case in the Taylor-Green vortex for $t^* < 5$.

In the case of high ADM orders, e.g. ADM10, or under-relaxation coefficients close to unity, e.g. $\omega_{(m-1)} = 0.9$, the span of the net dissipation is very narrow and cannot remove all the *folded* energy content. This is a numerical artifact which temporarily increases the energy content at some resolved wavenumbers. Subsequently, this energy content is transferred to smaller scales and eventually removed, resulting in non-physical increase in *apparent* energy-based dissipation rates. The importance of avoiding such aliasing, even temporarily, is the spurious noise generation due to energy re-injection into smaller wavenumbers. The observed oscillations in the temporal evolution of the energy-based dissipation rate suggests that the predicted far-field noise spectrum may exhibit some non-physical harmonics.

6.3 Proposed Future Works

The present work demonstrated the development and application of a differential filtering operator on structured and unstructured grids using a continuous Galerkin FEM scheme. The ADM-based FEM (AD-FEM) demonstrated strong stability even at very low Mach numbers, a regime in which the classical continuous Galerkin FEM is well-known to be unstable [140]. A full L_2 stability analysis of the AD-FEM scheme would shed more light on its stability limits. The works of Burman [198] and Clason *et al.* . [197] can be used as a reference for studying the stability and convergence of AD-FEM for transient problems, e.g. the advection diffusion problem.

Investigating the necessary and sufficient conditions for dissipation in an AD-LES is also very interesting. Such a study would open the door to study the existence of an optimal ADM for a given filter. Optimality of an ADM should be clearly defined as there is a trade-off between better reconstruction of flow dynamics near the grid cut-off and the undesirable temporary energy aliasing resulting in oscillations in the estimated energy-based dissipation rate. Studying the effect of such oscillatory behaviors on far-field noise predictions and *potential* appearance of non-physical harmonics would also be valuable in future research.

The presented numerical approach for large-eddy simulations was used for studying the canonical problem of Taylor-Green vortex. Application of this approach for simulation of a high Mach number jet flow using unstructured grids would add significant value to the research community active in the computational aeroacoustics (CAA). It paves the path towards simulation of more complex jet simulations on unstructured grids with better control over the noise foot print of the underlying numerical scheme. Extension of the filter design for wall-bounded flows would be necessary when nozzle geometry is included in the flow simulation.

Finally, the present work used Z-transform to design a *low-pass* spatial filtering operator. A similar approach can be adopted to devise a *high-pass* filter and even a *band-pass* filter for unstructured grids. Band-pass filtering can be used to study the role of coherent structures in sound generation, e.g. subsonic jet noise generation [82, 201, 202].

Appendices

APPENDIX A
Streamline Upwinding Petrov-Galerkin Scheme

In the family of Petrov-Galerkin schemes, the test function is defined as $w_i(x) = N_i(x) + \tau_i \mathcal{H}_i$ where $\mathcal{H}_i$ is a correction function and τ_i is a stabilizing matrix. The weak form of Navier-Stokes equations in Petrov-Galerkin formulation (without shock-capturing) can be expressed in a general stabilization form as

$$\sum_{e=1}^{n_e^{(i)}} \iiint_{\Omega_e} N_i(x) \left[\sum_{j=1}^{n} N_j(x) \frac{\partial \mathbf{U}_j(t)}{\partial t} + \left(\frac{\partial}{x_k} N_j(x) \right) \mathbf{F}_{j,k}(t) \right] d\Omega_e \quad =$$

$$-\sum_{e=1}^{n_e^{(i)}} \iiint_{\Omega_e} \tau_i \mathcal{H}_i(x) \left[\sum_{j=1}^{n} N_j(x) \frac{\partial \mathbf{U}_j(t)}{\partial t} + \left(\frac{\partial}{x_k} N_j(x) \right) \mathbf{F}_{j,k}(t) \right] d\Omega_e \ . \qquad \text{(A.1)}$$

The Streamline Upwind/Petrov-Galerkin (SUPG) is one of the most well-known stabilized FEM methods in this family. It was first developed for advection-diffusion equations and the incompressible Navier-Stokes equations by Brooks and Huges [168, 203, 204], and then to the compressible Navier-Stokes equations [205]. In the compresisble SUPG scheme developed by Shakib *et al.* [205] the correction function is given by

$$\mathcal{H}_i(x) = \mathcal{H}_{SUPG}(x) = \left([\mathbf{A}]_i \frac{\partial N_i}{\partial x} + [\mathbf{B}]_i \frac{\partial N_i}{\partial y} + [\mathbf{C}]_i \frac{\partial N_i}{\partial z} \right) \ . \qquad \text{(A.2)}$$

The matrices $[\mathbf{A}]_i$, $[\mathbf{B}]_i$, and $[\mathbf{C}]_i$ are the inviscid flux Jacobians evaluated at the node i defined as [206]

$$\mathbf{A} = \begin{bmatrix} 0 & 1 & 0 & 0 & 0 \\ -u^2 + \frac{(\gamma-1)}{2}u_iu_i & \Upsilon u_1 & -\chi u_2 & -\chi u_3 & \chi \\ -u_1u_2 & u_2 & u_1 & 0 & 0 \\ -u_1u_3 & u_3 & 0 & u_1 & 0 \\ (\chi u_iu_i - \gamma e_t)u_1 & \gamma e_t - \frac{\chi}{2}(2u_1^2 + u_iu_i) & -\chi u_1u_2 & -\chi u_1u_3 & \gamma u_1 \end{bmatrix}, \tag{A.3}$$

$$\mathbf{B} = \begin{bmatrix} 0 & 0 & 1 & 0 & 0 \\ -u_2u_1 & u_2 & u_1 & 0 & 0 \\ -u_2^2 + \frac{(\gamma-1)}{2}u_iu_i & -\chi u_1 & \Upsilon u_2 & -\chi u_3 & \chi \\ -u_2u_3 & 0 & u_3 & u_2 & 0 \\ (\chi u_iu_i - \gamma e_t)u_2 & -\chi u_2u_1 & \gamma e_t - \frac{\chi}{2}(2u_2^2 + u_iu_i) & -\chi u_2u_3 & \gamma u_2 \end{bmatrix}, \tag{A.4}$$

and

$$\mathbf{C} = \begin{bmatrix} 0 & 0 & 0 & 1 & 0 \\ -u_3u_1 & u_3 & 0 & u_1 & 0 \\ -u_3u_2 & 0 & u_3 & u_2 & 0 \\ -u^3 + \frac{(\gamma-1)}{2}u_iu_i & -\chi u_1 & -\chi u_2 & \Upsilon u_3 & \chi \\ (\chi u_iu_i - \gamma e_t)u_3 & -\chi u_3u_1 & -\chi u_2u_3 & \gamma e_t - \frac{\chi}{2}(2u_3^2 + u_iu_i & \gamma u_3 \end{bmatrix}, \tag{A.5}$$

with $\Upsilon = 3 - \gamma$ and $\chi = \gamma - 1$. Among various forms proposed for the stabilization matrix τ_i [168, 203–205, 207, 208], one of the most commonly used definitions are those of Shakib *et al.* [205] given for entropic variables. Aliabadi *et al.* [209] adopted these definitions for conservative variables and proposed

$$[\tau] = diag(\tau_c, \tau_m, \tau_m, \tau_m, \tau_e) \ , \tag{A.6}$$

where *diag* denotes a diagonal matrix, τ_c is the stabilization parameter for the continuity equation, τ_m for the momentum equations and τ_e is for the energy equation. These parameters are given by

$$\tau_c = \left(\frac{1}{\left(\tau_c^{(1)}\right)^r} + \frac{1}{\left(\tau_c^{(2)}\right)^r} \right)^{-1/r} , \tag{A.7}$$

$$\tau_m = \left(\frac{1}{\left(\tau_m^{(1)}\right)^r} + \frac{1}{\left(\tau_m^{(2)}\right)^r} + \frac{1}{\left(\tau_m^{(3)}\right)^r} \right)^{-1/r} , \tag{A.8}$$

and

$$\tau_e = \left(\frac{1}{\left(\tau_e^{(1)}\right)^r} + \frac{1}{\left(\tau_e^{(2)}\right)^r} + \frac{1}{\left(\tau_e^{(3)}\right)^r} \right)^{-1/r} , \tag{A.9}$$

where r is the switching factor [208] and typically $r = 2$. The terms $\tau^{(1)}$, $\tau(2)$, and $\tau^{(3)}$ represent the advection-dominated, the transient-dominated, and the diffusion-dominated limits respectively. These parameters are defined element-wise. The advection-dominated limit parameters, $\tau^{(1)}$, are given by

$$\tau_c^{(1)} = \tau_m^{(1)} = \tau_e^{(1)} = \left(\sum_j \left(c|\mathbf{r}_\rho \cdot \nabla N_j| + |\mathbf{u} \cdot \nabla N_j| \right) \right)^{-1} , \tag{A.10}$$

where

$$\mathbf{r}_\rho = \frac{\nabla \rho}{\|\nabla \rho\|} \ , \tag{A.11}$$

and c is the acoustic speed. The transient-dominated limit parameters, $\tau^{(2)}$, are given by

$$\tau_c^{(2)} = \tau_m^{(2)} = \tau_e^{(2)} = \frac{\Delta t}{2} \ . \tag{A.12}$$

The diffusion-dominated limit parameters, $\tau^{(3)}$, are given by

$$\tau_m^{(2)} = \frac{\rho h_{\mathbf{u}}^2}{4\mu} \ , \tag{A.13}$$

and

$$\tau_e^{(2)} = \frac{\rho c_p h_e^2}{4k} \ . \tag{A.14}$$

The element-wise flow-aligned length scale, $h_{\mathbf{u}}$, is defined as

$$h_{\mathbf{u}} = 2 \left(\sum_j |\mathbf{r}_{\mathbf{u}} \cdot \nabla N_j| \right)^{-1} \ , \tag{A.15}$$

where

$$\mathbf{r}_{\mathbf{u}} = \frac{\nabla \|\mathbf{u}\|}{\|\nabla \|\mathbf{u}\|\|} \ , \tag{A.16}$$

is the unit vector along the gradient of the velocity magnitude. The element-wise temperature-aligned length scale, h_e, is given by

$$h_e = 2 \left(\sum_j |\mathbf{r}_e \cdot \nabla N_j| \right)^{-1} \ , \tag{A.17}$$

where

$$\mathbf{r}_e = \frac{\nabla T}{\|\nabla T\|} \ , \tag{A.18}$$

is the unit vector along the gradient of the temperature. The unit vectors $\mathbf{r_u}$ and $\mathbf{r}_e$ are calculated within an element by using

$$\nabla \|\mathbf{u}\| = \sum_j (\nabla N_j) \|u\|_j \ , \tag{A.19}$$

and

$$\nabla T = \sum_j (\nabla N_j) T_j \ . \tag{A.20}$$

APPENDIX B
Taylor-Galerkin Schemes and Its Generalization

This appendix is adopted from a published article by Najafiyazdi *et al.* [139] in the International Journal of Aeroacoustics, 2018 with permission from the authors.

Introduction

In finite element methods (FEM), Galerkin/Runge-Kutta schemes are prone to exhibit node-to-node oscillations, which may lead to spurious wave packets and eventually numerical instabilities [210]. Taylor-Galerkin (TG) schemes [211] have been proposed as a solution to overcome this challenge. They are usually less dissipative than common implementations of SUPG and least square families [212]. Taylor-Galerkin schemes have been successfully used on unstructured grids for various aeroacoustics applications, including jet noise predictions [213–216]. The accuracy was comparable to that of high-order compact schemes on structured grids [217]. The major challenge in the implementation of Taylor-Galerkin schemes is the presence of time derivatives of order two and higher in the temporal integration algorithm. For a general partial differential equation of the form

$$\partial_t u = \mathcal{L}(u)\,, \tag{B.1}$$

a second-order temporal derivative, i.e. $\partial_{tt} u$, is substituted with $\partial_t \mathcal{L}(u)$. For convection-diffusion problems, this term would yield fourth-order spatial derivatives from diffusion terms, and flux Jacobians from non-linear convection terms. It becomes even more challenging for TG schemes when third- and fourth-order temporal derivatives appear that must be evaluated based on the spatial derivatives using $\mathcal{L}(u)$.

Taylor-Galerkin Schemes

The Euler-Taylor-Galerkin (ETG) scheme was first developed by Donea [211]. A Taylor expansion was used to march from t_n to t_{n+1},

$$u^{n+1} = u^n + \Delta t\,(\partial_t u)^n + \frac{1}{2!}\Delta t^2\,(\partial_{tt} u)^n + \frac{1}{3!}\Delta t^3\,(\partial_{ttt} u)^n + \cdots\,, \tag{B.2}$$

for an arbitrary variable, u. Time derivatives were then replaced by terms with spatial derivatives. For example, the one-dimensional advection equation

$$\partial_t u + c\partial_x u = 0\,, \tag{B.3}$$

yields

$$\partial_{tt} u = c^2 \partial_{xx} u\,, \tag{B.4}$$

for the second time derivative, and

$$\partial_{ttt} u = c^2 \partial_{xx}\left(\partial_t u\right)\,, \tag{B.5}$$

for the third time derivative. Donea substituted the time derivative in Eq. (B.5)) with a backward finite difference (Euler) approximation as

$$\begin{aligned} \partial_{ttt} u &= c^2 \partial_{xx}\left(\partial_t u\right) && \text{(B.6)} \\ &\approx c^2 \partial_{xx}\left(\frac{u^{n+1} - u^n}{\Delta t}\right)\,. && \text{(B.7)} \end{aligned}$$

Substitution of Eq. (B.3)– (B.6) into Eq. (B.2)) yields the semi-discrete equation

$$\left(1 - \frac{c^2 \Delta t^2}{6} \partial_{xx}\right) \left(\frac{u^{n+1} - u^n}{\Delta t}\right) = -c \partial_x u^n + \frac{c^2 \Delta t}{2} \partial_{xx} u^n \,. \tag{B.8}$$

The application of a weak Galerkin discretization with linear elements results in the fully discretized Euler Taylor-Galerkin (ETG) equation

$$\left[M - \frac{1}{6} C^2 \delta^2\right] \left(u_j^{n+1} - u_j^n\right) = -C \Delta_0 u_j^n + \frac{1}{2} C^2 \delta^2 u_j^n \,, \tag{B.9}$$

where $C = c\Delta t / \Delta x$ is the Courant-Friedrichs-Lewy (CFL) number, Δ_0 and δ^2 are the centered first- and second-order spatial difference operators, and M is the mass matrix defined as

$$\Delta_0 u_i = \frac{1}{2} \left(u_{i+1} - u_{i-1}\right) \,, \tag{B.10}$$

$$\delta^2 u_i = u_{i+1} - 2u_i + u_{i-1} \,, \tag{B.11}$$

and

$$M u_i = \frac{1}{6} \left(u_{i+1} + 4u_i + u_{i-1}\right) \,. \tag{B.12}$$

The CFL stability condition is $C < 1$ for one-dimensional, $C < 1/2$ for two-dimensional, and $C < 1/3$ for three-dimensional simulations [211].

Quartapelle *et al.* [218] developed two-step Taylor-Galerkin schemes, TTG3 and TTG4A to alleviate the need to approximate the third-order time derivatives. The time marching algorithm was defined as

$$
\begin{aligned}
\tilde{u}^n &= u^n + \frac{1}{3}\Delta t \partial_t u^n + \alpha \Delta t^2 \partial_{tt} u^n \,, && \text{(B.13)} \\
u^{n+1} &= u^n + \Delta t \partial_t u^n + \frac{1}{2}\Delta t^2 \partial_{tt} \tilde{u}^n \,, && \text{(B.14)}
\end{aligned}
$$

where $\alpha = 1/9$ yields the third-order scheme TTG3, and $\alpha = 1/12$ yields the fourth-order scheme TTG4A.

Colin and Rudgyard [212] showed that the accuracy of the ETG, TTG3, and TTG4A schemes is insufficient for LES applications due to dissipation at intermediate wavenumbers. They consequently proposed a new class of two-step Taylor-Galerkin schemes (TTGC); in which the time-marching stages are defined as

$$
\begin{aligned}
\tilde{u}^n &= u^n + \alpha \Delta t \partial_t u^n + \beta \Delta t^2 \partial_{tt} u^n \,, && \text{(B.15)} \\
u^{n+1} &= u^n + \Delta t \left(\theta_1 \partial_t u^n + \theta_2 \partial_t \tilde{u}^n\right) + \Delta t^2 \left(\epsilon_1 \partial_{tt} u^n + \epsilon_2 \partial_{tt} \tilde{u}^n\right) \,, && \text{(B.16)}
\end{aligned}
$$

where $\alpha, \beta, \theta_1, \theta_2, \epsilon_1$, and ϵ_2 are free parameters. The TTG4A and TTG3 schemes are special cases of the TTGC family with $\theta_2 = \epsilon_1 = 0$, $\theta_1 = 1, \epsilon_2 = 1/2$, $\alpha = 1/3$, $\beta = 1/9$ for TTG3, and $\beta = 1/12$ for TTG4A.

Colin and Rudgyard [212] considered four criteria for their scheme (TTGC3): first, it should provide at least third-order accuracy in time; second, it should have non-zero dissipation at the highest wavenumber, $k\Delta x = \pi$; third, it should reduce the need to calculate $\partial_{tt} u^n$ only for the first step; and fourth, it should remove the additional cost for storing $\partial_t u^n$ in the second step. To satisfy all these conditions, they imposed $\theta_2 = 1, \theta_1 = \epsilon_2 = 0, \alpha = 1/2 - \gamma$ and $\beta = 1/6$ and $\epsilon_1 = \gamma$ with the user-defined parameter $\gamma \in [0, 1]$. They suggested that $0 \leq \gamma \leq 0.2$ yields acceptable CFL limits.

Numerical challenges with Taylor-Galerkin schemes

The replacement of temporal derivatives with spatial derivatives is highly challenging in the case of multidimensional non-linear problems, especially for convection-diffusion problems [219]. There are two sources of complexity in Taylor-Galerkin schemes, especially for non-linear equations, e.g. Euler and Navier-Stokes. Firstly, flux Jacobians appear in the substitution of second-order time derivatives. Secondly, the mass matrix is modified due to the third-order time derivative approximation.

Jacobian Matrices and Substitution of Time Derivatives

Consider the following general governing equation,

$$\partial_t u = \mathcal{L}\left(u\right) \,, \tag{B.17}$$

where $\mathcal{L}(\cdot)$ is a spatial differential operator representing the right hand side of the equation. In FEM, the Galerkin formulation of spatial derivatives yields integrals that include the spatial derivatives of element shape functions and the test function. For an arbitrary node (i), the Eq. (B.17) is written in the weak form as

$$\begin{aligned} \langle \psi_i, \partial_t u_i^n \rangle &= \langle \psi_i, \mathcal{L}\left(u_i^n\right) \rangle \\ &= \int_\Omega \psi_i \mathcal{L}\left(u_i^n\right) d\Omega \,, \end{aligned} \tag{B.18}$$

where $\langle \cdot, \cdot \rangle$ is the inner product operator in $L^2(\Omega)$ space, ψ_i is the test function having compact support, i.e. nonzero only in the elements around the node (i) denoted by Ω_i, and Ω denotes the entire computational domain. A weak projection is also applied on the Taylor expansion in time, Eq. (B.2), which yields

$$\left\langle \psi_i, u_i^{n+1} \right\rangle = \langle \psi_i, u_i^n \rangle + \langle \psi_i, \Delta t \, (\partial_t u)_i^n \rangle + \left\langle \psi_i, \Delta t^2 \, (\partial_{tt} u)_i^n \right\rangle + \cdots . \tag{B.19}$$

To estimate the second time derivative, one can write

$$\begin{aligned} \partial_{tt} u &= \partial_t \left(\mathcal{L}(u) \right) \\ &= \partial_u \mathcal{L}(u) \partial_t u \, , \end{aligned} \tag{B.20}$$

where $\partial_u \mathcal{L}(u)$ is the Jacobian of $\mathcal{L}(\cdot)$ with respect to u.

The choice of element order is mainly based on the level of accuracy required to calculate integrations in the integrals on the right hand side of Eq. (B.18). Second- and higher-order temporal derivatives terms become highly non-linear when substituted with spatial derivatives terms, more so than the discretized governing equation itself. For example, the integration of the weak Galerkin form of Eq. (B.20), i.e.

$$\langle \psi, \partial_{tt} u \rangle = \langle \psi, \partial_u \mathcal{L}(u) \cdot \mathcal{L}(u) \rangle \ , \tag{B.21}$$

requires the element shape functions and the test function ψ to be polynomials of orders higher than that required for the integration of the original governing Eq. (B.18). It is because second-order spatial derivative operators are multiplied in the term $\partial_u \mathcal{L}(u) \cdot \mathcal{L}(u)$ and even the commonly used separation by parts technique cannot reduce the order of spatial derivatives. Consequently, the basis functions are required to be at least C^2 rather than C^1. The derivations required for the substitution of higher-order temporal derivatives can be mathematically tedious, involving the calculation of many terms [220] due to the second- and higher-order Jacbians, i.e. $\partial^j \mathcal{L}(u)/\partial u^j$ for $j \geq 2$.

Higher order basis polynomials enforce more quadrature points for accurate numerical integration. Kirby and Karniadakis [6] showed that the integration of non-linear flux terms in the weak form requires $3(N+1)/2$ Gauss-Lobatto-Legendre (GLL) quadrature points for incompressible and $2(N+1)$ for compressible Navier-Stokes equations, where N is the polynomial order element shape functions. This is commonly recognized as "over-integration", "consistent integration" or "super-collocation" in the discontinuous Galerkin (DG) and spectral FEM.

Three-dimensional computation costs would be significantly high for so many function evaluations. However, if over-integration is not used, spurious oscillations and numerical instability eventually appear in the solution, biasing the kinetic energy content at high wavenumbers.

The calculation of Jacboian terms is also numerically expensive as they form dense matrices and include transformations from the physical space to the local space. Ref. [212] provides extensive mathematical derivations for Jacobian matrices related to the second-order temporal derivative in the Euler equations on linear (triangle, tetrahedron) and bi-linear (quadrilateral, hexahedron) elements.

The need for numerical de-aliasing, and computationally expensive Jacobian calculations suggests that it is more desirable to reduce the number of second-order temporal derivatives in multi-stage Taylor-Galerkin (TTG and TTGC) schemes than to calculate them from high order spatial derivatives of the governing equations.

Third-Order Time Derivative Approximation and Modified Mass Matrix

In some Taylor-Galerkin schemes, such as ETG [211], Lax-Wendroff Taylor-Galerkin (LWTG) [221], and Lax-Friedrich Taylor-Galerkin (LFTG) [221], the third-order temporal derivative is approximated as shown in Eq. (B.6). It modifies the mass matrix, as seen in Eqs. (B.6)–(B.9). A modified mass matrix, e.g. $M - 1/6C^2\delta^2$ in Eq. (B.9), usually requires an update at every time step in Euler and Navier-Stokes equations resulting in excessive computational cost. The presence of even higher-order temporal derivatives exacerbates this problem.

A multi-stage (MS) formulation could circumvent the aforementioned difficulties through the introduction of additional intermediate stages. This general idea yields a set of time-integration schemes from existing Taylor-Galerkin schemes (e.g. TTG3, TTGC3, and TTG4A), to Runge-Kutta methods.

Multi-Stage (MS) Formulation for Taylor-Galerkin Schemes

In order to obtain formulations suitable for FEM, a multi-stage approach was adopted from Donea *et al.* [219]. The original approach was to re-write Padé-type methods such that each stage includes only the first-order temporal derivative. In Padé-type methods, time marching is achieved by first re-writing the temporal Taylor-series in terms of an exponential function

$$u^{n+1} = \left(1 + \Delta t \frac{\partial}{\partial t} + \frac{1}{2!}\Delta t^2 \frac{\partial^2}{\partial t^2} + \cdots \right) u^n = \exp\left(\Delta t \frac{\partial}{\partial t}\right) u^n \,. \tag{B.22}$$

The exponential term is evaluated using Padé approximation, i.e.

$$\exp(x) \approx \frac{P_L(x)}{Q_M(x)}\,, \tag{B.23}$$

where $P_L(x)$ and $Q_M(x)$ are polynomials of order L and M respectively, and $x = \Delta t\frac{\partial}{\partial t}$. It is used to re-write Eq. (B.22) in an implicit form as

$$Q_M(\Delta t\frac{\partial}{\partial t})u^{n+1} = P_L(\Delta t\frac{\partial}{\partial t})u^n\,. \tag{B.24}$$

Donea *et al.* [219] used nested factorization for P_L and Q_M polynomials. An arbitrary polynomial $f_m(x)$ of order m can be written in a nested factorization form with non-zero coefficients w_i and $w_0 = 1$ as

$$f(x) \;=\; \sum_{i=0}^{L} w_i x = 1 + w_1 x\left(1 + \frac{w_2}{w_1}x\,(\cdots)\right). \tag{B.25}$$

It can be re-written in a multi-stage formulation as

$$f^{(0)} \;=\; 1\,, \tag{B.26}$$

$$f^{(i)} \;=\; 1 + \frac{w_i}{w_{i-1}} f^{(i-1)}(x) \qquad \text{for } i = 1, \cdots, m \quad , \tag{B.27}$$

$$f(x) \;=\; f^{(m)}\,. \tag{B.28}$$

Approximate temporal integration is performed by choosing the independent variable, x, to be $x = \Delta t\frac{\partial}{\partial t}$. At each stage, $\frac{w_i}{w_{i-1}} f^{(i-1)}$ is readily available from a previous stage and $\frac{\partial u}{\partial t}$ is substituted with $\mathcal{L}(u)$. Most explicit time integration schemes such as explicit Runge-Kutta schemes, and even some multi-stage implicit schemes, e.g. that of Harten *et al.* [222], can be cast into this formulation. This approach allows for use of C^0 finite elements for the spatial discretization of $\mathcal{L}(u)$ with spatial derivatives up to second order.

Starting from the general two-stage formulation by Colin and Rudgyard [212] (TTGC), Eqs. (B.15)–(B.16), each stage can be written as a series of nested derivatives. For a non-zero parameter, α, Eq. (B.15) is then re-written in the form

$$\tilde{u}^n = u^n + \alpha \Delta t \partial_t \left[u^n + \frac{\beta}{\alpha} \Delta t \partial_t u^n \right] . \tag{B.29}$$

Division into two stages and substitution in Eq. (B.15) yields

$$u^{(1)} = u^n + \frac{\beta}{\alpha} \Delta t \partial_t u^n , \tag{B.30}$$

$$u^{(2)} = u^n + \alpha \Delta t \partial_t u^{(1)} \tag{B.31}$$

$$u^{n+1} = u^n + \Delta t \left(\theta_1 \partial_t u^n + \theta_2 \partial_t \tilde{u}^n \right) + \Delta t^2 \left(\epsilon_1 \partial_{tt} u^n + \epsilon_2 \partial_{tt} u^{(2)} \right) , \tag{B.32}$$

where second-order temporal derivatives, $\partial_{tt} u^n$ and $\partial_{tt} u^{(2)}$, are replaced by spatial derivatives to yield a family of three-stage TG schemes (TGN-1). This formulation eliminates the second-order temporal derivative in the first stage. Only one of the remaining second-order temporal derivatives, i.e. $\partial_{tt} u^n$ or $\partial_{tt} u^{(2)}$, can be further divided into additional stages. If both are treated similarly, the TG scheme will transform into a Runge-Kutta scheme [139]. An alternative formulation (TGN-2) is obtained by keeping the second-order time derivative in the first stage, Eq. (B.15), and splitting the second-order temporal derivatives in the second stage, Eq. (B.16). The TGN-1 formulation for TTG3 (TTGN3-1) and TTG4A (TTGN4A-1) are derived as

$$u^{(1)} = u^n + 3\beta\Delta t\partial_t u^n \tag{B.33}$$

$$u^{(2)} = u^n + \alpha\Delta t\partial_t u^{(1)} \tag{B.34}$$

$$u^{n+1} = u^n + \Delta t\partial_t u^n + \frac{1}{2}\Delta t^2\partial_{tt}u^{(2)}\,, \tag{B.35}$$

where $\beta = 1/3$ for TTG3, and $\beta = 1/12$ for TTG4A. The TGN-1 form of TTGC3 (TTGNC3-1) is defined as

$$u^{(1)} = u^n + \frac{1}{6\alpha}\Delta t\partial_t u^n \tag{B.36}$$

$$u^{(2)} = u^n + \alpha\Delta t\partial_t u^{(1)} \tag{B.37}$$

$$u^{n+1} = u^n + \Delta t\partial_t u^{(2)} + \gamma\Delta t^2\partial_{tt}u^n\,, \tag{B.38}$$

where $\alpha = 1/2 - \gamma$. Similarly, the TGN-2 formulations, TTGN3-2 TTGN4A-2, are given as

$$u^{(1)} = u^n + \frac{1}{3}\Delta t\partial_t u^n + \beta\Delta t^2\partial_{tt}u^n\,, \tag{B.39}$$

$$u^{(2)} = u^{(1)} + \Delta t\partial_t u^{(1)}\,, \tag{B.40}$$

$$u^{n+1} = u^n + \Delta t\partial_t u^n - \frac{1}{2}\Delta t\partial_t u^{(1)} + \frac{1}{2}\Delta t\partial_t u^{(2)}\,. \tag{B.41}$$

The TTGNC3-2 scheme is defined as

$$u^{(1)} = u^n + \alpha\Delta t\partial_t u^n + \frac{1}{6}\Delta t^2\partial_{tt}u^n\,, \tag{B.42}$$

$$u^{(2)} = u^n + \Delta t\partial_t u^n\,, \tag{B.43}$$

$$u^{n+1} = u^n - \gamma\Delta t\partial_t u^n + \Delta t\partial_t u^{(1)} + \gamma\Delta t\partial_t u^{(2)}\,. \tag{B.44}$$

von Neumann Analysis

To demonstrate that the MS formulation preserves the order of accuracy, a von Neumann analysis was performed for the TTGNC3-1 scheme applied on the linear advection equation with fixed speed, a, i.e.

$$\partial_t u = -a\partial_x u\,. \tag{B.45}$$

The application of the weak Galerkin method on 1D linear elements for spatial discretization and TTGNC3-1 for time integration yields

$$\begin{aligned}
Mu_i^{(1)} &= Mu_i^n - \frac{1}{6\alpha}C\Delta_0 u_i^n\,, && \text{(B.46)}\\
Mu_i^{(2)} &= Mu_i^n - \alpha C\Delta_0 u^{(1)}\,, && \text{(B.47)}\\
Mu_i^{n+1} &= Mu_i^n - C\Delta_0 u^{(2)} + \gamma C^2\delta^2 u^n\,. && \text{(B.48)}
\end{aligned}$$

where $C = a\Delta t/\Delta x$ is the CFL number. The Fourier transform of Eqs. (B.46)–(B.48) yields the amplification factors

$$\begin{aligned}
z^{(1)} &= 1 - \frac{1}{6\alpha}\frac{C\hat{\Delta}_0}{\hat{M}}\,, && \text{(B.49)}\\
z^{(2)} &= 1 - \alpha\frac{C\hat{\Delta}_0}{\hat{M}}z(1)\,, && \text{(B.50)}\\
z &= 1 - \frac{C\hat{\Delta}_0}{\hat{M}}z^{(2)} + \gamma\frac{C^2\hat{\delta}^2}{\hat{M}}\,, && \text{(B.51)}
\end{aligned}$$

where $\hat{\Delta}_0$, δ^2 and $\hat{M}$ are defined as

$$\hat{\Delta}_0(p) = i\sin(p)\,, \tag{B.52}$$

$$\hat{\delta}^2(p) = -4\sin^2(\frac{p}{2})\,, \tag{B.53}$$

and

$$\hat{M}(p) = 1 - \frac{2}{3}\sin^2(\frac{p}{2})\,, \tag{B.54}$$

with $p = k\Delta x$ as the normalized wavenumber, and $i = \sqrt{-1}$. The substitution of Eqs. (B.49)–(B.50) into Eq. (B.51) and a Taylor expansion to the fifth-order yields

$$z(p) = 1 - Cpi - \frac{C^2p^2}{2} + \frac{C^3P^3}{6}i + \frac{C^5p^5}{180}i + \mathcal{O}(p^6)\,. \tag{B.55}$$

A comparison between Eq. (B.55) and the Taylor expansion of the analytical amplification factor,

$$z_a(p) = 1 - Cpi - \frac{C^2p^2}{2!} + \frac{C^3P^3}{3!}i + \frac{C^4p^4}{4!}i + \mathcal{O}(p^5)\,, \tag{B.56}$$

shows that the TTGNC3-1 scheme is accurate up to the third-order in space. To demonstrate that the implemented scheme is truly third order, a grid convergence study was conducted for simulating convection of a subsonic Gaussian density distribution.

Figures B.1 and B.2 compare dissipation and dispersion errors of TTGN-1 and TTGN-2 schemes at $CFL = 0.7$, respectively, to that of the original TTG3, TTGC3, and TTG4A schemes as well as Shu & Osher's third-order RK method. The dissipation and dispersion errors of TTGNC3-2 are nearly identical to those of the original

TTGC3 scheme. This means that the dissipation at intermediate wavelengths, i.e. $2\Delta x < \lambda < 8\Delta x$, is mostly due to the term $\partial_{tt}u^n$ in Eq. (B.42); while the dissipation at grid cut-off, $\lambda = 2\Delta x$, needed for the attenuation of node-to-node oscillations originates from the term $\partial_{tt}u^n$ in Eq. (B.38), as shown by the dissipation error for TTGNC3-1. In multi-stage time-integration schemes, the last few stages are analogous to the highest modes in a Fourier series. When the spatial derivative terms appear in an intermediate stage, the dissipation appears in moderate wavenumbers. Similarly, spatial derivatives in the last stage mainly affect near grid cut-off wavenumbers.

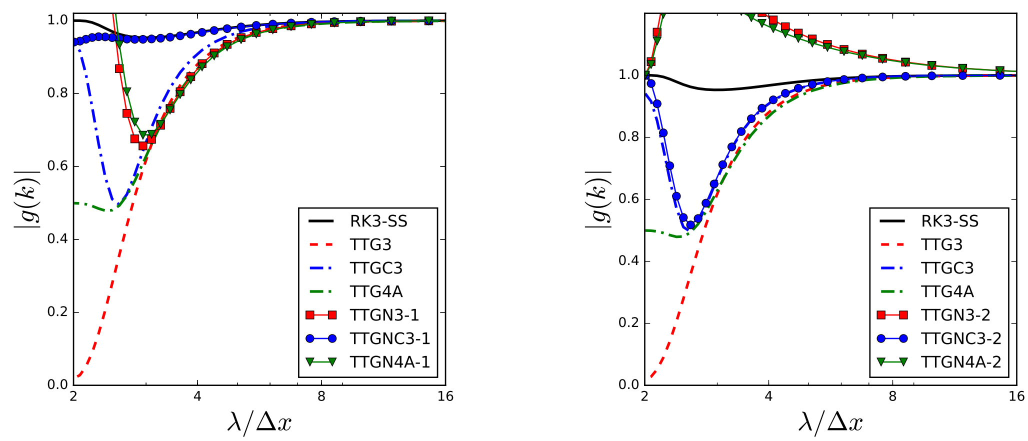

(a) TTGN-1

(b) TTGN-2

Figure B.1: Dissipation errors for (a) TTGN-1 and (b) TTGN-2 schemes compared with their original formulation and Shu & Osher's third-order RK method at $CFL = 0.7$.

In terms of its potential for the stabilization of FEM through the damping of node-to-node oscillations, it seems that TTGNC3-1 is the most suitable choice among all TGN schemes presented here. The dissipation error for TTGNC3-1 is very similar to that of a third-order Runge-Kutta scheme for wavelengths as small as $\lambda = 3\Delta x$. The

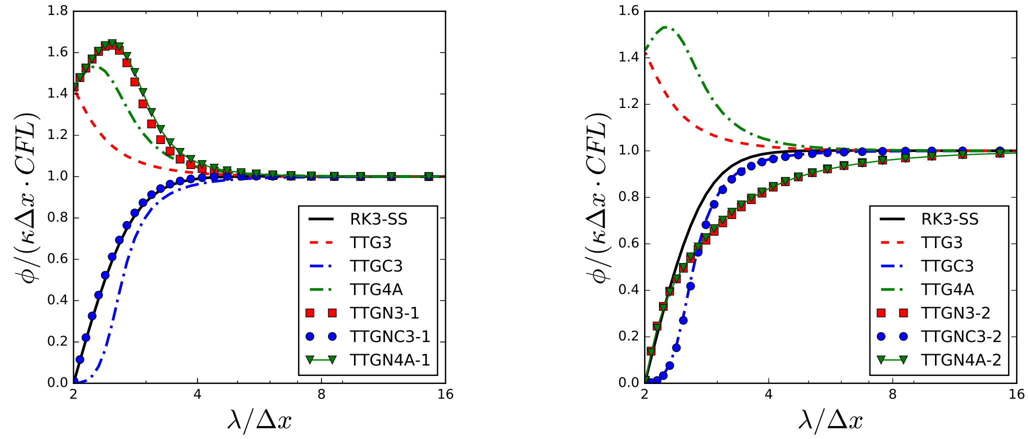

(a) TTGN-1 (b) TTGN-2

Figure B.2: Dispersion errors for (a) TTGN-1 and (b) TTGN-2 schemes compared with their original formulation and Shu & Osher third-order RK method at $CFL = 0.7$.

new scheme provides the same level of attenuation at grid cut-off, $\lambda = 2\Delta x$, as the original TTGC3 scheme by Colin and Rudgyard [212]. The TTGNC3-1 scheme's dispersion error is even slightly smaller than that of third-order Runge-Kutta schemes, making it suitable for aerocoustics applications.

The dissipation and dispersion errors of the TTGNC3-1 scheme are compared against those of the original TTGC3 scheme at different CFL numbers for a fixed $\gamma = 0.01$ in Fig. B.3, and for various γ at a fixed $CFL = 0.3$ in Fig. B.4. These results exhibit the low dissipation and low dispersion properties of a Runge-Kutta scheme and the non-zero attenuation at the grid cut-off of a Taylor-Galerkin scheme. Therefore, the TTGNC3-1 scheme can be considered as a low-dissipation low-dispersion Taylor-Galerkin (LDDTG) scheme. The TTGNC3-1 CFL condition is smaller than that of TTGC3 for $\gamma < 0.4$ as seen in Fig. B.5. A range of $0 < \gamma < 0.05$ should allow simulations at practical CFL numbers.

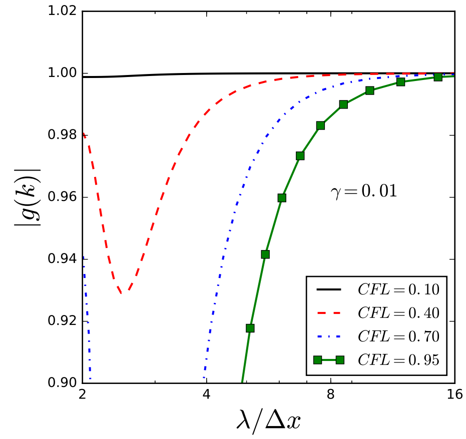

(a) TTGC3

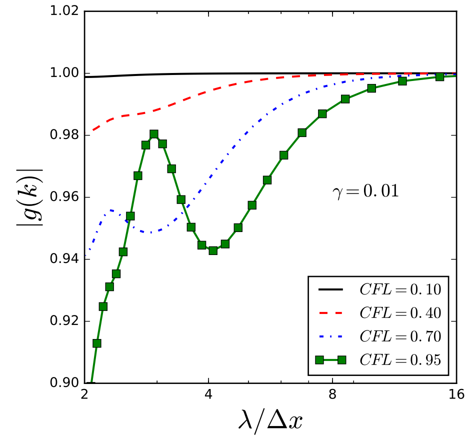

(b) TTGNC3-1

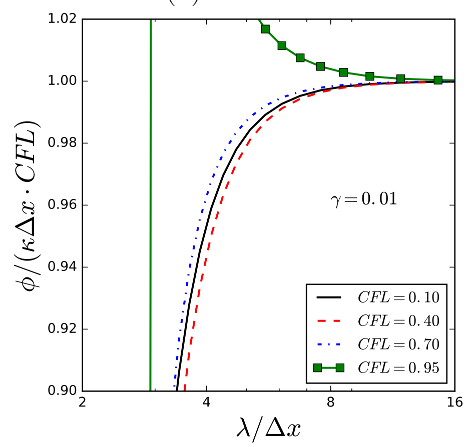

(c) TTGC3

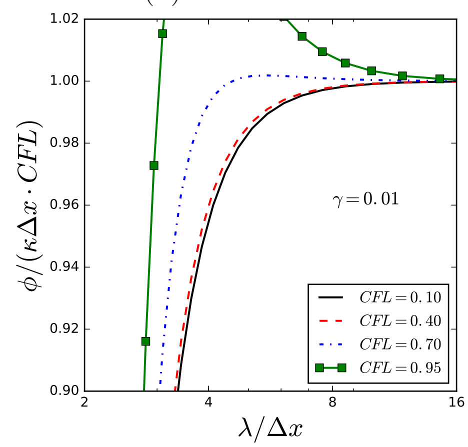

(d) TTGNC3-1

Figure B.3: Dissipation errors for (a) TTGC3 and (b) TTGNC3-1 schemes; Dispersion errors for (c) TTGC3 and (d) TTGNC3-1 at different CFL values and $\gamma = 0.01$.

Runge-Kutta-based high-Order Taylor-Galerkin schemes

The multi-stage approach introduced in the previous section suggested a reverse approach for developing high-order Taylor-Galerkin schemes while avoiding the challenging third- and higher-order temporal derivatives.

The last two stages of a Runge-Kutta scheme can be combined into a single stage in

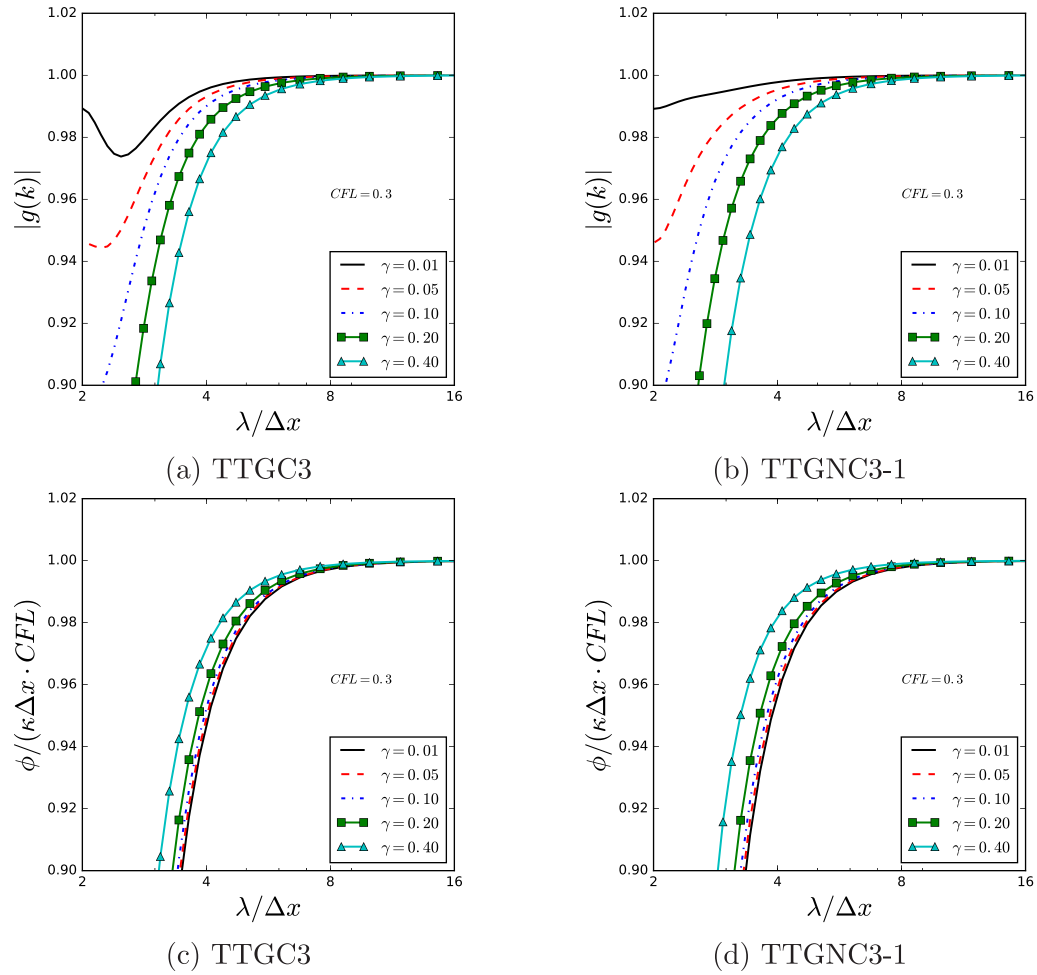

(a) TTGC3 (b) TTGNC3-1

(c) TTGC3 (d) TTGNC3-1

Figure B.4: Dissipation errors for (a) TTGC3 and (b) TTGNC3-1 schemes; Dispersion errors for (c) TTGC3 and (d) TTGNC3-1 at different γ values and $CFL = 0.3$.

which second-order temporal derivatives appear. This manipulation yields a Taylor-Galerkin scheme of the same order of accuracy, with some dissipation at the grid cut-off to remove node-to-node oscillations.

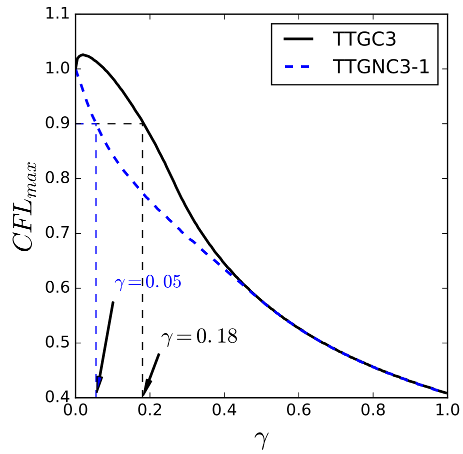

Figure B.5: Stability region for TTGNC3-1 compared with TTGC3.

To demonstrate this approach, a Taylor-Galerkin scheme was derived from the standard fourth-order Runge-Kutta scheme (RK4). Combining the last two stages yields

$$u^{(1)} = u^n + \frac{1}{2}\Delta t \partial_t u^n \,, \tag{B.57}$$

$$u^{(2)} = u^n + \frac{1}{2}\Delta t \partial_t u^{(1)} \,, \tag{B.58}$$

$$\begin{aligned} u^{n+1} = {} & u^n + \frac{1}{6}\Delta t \partial_t u^n + \frac{1}{3}\Delta t \partial_t u^{(1)} + \frac{1}{3}\Delta t \partial_t u^{(2)} + \\ & \frac{1}{6}\Delta t \partial_t u^n + \frac{1}{6}\Delta t^2 \partial_{tt} u^{(2)} \,. \end{aligned} \tag{B.59}$$

Figur B.6 compares the dissipation and dispersion errors at $CFL = 0.9$ for RK4 with those of its corresponding Taylor-Galerkin scheme, TGN-RK4. The stability condition for TGN-RK4 is $CFL \leq 1$.

Figure B.7 shows the dissipation and dispersion errors for the third-order three-stage RK scheme developed by Shu & Osher [223] (SSRK3), and its corresponding TG scheme (TGN-SSRK3) at $CFL = 0.7$. The stability condition for TGN-SSRK3 is $CFL \leq 0.707$, in contrast to $CFL < 1.0$ for the original SSRK3 scheme. The

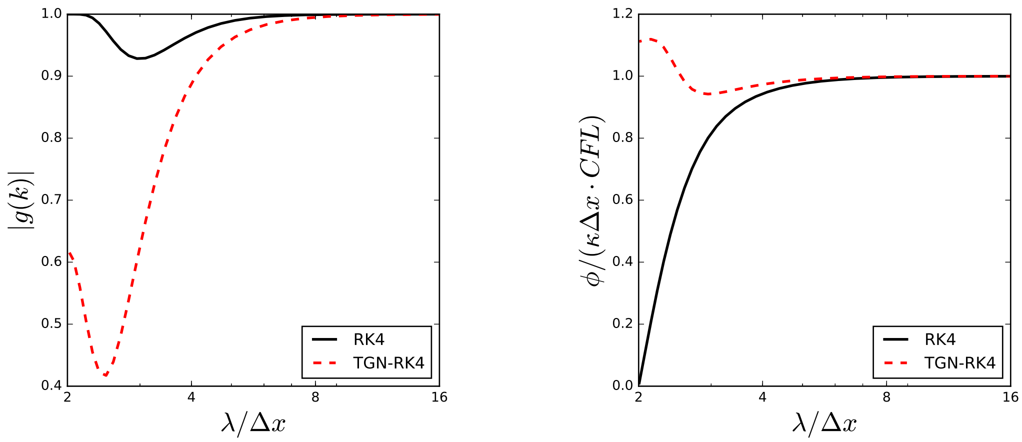

(a) Dissipation (b) Dispersion

Figure B.6: The (a) dissipation and (b) dispersion errors for RK4 and TGN-RK4.

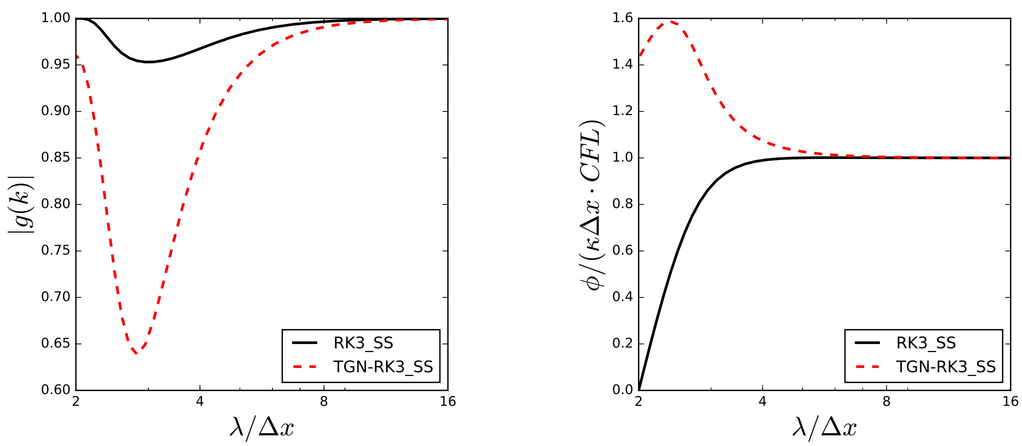

(a) Dissipation (b) Dispersion

Figure B.7: The (a) dissipation and (b) dispersion errors for SSRK3 and TGN-SSRK3.

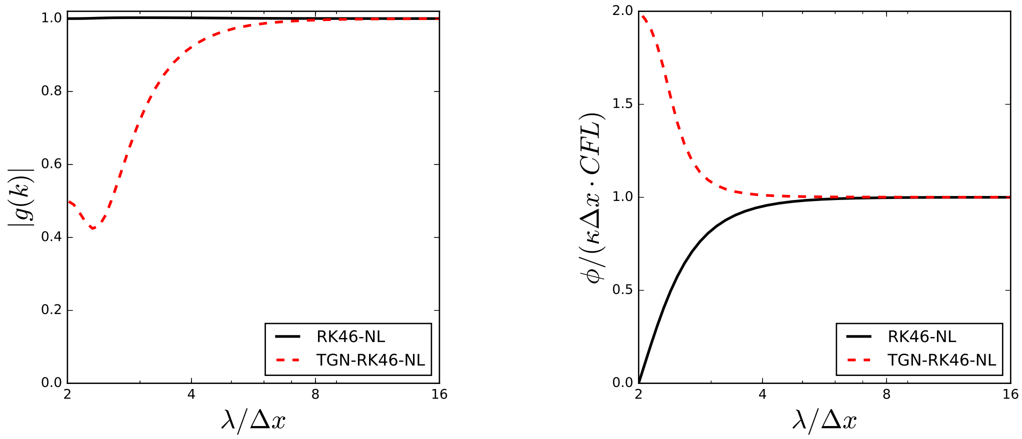

(a) Dissipation (b) Dispersion

Figure B.8: The (a) dissipation and (b) dispersion errors for RK46-NL and TGN-RK46-NL.

characteristics of the fourth-order six-stage low-dissipation low-dispersion RK scheme developed by Berland *et al.* [138] (RK46-NL), and its corresponding TG scheme (TGN-RK46-NL) at $CFL = 0.5$, are shown in Fig. B.8. The stability condition for TGN-RK46-NL is $CFL \leq 0.578$, in contrast to $CFL < 1.65$ for the original RK46-NL scheme.

Taylor-Galerkin vs Turan-Type Multi-Derivative Runge-Kutta

Taylor-Galerkin schemes could be considered as a sub-class of Turan-type multi-derivative Runge-Kutta schemes [224–227]. For a general differential equation $\partial u/\partial t = \mathcal{L}(u)$, a general Turan-type multi-derivative Runge-Kutta (TMDRK) scheme is given as

$$u^{n+1} = u^n + h \sum_{k=1}^{m} \frac{h^k}{k!} \sum_{j=1}^{s} b_j^{(k)} g_j^{(k)} \,, \tag{B.60}$$

where

$$g_i^{(k)} = \left(D^k u\right) \left(u_n + \sum_{k=1}^{m} \frac{h^k}{k!} \sum_{j=1}^{s} a_{ij}^{(k)} g_j^{(k)} \right) , \tag{B.61}$$

and the differential operator D is defined as

$$\begin{aligned} D &= \mathcal{L}(u) \frac{\partial}{\partial u} \,, \\ D^0 u &= u \,, \\ D^1 u &= \mathcal{L}(u) \,, \\ D^k u &= D(D^{k-1} u) \,. \end{aligned} \tag{B.62}$$

It can be presented in a generalized Butcher tableau as

$$\begin{array}{c|c|c|c|c} \mathbf{C} & \mathbf{A^{(1)}} & \mathbf{A^{(2)}} & \cdots & \mathbf{A^{(m)}} \\ \hline & \mathbf{B^{(1)}} & \mathbf{B^{(2)}} & \cdots & \mathbf{B^{(m)}} \end{array} , \tag{B.63}$$

where $\mathbf{A^k} = [a_{kj}]$, $\mathbf{B^{(k)}} = [b_j^{(k)}]$, $\mathbf{C} = [c^{(k)}]$.

Matrices $\mathbf{A^k}$ denote coefficients corresponding to derivative operators D^k for $k = 1, \cdots, m$. A comparison with Eqs. (B.13)–(B.16) shows that TTG3, TTG4A, and TTGC3 are all special cases of TMDRK. The terminology "Taylor-Galerkin" refers to the use of the temporal Taylor series for time integration, as for TMDRK, and a Galerkin-projection in the weak form for the spatial discretization in FEM.

This framework for RK methods and their counterpart the TG formulation suggests that the desirable attenuation at grid cut-off is obtained when the second-order temporal derivative, $\partial_{tt} u$, is kept in the last stage. The second-order temporal derivative terms in other stages mostly increase the scheme's dissipation in the low to moderate wavenumbers. This implies that the specific subclass of TMDRK with second derivatives appearing only in the last stage, i.e. TG schemes, "may" be well suited for Galerkin-based schemes. Further studies are required to verify this observation.

Numerical results

Numerical results were obtained for a one-dimensional Sod shock tube problem and a one-dimensional periodic Burger's problem using TTGC3, and TTGNC3-1 time integration schemes. For both cases, the one-dimensional form of the filter proposed by Najafi-Yazdi et. al [27] with a very sharp cut-off, $k_f \Delta x \approx 0.86\pi$ corresponding to $\lambda/\Delta x \approx 2.33$, was applied on the solution at each time step to prevent numerical instability. The filter cut-off is shown as a vertical dotted line for the Energy spectra, i.e. Figs. B.11 and B.14.

Sod shock tube

The classical Sod shock tube problem [228] was simulated using the initial conditions $(\rho, u, p) = (1, 0, 0)$ for $x < 0$ and $(\rho, u, p) = (0.125, 0, 0.1)$ for $x \geq 0$. Although classical continuous Galerkin schemes are not suitable for capturing discontinuities, a shock that contains energy in all wavelengths is a suitable benchmark to demonstrate the differences between TTGC3 and TTGNC3-1 schemes. The simulations were performed on a 64-cell computational grid defined on $x \in [-0.5, 0.5]$ with $CFL = 0.5$. Density distributions along the computational domain at $t = 0.2$ obtained from TTGC3, and TTGNC3-1 schemes are presented in Fig. B.9 and compared with the exact solution. The region between the shock and the entropy discontinuity is enlarged in Fig. B.10.

The difference between the TTGC3 and TTGNC3-1 is revealed by their energy content in the range $2 \leq \lambda < 4$, i.e. Fig. B.11. The small spurious noise in the exact solution energy spectrum is due the uniform sample size of 2000 points. The TTGNC3-1 result shows less attenuation than that of TTGC3, as expected from their dissipation properties in Fig. B.1. The difference in this case is small because the energy transfer to wavelengths near grid cut-off occurs only due to numerical dispersion.

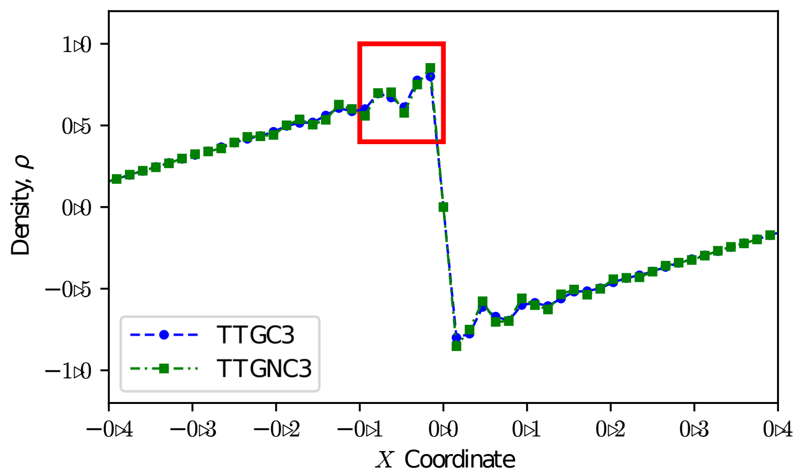

Figure B.9: Density (ρ) distributions for (solid) exact, (circle) RK4, (square) SSRK3, (star) TTGC3, and (triangle) TTGNC3 solutions. The part in the red square is enlarged in Fig. B.10.

Periodic Burger's Problem

Using a Burger's problem defined as $u(x, t = 0) = -\sin(2\pi x)$ for $x \in [-0.5, 0.5]$ on a periodic domain, the low dissipation feature of TTGNC3-1 can be demonstrated more clearly. The energy content of the monotonic initial condition transfers into all wavenumbers as the smooth flow evolves into a discontinuity. This continuous feed of energy from large wavelengths to small provides a means to determine the numerical schemes' dissipation in the energy spectrum. In the Sod shock tube problem, the

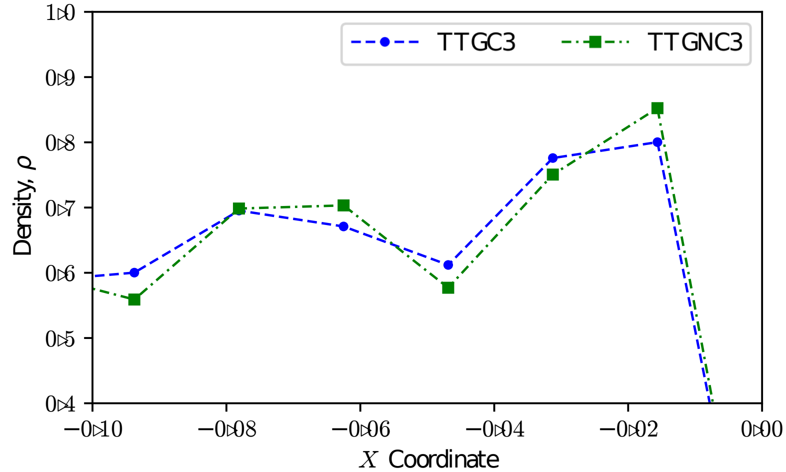

Figure B.10: Density (ρ) distributions for (solid) exact, (circle) RK4, (square) SSRK3, (star) TTGC3, and (triangle) TTGNC3 solutions, zoomed over the region between the shock and the entropy discontinuity.

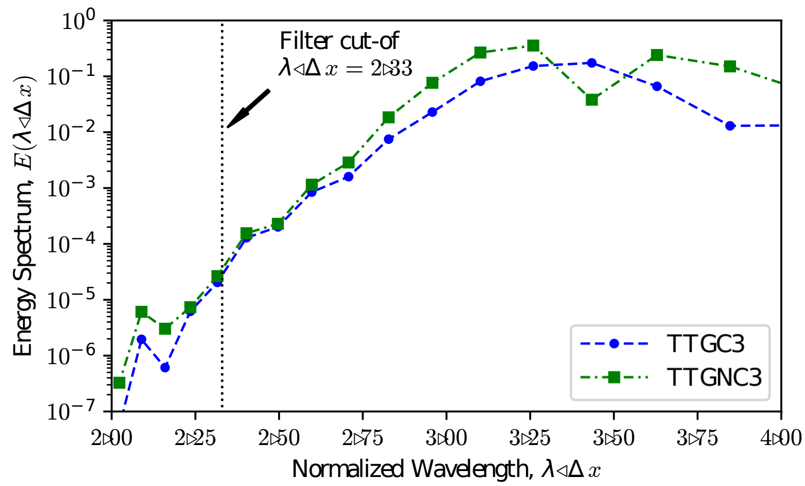

Figure B.11: Energy spectrum (E) versus normalized wavelength ($\lambda/\Delta x$) for (solid) exact, (circle) RK4, (square) SSRK3, (star) TTGC3, and (triangle) TTGNC3 solutions.

energy transfer was due to numerical dispersion. The physical mechanism modeled in Burger's problem yields much more significant transfer.

Figures B.12 and B.13 demonstrate the velocity distribution over the computational domain at $t = 0.44$, showing visible differences between TTGC3 and TTGNC3-1. The energy spectrum, Fig. B.14 shows a decrease of dissipation for medium to low wavelengths for TTGNC3-1 over TTGC3. For example, the energy content at $\lambda/\Delta x = 3.0$ for TTGNC3-1 is 3.5 times that of TTGC3.

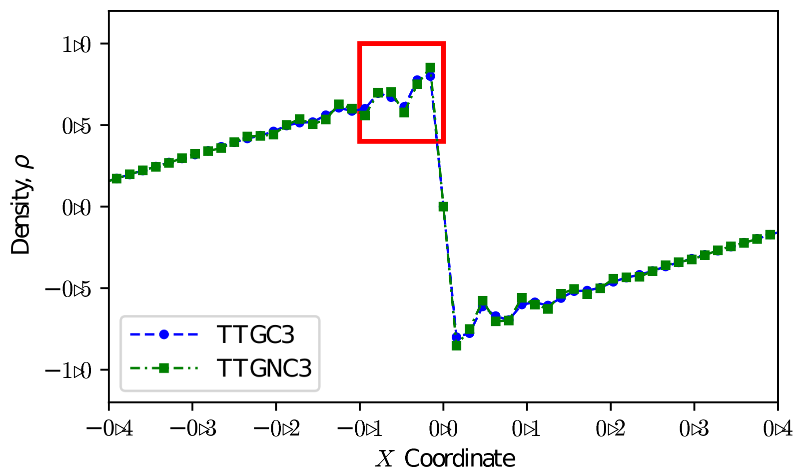

Figure B.12: Density (ρ) distributions for (solid) TTGC3, and (circles) TTGNC3 solutions. The part in the red square is enlarged in Fig. B.13.

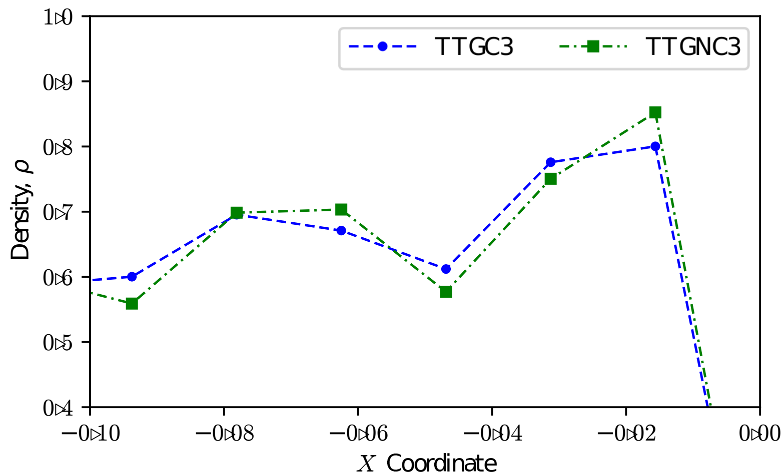

Figure B.13: Density (ρ) distributions for (solid) TTGC3, and (circles) TTGNC3 solutions, zoomed over the region before the discontinuity.

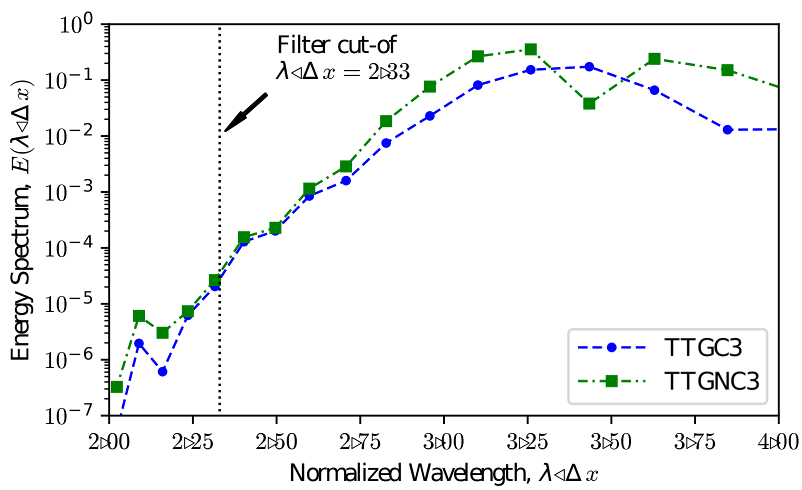

Figure B.14: Energy spectrum (E) versus normalized wavelength ($\lambda/\Delta x$) for (solid) TTGC3, and (circles) TTGNC3 solutions.

APPENDIX C
Generalized Multi-dimensional Z-Transform for Unstructured Sampling

Definition

A generalized definition for the Z-transform of a finite signal of the form $u[N] = [u_1, u_2, \cdots, u_N]$ defined on N points in a D-dimensional space is given by

$$\boldsymbol{\mathcal{U}}\{z_{1,k}, z_{2,k}, \cdots, z_{D,k}\} = \sum_{m=1}^{N} u[m] \prod_{d=1}^{D} z_{d,k}^{-\hat{r}_{d,m}} \ , \tag{C.1}$$

for the data in a *local* vicinity of an arbitrary point 1, and where $\hat{r}_{d,m} = (r_{d,m}/r_{d,\min})$ is a normalized distance, and $r_{d,m} = x_{d,m} - x_{d,1}$ is the d-th component of the relative coordinate from point 1 to point m, as shown in figure C.1. $r_{d,\min}$ is a characteristic length representing the minimum distance of surrounding points to point 1 in the d-th direction, i.e.

$$r_{d,\min} = \min\{r_{d,j} \text{ for } j = 1, 2, \cdots, m\} \ . \tag{C.2}$$

As an example, for a 2D unstructured grid, as shown in figure C.1 the generalized Z-transform is given by

$$\boldsymbol{\mathcal{U}}\{z_1, z_2\} = \sum_{m=1}^{N} u[m] z_1^{-r_{1,m}/r_{1,min}} z_2^{-r_{2,m}/r_{2,min}} \ , \tag{C.3}$$

where $r_{1,m} = x_m - x_1$ and $r_{2,m} = y_m - y_1$.

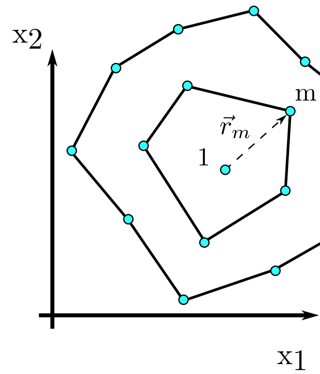

Figure C.1: Schematics of the local vicinity of an arbitrary node 1 in a 2D unstructured grid where a generalized Z-transform is defined.

Linearity

The generalized Z-transform is a linear operator, i.e. for $u[N] = a_1 u_1[N] + a_2 u_2[N]$

$$\boldsymbol{\mathcal{U}}\{z_1, z_2\} = a_1 \boldsymbol{\mathcal{U}}_1 + a_2 \boldsymbol{\mathcal{U}}_2 \ . \tag{C.4}$$

Linear Convolution

The generalized Z-transform has the same property as the traditional definitions (both uniform and non-uniform) have for linear convolution of two data. Consider $u[N]$ and $v[N]$ as two sets of data sampled on a D-dimensional unstructured grid, the Z-transform of their convolution satisfies

$$\boldsymbol{\mathcal{Z}}\{u[N] \circledast v[N]\} = \boldsymbol{\mathcal{U}}\boldsymbol{\mathcal{V}} \ . \tag{C.5}$$

Shift

A shift in the data from point 1 to an arbitrary point j, $u[N] \to \tilde{u}[N]$, with a relative coordinate vector $\vec{r}_{i,j} = \vec{r}_j - \vec{r}_i = (r_{1,j}, r_{2,j}, \cdots, r_{D,j})$ yields

$$\boldsymbol{\mathcal{Z}}\{\tilde{u}\} = \boldsymbol{\mathcal{Z}}\{u[N]\} \prod_{d=1}^{D} z_{d,k}^{-r_{d,j}} \ . \tag{C.6}$$

Special Case #1: Uniform Sampling

A uniformly sampled data is a special case of this generalized definition such that $\Delta = \Delta x_1 = \Delta x_2 = \cdots \Delta x_D = (r_{d,m} - r_{d,1})/m$. The Z-transform of a signal of size $N = N_1 \times N_2 \times \cdots \times N_D$, $\boldsymbol{\mathcal{U}}_u$, can be re-expressed as

$$\boldsymbol{\mathcal{U}}_U \ = \ \sum_{n_1=1}^{N_1} \sum_{n_2=1}^{N_2} \cdots \sum_{n_D=1}^{N_D} u[n_1, n_2, \cdots, n_D] z_1^{-n_1} z_2^{-n_2} \cdots z_D^{-n_D} \ . \tag{C.7}$$

Special Case #2: Non-Uniform Sampling on a Curvilinear Grid

A structured non-uniformly sampled signal of size $N = N_1 \times N_2 \times \cdots \times N_D$ is another special case. The relative distance between point m and point 1 along d-axis can be expressed as

$$r_{d,m} = \sum_{j=2}^{m} \Delta_{d,j} \ , \tag{C.8}$$

where

$$\Delta_{d,j} = r_{d,j} - r_{d,j-1} \ . \tag{C.9}$$

The generalized Z-transform in this physical domain can be written as

$$\boldsymbol{\mathcal{U}}_{NU} = \sum_{n_1=1}^{N_1} \sum_{n_2=1}^{N_2} \cdots \sum_{n_D=1}^{N_D} u[n_1, n_2, \cdots, n_D] z_1^{-\frac{\Delta_{1,n_1}}{r_{1,\min}}} z_2^{-\frac{\Delta_{2,n_2}}{r_{2,\min}}} \cdots z_D^{-\frac{\Delta_{D,n_D}}{r_{D,\min}}} \ . \tag{C.10}$$

This can be further simplified by using $r_{d,\min} = r_{d,2} = \Delta_{d,2}$ to result in

$$\boldsymbol{\mathcal{U}}_{NU} = \sum_{n_1=1}^{N_1} \sum_{n_2=1}^{N_2} \cdots \sum_{n_D=1}^{N_D} u[n_1, n_2, \cdots, n_D] \left(z_1^{-n_1} z_2^{-n_2} \cdots z_D^{-n_D} \right) \left(z_1^{n_1 - \frac{\Delta_{1,n_1}}{\Delta_{1,2}}} z_2^{n_1 - \frac{\Delta_{2,n_2}}{\Delta_{2,2}}} z_D^{n_D - \frac{\Delta_{D,n_D}}{\Delta_{D,2}}} \right) . \tag{C.11}$$

The last term in eq. (C) represents the warpage of the generalized Z-transform due to deviation in grid spacing, i.e. $n_j - \Delta_{j,n_j}/\Delta_{j,2}$. Note that point 2 in each direction is the immediate point before or after point 1. When the non-uniform physical space is mapped into a computational space where grid spacing is uniform, $\mathbf{x} \to \hat{\mathbf{x}}$, the deviation exponents become zero, i.e. $n_j - \hat{\Delta}_{j,n_j}/\hat{\Delta}_{j,2} = n_j - n_j = 0$. This is equivalent to mapping the z-space with the transformation $\hat{z}_d = z_1^{\frac{1}{n_j - \Delta_{j,n_j}/\Delta_{j,2}}}$. This is as if the Z-transform is dewarped.

Bibliography

[1] Sanjiva K. Lele and Joseph W. Nichols. “A second golden age of aeroacoustics?” In: *Philosophical Transactions of the Royal Society A: Mathematical, Physical and Engineering Sciences* 372.2022 (2014), p. 20130321.

[2] Tim Colonius and Sanjiva K. Lele. “Computational aeroacoustics: progress on nonlinear problems of sound generation”. In: *Progress in Aerospace sciences* 40.6 (2004), pp. 345–416.

[3] Christopher K. W. Tam. “Computational aeroacoustics: an overview of computational challenges and applications”. In: *International Journal of Computational Fluid Dynamics* 18.6 (2004), pp. 547–567.

[4] Jean Donea, Bernardino Roig, and Antonio Huerta. “High-order accurate time-stepping schemes for convection-diffusion problems”. In: *Computer methods in applied mechanics and engineering* 182.3-4 (2000), pp. 249–275.

[5] Paul Fischer and Julia Mullen. “Filter-based stabilization of spectral element methods”. In: *Comptes Rendus de l’Académie des Sciences-Series I-Mathematics* 332.3 (2001), pp. 265–270.

[6] Robert M. Kirby and George Em Karniadakis. “De-aliasing on non-uniform grids: algorithms and applications”. In: *Journal of Computational Physics* 191.1 (2003), pp. 249–264.

[7] Meng Wang, Jonathan B. Freund, and Sanjiva K. Lele. “Computational prediction of flow-generated sound”. In: *Annu. Rev. Fluid Mech.* 38 (2006), pp. 483–512.

[8] Daniel J. Bodony and Sanjiva K. Lele. “Current status of jet noise predictions using large-eddy simulation”. In: *AIAA journal* 46.2 (2008), pp. 364–380.

[9] Michael J. Lighthill. “On sound generated aerodynamically I. General theory”. In: *Proceedings of the Royal Society of London. Series A. Mathematical and Physical Sciences* 211.1107 (1952), pp. 564–587.

[10] David G. Crighton. “Basic principles of aerodynamic noise generation”. In: *Progress in Aerospace Sciences* 16.1 (1975), pp. 31–96.

[11] Parviz Moin et al. “A dynamic subgrid-scale model for compressible turbulence and scalar transport”. In: *Physics of Fluids A: Fluid Dynamics* 3.11 (1991), pp. 2746–2757.

[12] Thibault Dairay et al. “Numerical dissipation vs. subgrid-scale modelling for large eddy simulation”. In: *Journal of Computational Physics* 337 (2017), pp. 252–274.

[13] Anna Witkowska, Daniel Juvé, and James G. Brasseur. “Numerical study of noise from isotropic turbulence”. In: *Journal of Computational Acoustics* 5.03 (1997), pp. 317–336.

[14] Guo-Wei He, Robert Rubinstein, and Lian-Ping Wang. “Effects of subgrid-scale modeling on time correlations in large eddy simulation”. In: *Physics of Fluids* 14.7 (2002), pp. 2186–2193.

[15] Ugo Piomelli, Craig L. Streett, and Sutanu Sarkar. "On the computation of sound by large-eddy simulations". In: *Journal of Engineering Mathematics* 32.2-3 (1997), pp. 217–236.

[16] Daniel Bodony and Sanjiva K. Lele. "Spatial scale decomposition of shear layer turbulence and the sound sources associated with the missing scales in a large-eddy simulation". In: *8th AIAA/CEAS Aeroacoustics Conference & Exhibit*. 2002, p. 2454.

[17] Christelle Seror et al. "Subgrid-scale contribution to noise production in decaying isotropic turbulence". In: *AIAA journal* 38.10 (2000), pp. 1795–1803.

[18] Christelle Seror et al. "On the radiated noise computed by large-eddy simulation". In: *Physics of Fluids* 13.2 (2001), pp. 476–487.

[19] Guo-Wei He, Meng Wang, and Sanjiva K Lele. "On the computation of space-time correlations by large-eddy simulation". In: *physics of fluids* 16.11 (2004), pp. 3859–3867.

[20] Christophe Bogey and Christophe Bailly. "Effects of inflow conditions and forcing on subsonic jet flows and noise." In: *AIAA journal* 43.5 (2005), pp. 1000–1007.

[21] Steven A. Stolz and Nikolaus A. Adams. "An approximate deconvolution procedure for large-eddy simulation". In: *Physics of Fluids* 11.7 (1999), p. 1699.

[22] William Layton. "Bounds on Energy and Helicity Dissipation Rates of Approximate Deconvolution Models of Turbulence". In: *SIAM Journal on Mathematical Analysis* 39.3 (Jan. 2007), pp. 916–931. ISSN: 0036-1410.

[23] William J. Layton et al. “The joint Helicity-Energy cascade for homogeneous, isotropic turbulence generated by approximate deconvolution models”. In: *Advances and Applications in Fluid Mechanics* 4.1 (2008), pp. 1–46.

[24] Alison L. Marsden, Oleg V. Vasilyev, and Parviz Moin. “Construction of commutative filters for LES on unstructured meshes”. In: *Journal of Computational Physics* 175.2 (2002), pp. 584–603.

[25] Andreas Haselbacher and Oleg V. Vasilyev. “Commutative discrete filtering on unstructured grids based on least-squares techniques”. In: *Journal of Computational Physics* 187.1 (2003), pp. 197–211.

[26] Sajeeb T. Bose, Parviz Moin, and Frank E. Ham. “Explicitly filtered large eddy simulation on unstructured grids”. In: *Center of Turbulence Research Annual Research Briefs* (2011), pp. 87–96.

[27] Alireza Najafi-Yazdi, Mostafa Najafi-Yazdi, and Luc Mongeau. “A high resolution differential filter for large eddy simulation: Toward explicit filtering on unstructured grids”. In: *Journal of Computational Physics* 292 (2015), pp. 272–286.

[28] Thomas S. Lund and Hans-Jakob Kaltenbach. “Experiments with explicit filtering for LES using a finite-diference method”. In: *Annual Research Briefs (Center for Turbulence Research)* (1995), pp. 91–105.

[29] Thomas S. Lund. “On the use of discrete filters for large eddy simulation”. In: *Annual Research Briefs (Center for Turbulence Research)* (1997), pp. 1–13.

[30] Thomas S. Lund. “The Use of Explicit Filters Large Eddy Simulation”. In: *Computers & Mathematics with Applications* 46 (2003), pp. 603–616.

[31] Oleg V. Vasilyev, Thomas S. Lund, and Parviz Moin. "A general class of commutative filters for LES in complex geometries". In: *Journal of computational physics* 146.1 (1998), pp. 82–104.

[32] Nikolaus A. Adams and Steven A. Stolz. "A Subgrid-Scale Deconvolution Approach for Shock Capturing". In: *Journal of Computational Physics* 178.2 (May 2002), pp. 391–426.

[33] Robert A. Clark, Joel H. Ferziger, and William C. Reynolds. "Evaluation of subgrid-scale models using an accurately simulated turbulent flow". In: *Journal of fluid mechanics* 91.1 (1979), pp. 1–16.

[34] Robert S. Rogallo and Parviz Moin. "Numerical simulation of turbulent flows". In: *Annual review of fluid mechanics* 16.1 (1984), pp. 99–137.

[35] Arthur G. Kravchenko and Parviz Moin. "Numerical studies of flow over a circular cylinder at $Re_D = 3900$". In: *Physics of fluids* 12.2 (2000), pp. 403–417.

[36] Johan Meyers and Pierre Sagaut. "Is plane-channel flow a friendly case for the testing of large-eddy simulation subgrid-scale models?" In: *Physics of Fluids* 19.4 (2007), p. 048105.

[37] Massimo Germano et al. "A dynamic subgrid-scale eddy viscosity model". In: *Physics of Fluids A: Fluid Dynamics* 3.7 (1991), pp. 1760–1765.

[38] Johan Meyers and Pierre Sagaut. "Evaluation of Smagorinsky variants in large-eddy simulations of wall-resolved plane channel flows". In: *Physics of Fluids* 19.9 (2007), p. 095105.

[39] Joseph Smagorinsky. “General circulation experiments with the primitive equations: I. The basic experiment”. In: *Monthly weather review* 91.3 (1963), pp. 99–164.

[40] Douglas K. Lilly. “A proposed modification of the Germano subgrid-scale closure method”. In: *Physics of Fluids A: Fluid Dynamics* 4.3 (1992), pp. 633–635.

[41] Shewen Liu, Charles Meneveau, and Joseph Katz. “Experimental study of similarity subgrid-scale models of turbulence in the far-field of a jet”. In: *Applied scientific research* 54.3 (1995), pp. 177–190.

[42] Gordon Erlebacher et al. “Toward the large-eddy simulation of compressible turbulent flows”. In: *Journal of fluid mechanics* 238 (1992), pp. 155–185.

[43] Charles Meneveau and Joseph Katz. “Scale-invariance and turbulence models for large-eddy simulation”. In: *Annual Review of Fluid Mechanics* 32.1 (2000), pp. 1–32.

[44] Daniele Carati, Alan Wray, and W Cabot. “Ensemble averaged dynamic modeling”. In: (1996).

[45] Charles Meneveau, Thomas S Lund, and William H Cabot. “A Lagrangian dynamic subgrid-scale model of turbulence”. In: *Journal of fluid mechanics* 319 (1996), pp. 353–385.

[46] Fady M. Najjar and Danesh K. Tafti. “Study of discrete test filters and finite difference approximations for the dynamic subgrid-scale stress model”. In: *Physics of Fluids* 8.4 (1996), pp. 1076–1088.

[47] JA Domaradzki. *Subgrid Scale Models with Backscatter.* Tech. rep. University of California Los Angeles Department of Aerospace Engineering, 1996.

[48] Ugo Piomelli, Amirreza Rouhi, and Bernard J Geurts. “A grid-independent length scale for large-eddy simulations”. In: *Journal of fluid mechanics* 766 (2015), pp. 499–527.

[49] Amirreza Rouhi, Ugo Piomelli, and Bernardus J Geurts. “Dynamic subfilter-scale stress model for large-eddy simulations”. In: *Physical review fluids* 1.4 (2016), p. 044401.

[50] Bernard J Geurts, Amirreza Rouhi, and Ugo Piomelli. “Recent progress on reliability assessment of large-eddy simulation”. In: *Journal of Fluids and Structures* (2019).

[51] Fotini K. Chow and Parviz Moin. “A further study of numerical errors in large-eddy simulations”. In: *Journal of Computational Physics* 184.2 (2003), pp. 366–380.

[52] Dieter Fauconnier, Chris De Langhe, and Erik Dick. “A family of dynamic finite difference schemes for large-eddy simulation”. In: *Journal of Computational Physics* 228.6 (2009), pp. 1830–1861.

[53] Sanjeeb T. Bose, Parviz Moin, and Donghyun You. “Grid-independent large-eddy simulation using explicit filtering”. In: *Physics of Fluids* 22.10 (2010), p. 105103.

[54] Dongyhun You, Sanjeeb T. Bose, and Parviz Moin. “Grid-independent large-eddy simulation of compressible turbulent flows using explicit filtering”. In: *Proceedings of the Summer Program.* 2010, p. 203.

[55] Nishant Kumar Singh. "Large Eddy Simulation of acoustic propagation in turbulent flow through ducts and mufflers". PhD thesis. University of Hull, 2012.

[56] Guillaume Aubard et al. "Comparison of subgrid-scale viscosity models and selective filtering strategy for large-eddy simulations". In: *Flow, Turbulence and Combustion* 91.3 (2013), pp. 497–518.

[57] Giuliano De Stefano and Oleg V. Vasilyev. "Wavelet-based adaptive large-eddy simulation with explicit filtering". In: *Journal of Computational Physics* 238 (2013), pp. 240–254.

[58] Grégoire S. Winckelmans and Hervé Jeanmart. "Assessment of some models for LES without/with explicit filtering". In: *Direct and Large-Eddy Simulation IV*. Springer, 2001, pp. 55–66.

[59] Steven A. Stolz, Nikolaus A. Adams, and Leonhard Kleiser. "The approximate deconvolution model for large-eddy simulations of compressible flows and its application to shock-turbulent-boundary-layer interaction". In: *Physics of Fluids* 13.10 (2001), pp. 2985–3001.

[60] Steven A. Stolz, Nikolaus A. Adams, and Leonhard Kleiser. "The approximate deconvolution model for compressible flows: isotropic turbulence and shock-boundary-layer interaction". In: *Advances in LES of Complex Flows*. Ed. by R. Friedrich and W. Rodi. Kluwer Academic Publishers, Netherlands, 2002, pp. 33–47.

[61] Nikolaus A. Adams. "A stochastic extension of the approximate deconvolution model". In: *Physics of Fluids* 23.5 (2011), p. 055103.

[62] William J. Layton and Leo G. Rebholz. *Approximate Deconvolution Models of Turbulence*. Berlin, Heidelberg: Springer-Verlag, 2011.

[63] William Layton and Monika Neda. “A similarity theory of approximate deconvolution models of turbulence”. In: *Journal of mathematical analysis and applications* 333.1 (2007), pp. 416–429.

[64] Steven A. Stolz, Nikolaus A. Adams, and Leonhard Kleiser. “An approximate deconvolution model for large-eddy simulation with application to incompressible wall-bounded flows”. In: *Physics of fluids* 13.4 (2001), pp. 997–1015.

[65] Leo G. Rebholz. “Well-posedness of a reduced order approximate deconvolution turbulence model”. In: *Journal of Mathematical Analysis and Applications* 405.2 (2013), pp. 738–741.

[66] Christophe Bogey and Christophe Bailly. “Computation of a high Reynolds number jet and its radiated noise using large eddy simulation based on explicit filtering”. In: *Computers & Fluids* 35.10 (Dec. 2006), pp. 1344–1358.

[67] Christophe Bogey and Olivier Marsden. “Identification of the effects of the nozzle-exit boundary-layer thickness and its corresponding Reynolds number in initially highly disturbed subsonic jets”. In: *Physics of Fluids* 25.5 (2013), p. 055106.

[68] Julien Berland et al. “Filter shape dependence and effective scale separation in large-eddy simulations based on relaxation filtering”. In: *Computers & Fluids* 47.1 (2011), pp. 65–74.

[69] Dieter Fauconnier, Christophe Bogey, and Erik Dick. "On the performance of relaxation filtering for large-eddy simulation". In: *Journal of Turbulence* 14.1 (2013), pp. 22–49.

[70] Giuliano De Stefano and Oleg V. Vasilyev. "Sharp cutoff versus smooth filtering in large eddy simulation". In: *Physics of Fluids* 14.1 (2002), pp. 362–369.

[71] Giuliano De Stefano and Oleg V. Vasilyev. "A Study of the Effect of Smooth Filtering in LES". In: *Proceedings of the Third AFOSR International Conference on DNS/LES (TAICDL)*. Arlington: University of Texas at Arlington, 2002, pp. 247–254.

[72] Giuliano De Stefano and Oleg V. Vasilyev. ""Perfect" modeling framework for dynamic SGS model testing in large eddy simulation". In: 18.1 (2004), pp. 27–41.

[73] Julien Berland, Christophe Bogey, and Christophe Bailly. "A study of differentiation errors in large-eddy simulations based on the EDQNM theory". In: *Journal of Computational Physics* 227.18 (2008), pp. 8314–8340.

[74] Timothy Barth. "Recent developments in high order k-exact reconstruction on unstructured meshes". In: *31st Aerospace Sciences Meeting*. 1993, p. 668.

[75] Massimo Germano. "Differential filters for the large eddy numerical simulation of turbulent flows". In: *The Physics of fluids* 29.6 (1986), pp. 1755–1757.

[76] Massimo Germano. "Differential filters of elliptic type". In: *The Physics of fluids* 29.6 (1986), pp. 1757–1758.

[77] Lehmkuhl, Oriol and Borrell, R and Rodríguez, I. and Pérez-Segarra, Carlos David and Oliva, A. "Assessment of the symmetry-preserving regularization model on complex flows using unstructured grids". In: *Computers & Fluids* 60 (2012), pp. 108–116.

[78] Sanjeeb T. Bose and Parviz Moin. "A dynamic slip boundary condition for wall-modeled large-eddy simulation". In: *Physics of Fluids* 26.1 (2014), p. 015104.

[79] Parviz Moin et al. "Wall-modeling in complex turbulent flows". In: *Advances in Fluid-Structure Interaction*. Springer, 2016, pp. 207–219.

[80] David E. Aljure et al. "Flow and turbulent structures around simplified car models". In: *Computers & Fluids* 96 (2014), pp. 122–135.

[81] Eric J Ching et al. "Shock capturing for discontinuous Galerkin methods with application to predicting heat transfer in hypersonic flows". In: *Journal of Computational Physics* (2018).

[82] Alireza Najafiyazdi, Ali Uzun, and Luc G Mongeau. "On the sources of jet noise: a numerical study using band-pass filtering". In: *19th AIAA/CEAS Aeroacoustics Conference*. 2013, p. 2233.

[83] M. Montagnac. *Variable normalization (nondimensionalization and scaling) for Navier-Stokes equations: A practical guide*. Technical Report TR-CFD-13-77. 42 avenue Coriolis, 31057 Toulouse Cedex 1, France: Centre Européen de Recherche et de Formation Avancée en Calcul Scientifique (CERFACS), 2013.

[84] Mårten Teodor Landahl, Marten T. Landahl, and Eric L. Mollo-Christensen. *Turbulence and random processes in fluid mechanics*. Cambridge University Press, 1992.

[85] Christophe Bailly and Geneviève Comte-Bellot. *Turbulence*. Sciences et techniques de l'ingénieur. CNRS éditions, 2003. ISBN: 9782271060082.

[86] Stephen B. Pope. *Turbulent Flows*. 2001.

[87] Eric Garnier, Nikolaus Adams, and Pierre Sagaut. *Large eddy simulation for compressible flows*. Springer Science & Business Media, 2009.

[88] Athony Leonard. "Energy cascade in large-eddy simulations of turbulent fluid flows". In: *Advances in geophysics*. Vol. 18. Elsevier, 1975, pp. 237–248.

[89] Saad Ragab, Shaw-Ching Sheen, and Madhu Sreedhar. "An investigation of finite-difference methods for large-eddy simulation of a mixing layer". In: *30th Aerospace Sciences Meeting and Exhibit*. 1992, p. 554.

[90] Ugo Piomelli. "Large-eddy simulation: achievements and challenges". In: *Progress in Aerospace Sciences* 35.4 (1999), pp. 335–362.

[91] Branko Kosović, Dale I. Pullin, and Ravi Samtaney. "Subgrid-scale modeling for large-eddy simulations of compressible turbulence". In: *Physics of Fluids* 14.4 (2002), pp. 1511–1522.

[92] Thierry Dubois, Julian A. Domaradzki, and Albert Honein. "The subgrid-scale estimation model applied to large eddy simulations of compressible turbulence". In: *Physics of Fluids* 14.5 (2002), pp. 1781–1801.

[93] Bert Vreman, Bernard Geurts, and Hans Kuerten. “A priori tests of large eddy simulation of the compressible plane mixing layer”. In: *Journal of engineering mathematics* 29.4 (1995), pp. 299–327.

[94] Marcel Lesieur and Pierre Comte. “Large-eddy simulations of compressible turbulent flows”. In: *Institut de Mecanique de Grenoble, Turbulence in Compressible Flows p 4. 1-4. 39(SEE N 97-22569 01-34)* (1997).

[95] Marcel Lesieur and Pierre Comte. “Favre filtering and macro-temperature in large-eddy simulations of compressible turbulence”. In: *Comptes Rendus de l’Académie des Sciences-Series IIB-Mechanics* 329.5 (2001), pp. 363–368.

[96] Albertus W. Vreman. *Direct and large-eddy simulation of the compressible turbulent mixing layer*. Universiteit Twente, 1995.

[97] DO Martínez et al. “Energy spectrum in the dissipation range of fluid turbulence”. In: *Journal of Plasma Physics* 57.1 (1997), pp. 195–201.

[98] Sandip Ghosal and Parviz Moin. “The Basic Equations for the Large Eddy Simulation of Turbulent Flows in Complex Geometry”. In: (1993).

[99] Pierre Sagaut. *Large eddy simulation for incompressible flows: an introduction*. Springer Science & Business Media, 2006.

[100] Julian A. Domaradzki and Nikolaus A. Adams. “Direct modelling of subgrid scales of turbulence in large eddy simulations”. In: *Journal of Turbulence* 3.024 (2002), p. 1.

[101] Charles G. Speziale et al. “The subgrid-scale modeling of compressible turbulence”. In: *The Physics of fluids* 31.4 (1988), pp. 940–942.

[102] Julian A. Domaradzki and Eileen M. Saiki. “A subgrid-scale model based on the estimation of unresolved scales of turbulence”. In: *Physics of Fluids* 9.7 (1997), pp. 2148–2164.

[103] Thierry Dubois, François Jauberteau, and Roger Temam. *Dynamic multilevel methods and the numerical simulation of turbulence*. Cambridge University Press, 1999.

[104] Marc Terracol, Pierre Sagaut, and Claude Basdevant. “A multilevel algorithm for large-eddy simulation of turbulent compressible flows”. In: *Journal of Computational Physics* 167.2 (2001), pp. 439–474.

[105] Marc Terracol, Pierre Sagaut, and Claude Basdevant. “A time self-adaptive multilevel algorithm for large-eddy simulation”. In: *Journal of Computational Physics* 184.2 (2003), pp. 339–365.

[106] Ashish Misra and Dale I. Pullin. “A vortex-based subgrid stress model for large-eddy simulation”. In: *Physics of Fluids* 9.8 (1997), pp. 2443–2454.

[107] Thomas Jr. Hughes, Luca Mazzei, and Kenneth E. Jansen. “Large eddy simulation and the variational multiscale method”. In: *Computing and visualization in science* 3.1-2 (2000), pp. 47–59.

[108] Thomas Jr. Hughes et al. “The multiscale formulation of large eddy simulation: Decay of homogeneous isotropic turbulence”. In: *Physics of fluids* 13.2 (2001), pp. 505–512.

[109] Bernard J. Geurts and Darryl D. Holm. “Regularization modeling for large-eddy simulation”. In: *Physics of Fluids* 15.1 (2003), p. L13. ISSN: 10706631.

[110] LC Berselli, T Iliescu, and WJ Layton. *Mathematics of large eddy simulation of turbulent flows*. Springer, 2006.

[111] Steven A. Stolz, Nikolaus A. Adams, and Leonhard Kleiser. "Analysis of sub-grid scales and sub-grid scale modeling for shock-boundary-layer interaction". In: *Turbulence and Shear Flow I* (1999), pp. 881–886.

[112] Christophe Bogey and Christophe Bailly. "Large eddy simulations of round free jets using explicit filtering with/without dynamic Smagorinsky model". In: *International Journal of Heat and Fluid Flow* 27.4 (Aug. 2006), pp. 603–610.

[113] Christophe Bogey, Nicolas de Cacqueray, and Christophe Bailly. "A shock-capturing methodology based on adaptative spatial filtering for high-order non-linear computations". In: *Journal of Computational Physics* 228.5 (Mar. 2009), pp. 1447–1465.

[114] Argus Dunca and Yekaterina Epshteyn. "On the Stolz–Adams Deconvolution Model for the Large-Eddy Simulation of Turbulent Flows". In: *SIAM Journal on Mathematical Analysis* 37.6 (2006), pp. 1890–1902.

[115] Steffen Stolz, Nikolaus A Adams, and Leonhard Kleiser. "The approximate deconvolution model for compressible flows: isotropic turbulence and shock-boundary-layer interaction". In: *Advances in LES of Complex Flows*. Springer, 2002, pp. 33–47.

[116] Joseph Mathew et al. "An explicit filtering method for large eddy simulation of compressible flows". In: *Physics of fluids* 15.8 (2003), pp. 2279–2289.

[117] Joseph Mathew, Holger Foysi, and Rainer Friedrich. "A new approach to LES based on explicit filtering". In: *International journal of heat and fluid flow* 27.4 (2006), pp. 594–602.

[118] Stephen A. Jordan and Saad Ragab. "A large-eddy simulation of the shear-driven cavity flow using dynamic modeling". In: *International Journal of Computational Fluid Dynamics* 6.4 (1996), pp. 321–335.

[119] Pierre Sagaut and Yves Grohens. "Discrete filters for large eddy simulation". In: *International Journal for Numerical Methods in Fluids* 31.8 (1999), pp. 1195–1220.

[120] Julie S. Mullen and Paul F. Fischer. "Filtering techniques for complex geometry fluid flows". In: *Communications in numerical methods in engineering* 15.1 (1999), pp. 9–18.

[121] C. David Pruett and Nikolaus A. Adams. "A priori analyses of three subgrid-scale models for one-parameter families of filters". In: *Physics of Fluids* 12.5 (2000), pp. 1133–1142.

[122] Julien Berland, Christophe Bogey, and Christophe Bailly. "Investigation using statistical closure theory of the influence of the filter shape on scale separation in large-eddy simulation". In: *Journal of Turbulence* 9 (2008), N21.

[123] Omer San, Anne E. Staples, and Traian Iliescu. "A posteriori analysis of low-pass spatial filters for approximate deconvolution large eddy simulations of homogeneous incompressible flows". In: *International Journal of Computational Fluid Dynamics* 29.1 (2015), pp. 40–66.

[124] Marcel Lesieur and Olivier Metais. "New trends in large-eddy simulations of turbulence". In: *Annual review of fluid mechanics* 28.1 (1996), pp. 45–82.

[125] Ugo Piomelli et al. "Subgrid-scale backscatter in turbulent and transitional flows". In: *Physics of Fluids A: Fluid Dynamics* 3.7 (1991), pp. 1766–1771.

[126] Bo Tao, Joseph Katz, and Charles Meneveau. "Statistical geometry of subgrid-scale stresses determined from holographic particle image velocimetry measurements". In: *Journal of Fluid Mechanics* 457 (2002), pp. 35–78.

[127] Ugo Piomelli, Yunfang Yu, and Ronald J Adrian. "Subgrid-scale energy transfer and near-wall turbulence structure". In: *Physics of Fluids* 8.1 (1996), pp. 215–224.

[128] J Urzay et al. "Backscatter of turbulent kinetic energy in chemically-reacting compressible flows". In: *Center for Turbulence Research, Annual Research Briefs 2013* (2013), pp. 123–139.

[129] Sina Khani and Michael L Waite. "Backscatter in stratified turbulence". In: *European Journal of Mechanics-B/Fluids* 60 (2016), pp. 1–12.

[130] James G Brasseur and Chao-Hsuan Wei. "Interscale dynamics and local isotropy in high Reynolds number turbulence within triadic interactions". In: *Physics of Fluids* 6.2 (1994), pp. 842–870.

[131] Sanjiva K. Lele. "Compact finite difference schemes with spectral-like resolution". In: *Journal of computational physics* 103.1 (1992), pp. 16–42.

[132] Christophe Bogey, Olivier Marsden, and Christophe Bailly. "Large-eddy simulation of the flow and acoustic fields of a Reynolds number 10 5 subsonic

jet with tripped exit boundary layers". In: *Physics of Fluids* 23.3 (2011), p. 035104.

[133] Jean-Pierre Chollet and Marcel Lesieur. "Parameterization of small scales of three-dimensional isotropic turbulence utilizing spectral closures". In: *Journal of the Atmospheric Sciences* 38.12 (1981), pp. 2747–2757.

[134] Miguel R. Visbal and Donald P. Rizzetta. "Large-Eddy Simulation on Curvilinear Grids Using Compact Differencing and Filtering Schemes". In: *Journal of Fluids Engineering* 124.4 (2002), p. 836.

[135] Donald P. Rizzetta, Miguel R. Visbal, and Gregory A. Blaisdell. "A time-implicit high-order compact differencing and filtering scheme for large-eddy simulation". In: *International Journal for Numerical Methods in Fluids* 42.6 (2003), pp. 665–693.

[136] Sonali Bagchi and Sanjit Kumar Mitra. "The nonuniform discrete Fourier transform and its applications in signal processing Kluwer Academic Publishers". In: *Norwell, Mass., USA* (1999).

[137] Christophe Bogey and Christophe Bailly. "A family of low dispersive and low dissipative explicit schemes for flow and noise computations". In: *Journal of Computational physics* 194.1 (2004), pp. 194–214.

[138] Julien Berland, Christophe Bogey, and Christophe Bailly. "Low-dissipation and low-dispersion fourth-order Runge–Kutta algorithm". In: *Computers & Fluids* 35.10 (2006), pp. 1459–1463.

[139] Mostafa Najafiyazdi, Luc Mongeau, and Siva Nadarajah. "Low-dissipation low-dispersion explicit Taylor-Galerkin schemes from the Runge-Kutta kernels". In: *International Journal of Aeroacoustics* 17.1-2 (2018), pp. 88–113.

[140] Olek C Zienkiewicz, Robert L Taylor, and Perumal Nithiarasu. *The finite element method for fluid dynamics*. Seventh Edition. Oxford: Butterworth-Heinemann, 2014.

[141] Thomas Jr. Hughes and Gregory M. Hulbert. "Space-time finite element methods for elastodynamics: formulations and error estimates". In: *Computer methods in applied mechanics and engineering* 66.3 (1988), pp. 339–363.

[142] L Spradley, J Stalnaker, and A Ratliff. "Computation of three-dimensional viscous flows with the Navier-Stokes equations". In: *13th Fluid and Plasma-Dynamics Conference*. 1980, p. 1348.

[143] Christie, Ian and Griffiths, David F and Mitchell, A Ronald and Sanz-Serna, Jesús María. "Product approximation for non-linear problems in the finite element method". In: *IMA Journal of Numerical Analysis* 1.3 (1981), pp. 253–266.

[144] Clive AJ Fletcher. "The group finite element formulation". In: *Computer Methods in Applied Mechanics and Engineering* 37.2 (1983), pp. 225–244.

[145] Thomas Jr. Hughes, Guglielmo Scovazzi, and Tayfun E Tezduyar. "Stabilized methods for compressible flows". In: *Journal of Scientific Computing* 43.3 (2010), pp. 343–368.

[146] Thierry J. Poinsot and Sanjiva K. Lele. "Boundary conditions for direct simulations of compressible viscous flows". In: *Journal of computational physics* 101.1 (1992), pp. 104–129.

[147] Guido Lodato, Pascale Domingo, and Luc Vervisch. "Three-dimensional boundary conditions for direct and large-eddy simulation of compressible viscous flows". In: *Journal of Computational Physics* 227.10 (2008), pp. 5105–5143.

[148] Charles Hirsch. *Numerical computation of internal and external flows: The fundamentals of computational fluid dynamics*. Elsevier, 2007.

[149] Kevin W. Thompson. "Time dependent boundary conditions for hyperbolic systems". In: *Journal of computational physics* 68.1 (1987), pp. 1–24.

[150] Kevin W. Thompson. "Time-dependent boundary conditions for hyperbolic systems, II". In: *Journal of computational physics* 89.2 (1990), pp. 439–461.

[151] John C. Strikwerda. "Initial boundary value problems for incompletely parabolic systems". In: *Communications on Pure and Applied Mathematics* 30.6 (1977), pp. 797–822.

[152] Oliger, Joseph and Sundström, Arne. "Theoretical and practical aspects of some initial boundary value problems in fluid dynamics". In: *SIAM Journal on Applied Mathematics* 35.3 (1978), pp. 419–446.

[153] David H. Rudy and John C. Strikwerda. "A nonreflecting outflow boundary condition for subsonic Navier-Stokes calculations". In: *Journal of Computational Physics* 36.1 (1980), pp. 55–70.

[154] Arnaud Fosso P. et al. "Comparison of outflow boundary conditions for subsonic aeroacoustic simulations". In: *International journal for numerical methods in fluids* 68.10 (2012), pp. 1207–1233.

[155] Satish Balay et al. *PETSc Web page.* `https://www.mcs.anl.gov/petsc`. 2019.

[156] Satish Balay et al. *PETSc Users Manual.* Tech. rep. ANL-95/11 - Revision 3.11. Argonne National Laboratory, 2019. URL: `https://www.mcs.anl.gov/petsc`.

[157] Satish Balay et al. "Efficient Management of Parallelism in Object Oriented Numerical Software Libraries". In: *Modern Software Tools in Scientific Computing.* Ed. by E. Arge, A. M. Bruaset, and H. P. Langtangen. Birkhäuser Press, 1997, pp. 163–202.

[158] George Karypis and Vipin Kumar. "A fast and high quality multilevel scheme for partitioning irregular graphs". In: *SIAM Journal on scientific Computing* 20.1 (1998), pp. 359–392.

[159] William Layton and Iuliana Stanculescu. "K-41 optimized approximate deconvolution models". In: *International Journal of Computing Science and Mathematics* 1.2-4 (2007), p. 396.

[160] Iuliana Stanculescu. "Existence theory of abstract approximate deconvolution models of turbulence". In: *Annali dell'Universita'di Ferrara* 54.1 (2008), pp. 145–168.

[161] Guang-Shan Jiang and Chi-Wang Shu. “Efficient implementation of weighted ENO schemes”. In: *Journal of computational physics* 126.1 (1996), pp. 202–228.

[162] Steven J Ruuth and Raymond J Spiteri. “High-order strong-stability-preserving Runge–Kutta methods with downwind-biased spatial discretizations”. In: *SIAM Journal on Numerical Analysis* 42.3 (2004), pp. 974–996.

[163] David I. Ketcheson and Matteo Parsani. *SharpClaw software*. `http://www.clawpack.org/sharpclaw/doc/index.html`. 2011.

[164] Todd Dupont. “L^2-estimates for Galerkin methods for second order hyperbolic equations”. In: *SIAM journal on numerical analysis* 10.5 (1973), pp. 880–889.

[165] John Tinsley Oden and Junuthula Narasimha Reddy. *An introduction to the mathematical theory of finite elements*. Courier Corporation, 2012.

[166] YR Yuan. “Stability and convergence of the finite element method for a class of second order nonlinear hyperbolic equations”. In: *Math Numer Sinica* 5.2 (1983), pp. 149–161.

[167] Q Li. “The generalized Galerkin method for a class of nonlinear hyperbolic equations”. In: *Comput Math* 2 (1986), pp. 150–158.

[168] Tayfun E. Tezduyar and Thomas Jr.. Hughes. “Development of time-accurate finite element techniques for first-order hyperbolic systems with particular emphasis on the compressible Euler equations”. In: *NASA Technical Report NASA-CR-204772, NASA* (1982).

[169] Erik Burman, Alexandre Ern, and Miguel A Fernandez. "Explicit Runge–Kutta schemes and finite elements with symmetric stabilization for first-order linear PDE systems". In: *SIAM Journal on Numerical Analysis* 48.6 (2010), pp. 2019–2042.

[170] Urmila Ghia, Karman N Ghia, and C.T. Shin. "High-Re solutions for incompressible flow using the Navier-Stokes equations and a multigrid method". In: *Journal of computational physics* 48.3 (1982), pp. 387–411.

[171] Robert Vichnevetsky. "Invariance theorems concerning reflection at numerical boundaries". In: *Journal of Computational Physics* 63.2 (1986), pp. 268–282.

[172] Robert Vichnevetsky and John B Bowles. *Fourier analysis of numerical approximations of hyperbolic equations*. Vol. 5. Siam, 1982.

[173] R Vichnevetsky and EC Pariser. "Nonreflecting upwind boundaries for hyperbolic equations". In: *Numerical Methods for Partial Differential Equations* 2.1 (1986), pp. 1–12.

[174] Genevieve Comte-Bellot and Stanley Corrsin. "Simple Eulerian time correlation of full-and narrow-band velocity signals in grid-generated,isotropic turbulence". In: *Journal of Fluid Mechanics* 48.2 (1971), pp. 273–337.

[175] Dochan Kwak, William C Reynolds, and Joel H Ferziger. "Three-dimensional time dependent computation of turbulent flow". In: (1975).

[176] Ashish Misra and T. S. Lund. "Evaluation of a vortex-based subgrid stress model using DNS databases". In: *Proceedings of the Summer Program 1996, Center of Turbulence Research*. CA, United States: NASA, 1996, pp. 359–368.

[177] Sandip Ghosal et al. “A dynamic localization model for large-eddy simulation of turbulent flows”. In: *Journal of fluid mechanics* 286 (1995), pp. 229–255.

[178] T Tantikul and JA Domaradzki. “Large eddy simulations using truncated Navier–Stokes equations with the automatic filtering criterion”. In: *Journal of Turbulence* 11 (2010), N21.

[179] Orestis Malaspinas and Pierre Sagaut. “Advanced large-eddy simulation for lattice Boltzmann methods: The approximate deconvolution model”. In: *Physics of Fluids* 23.10 (2011), p. 105103.

[180] Jens Keiner, Stefan Kunis, and Daniel Potts. “Using NFFT 3—a software library for various nonequispaced fast Fourier transforms”. In: *ACM Transactions on Mathematical Software (TOMS)* 36.4 (2009), p. 19.

[181] Geoffrey Ingram Taylor and Albert Edward Green. “Mechanism of the production of small eddies from large ones”. In: *Proceedings of the Royal Society of London. Series A-Mathematical and Physical Sciences* 158.895 (1937), pp. 499–521.

[182] Stefan Hickel, Nikolaus A Adams, and J Andrzej Domaradzki. “An adaptive local deconvolution method for implicit LES”. In: *Journal of Computational Physics* 213.1 (2006), pp. 413–436.

[183] Olivier Métais and Marcel Lesieur. “Spectral large-eddy simulation of isotropic and stably stratified turbulence”. In: *Journal of Fluid Mechanics* 239 (1992), pp. 157–194.

[184] Jonathan R Bull and Antony Jameson. "Simulation of the Taylor–Green vortex using high-order flux reconstruction schemes". In: *AIAA Journal* 53.9 (2015), pp. 2750–2761.

[185] Marc E Brachet et al. "Small-scale structure of the Taylor–Green vortex". In: *Journal of Fluid Mechanics* 130 (1983), pp. 411–452.

[186] ME Brachet et al. "Numerical evidence of smooth self-similar dynamics and possibility of subsequent collapse for three-dimensional ideal flows". In: *Physics of Fluids A: Fluid Dynamics* 4.12 (1992), pp. 2845–2854.

[187] Satya P Jammy, Christian T Jacobs, and Neil D Sandham. "Performance evaluation of explicit finite difference algorithms with varying amounts of computational and memory intensity". In: *Journal of Computational Science* (2016).

[188] JH Williamson. "Low-storage runge-kutta schemes". In: *Journal of Computational Physics* 35.1 (1980), pp. 48–56.

[189] Zhijian J Wang et al. "High–order CFD methods: current status and perspective". In: *International Journal for Numerical Methods in Fluids* 72.8 (2013), pp. 811–845.

[190] Chi-Wang Shu et al. "Numerical convergence study of nearly incompressible, inviscid Taylor–Green vortex flow". In: *Journal of Scientific Computing* 24.1 (2005), pp. 1–27.

[191] Scott C Morris and John F Foss. "Vorticity spectra in high Reynolds number anisotropic turbulence". In: *Physics of Fluids* 17.8 (2005), p. 088102.

[192] Robert H Kraichnan. "The structure of isotropic turbulence at very high Reynolds numbers". In: *Journal of Fluid Mechanics* 5.4 (1959), pp. 497–543.

[193] Katepalli R Sreenivasan. "On the scaling of the turbulence energy dissipation rate". In: *The Physics of fluids* 27.5 (1984), pp. 1048–1051.

[194] Seyed G Saddoughi and Srinivas V Veeravalli. "Local isotropy in turbulent boundary layers at high Reynolds number". In: *Journal of Fluid Mechanics* 268 (1994), pp. 333–372.

[195] Seyed G Saddoughi. "Local isotropy in complex turbulent boundary layers at high Reynolds number". In: *Journal of Fluid Mechanics* 348 (1997), pp. 201–245.

[196] Cedric Poulain et al. "Spectral vorticity and lagrangian velocity measurements in turbulent jets". In: *Flow, Turbulence and Combustion* 72.2-4 (2004), pp. 245–271.

[197] Christian Clason. "Finite Element Methods". In: *arXiv preprint arXiv:1709.08618* (2017).

[198] Erik Burman. "Consistent SUPG-method for transient transport problems: Stability and convergence". In: *Computer Methods in Applied Mechanics and Engineering* 199.17-20 (2010), pp. 1114–1123.

[199] Julien Berland, Christophe Bogey, and Christophe Bailly. "Analysis of Numerical Error Reduction in Explicitly Filtered LES Using Two-Point Turbulence Closure". In: *Quality and Reliability of Large-Eddy Simulations*. Springer, 2008, pp. 143–154.

[200] Marcel Lesieur. *Turbulence in fluids: stochastic and numerical modelling*. Nijhoff Boston, MA, 1987.

[201] Alireza Najafi-Yazdi. "Large eddy simulation of sound generation by turbulent reacting and nonreacting shear flows". PhD thesis. McGill University Libraries, 2011.

[202] Alireza Najafiyazdi, Phoi-Tack Lew, and Luc Mongeau. "Large Eddy Simulation of Jet Noise Suppression by Impinging Microjets". In: *17th AIAA/CEAS Aeroacoustics Conference (32nd AIAA Aeroacoustics Conference)*. 2011, p. 2748.

[203] Tayfun E. Tezduyar and Thomas J. R. Hughes. "Finite element formulations for convection dominated flows with particular emphasis on the compressible Euler equations". In: *21st Aerospace Sciences Meeting*. 1983, p. 125.

[204] Thomas Jr. Hughes and Tayfun E. Tezduyar. "Finite element methods for first-order hyperbolic systems with particular emphasis on the compressible Euler equations". In: *Computer methods in applied mechanics and engineering* 45.1-3 (1984), pp. 217–284.

[205] Shakib, Farzin and Hughes, Thomas Jr. and Johan, Zdeněk. "A new finite element formulation for computational fluid dynamics: X. The compressible Euler and Navier-Stokes equations". In: *Computer Methods in Applied Mechanics and Engineering* 89.1-3 (1991), pp. 141–219.

[206] Culbert B. Laney. *Computational gasdynamics*. Cambridge university press, 1998.

[207] Tayfun E Tezduyar and Y. J. Park. "Dinscontinuity capturing finite element formulations for nonlinear onvection-diffusion-reaction equations". In:

Computational Methods in Applied Mechanics and Engineering 59.3 (1986), pp. 307–325.

[208] Thomas J. R. Hughes, Guglielmo Scovazzi, and Leopoldo P. Franca. “Multiscale and Stabilized Methods”. In: *Encyclopedia of Computational Mechanics*. Ed. by Erwin Stein, René de Borst, and Thomas J. R. Hughes. 2nd ed. Vol. 3. John Wiley & Sons, Ltd., 2018, pp. 1–64.

[209] Shahrouz K. Aliabadi, Stephen Edward Ray, and Tayfun E. Tezduyar. “SUPG finite element computation of viscous compressible flows based on the conservation and entropy variables formulations”. In: *Computational Mechanics* 11.5-6 (1993), pp. 300–312.

[210] Michael B. Giles and William T. Thompkins. “Propagation and stability of wavelike solutions of finite difference equations with variable coefficients”. In: *Journal of Computational Physics* 58.3 (1985), pp. 349–360.

[211] Jean Donea. “A Taylor–Galerkin method for convective transport problems”. In: *International Journal for Numerical Methods in Engineering* 20.1 (1984), pp. 101–119.

[212] Olivier Colin and Michael Rudgyard. “Development of high-order Taylor–Galerkin schemes for LES”. In: *Journal of Computational Physics* 162.2 (2000), pp. 338–371.

[213] Arnaud Fosso-Pouangue, Marléne Sanjosé, and Stephane Moreau. “Jet noise simulation with realistic nozzle geometries using fully unstructured LES solver”. In: *18th AIAA/CEAS Aeroacoustics Conference (33rd AIAA Aeroacoustics*

Conference). Reston, Virigina: American Institute of Aeronautics and Astronautics, June 2012.

[214] Fosso Pouangué, A. and Sanjosé, M. and Moreau, S. and Daviller, G. and Deniau, H. "Subsonic Jet Noise Simulations Using Both Structured and Unstructured Grids". In: *AIAA Journal* 53.1 (Jan. 2015), pp. 55–69.

[215] Junhui Liu et al. "Large-Eddy Simulations of a Supersonic Jet and Its Near-Field Acoustic Properties". In: *AIAA Journal* 47.8 (2009), pp. 1849–1865.

[216] Pouangué, A Fosso and Sanjosé, M and Moreau, S. "Large Eddy Simulation of a jet with an internal lobed mixer". In: *21st Annual Meeting of the Canadian Society of CFD, Sherbrooke, Canada*. 2013.

[217] Marléne Sanjosé et al. "A comparison between Garlerkin and compact schemes for jet noise simulations". In: *AIAA Paper* 2833 (2011), pp. 7–9.

[218] L Quartapelle and V Selmin. "High-order Taylor-Galerkin methods for nonlinear multidimensional problems". In: *Finite Elements in Fluids* 76.90 (1993), p. 46.

[219] J. Donea, B. Roig, and A. Huerta. "High-order accurate time-stepping schemes for convection-diffusion problems". In: *Computer Methods in Applied Mechanics and Engineering* 182.3-4 (2000), pp. 249–275.

[220] A. J. Baker and J. W. Kim. "A Taylor weak-statement algorithm for hyperbolic conservation laws". In: *International Journal for Numerical Methods in Fluids* 7.5 (1987), pp. 489–520.

[221] Jean Donea and Luigi Quartapelle. "An introduction to finite element methods for transient advection problems". In: *Computer Methods in Applied Mechanics and Engineering* 95.2 (1992), pp. 169–203.

[222] Amiram Harten and Hillel Tal-Ezer. "On a fourth order accurate implicit finite difference scheme for hyperbolic conservation laws. I. Nonstiff strongly dynamic problems". In: *Mathematics of Computation* 36.154 (1981), pp. 353–373.

[223] Chi Wang Shu and Stanley Osher. "Efficient implementation of essentially non-oscillatory shock-capturing schemes". In: *Journal of Computational Physics* 77.2 (1988), pp. 439–471.

[224] P. Turan. "On the theory of the mechanical quadrature". In: *Acta Scientiarum Mathematicarum* 12A (1950), pp. 30–37.

[225] K H Kastlunger and G Wanner. "Runge Kutta Processes with Multiple Nodes". In: *Computing* 9 (1972), pp. 9–24.

[226] K. Kastlunger and G. Wanner. "On Turan type implicit Runge-Kutta methods". In: *Computing* 9.4 (1972), pp. 317–325. ISSN: 0010485X.

[227] R. P K Chan and A. Y J Tsai. "On explicit two-derivative Runge-Kutta methods". In: *Numerical Algorithms* 53.2-3 (2010), pp. 171–194. ISSN: 10171398.

[228] Gary A Sod. "A survey of several finite difference methods for systems of nonlinear hyperbolic conservation laws". In: *Journal of Computational Physics* 27.1 (Apr. 1978), pp. 1–31.